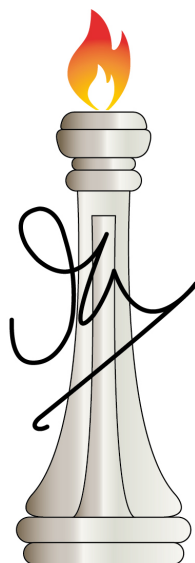# Studies on the Photophysics and Charge Carrier Dynamics in Solution-Processed Semiconductors using Time and Frequency Domain Measurements

A Thesis for the partial fulfillment of
DOCTOR OF PHILOSOPHY
by
ANARANYA GHORAI

JNCASR

CHEMISTRY AND PHYSICS OF MATERIALS UNIT
JAWAHARLAL NEHRU CENTRE FOR ADVANCED
SCIENTIFIC RESEARCH
(A DEEMED UNIVERSITY)
BANGALORE - 560064
DECEMBER 2022

Dedicated to my parents and my brother

DECLARATION

I hereby declare that the matter embodied in this thesis titled "**Studies on the Photophysics and Charge Carrier Dynamics in Solution-Processed Semiconductors using Time and Frequency Domain Measurements**" is the result of the work carried out by me under the supervision of Prof. K. S. Narayan, at Molecular Electronics Laboratory, in Chemistry and Physics of Materials Unit, Jawaharlal Nehru Centre for Advanced Scientific Research, Bangalore, India. It has not been submitted for the Award of any degree or diploma or associateship of any other university or institute.

In keeping with the general practice in reporting scientific observations, due acknowledgment has been made whenever the work described is based on the findings of other investigators.

(Anaranya Ghorai)

Candidate

JAWAHARLAL NEHRU CENTRE FOR ADVANCED SCIENTIFIC RESEARCH
Jakkur, Bangalore 560064, India

K. S. NARAYAN
Professor
PHONE: 91 80 22082822
FAX: 91 80 22082766
e-mail: narayan@jncasr.ac.in
URL: www.jncasr.ac.in/narayan

15th December 2022

CERTIFICATE

I hereby certify that the matter embodied in the thesis entitled "**Studies on the Photophysics and Charge Carrier Dynamics in Solution-Processed Semiconductors using Time and Frequency Domain Measurements**" has been carried out by Mr. Anaranya Ghorai at the Molecular Electronics Laboratory, Chemistry and Physics of Materials Unit, Jawaharlal Nehru Centre for Advanced Scientific Research, Bangalore, India, under my supervision and it has not been submitted elsewhere for the award of any degree or diploma.

Prof. K. S. Narayan

(Research Supervisor)

Acknowledgements

I would like to express my sincere thanks and gratitude to my research supervisor Prof. K. S. Narayan, for his constant source of support and encouragement. His guidance and suggestions on the choice of research topics have given me confidence in exploring this field. I am ever grateful to him for giving me the opportunity to pursue science and introducing me to the scientific community. He has given me abundant scientific inputs and also provided me with utmost freedom to explore while at the same time ensuring scientific rigour and accountability.

I consider myself extremely lucky to be a part of the Molecular Electronics Lab where I was involved with many exceptional researchers and exchanged ideas and perspectives in academic and non-academic subjects. I would like to thank all the past and present lab members: Sumukh, Manish, Sinay, Pratik, Shreyas, Dr Ganesh, Dr Prashant, Dr Swathi, Dr Raaghesh, Dr. Anita, Dr Suman Banerjee, Dr Ashar, Dr Ishan, Dr Swanand, Dr Kanti, Dr Rahul Sharma, Dr Ravichandran Shivanna, Nisha, Apoorva, Sukanya, Gaurav, Deepak, Abhijit, Abdul Azeez, Sunoj, Shilauni, Girish, Chandan, Gulshan, Ambika and Late Anil Krishna. I would like to especially thank Sumukh, Manish and Sinay, with whom I worked on various projects and gained many insights into this research field. I am blessed to have had many discussions with my seniors, especially with Dr Swathi, Dr Raaghesh, Dr Prashant and Dr Ravichandran Shivanna and learnt the art of handling all the sophisticated equipment in the lab. Heartfelt thanks to Late Anil Krishna, with whom I had so many fun-filled memories inside and outside the lab.

In the thesis

- **Anaranya Ghorai**, Prashant Kumar, Suhas Mahesh, Yen-Hung Lin, Henry J Snaith, and KS Narayan, "Insights into the charge carrier dynamics in perovskite/Si tandem solar cells using transient photocurrent spectroscopy," Applied Physics Letters 120 (17), 173504 (2022).

  Author Contributions: The author has performed the transient photocurrent measurements, scattering matrix modelling and analysed the results, under the supervision of Prof. K.S Narayan. Prof. K.S. Narayan conceptualised the problem. The paper was jointly written by the author, Prashant Kumar and Prof. K.S. Narayan.

- **Anaranya Ghorai**, Sinay Simanta Behera, Sumukh Purohit and KS Narayan, "Probing charge carrier and triplet dynamics in TADF-based OLEDs using transient electroluminescence studies" (*Manuscript submitted*).

  Author Contributions: The author has fabricated OLEDs and performed the transient electroluminescence measurements jointly with Sinay Simanta Behera, kinetic modelling and analysed the results under the supervision of Prof. K.S Narayan. Prof. K.S. Narayan conceptualised the problem. The paper was jointly written by the author, Sinay Simanta Behera and Prof. K.S.

Narayan.

- **Anaranya Ghorai**, Pratik Walvekar, Shreyas Nayak, and KS Narayan, "Influence of non-line of sight luminescent emitters in visible light communication systems," Journal of Optics 20 (1), 015703 (2017).

  Author Contributions: The author has performed the fluctuation measurements in different emitters and analysed the results under the supervision of Prof. K.S Narayan. Prof. K.S. Narayan conceptualised the problem. The paper was jointly written by the author and Prof. K.S. Narayan

- **Anaranya Ghorai**, Manish Tiwari, Sumukh Purohit, and KS Narayan, "Photon Correlation Spectroscopy of TADF molecules" (*Manuscript submitted*).

  Author Contributions: The author has built the microscope jointly with Manish Tiwari and Sumukh Purohit, fabricated and measured the samples and analysed the results under the supervision of Prof. K.S Narayan. Prof. K.S. Narayan conceptualised the problem. The paper was jointly written by the author and Prof. K.S. Narayan

- **Anaranya Ghorai**, Sumukh Purohit, Manish Tiwari, and KS Narayan, "Electrospun Fibers Doped with Emissive Thermally activated delayed fluorescence molecules" (*Manuscript under preparation*).

  Author Contributions: The author has fabricated the fibers jointly with Sumukh Purohit, measured the samples jointly with Manish Tiwari, simulated the eigenmodes and analysed the results under the supervision of Prof. K.S Narayan. Prof. K.S. Narayan conceptualised the problem. The author and Prof. K.S. Narayan is jointly writing the paper.

Miscellaneous

- Suman Kuila, **Anaranya Ghorai**, Pralok K Samanta, Raja BK Siram, Swapan K Pati, KS Narayan, and Subi J George, "Red Emitting Delayed Fluorescence and Room Temperature Phosphorescence from Core –Substituted Naphthalene Diimides," Chemistry –A European Journal 25 (70), 16007 –16011 (2019).

- N Ganesh, **Anaranya Ghorai**, Shrreya Krishnamurthy, Suman Banerjee, KL Narasimhan, Satishchandra B Ogale, and KS Narayan, "Impact of trap filling on carrier diffusion in MAPbBr$_3$ single crystals," Physical Review Materials 4 (8), 084602 (2020).

- Bhanu Pratap Dhamaniya, Amit Kumar, N Ganesh, Priyanka Chhillar, **Anaranya Ghorai**, Krishna Priya Ganesan, Suresh E Puthanveettil, Narayan KS, and Sandeep Kumar Pathak, "Morphology and Crystallinity Amelioration of MAPbI$_2$ Perovskite in Virtue of PbI$_2$ Thermal Absorption Drifted Performance Enhancement in Planer n –i –p Solar Cells," Advanced Engineering Materials 23 (3), 2000990 (2021).

Contents

XIX

Synopsis

The range of solution-processed semiconductors from perovskites to organic molecular systems with long emission lifetimes poses many interesting questions and offers novel applications. The thesis focuses on the photo-physical studies in different classes of semiconductors in response to optical and electrical excitations. The recombination and charge carrier dynamics in these materials were probed using time and frequency domain measurements.

The first part of the thesis (Chapter 2) deals with the studies on the charge carrier dynamics using transient photocurrent (TPC) spectroscopy measurements on tandem solar cells under optical excitation. The active layers composed of direct bandgap perovskite and the indirect band gap Si, have different optoelectronic properties and thicknesses. The TPC measurements directly assess the timescales of photogenerated charge carriers extracted at the electrodes. Moreover, spectral dependence of TPC measurements exhibits two distinct lifetime magnitudes: τ_1 and τ_2. $\tau_1 \sim 500$ ns, represents the absorption in the top perovskite sub-cell (λ - 300 nm to 750 nm), while $\tau_2 \sim 25$ μs correspond to absorption in the rear Si sub-cell ($\lambda > 700$ nm). Further analysis shows that the carriers are extracted via drift and diffusion processes in the perovskite sub-cell, whereas Si sub-cell follows a diffusion-limited carrier extraction process. In the absence of background illumination, sub-cell processes are uncorrelated, and the current magnitude depends on the shunt resistance of the other sub-cell in the dark. A crossover of the dynamics of the perovskite sub-cell to a coupled regime with the

Si sub-cell is observed beyond a threshold dc-light illumination. The studies indicate that fine-tuning the two active layer thicknesses can further optimize absorption, carrier transit times and lifetimes and lead to higher efficiencies.

The next part of the thesis focuses on thermally activated delayed fluorescence (TADF) in organic light-emitting diodes (OLEDs). These systems are expected to show increased emissive yield due to efficient back-conversion of nonemissive triplet states to emissive singlet states via reverse intersystem crossing (RISC). Chapter three presents the charge carrier and exciton dynamics in solution-processed 4CzFCN molecules using temperature-dependent transient electroluminescence (trEL) studies. The temperature (T) dependent results show an overall reduction in light emission at low temperatures due to reduced current injection and transport barriers. However, the delayed light emission fraction increases as T is reduced and this feature is attributed to triplet-triplet annihilation (TTA) processes. Triplet harvesting occurs via both RISC and TTA. Further analysis suggests that TADF processes are dominant at high T, and at low T TTA processes appear to be dominant.

Chapter four deals with an application where the difference in recombination timescales of emitters is utilized to alter signal transmission in visible light communication (VLC) systems. A non-line of sight VLC system was demonstrated where detectors respond to contributions from the light source scattered off a surface embedded with fluorescent and phosphorescent emitters besides the direct line of sight signal. It is observed that the phosphorescent medium has the ability to change the photon number distribution and therefore can be used to intervene and distort the transmitted signal. Contribution from the emitters takes the form of discernible fluctuations in the detector signal, thus limiting their bandwidth to a great extent. The spatial dependence of the light scattering sites offers tunability of the S/N ratio levels, and this feature can be utilized to design smart environments where signal access could be controlled and restricted.

Chapter five deals with the imaging of organic dyes at low con-

centration levels to enable single molecule studies. This methodology is helpful since the dyes exhibit different photo-physical kinetics at the single molecule level owing to reduced intermolecular interactions. A custom-built confocal microscopy assembly was constructed to study these emitters at dilute concentrations. Photon statistics of various concentrations of molecules were measured using a single photon avalanche diode (SPAD) integrated with the microscope. The photon statistics reveal correlations between the emitted photon from a TADF emitter at the initial timescales.

Finally, in chapter six, the recombination dynamics of TADF molecules are studied in a fibre cavity formed by electrospinning method. The TADF-dispersed PMMA fibres exhibit high luminescence and stability. The spatially uniform fibre emission suggests the homogenous distribution of dye molecules extended over the fibre, highlighting light confinement and waveguiding. Eigenmode analysis suggests the presence of cavity modes where the electric field profiles have nodes at the centre of the fibre.

List of Figures

List of Tables

1

Introduction

The development of conductive polymers to solution-processed semiconductors in the last few decades paved the way for flexible electronic devices in applications not fulfilled by conventional electronics. Flexible electronic devices (displays, memories, detectors, electrodes, and circuits) from solution-processed materials form essential components in the new generation of smart technology. The solution-processed semiconductors have a vast array of advantages, including bandgap tunability, high absorption coefficient, low cost, low material consumption, low-temperature processability, etc. The cost-effective techniques for fabricating flexible devices include spin-coating, inkjet printing, screen printing and roll-to-roll processing. An extensive library of these semiconductors is available, allowing for application-specific material selection.

This thesis uses two broad classes of solution-processed semiconductors: organic molecular and hybrid organic-inorganic perovskites (HOIP). *The thesis focusses on probing the various recombination and charge transport mechanisms in these semiconductors using a combination of frequency and time domain measurements.* The field of solution-processed electronics is vast; hence, only the relevant background for the problems undertaken in this thesis has been selected for discussion in this chapter. This chapter initially introduces excitonic processes in organic semiconductors, followed by a discussion on hybrid organic-inorganic perovskite semiconductors. An introduction to various solution-processed optoelectronic devices like light-emitting diodes (LEDs) and solar cells have also been included. Lastly, the various

measurements in the time and frequency are listed with a particular emphasis on time-correlated single photon counting.

1.1 Organic Semiconductors

The origin of organic semiconductors can be traced to conjugated molecules that consist of alternate single and double bonds linking carbon atoms. These materials form a category of semiconductor systems that combine a semiconducting attribute with the mechanical and chemical features of organic materials (e.g., polymers). They can be modified chemically to tune their electronic properties (absorption and emission wavelength) and allow the fabrication of flexible and robust thin films. The conductivity in organic semiconductors usually arises from charge injection at the electrodes or the carriers derived from the dissociation of excitons [1]. This is a consequence of two distinct properties in organic semiconductors. Firstly, the energy associated with absorption and emission processes usually lies in the range of 2-3 eV, which reduces the probability of generating intrinsic carriers at room temperatures via thermal excitation. Secondly, the dielectric constant (ϵ_r) of organic molecules are relatively low (~ 3.5), implying significant Coulombic interactions (~ 0.5–1 eV) between a photogenerated electron-hole pair (exciton).

1.1.1 Orbital picture of organic molecules

The building block of organic/polymer electronic materials are mostly carbon and hydrogen atoms. The organic molecules also contain nitrogen, oxygen and sulphur alongside them. The electronic structure of a typical organic molecule can be visualised using the molecular orbital (MO) theory. The MO theory gives insights into the various transitions occurring inside the molecules. A molecular orbital (ψ) in an organic molecule is approximately a linear combination of atomic orbitals (LCAO), i.e., $\psi = \sum_i c_i \phi_i$ where ϕ_i represents the wavefunction of the ith molecular orbital. For example, the molecular orbitals for the ethene molecule take into account the interactions between two 1s orbitals, two 2sp^2 hybrid orbitals (threefold degenerate) and two 2p$_z$ orbitals of the respective carbon atoms [1, 2]. The 1s orbitals form
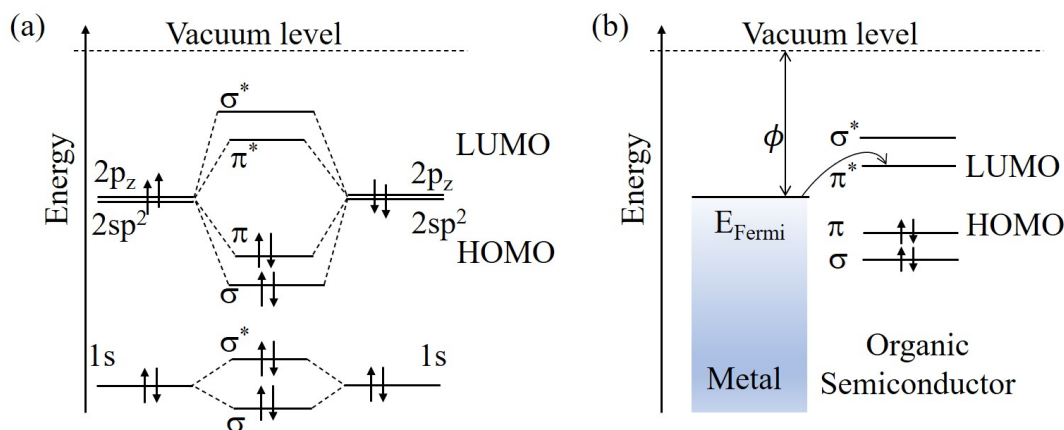
Figure 1.1: (a) The formation of σ and π orbitals in ethene and (b) frontier orbitals of organic semiconductors relative to electrode work functions.

σ and σ^* orbitals with negligible resonance interaction between them owing to them being close to the nucleus. One of the 2sp^2 orbitals lie along the internuclear axis resulting in a large resonance integral splitting the σ and σ^* orbitals due to the large charge density overlap between the nuclei. The other 2sp^2 orbitals interact with the 1s orbitals of hydrogen, resulting in strongly bonded σ and σ^* orbitals. However, the interaction of 2p_z orbital takes place away from the nuclear plane, resulting in a comparatively weaker splitting between the π and π^* orbitals. Figure 1.1a shows the interaction of carbon atoms in ethene. Upon filling, the electrons get filled only till π orbital. Thus, for ethene, the π orbital acts as the highest occupied molecular orbital (HOMO) and π^* acts as the lowest unoccupied molecular orbital (LUMO).

When carriers (electron or hole) are injected into the molecule, the electron gets filled to the LUMO. Similarly, an electron being withdrawn from the HOMO results in the injection of a hole (Figure 1.1b) [1]. Owing to the significant resonance interaction involved in the case of σ and σ^* orbitals, they are at very high and low energies making charge injection very difficult. Molecules having σ as their frontier orbitals, the $\sigma \rightarrow \sigma^*$ transition generally corresponds to a larger energy range, typically in the deep ultraviolet. However, $\pi \rightarrow \pi^*$ transitions in molecules lie in a lower-energy range owing to them having comparatively lower splitting. There can also be transitions between the HOMO which can be a non-bonding (n) orbital (lone

pairs of oxygen or nitrogen lying on the molecular plane) possessing some σ character and the LUMO (a π^* orbital not located on the molecular plane) [1]. These transitions are called $n \rightarrow \pi^*$ transitions. The transitions in a molecule are usually visualised in terms of ground and excited states, which are discussed in the next section.

1.1.2   States in an organic molecule

The energies of the orbitals in a molecule are calculated using the Schrodinger equation. However, these calculations cannot be done analytically for many-electron systems owing to the motion of electrons. Thus, a molecule consisting of several electrons is approximated in a hypothetical case where the molecule has only one electron, and a mean-field approximates the potential energy corresponding to the other electrons [1]. The molecular orbitals in these cases are one-electron orbitals, and one can calculate and fill them with electrons present in the molecule. Thus, the many-electron wavefunction for the molecular ground state is given as $\psi_{el} = \prod_i \psi_{el,i}$ [1]. However, this rough approximation does not consider any interaction between the electrons.

The electronic wavefunction ψ_{el}, generally describes the function of the spatial coordinates of the electrons and the nuclei. The total spin of all electrons gives the spin of an electronic state. The electrons in the filled orbitals are usually paired with anti-parallel spins, thus having zero contribution to the total net spin. Therefore, it is adequate to consider only the unpaired electrons at the frontier orbitals in an excited state configuration, i.e., a single electron both in π and π^* orbital. The configuration of a molecule in the excited state where the frontier orbitals (π and π^*) both have opposite spins is known as the *singlet* state, and the total spin adds up to zero (Figure 1.2a). When the spin in both π and π^* orbital are the same, adding the total spin to be one in units of $\hbar$, the configuration is known as a *triplet* state (Figure 1.2a). Thus, the excited states in a molecule are arranged in an energetic order S_1, S_2, or T_1, T_2, and so on for singlets and triplets. These unpaired electrons in the frontier orbitals form a two-particle system. Considering α and β as the one-electron spin wavefunctions,

the four eigenstates corresponding to the two-particle in the absence of a magnetic field are [3]:

$$\psi_{spin,T_x}) = \frac{1}{\sqrt{2}}(\beta_1\beta_2 + \alpha_1\alpha_2)$$
$$\psi_{spin,T_z} = \frac{1}{\sqrt{2}}(\alpha_1\beta_2 + \beta_1\alpha_2)$$
$$\psi_{spin,T_y} = \frac{1}{\sqrt{2}}(\beta_1\beta_2 + \alpha_1\alpha_2)$$
$$\psi_{spin,S} = \frac{1}{\sqrt{2}}(\alpha_1\beta_2 - \beta_1\alpha_2)$$

(1.1)

The indices 1 and 2 correspond to electrons 1 and 2. The first three spin wavefunctions correspond to $S = 1$ and are known as *triplets*, while the fourth wavefunction corresponds to $S = 0$ and is referred to as a *singlet* (Figure 1.2b) [1].
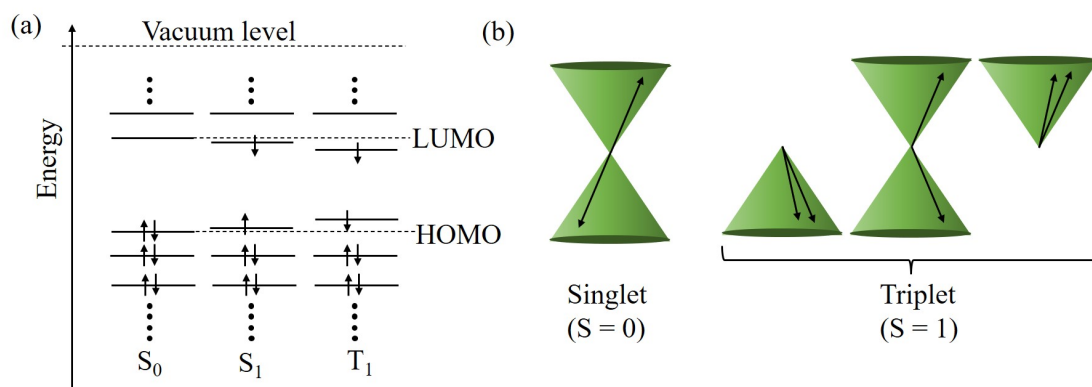
Figure 1.2: (a) Orbital picture of singlet and triplet states. Only one spin configuration is shown for the triplet state, (b) Vector diagram illustrating the relative orientations of the two electron spins in the singlet and triplet states

The atomic nuclei in a molecule oscillate with vibrational frequency ω around their equilibrium positions. The potential energy corresponding to the nuclei for low vibrational energies can be approximated as a harmonic oscillator potential. The vibrational energy corresponding to the oscillations is $(n + 1/2)\hbar\omega$, where n is the number of vibrational states. The vibrational wavefunction ψ_{vib} describe the oscillations of the nuclei in the molecule.

Thus, the total wavefunction of the state of an organic molecule

can be approximated as [1].

$$\psi_{total} = \psi_{wl}\psi_{vib}\psi_{spin} \qquad (1.2)$$

1.1.3 Transitions between the states of a molecule

The understanding of light-molecule interaction lays the foundations for photophysical studies in these materials. The transitions in a molecule (absorption and emission) are usually described using the electric dipole operator $e\hat{r}$ which acts as the perturbing Hamiltonian operator H'. Thus, the transition rate (k_{if}) between two states is given by Fermi's golden rule, which is [1]

$$k_{if} = \frac{2\pi}{\hbar} < \psi_{el,f}\psi_{vib,f}\psi_{spin,f}|e\hat{r}|\psi_{el,i}\psi_{vib,i}\psi_{spin,i} > \rho \qquad (1.3)$$

where ρ is the final density of states.

The electromagnetic (EM) wave can be physically interpreted as a time-dependent electric dipole that resonantly oscillates the electrons. However, the nuclei in the molecule are too bulky to respond to the timescale of these oscillating electric fields. Further, the spins also remain unaffected by these oscillating electric field. So, the dipole operator does not affect $\psi_{spin}(\alpha_i, \beta_i)$ and $\psi_{vib}(R_i)$ thereby acting only on $\psi_{el}(r_i, R_i)$. Thus, Eq. 1.3 can be rearranged and written as [1]

$$k_{if} = \frac{2\pi}{\hbar} < \psi_{el,f}|e\hat{r}|\psi_{el,i} >< \psi_{vib,f}|\psi_{vib,i} >< \psi_{spin,f}|\psi_{spin,i} > \rho \quad (1.4)$$

The integral expression $< \psi_{el,f}|e\hat{r}|\psi_{el,i} >$ is called the electronic factor in a transition and is dependent on the spatial overlap of orbitals and therefore controls the overall strength of a transition. The oscillator strength gives the experimental measure of the intensity of this transition [1]. The rates between orbitals on the same parts of the molecule are higher than those between those at a spatially different place. Charge transfer (CT) transitions, $n \to \pi^*$ transitions, and metal-to-ligand charge transfer (MLCT) are some examples of transitions where the HOMO and LUMO are located at different spatial positions. Donor-acceptor molecules or systems commonly possess CT states and undergo these CT transitions.

The overlap function, $< \psi_{vib,f}|\psi_{vib,i} >$ controls the shape of the absorption or emission spectrum [1]. Th energy difference between two consecutive vibrational energy levels lies in the range of 0.1 to 0.3 eV, thus inferring the occupancy of only the lowest vibrational level at room temperature [1]. In the excited state, the electrons reside in the antibonding orbital. This configuration, therefore, reduces the overall density between the atomic cores leading to a larger equilibrium distance compared to the ground state. Thus, the potential energy curve of the excited state has a larger magnitude of configuration coordinate Q. The transition probability from the 0th vibrational level in the ground state to the mth vibrational level in the excited state is given by the *Frank Condon factor* [1], $| < \psi_{vib,f}|\psi_{vib,i} > |^2$.

The value of the final term $< \psi_{spin,f}|\psi_{spin,i} >$ becomes zero when initial and final states have different spins, and equals one when they are same. Thus, transitions between singlet states ($S_1 \rightarrow S_0$ and $S_n \rightarrow S_1$) or triplet states ($T_n \rightarrow T_1$) are allowed. However, transition between $T_1 \rightarrow S_0$ is forbidden. The spin-forbidden transition $T_1 \rightarrow S_0$ transition is only possible when, by perturbation, the wavefunction corresponding to the triplets acquires contributions from the singlet state and vice versa.

1.1.4   Excited state processes in organic semiconductors

The ground state of organic molecules generally consists of a pair of bonded electrons or non-bonded lone pairs. This generally results in the ground state of a molecule being a singlet. However, the excited states in a molecule can be very different and depend on the excitation process. Under optical excitation, 100% of singlets are generated, as the direct population of triplets from ground-state singlets is spin forbidden. However, under electrical excitation, the electrons and holes generally get injected into the frontier orbitals of the molecule. The carriers combine to form 25% singlets and 75% triplets, owing to prevailing spin statistics [4].

When an organic molecule absorbs a photon (optical excitation),
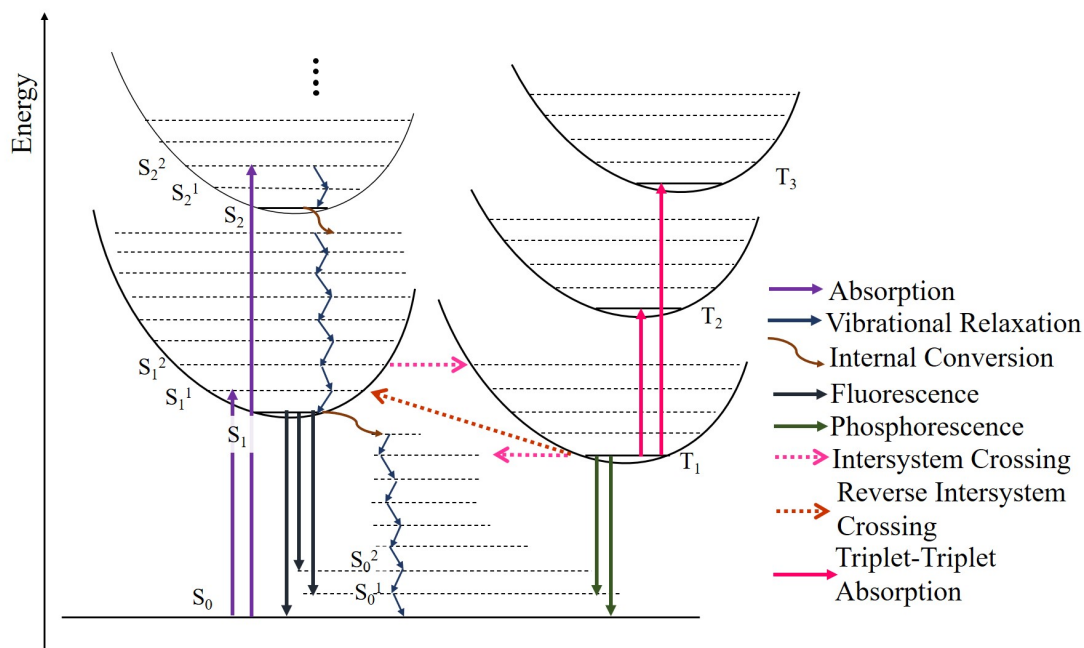
Figure 1.3: The Perrin-Jablonski diagram showing the important excited state transitions upon photoexcitation. The process of triplet absorption ($T_1 \rightarrow T_n$) occurs under specific experimental conditions.

it transitions from the lowest vibrational state of S_0 to one of the vibrational levels of excited singlet states (S_n, $n > 0$) by Fermi's golden rule. The timescale of this process lies in the range of $\sim$fs. The absorption process follows the total angular momentum conservation, so only singlet-singlet transition is allowed, whereas singlet-triplet transition is forbidden [5].

In the excited state, the molecule reaches a non-equilibrium state, dissipates the energy, and returns to the ground state. Initially, it follows a vibrational relaxation (VR) pathway, a non-radiative transition to the lower vibrational level within the same electronic state. The excess energy in this process is dissipated by heat to the vibrational modes of the molecule until it reaches the lowest vibrational level of that particular electronic state. The timescale of VR ranges from 10^{-12} to 10^{-10} s.

Once the molecule is in the lowest vibrational state of a higher-lying singlet state (say S_2 state), it quickly undergoes internal conversion (IC) to reach the lowest excited singlet state, S_1. A quick VR again follows this process to reach the lowest vibrational level of S_1. Internal

conversion is a non-radiative transition between two states having the same spin multiplicity. This process also applies to triplets where the high-lying triplet state T_n undergoes a transition back to T_1. The rate at which IC takes place depends on the energy difference between the initial and final states. The rate is much faster for closely lying singlet states (say $S_3 \rightarrow S_2$) than compared to $S_1 \rightarrow S_0$. When a molecule reaches the S_1 state, the IC process competes with other relaxation processes like fluorescence and intersystem crossing (ISC) (described in the following paragraphs).

The radiative transition from S_1 to S_0 is known as a fluorescence process. The timescale of a fluorescence process ranges from 10^{-10} to 10^{-7} s. Fluorescence transition always occurs from the lowest vibrational level of the first singlet excited state (S_1) to the ground singlet state (S_0). This empirical rule is famously known as Kasha's rule, which states that "luminescence only occurs with appreciable yield from the lowest excited state of a given multiplicity". Kasha's rule explains the Stokes shift, where the fluorescence spectra are generally red-shifted compared to the absorbance spectra.

The S_1 state can also undergo another transition called ISC, a non-radiative transition between two iso-energetic vibrational levels belonging to states with different spin multiplicity, i.e., from singlet to triplet. This process is formally spin-forbidden as the total angular momentum is not conserved. This process is inefficient and requires the triplet to acquire a partial character from the singlet state and vice versa. This is generally achieved using a strong spin-orbit coupling which makes the ISC process competitive compared to IC and fluorescence. The typical timescales of an ISC range from 10^{-10} to 10^{-8} s in a molecule possessing a sizeable spin-orbit coupling strength.

The molecule in the triplet state (T_1) undergoes VR to reach the lowest vibrational state. The radiative transition from the $T_1 \rightarrow S_0$ state is known as phosphorescence. However, this is also a spin-forbidden process similar to ISC, requiring the triplet to acquire a partial singlet character. The timescales of phosphorescence are longer

than the processes described before, ranging from 10^{-6} to 10 s. Due to triplets' long lifetime, they are highly susceptible to non-radiative vibrational relaxations dissipating the excited energy as heat. The most efficient way to counter it is to freeze the molecular motions using either cryogenic conditions or by designing molecules with restricted molecular motions. Additionally, due to the spin allowed triplet-triplet energy transfer to molecular oxygen, owing to the molecular oxygen ground state being of triplet nature, the triplets are quenched in the presence of oxygen. Thus, triplets generally act as energy loss pathways in organic semiconductors.

The T_1 state can also undergo a reverse intersystem crossing (RISC) if the energy difference between the S_1 and T_1 is less than the room temperature. The RISC process involves harvesting the triplets, which are major efficiency bottlenecks in molecules where the excitation is electrical, for example, in light-emitting diodes (LEDs). The various excited state transitions under optical excitation are shown in Figure 1.3.

1.1.5   Organic Light Emitting Diodes (OLEDs)

The major goal for designing highly emissive organic molecules is for them to finally be realized as light-emitting structures under electrical injection. The solution processability feature of organic molecules make them excellent candidates for realizing efficient, low cost and robust light-emitting structures. Tang and Van Slyke in 1987, reported the first low voltage operated amorphous thin film OLED using the molecule Alq$_3$ [6]. In 1990, this was followed by a demonstration of a solution-processed OLED using a non-doped π-conjugated polymer (PPV) [7]. These demonstrations kick-started the field of OLEDs, which are now used extensively as displays [8, 9] for cell phones and televisions.

The simplest structure of an OLED consists of a thin film of an organic molecule sandwiched between two electrodes. One of the two electrodes acts as the anode and the other as the cathode, injecting holes and electrons, respectively. A transparent conducting electrode Indium Tin Oxide (ITO) is generally used as the anode and Al as the

cathode. This structure is a metal/insulator/metal (MIM) architecture due to the organic semiconductor's low mobilities and relatively absent intrinsic carrier density [1]. Under zero bias and at open circuit conditions, Figure 1.4b shows the alignment of the energy levels with the electrodes. The energy required for the ejection of an electron from the electrodes into the vacuum level is termed the work function (ϕ) of that particular electrode. ϕ is usually negative of the magnitude of the Fermi energy (E_F) of an electrode [1]. Similarly, the energy required to remove (add) an electron from (to) the semiconductor is termed ionization potential, I_p (electron affinity, E_a) [1]. These are generally indicated to be equal to the energy values of one electron HOMO and LUMO, although this picture does not take into account the electron-electron interactions. The HOMO and LUMO levels of the semiconductor usually obey a Gaussian distribution, but for simplicity, they are indicated as straight lines in Figure 1.4. In the open circuit condition, a potential drop does not develop across the semiconductor since there is no flow of charges, and it is referred to as a flat level condition [1].The energies of the HOMO and LUMO do not change along the entire thin film thickness in this case.

Under short circuit conditions (Figure 1.4c), i.e., when ITO and Al are at the same potential, the carriers flow across the electrodes to equilibrate the Fermi energies. The equilibration occurs owing to Fermi energy (potential energy corresponding to the highest energy electrons at 0 K) being the same everywhere in space in interconnected systems. The difference in electrode work-functions gives rise to a potential difference and is termed the built-in potential (V_{bi}) [1]. Unlike organic semiconductors, the Fermi energy of the electrodes is not altered by the addition (removal) of charges to (from) them. The energy gap of the semiconductor (difference between HOMO and LUMO energy levels) remains the same, leading to a tilt throughout the dimensions of the film. The "flat level" condition gets recovered only when a voltage corresponding to the difference in the electrode work functions is applied, i.e.,

$$V_{bi} = \frac{1}{e}(\phi_{Al} - \phi_{ITO}) \qquad (1.5)$$
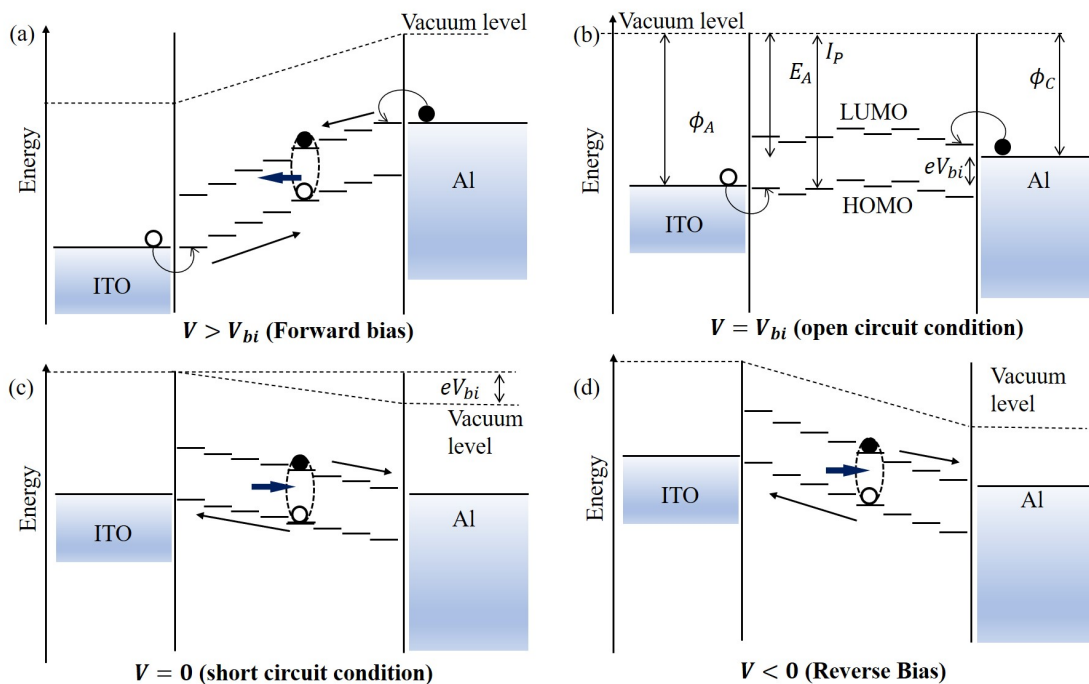
Figure 1.4: A metal/insulator/metal (MIM) energy diagram illustrating the alignment of the molecular frontier orbitals under (a) forward bias, (b) open circuit, (c) short circuit, and (d) reverse bias conditions.

An application of an external voltage gets added to V_{bi} which lowers the Fermi level of Al compared to ITO. This drives the MIM device into a reverse bias (Figure 1.4d). In reverse bias conditions, the tilt in the energy levels throughout the organic layer is steeper, resulting in no flow of current through the device. However, the presence of pinholes and other thermal processes leads to a parasitic leakage current in the device. On reversing the applied voltage, the tilt in the level reduces. The flat band condition can again be arrived at when the applied voltage equals V_{bi}. When the applied voltage is increased beyond V_{bi}, the tilt of the levels in the organic layer reverses, driving the device into forward bias (Figure 1.4a). After a sufficient voltage, namely the turn-on voltage, the electrons (holes) can overcome the energy barrier between the Al (ITO) Fermi level and the molecular LUMO (HOMO), enabling injection. The tilt of the energy levels facilitates the transport of carriers throughout the film. Some of the carriers also leave at the counter electrode if they do not find the opposite charges to recombine, leading to device heating. Most of the carriers, however, form an
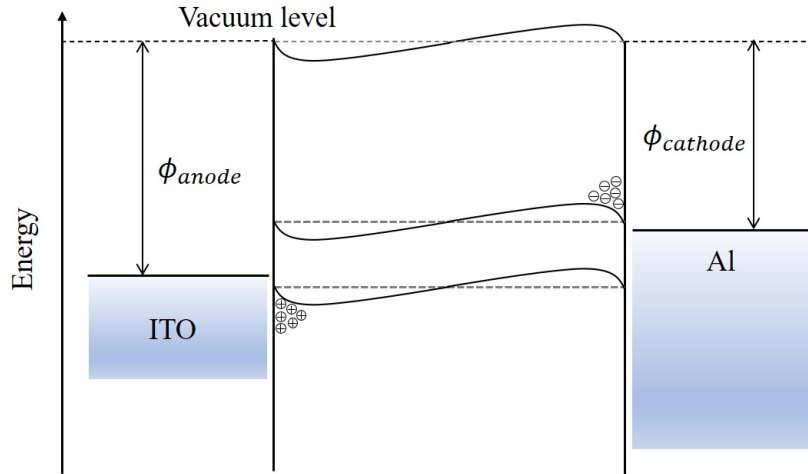
Figure 1.5: Band bending effect at the molecule-electrode interface in a MIM device

exciton with opposite charges, which can lead to electroluminescence according to Fermi's Golden rule. The exciton should preferably form in the center of the active layer to reduce quenching of the excitons by the electrodes.

The device current can depend on either the carrier injection from the corresponding electrodes or the transport of these carriers across the organic semiconductor [1]. The current in the first case is said to be injection limited and in the second case space charge limited (SCLC). Under an infinite supply of injected carriers, the device currents are limited by the space charge in the semiconductor responsible for shielding the electric field between the injection electrodes. An electrode that can inject carriers far higher than the semiconductor can transport is usually referred to as an Ohmic electrode [1]. The ability of an electrode to sustain a space charge-limited current depends both on the injection barrier and carrier mobility of the organic semiconductor. An optimum luminance is only achieved in OLEDs when ITO and Al can deliver space charge-limited currents, i.e., the electrodes should be ohmic [1].

The anode can usually accept an unlimited number of electrons. Thus, the hopping of electrons usually happens from the molecular HOMO to the Fermi level of the anode. This process is similar to the injection of a hole, and it changes the molecular energy levels (called a molecular cation) in contrast to the case when it was neutral. In other

words, the LUMO and HOMO shift to larger negative values. Thus, a space charge layer is formed along the electrode-molecule interface whenever a hole is injected. This phenomenon where there is a change in the energy levels due to the formation of interfacial space charge is usually termed a band bending effect (Figure 1.5) [1]. Similar band bending happens when an electron is injected from an ohmic contact for electrons.

1.1.6   Charge carrier transport in organic semiconductors
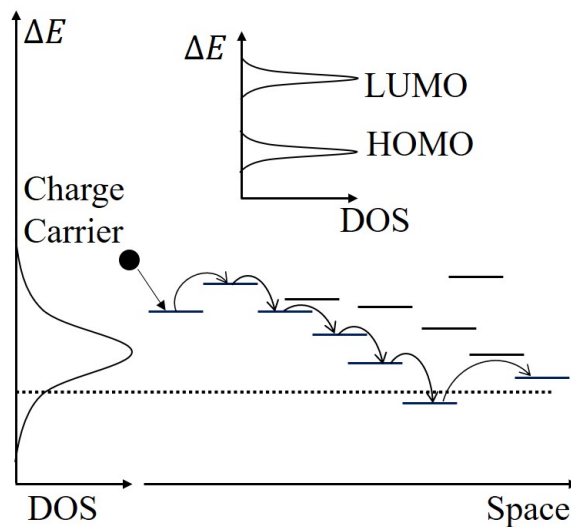
Figure 1.6: Illustration of a charge carrier hopping within a Gaussian density of states (DoS).

Charge transport in amorphous organic semiconductors is influenced by inherent structural and energy disorders. Unlike crystalline semiconductors, transport is dominated by the hopping mechanism. Carriers hop from one site to another, determined by a probability that minimizes the total energy. The density of states (DoS) about the HOMO and LUMO levels of the organic semiconductor is represented by a Gaussian distribution given by (Figure 1.6) [10–12]:

$$g(E) = \frac{1}{\sqrt{2\pi}\sigma} exp[-(\frac{E - E_0}{\sqrt{2}\sigma})^2] \qquad (1.6)$$

where E is the energy, E_0 is the centre of the distribution, and σ is the width of the Gaussian, often referred to as the disorder parameter. The localised states hinder the charge transport process as the charges get

captured or trapped. The trap states can originate from sources like impurities, structural defects and geminate pairs. The phenomenon of transport in disordered organic semiconductors has been well explained by Monro et al. using the concept of thermally activated transport energy (E_t) [13]. The states that lie below E_t are trap states while the states above are regular transport sites. The Gaussian disorder model of charge transport is based on cubic arrangement of charge transport sites [14]. The Marcus model proposes that the hopping probability between two sites depends on the overlap of wavefunctions of the two sites and the thermal energy [15]. Thus, thermal excitations can release charge carriers from the trap states to the regular transport sites. In a similar fashion, thermal activation lowers the injection barrier for charge carriers in an organic semiconductor. Originally introduced by Garstein and Conwell [16], the thermally activated jump raises an electron from the Fermi level of the electrode to the tail states of the DoS of transport sites in the dielectric medium. The model of thermally activated injection into the Gaussian DoS distribution of hopping sites highlights that disorder facilitates lowering of the injection barrier. However, the transport velocity decreases with increasing disorder. The probability of hopping for a charge carrier from i to j considering spatial disorder and thermal activation is given by the Miller Abrahams expression [17].

$$w_{ij} = \nu_0 exp(-2\gamma r_{ij}) \begin{cases} exp(-\frac{\Delta E_{ij}}{k_B T}), \Delta E_{ij} > 0 \text{ (up-hop)} \\ 1, \Delta E_{ij} \leq 0 \text{ (down-hop)} \end{cases} \qquad (1.7)$$

where w_{ij} is the hopping rate, ν_0 is the frequency prefactor, also known as an attempt to hop frequency, r_{ij} is the distance of jump between site i and j, γ is the inverse localization radius of the electron wavefunction which is related to the electronic coupling matrix element [1].

1.1.7 Charge Injection and Blocking Layers

In efficient OLEDs, the electrons and holes should be injected with as little bias as possible, and the electrons should recombine with the hole in the semiconductor rather than departing at the counter electrode. The former is usually achieved by the insertion of injection layers (IL) whose HOMO (LUMO) lies between the work-function of the anode
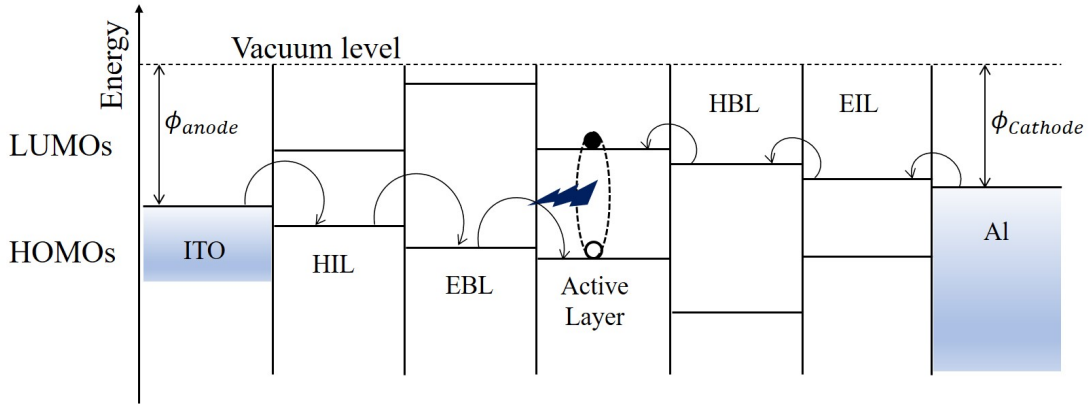
Figure 1.7: Energy level diagram of a multilayer device showing hole-injection layer (HIL), electron blocking layer (EBL), active layer, hole blocking layer (HBL), electron injection layer (EIL) with the anode (ITO) and cathode (Al).

(cathode) and the HOMO (LUMO) of the active layer. The graded junction facilitates a reduction in the turn-on voltage for light emission. Blocking layers are used to prevent counter-charges from exiting the active layer. Materials with low HOMO (high LUMO) are usually put in between the IL and the active layer at the cathode (anode) side. Sometimes one single material with suitable energy levels can perform the dual function of injection and blocking layers. A balanced hole and electron currents can be achieved by fine-tuning the different energy barriers at both sides of the active layer. Figure 1.7 gives the structure of a multilayer OLED at open circuit conditions.

1.1.8 Phosphorescent OLEDs

Electrical injection of holes and electrons leads to 75% triplets and 25% singlets [4]. Triplet excitons are an undesirable energy loss channel under electrical excitation because they are spin forbidden from light emission [1, 18–21]. This limits the theoretical maximum internal quantum efficiency in fluorescent OLEDs to 25% [4]. The second generation of OLEDs used a phosphorescence mechanism to drive the theoretical limit for the internal quantum efficiency of OLED to 100%. The spin-forbidden radiative transition $(T_1 \rightarrow S_0)$ called phosphorescence is achieved via the mechanism of spin-orbit coupling by which the triplets acquire some contributions from the singlet state and vice versa [22, 23].

The spin-orbit coupling is generally small compared to the total

energy of the molecule. Thus, the effect of spin-orbit coupling on the wavefunction of a state can be described using the framework of time-independent perturbation theory [1]. The pure triplet excited state $|^3\psi_1^0>$ obtains admixtures of high energy singlet states $|^1\psi_k^0>$ i.e.,

$$|^3\psi_1^{'}> = |^3\psi_1^0> + \sum_k \frac{<^1\psi_k^0|\hat{H}_{so}|^3\psi_1^0>}{E(T_1) - E(S_k)}|^1\psi_k^0> \quad (1.8)$$

with $|^3\psi_1^{'}>$ denoting the perturbed triplet state. Similar analogous expression can be written for the ground singlet states, i.e.,

$$|^1\psi_0^{'}> = |^1\psi_0^0> + \sum_k \frac{<^3\psi_k^0|\hat{H}_{so}|^1\psi_0^0>}{E(S_0) - E(T_k)}|^3\psi_k^0> \quad (1.9)$$

Owing to the large energy separation between the ground singlet and the higher energy triplet states, the triplet admixture in the ground singlet state is quite small. Here, the mathematical expression for the spin-orbit coupling Hamiltonian operator is given by [2]

$$\hat{H}_{so} = -\frac{Z^4 e^2}{8\pi\epsilon_0 m_e^2 c^2}\mathbf{l}.\mathbf{s} \quad (1.10)$$

Thus, Fermi's golden rule for triplet to singlet transitions (Eq. 1.4) becomes [1]

$$k_{if} = \frac{2\pi}{\hbar}\rho| <^3\psi_1^{'}|e\hat{r}|^1\psi_0^{'}> |^2 = \frac{2\pi}{\hbar}\rho(A + B + C + D)^2 \quad (1.11)$$

where

$$A = <^3\psi_1^0|e\hat{r}|^1\psi_0^0>$$

$$B = \sum_k \frac{<^1\psi_k^0|\hat{H}_{so}|^3\psi_1^0>}{E(T_1) - E(S_k)} <^1\psi_k^0|e\hat{r}|^1\psi_0^0>$$

$$C = \sum_k \frac{<^3\psi_k^0|\hat{H}_{so}|^1\psi_0^0>}{E(S_0) - E(T_k)} <^3\psi_1^0|e\hat{r}|^3\psi_k^0>$$

$$D = \sum_k \frac{<^1\psi_k^0|\hat{H}_{so}|^3\psi_1^0>}{E(T_1) - E(S_k)} \sum_j \frac{<^3\psi_j^0|\hat{H}_{so}|^1\psi_0^0>}{E(S_0) - E(T_j)} <^1\psi_k^0|e\hat{r}|^3\psi_j^0>$$

The terms A and D vanish as they contain orthogonal spins, whereas B and C contribute to k_{if} with C being only a minor contribution due to

a large energy difference between S_0 and T_k. Thus, the phosphorescence intensity results from the admixture of the singlet wavefunctions in the T_1 state. The rate of phosphorescence also depends on the magnitude of $(\hat{H}_{so})$ which is proportional to Z^4 thus highly sensitive to the charge of the nucleus. Heavy atomic nucleus such as Pt, Ir, or halogens (Br or I) [24, 25] can facilitate the spin-orbit coupling in a molecule giving rise to phosphorescence. Since McClure in 1949 first demonstrated the heavy atom effect [26], several halogens or large atomic number metal atoms have been incorporated into luminescent molecules to enhance phosphorescence.

Even in the absence of heavy atoms, phosphorescence can also exist however at much weaker intensities owing to vibrationally induced spin-orbit coupling. In the semi-classical picture, the presence of phosphorescence can be attributed to the fact that the sum $j = s + l$ of spin needs to be preserved where s and l denote the spin and orbital angular momentum. The vibrations in the molecule can lead to a change in l resulting in a flip in the spin. In other words, the torsions provide the perturbations to mix orbitals with different angular momentum [27–29]. Mostafa El-Sayed postulated this rule in the 1960s in the context of ISC transitions[30, 31]. The rule states that the rate of ISC is large when the transition occurs between the electronic states of different multiplicity with a change in their respective orbital configuration. In other words, the ISC transition is fast and efficient when the transition involves a change in the orbital type, i.e., the singlet is of $\pi - \pi^*$ and the triplet is of $n - \pi^*$ in nature or vice versa [32]. On the other hand, the rate is much slower when both the triplet and singlet are $\pi - \pi^*$ or $n - \pi^*$.

The first breakthrough for harvesting triplet excitons in an OLED device to generate phosphorescence under electrical injection was achieved by Forrest and co-workers using a heavy Pt-based porphyrin complex [22]. The IQE in the phosphorescent OLEDs was achieved to be 100%. However, these OLEDs suffer from stability, especially for blue emission. The scarcity and expense of heavy metals also restrict them from commercialization.

The energy gap between the S_0 state and T_n also controls the extent of the admixture of triplets and singlets. In the case of phosphorescence emission, a small gap between S_1 and T_1 has been assumed. This factor has importance on the mechanism and design strategies of thermally activated delayed fluorescence (TADF) molecules.

1.1.9 Thermally Activated Delayed Fluorescence OLEDs

In the last decade, TADF emitters have emerged as the most efficient way of harvesting the triplet excitons in metal-free organic compounds. These systems utilize a RISC process between very close lying T_1 and S_1 states. Thermal activation facilitates the RISC process when the gap between S_1 and T_1 is of the orders of a few tens of meV and generates a delayed fluorescence ($S_1 \rightarrow S_0$), increasing the overall luminance of the molecule. The concept of the TADF phenomenon has been given in the pioneering work of Perrin [33] and later by Lewis-Kasha [34, 35]. However, the systematic investigation of TADF materials has been done only in the last decade by Adachi and co-workers [36–41]. This group was also the first to demonstrate that simple metal-free compounds have the ability to achieve 100% IQE [36].

The key photophysical processes in a TADF molecule include fast prompt fluorescence (PF) and much longer delayed fluorescence (DF). They can be distinguished by their difference in lifetimes when monitored at the same wavelength (PF and DF generally have the same spectral distribution). Under optical excitation, the T_1 state is populated from the initially formed S_1 state via ISC. This process is followed by the up-conversion of the triplets back to singlets via RISC. The S_1 state finally fluoresces at longer timescales (usually in the range of a few μs to ms). The prompt fluorescence (PF) timescales are usually in the range of a few nanoseconds. On the other hand, under electrical excitation, the 75% triplets and 25% singlets relax to the lowest excited S_1 and T_1 states, following Kasha's rule via rapid vibrational relaxation and internal conversion. The lowest excited T_1 state upconverts to the S_1 state by thermal activation via the RISC process. Thus, the singlet states are populated by these triplet states, which gets emitted as delayed fluorescence.

According to Hund's rule of spin multiplicity, the T_1 state is always lower in energy than the S_1 state. This causes a competitive ISC process which further generates the triplet states even after the first cycle of RISC is over. The ISC rate is seen to be generally faster than the RISC process. Thus, there is always a balance of S_1 and T_1 exciton distribution, and the T_1 population will have more population as it is energetically lower. Hence, to harvest all the triplet excitons, the rate of RISC needs to be maximized. To achieve a quantitative RISC, it has been shown that the optimum energy gap between S_1 and T_1 should be below $\sim$100 meV at room temperature (300 K)[42–44].

The rate of RISC determines the efficiency of the TADF mechanism and is proportional to [45, 46]

$$k_{RISC} \propto exp(-\frac{\Delta E_{ST}}{k_B T}) \qquad (1.12)$$

where the energy gap ΔE_{ST} is the energy gap between the excited singlet and triplet states. The gap ΔE_{ST} should be minimized ideally to a few tens of meV for an efficient RISC process. The lowest excited singlets (S_1) and triplets (T_1) mostly depend on three factors: (i) the energy gap between the HOMO and LUMO (where one electron is residing in the HOMO and the other in the LUMO), (ii) the electron repulsion energy (K) which is a first-order Coulombic correction, and (iii) the exchange energy (J) which is a first-order quantum mechanical correction due to electron-electron repulsion following Pauli's Exclusion Principle [1]. Thus,

$$E_{S_1} = E_{HOMO-LUMO} + K + J \qquad (1.13)$$

$$E_{T_1} = E_{HOMO-LUMO} + K - J \qquad (1.14)$$

$$\Delta E_{ST} = E_{S_1} - E_{T_1} = 2J \qquad (1.15)$$

To reduce the energy gap (ΔE_{ST}), which is twice the exchange energy term $(2J)$, one has to reduce the exchange energy between the electrons residing in the HOMO and LUMO orbitals. The exchange energy is mathematically propotional to [1] $\int \phi_a \phi_b d\tau$ where $\int d\tau$ denotes the integral over space, ϕ_a and ϕ_b represent the HOMO and LUMO

wavefunctions. Therefore, J can be reduced by minimising the spatial overlap between the HOMO and LUMO orbitals. This minimization is achieved by designing molecules with donor-acceptor subunits that facilitate donor-acceptor electron transfer in the excited state and lead to strong charge transfer (CT) characteristics in the molecule. Thus, TADF molecules are generally donor-acceptor type molecules where the subunits are covalently linked by aromatic bridges, spiro-junction, or a simple sp^3 hybridized carbon (like $-CH_2$ or $-CF_2$) to further reduce the spatial overlap because of a near orthogonal confirmation of the donor/acceptor subunits. However, a $\sim 90^o$ relative orientation between the donor and acceptor subunits would completely reduce the oscillator strength ($< \psi_{el,f}|e\hat{r}|\psi_{el,i} >$) as discussed in Section 1.1.3. Thus, it is always difficult to design a TADF molecule with low ΔE_{ST} and simultaneously high oscillator strength.

Since the pioneering work of Adachi in 2012 [38], several small molecule TADF systems have been exploited to achieve all colour electroluminescence with excellent efficiency [47]. TADF emitters have shown promising results for replacing blue as well as white-emitting OLEDs commercially [48]. However, a few challenges still need to be addressed to make TADF a more attractive replacement for solid-state lighting technologies. The biggest disadvantage of these systems is their inherent broad emission which is undesirable for pure colour pixels in a device. To resolve this issue, Adachi and co-workers have developed a unique 'hyper-fluorescence' mechanism in which Förster Resonance Energy Transfer (FRET) happens from the TADF emitter to the highly emitting fluorescence dopants [49]. This simultaneously improves the device's color purity and operational lifetime. Wise Chip Semiconductor Inc recently announced the world's first hyperfluorescent OLED display in collaboration with Kylux Inc. with an operational lifetime of 50,000 hours [50].
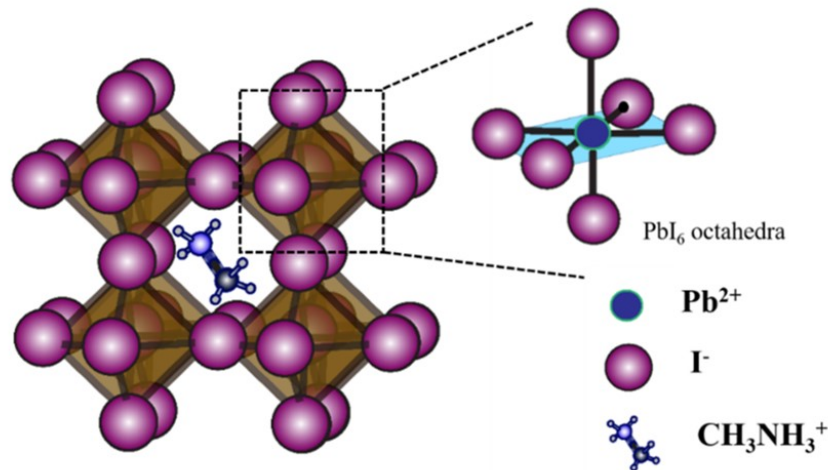
Figure 1.8: Schematic representation of organic-inorganic hybrid perovskite unit cell of the form ABX_3 where $A = CH_3NH_3$, $B = Pb$ and $X = I$. The methylammonium ion is surrounded by the PbI_6 octahedral cage, with a coordination number of 12.

1.2 Hybrid Organic-Inorganic Perovskite semiconductors

Hybrid organic-inorganic perovskites (HOIP) are another class of solution-processed semiconductors that have made rapid strides over the last decade owing to their excellent optoelectronic properties. Unlike organic semiconductors, which mostly form amorphous or semi-crystalline films, HOIPs are crystalline in nature. The crystallinity results in the formation of conduction and valence bands separated by the characteristic direct bandgap. The perovskites are compounds with the formula of ABX_3 where A is a monovalent organic cation, B is a heavy metal divalent heavy cation, and X is a monovalent halide anion (I^-, Br^- or Cl^-). Ionic and hydrogen bonding maintains the lattice structure, making them soft materials compared to inorganic perovskites [51].

The typical perovskite lattice structure is shown in Figure 1.8. The BX_6 (B = Pb, X = I) octahedral forms the corner sharing points of the lattice, and the A-site cation ($CH_3NH_3^+$) occupies the centre position having a coordination number of 12. Goldschmidt Tolerance

factor (t) gives the selection rule for the formation of the 3D perovskite phase as [52]

$$t = \frac{r_A + R_X}{\sqrt{2(r_B + r_X)}} \tag{1.16}$$

where r_A and r_B are the iconic radii of A and B site cations, respectively, and r_X is the anion ionic radius. The perovskite phase forms for t ranging from 0.8 to 1. $t > 1$ indicates a large size of the A-site cation, and this precludes the formation of a perovskite phase. $t < 0.8$ suggests that the A cation is too small, leading to the formation of other phases apart from perovskite. Generally, monovalent organic cation methylammonium ($CH_3NH_3^+$, r_A ~0.216 nm) is used for A site and Pb^{2+} or Sn^{2+} for site B [53].

The A and B cations and the halide substitution can tune the bandgap in HOIP semiconductors. The methylammonium cation (in the A site) stabilizes the perovskite to a reasonable tolerance factor. Still, it does not contribute to the conduction and valence band states except for donating an electron to the Pb-I framework [54]. The orientation of the methylammonium cation distorts the PbI_6 octahedral cage, thus indirectly playing a role in the electronic properties. A dynamic change in the band structure caused by such molecular rotations

Table 1.1: Bandgaps of commonly used hybrid perovskites

Perovskites	Bandgap
$MAPbI_3$	~1.6 eV [56]
$MAPbI_{3-x}Br_x$	1.6-2.3 eV [59]
$MAPbBr_3$	~ 2.3 eV [60]
$MAPbBr_{3-x}Cl_x$	2.3-2.9 eV [61]
$MAPbCl_3$	~2.9 eV [62]
$FAPbI_3$	~1.45 eV [63]
$FA_xMA_{1-x}Pb(I_yBr_{1-y})_3$	1.45-2.33 eV [58]

partially results in the unique properties of slow carrier recombination and long diffusion length for MAPbI$_3$ perovskites [55].

The most commonly studied perovskite, MAPbI$_3$, has a bandgap of $\sim$1.6 eV [56] formed between Pb's unoccupied p-orbital and I's occupied p-orbital. In MAPbX$_3$, the valence orbital of X changes from 3p, 4p to 5p when X is varied from Cl, Br to I, respectively, decreasing the bandgap of MAPbX$_3$ monotonically. The bandgap can also be engineered by controlling the steric size of the cation molecule, which is observed in the case of formamidium lead iodide perovskite (FAPbI$_3$). FAPbI$_3$ has a narrower bandgap compared to MAPbI$_3$ owing to the steric size of FA$^+$ cation [57]. Further, the bandgap can be tuned in mixed cation perovskite by control of the relative cation composition [58]. The bandgap of the commonly used hybrid perovskites is given in Table 1.1.

The HOIP semiconductors exhibit a high absorption coefficient of up to 10^5 cm^{-1}. This allows for most of the incident light to get absorbed in 200 - 400 nm of the perovskite film. The emission in HOIP semiconductors has been experimentally shown to originate from a direct band transition of cold carriers that have relaxed to the band edge [64]. Upon photoexcitation, the species that are generated depend largely on the exciton binding energy (E_b). E_b for MAPbI$_3$ perovskites lie in the range of 2-25 meV [65–67] which is smaller than the thermal energy at 300 K ($k_B T = 26$ meV), making them excellent candidates for solar cells. The E_b in the case of MAPbBr$_3$ lies in a slightly higher range of 15.3 - 150 meV [68–70] leading to a coexistence of excitons and free charges with their ratio depending on the excitation density. The crystal structure, chemical nature, dielectric constant of the surrounding environment and the dimensionality strongly affect the binding energy. The binding energies of small nanocrystals can increase up to 375 meV [69, 71]. Binding energies higher than the thermal energy (~ 26 meV) suits luminescence-based applications such as LEDs and lasers [71, 72].

1.2.1 Carrier Transport and Recombination in HOIP Semiconductors

The long-range order of HOIP semiconductors allows for the drift-diffusion formalism to model transport equations. Thus, the electron and hole current density in a HOIP semiconductor can be written as [73]:

$$J_n = e(\mu_n n E + D_n \nabla n) \tag{1.17}$$

$$J_p = e(\mu_p n E - D_p \nabla p) \tag{1.18}$$

where e is the electronic charge, E is the electric field, $n(p)$ and $\mu_{(n(p))}$ are the electron (hole) concentrations and mobilities with $\mu_{(n(p))} = v_{n(p)}/E$. $v_{n(p)}$ and $D_{n(p)}$ are the drift velocity and diffusion constant of electrons (holes) satisfying the Einstein relation $D_{n(p)} = \mu_{n(p)}(k_B T/e)$.

The continuity equation for hole and electron is written as [73]:

$$e\frac{\partial n}{\partial t} = \nabla J_n + e(G - R) \tag{1.19}$$

$$e\frac{\partial p}{\partial t} = \nabla J_p + e(G - R) \tag{1.20}$$

where G and R are the carrier generation and recombination rates. Poisson's equation expresses the electric field due to the carrier concentration as [73]

$$\epsilon.\nabla E = e(p - n + N_d) \tag{1.21}$$

where ϵ is the permittivity of the medium and N_d is the concentration of any dopants, impurities, or trapped carriers. Combining equations 1.19, 1.20, and 1.21, the ambipolar transport equation is expressed as [73]:

$$D'\nabla^2 n + \mu' E \nabla n + G - R = \frac{\partial n}{\partial t} \tag{1.22}$$

where $D' = \frac{\mu_n n D_p + \mu_p p D_n}{\mu_n + \mu_p}$ is the ambipolar diffusion coefficient and $\mu' = \frac{\mu_n \mu_p (p-n)}{\mu_n + \mu_p}$ is the ambipolar mobility. For 1D transport in case of excess minority carriers, Eq. 1.22 reduces to

$$D_n \frac{\partial^2 n}{\partial x^2} + \mu_n E \frac{\partial n}{\partial x} + G - R = \frac{\partial n}{\partial t} \tag{1.23}$$
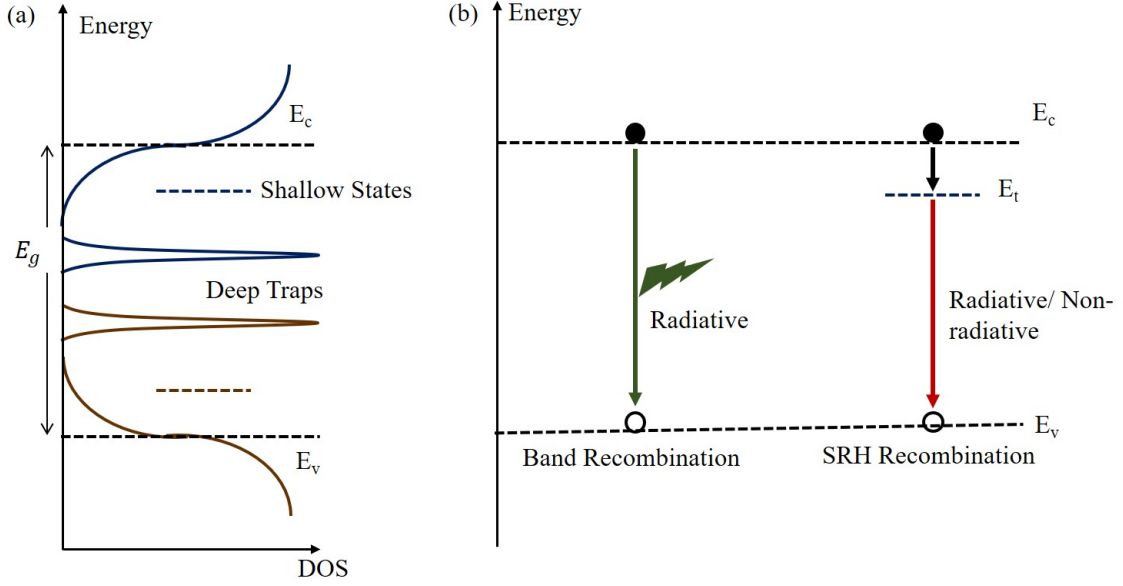
Figure 1.9: (a) Schematic representing the distribution of band states, sub-bandgap states that form the shallow defects and the deep trap states. The shallow defects have a low activation energy $\sim k_B T$, while the deep traps have higher activation energies, (b) Schematic illustration depicting the carrier recombination pathways in HOIP under excitation densities $< 10^{17}$ photons/cm^2, i.e., the band recombination process and Trap-assisted recombination process given by the Shockley-Read-Hall (SRH) statistics.

$$D_p \frac{\partial^2 p}{\partial x^2} + \mu_p E \frac{\partial p}{\partial x} + G - R = \frac{\partial p}{\partial t} \qquad (1.24)$$

for excess electrons and holes respectively [73].

The recombination dynamics denoted by R play a crucial role and influences carrier dynamics and device performance. Diffusion length (L_d) a parameter that indicates the efficiency of transport depends on the carrier recombination lifetime ($L_d = \sqrt{D\tau}$, D is the diffusion coefficient). The principle of detailed balance requires that photons are exchanged continuously between the semiconductor and the environment [74]. Thus, to maintain a steady state photo-generation, recombination is necessary. Photogenerated excess carriers recombine via mainly three processes (Figure 1.9): (i) Band recombination (radiative recombination of free carriers), (ii) trap-assisted recombination (either radiative or non-radiative given by Shockley-Reed-Hall statistics), and (iii) Auger recombination (mainly a non-radiative process involving three carriers). A spatially localized defect in a semiconductor leads to the formation

of a defect state within the bandgap and acts as a trap centre. Defects in crystalline semiconductors usually originate from discontinuities in the periodicity in a perfect crystal lattice (called as crystallographic defects) or due to foreign atoms (impurities). The extent of trapping depends on the energy level of the trap state. The trapped carrier is likely de-trapped if its activation energy is sufficiently small. If the activation energy is high, the trapped carrier recombines with a counter carrier, and this process is given by Shockley-Reed-Hall (SRH) statistics which is a loss mechanism in solar cells [75, 76]. The SRH recombination lifetime can be expressed as

$$\frac{1}{\tau_{SRH}} = R_{SRH}.N_T \tag{1.25}$$

where R_{SRH} is the trap-assisted recombination constant and N_T the trap density.

In Auger recombination, when an electron-hole pair recombines, an electron is either excited higher into the conduction band or hole into the valence band. This process becomes prominent at much higher excitation densities ($> 10^{17}$ photons/cm^2). The excitation intensities used in the thesis are $< 10^{17}$ photons/cm^2; hence, Auger mechanism is not considered.

The efficiency of the recombination pathways depends on the re-combination rate and the density of states or species available for recombination. The effective recombination lifetime in HOIP semi-conductors under low and intermediate excitation intensities is given as

$$\frac{1}{\tau} = \frac{1}{\tau_R} + \frac{1}{\tau_{SRH}} \tag{1.26}$$

The radiative recombination rate is given as:

$$\frac{\delta n}{\tau_R} = A_R \delta n + B(\delta n)^2 \tag{1.27}$$

where δn is the excess carrier density, $A_R = B.N_A$ with B being the radiative constant and N_A the background doping constant. The first term in the right-hand side of the expression refers to the monomolecu-

lar recombination and it varies linearly with excess carrier density. The second term is bimolecular recombination which depends quadratically on the carrier density. At very low excitation energies, the photoexcited population decays with a monomolecular rate through interaction with the background carriers and trap states. With the increase in excitation intensity, the monomolecular decay channels saturate, and the bimolecular band-to-band recombination determines the overall recombination rate [77].

1.2.2 HOIP Solar cells

HOIP semiconductors have emerged as one of the most efficient materials for solar cell applications. Miyasaka and co-workers reported in 2009, MAPbI$_3$ and MAPbBr$_3$ based solar cells with a power conversion efficiency of 3.9%. In the last decade, the record efficiency of perovskite solar cells has reached higher values, up to 25.7% [78].

Photoexcitation of a HOIP solar cell leads to the formation of both free charge carriers and excitons. Based on the value of exciton binding energy, the exciton dissociation could occur at room temperature leading to more charge carriers. The built-in field assists in the process of charge carrier extraction following the drift-diffusion formalism. The process of charge extraction can be improved by using charge transport layers similar to the layers discussed in Section 1.1.7. A good charge transport layer is characterized by good interfaces, low contact resistances, selective carrier mobility, the presence of an Ohmic contact, and energy levels to facilitate efficient charge extraction. Thus, the efficiency of photon-to-electron conversion in a HOIP solar cell (Figure 1.10) can be expressed as

$$\eta = \frac{\text{charges collected}}{\text{incident photons}} = \eta_A \eta_{CS} \eta_{CT} \eta_{CC} \tag{1.28}$$

where η_A, η_{CS}, η_{CT} and η_{CC} representing the efficiency of photon absorption, charge separation, charge transfer, and charge collection, respectively. Upon photoexcitation, the electron-hole pair are swept out of the device to produce a photocurrent I_L. The I-V of a solar cell is

$$\eta_A = \frac{\text{photons absorbed}}{\text{photons incident}}$$

$$\eta_{CS} = \frac{\text{seperated free carriers}}{\text{excitons generated}}$$

$$\eta_{CT} = \frac{\text{carriers transferred to transport layers}}{\text{free carriers in active layer}}$$

$$\eta_{CC} = \frac{\text{carriers collected in external circuit}}{\text{total carriers transferred}}$$
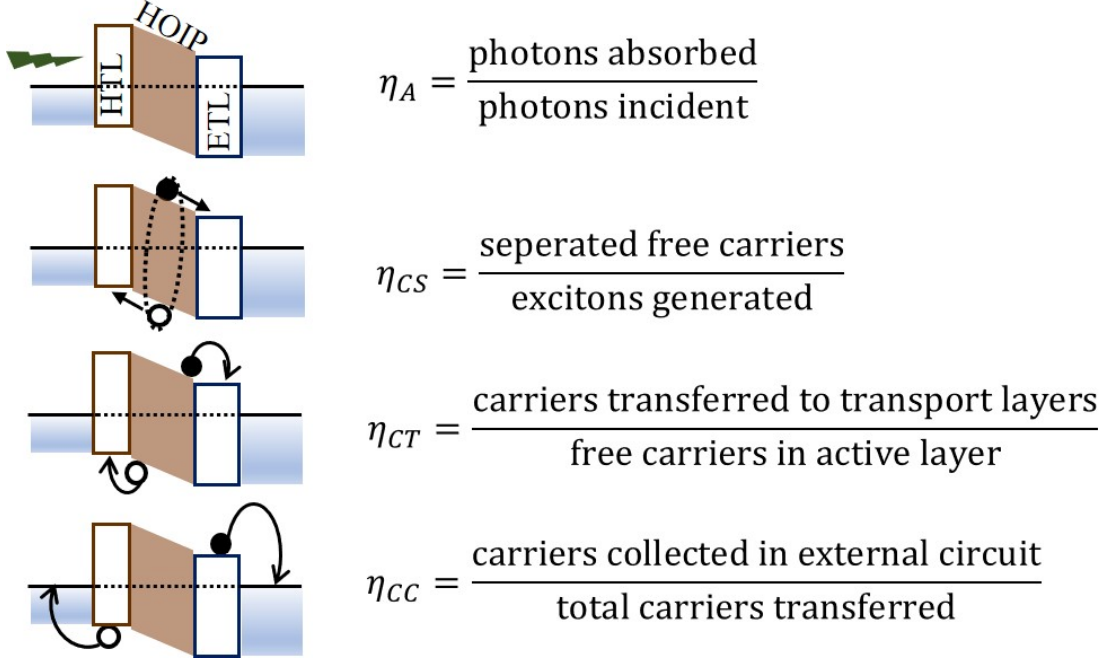
Figure 1.10: Schematic illustrating the carrier generation and separation dynamics in a typical HOIP device (electrode/HTL/HOIP/ETL/electrode). η_A depicts the process relating to the efficiency of photon absorption, η_{CS} the process of exciton generation and dissociation to form free carriers, η_{CT} the charge transfer process to the respective charge transport layers and η_{CC} depicts the charge collection to the respective electrodes.

expressed as

$$I = I_L + I_0[exp(\frac{eV}{mk_BT}) - 1] \tag{1.29}$$

where I_0 is the reverse saturation current, V the applied voltage, and m the ideality factor. Owing to the large absorption coefficient, only a thin layer of material would be required to absorb light with energy above the bandgap fully. This reduces the charge recombination and induces a reverse saturation dark current and contributing to a large V_{oc} as described by Shockley-Queisser [79] i.e.,

$$V_{oc} = \frac{k_BT}{e}ln(\frac{J_{sc}}{J_0}) = \frac{k_BT}{e}ln(\frac{J_{sc}N_D\tau}{en_i^2d}) \tag{1.30}$$

where J_{sc} is the short circuit current density, J_0 is the initial current density, N_D is the doping concentration, τ is the effective carrier lifetime, n_i is the intrinsic carrier concentration and d is the thickness of the active layer. The thickness of the most reported high-efficiency HOIP solar cells ranges from 0.3-0.6 μm [80, 81] due to its high

absorption coefficient, whereas the thicknesses of crystalline Si solar cells are of ~ 300 μm [82].

The trap-assisted non-radiative recombination process also plays a detrimental effect on the V_{oc} in a HOIP solar cell. The excess photogenerated charge carriers result in quasi-Fermi-level splitting (QFLS) for the electrons and holes. This difference in QFLS results in the V_{oc} of the solar cells. The presence of a faster non-radiative recombination channel reduces the excess charge carriers that contribute to QFLS, thereby reducing the difference in QFLS levels and V_{oc}. In other words, the external quantum efficiency (EQE) for electroluminescence in solar cells is directly related to the V_{oc} loss due to non-radiative recombination. This is given as [83]

$$\Delta V_{nr} = -\frac{k_B T}{e} ln(EQE_{EL}) \qquad (1.31)$$

where EQE_{EL} is dependent on both the radiative and non-radiative recombination rates (k_r and k_{nr}, respectively) i.e., $EQE_{EL} \propto \frac{k_r}{k_r + k_{nr}}$). In solar cells, for every reduction in the order of EQE_{EL}, the V_{oc} of the solar cell reduces by 60 mV.

The performance of a solar cell is characterized by four quantities, namely open circuit voltage (V_{oc}), short circuit current (J_{sc}), fill factor (FF), and power conversion efficiency (PCE). The power delivered in short-circuit is zero as the voltage is zero. Similarly, the power delivered is zero at open-circuit conditions since there is no photocurrent. Thus, the maximum power that can be delivered requires the presence of an optimized open-circuit voltage and photocurrent and is known as the maximum power point (MPP). MPP is the rectangle defined by $J_{max}.V_{max}$ under the J-V curve that has the largest area. The fill factor is a simple geometrical factor that is defined as

$$FF = \frac{J_{max} V_{max}}{J_{sc} V_{oc}} \qquad (1.32)$$

The PCE of a solar cell is the fraction of input power that is delivered as output as electrical power and is defined as

$$PCE = \frac{J_{max}V_{max}}{P_{in}} \tag{1.33}$$

The standard reference for measuring this parameter is at AM 1.5G illumination (1 Sun = 100 mW/cm^2).

The J-V characteristics (Figure 1.11) provide quantitative information about various device parameters like recombination losses and leakage currents. A solar cell can be represented as an ideal diode with two parasitic resistances, namely the series resistance and shunt resistance. The series resistance describes the influence of contact resistances like injection barriers and sheet resistance of the transparent conducting electrode and metals. The shunt resistance takes into account the alternative current pathways between the two electrodes. Thus, the net current density consists of the contribution of photoinduced short circuit current (J_L), diode current and the parallel current through the shunt resistance and is expressed as

$$J(V) = J_L + J_0[exp(\frac{e(V - JR_s)}{mk_BT}) - 1] + \frac{V - JR_S}{R_{sh}} \tag{1.34}$$

where R_s and R_{sh} are the series and shunt resistance of the solar cell respectively. For ideal solar cells, $R_s \to 0$ and $R_{sh} \to \infty$.

1.2.3 The thermodynamic efficiency limit of solar cells

Shockley and Queisser [74] used thermodynamic considerations to achieve the theoretical limit for the efficiency of a solar cell. The upper limit of efficiency that can be attained in a solar cell was considered to be u. All the photons incident on the solar cell having energy higher than the bandgap $E_g = h\nu_g$ contributes to the photocurrent. No losses are present if the cell is at 0 K. The PCE is then expressed as

$$u = \frac{h\nu_g Q}{P} \tag{1.35}$$

where Q is the number of photons absorbed per area and time (flux), and P is the intensity incident on the cell, defined using Planck's blackbody
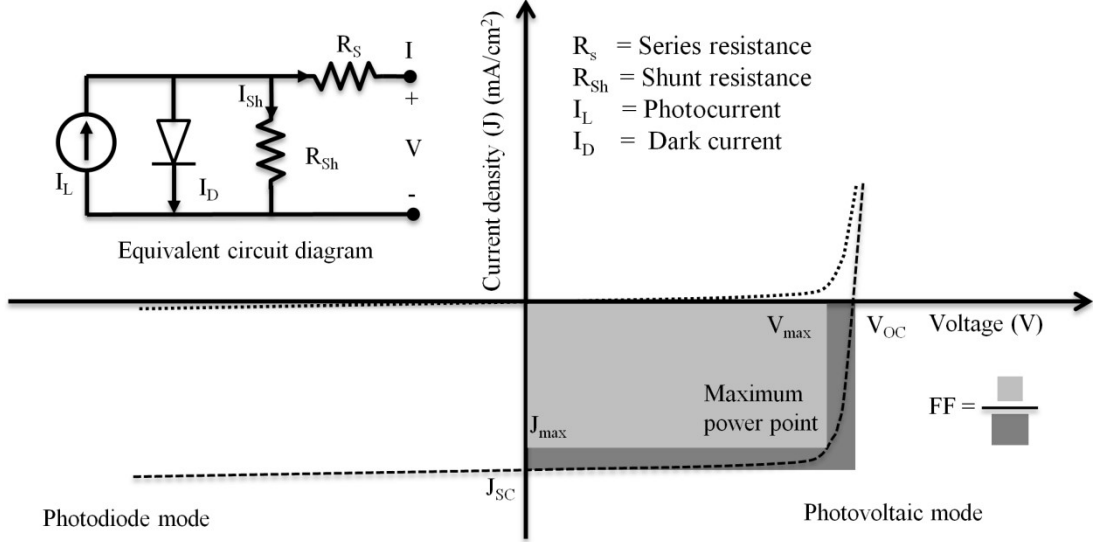
Figure 1.11: Schematic representation of the J-V characteristics of the solar cell. The inset shows the equivalent circuit model for a typical solar cell.

distribution as

$$
\begin{aligned}
Q &= \frac{2\pi}{c^2} \int_{\nu_g}^{\infty} \frac{\nu^2}{e^{h\nu/k_B T} - 1} d\nu \\
P &= \frac{2\pi h}{c^2} \int_{\nu_g}^{\infty} \frac{\nu^3}{e^{h\nu/k_B T} - 1} d\nu
\end{aligned}
\tag{1.36}
$$

By employing $x = h\nu/k_B T$ and $x_g = h\nu_g/k_B T$, Eq. 1.35 can be rewritten as

$$
u = \frac{x_g \int_{x_g}^{\infty} (e^x - 1) x^2 dx}{\int_0^{\infty} (e^x - 1) x^3 dx}
\tag{1.37}
$$

Thus, $u(x_g)$ depends on the bandgap $h\nu_g$. Eq. 1.37 gives a maximum value of about 44% for an energy gap of 1.1 eV [1]. The value of u is calculated considering that the sun's spectrum has a blackbody temperature of $T = 6000$ K. The rest 56% of the photon energy does not contribute to photogenerated carriers and gets lost. Further, the excess energy of photons beyond E_g is also not useful.

When the solar cell is held at 300 K, four processes need to be considered: photogeneration of electron-hole pairs, their both radiative and non-radiative recombination, generation of electron-hole pairs via non-radiative processes, and extraction of charges. Shockley and Queisser argue that the principle of detailed balance states that in thermal equilibrium, all microscopic processes in a cell get exactly

compensated by their respective inverse process [74]. Thus, the radiative recombination rate is the same as the photon absorption rate. Therefore, the current due to radiative recombination processes for the cell at equilibrium is

$$j_{0,r} = 2eA\frac{2\pi}{c^2} \int_{\nu_g}^{\infty} \frac{\nu^2}{e^{h\nu/k_B T} - 1} d\nu \qquad (1.38)$$

Similarly, in the thermal equilibrium condition, the rate of non-radiative recombination and generation processes is same. So, the current due to the non-radiative processes at thermal equilibrium is

$$j_{0,nr} = R(0) \qquad (1.39)$$

and the percentage of radiative recombination rates to that of non-radiative recombination becomes independent of voltage. By setting the sum of these four processes to be equal to zero, a steady state current-voltage relation is derived, i.e.,

$$j(V) = J_L + J_0[exp(\frac{eV}{k_B T}) - 1] \qquad (1.40)$$

with $j_0 = j_{0,r} + j_{0,nr} = \frac{2\pi}{c^2} \int_{\nu_g}^{\infty} \frac{\nu^2}{e^{h\nu/k_B T} - 1} d\nu + R(0)$ which is similar to Eq. 1.29. J_L is the photocurrent extracted into the external circuit at $V = 0$. The maximum power from the solar cell was derived by Shockley and Queisser by introducing the concepts of MPP and FF (called as impedance matching factor in their paper). They show the power conversion efficiency to be

$$PCE = \frac{J_{max}V_{max}}{P_{inc}A} = t_s u(x_g)\nu(fx_g x_c)FF(fx_g x_c) \qquad (1.41)$$

where P_{inc} is the light power per solid angle, A is the surface area of the solar cell, t_s is the probability of photons having energy above $h\nu_g$ that is incident from the sun's black body spectrum producing an electron hole pair, x_c is the ratio of the solar cell's temperature to the sun's temperature and $\nu(fx_g x_c)$ is a relation between V_{oc} and the optical gap i.e.,

$$\nu(fx_g x_c) = \frac{eV_{oc}}{h\nu_g} \qquad (1.42)$$

u ultimately depends only on E_g, while ν and FF depend on a number of factors that can be collectively expressed using the parameter f. f includes the product of the percentage of the radiative recombination current, the percentage of conversion of incident photons to carriers at 300 K, and a geometrical factor which quantifies the solid angle of the photons' incident on the cell. For an ideal cell in the limit of detailed balance, $t_s = 1$ and f reduces to the quantification of the half-sphere solid angle. Using Eq. 1.41, Shockley and Queisser the maximum attainable limit to be 30% for a band gap of 1.3 eV. For a more appropriate AM1.5 solar spectrum, the maximum PCE is found to be 33.7% for a single pn-junction solar cell with a bandgap of 1.34 eV [1]. The Shockley-Queisser limit of solar cells can be overcome by the implementation of various strategies like using tandem or multi-junction cells, multiple excitonic systems, and photonic crystal based solar cells.

1.2.4 Multi-junction solar cells
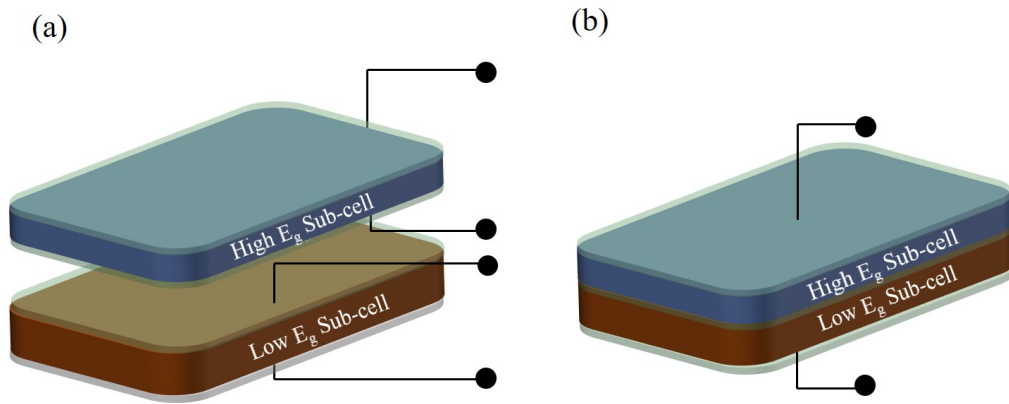
Figure 1.12: Schematic of a (a) four-terminal and a (b) two-terminal tandem solar cell. In both cases, the high-energy region of the solar spectrum is absorbed by the top sub-cell and the low-energy region by the bottom sub-cell.

Multijunction solar cells consist of stacking different bandgap junctions in optical series, allowing the wider bandgap at the top to absorb the higher energy photons and the less energetic photons to transmit onto the smaller bandgap materials below. The highest power can be extracted when the output from the independent junctions can be optimized. A multijunction cell having two bandgaps is called a tandem cell. A four-terminal tandem requires independent electrical

connections for the top and bottom sub-cell, which is difficult to achieve practically. The best way is just to connect the two sub-cells directly in series. This causes a current to pass through the cells and the voltages developed across the individual sub-cells to be added. However, the two-terminal arrangement suffers from a bottleneck in which the currents in the individual sub-cells must be matched. This restricts the performance; hence, the maximum output power obtained is less. Further, the current matching condition cannot be achieved for all the illumination conditions, which subject the two-terminal cell to additional losses.

In the four-terminal tandem cell, the maximum power output is the sum of the maximum power output of the two individual sub-cells. Assuming a perfect spectral splitting i.e., the photons with energy $E > E_{g2}$ are absorbed by the top sub-cell and the photons with $E_{g1} < E < E_{g2}$ are absorbed by the bottom cell where E_{g1} and E_{g2} are the bandgaps of the bottom and top cell, respectively. Therefore, for the maximum concentration of solar light, the maximum power output is given as [84]

$$
\begin{aligned}
P_{max} = & eV_{m1}[n(E_{g1}, E_{g2}, 0) - n(E_{g1}, E_{g2}, eV_{m1})] \\
& + eV_{m2}[n(E_{g2}, \infty, 0) - n(E_{g2}, \infty, eV_{m2})]
\end{aligned}
\tag{1.43}
$$

where V_{m2} and V_{m1} is the voltage across the top and bottom cell respectively at maximum power. A maximum efficiency of over 55% can be reached with $E_{g1} = 0.75$ eV and $E_{g2} = 1.65$ eV under full concentration [84]. In the two-terminal tandem cell, the maximum output power is

$$
P_{max} = e(V_1 + V_2)[n(E_{g1}, E_{g2}, 0) - n(E_{g1}, E_{g2}, eV_1)]
\tag{1.44}
$$

where V_1 and V_2 are no longer the optimized voltages, and they satisfy the current matching constraint [84], i.e.,

$$
n(E_{g1}, E_{g2}, 0) - n(E_{g1}, E_{g2}, eV_1) = (E_{g2}, \infty, 0) - n(E_{g2}, \infty, eV_{m2})
\tag{1.45}
$$

The overall PCE penalty in case of unmatched current between the two

sub-cells is given as

$$\Delta PCE = \frac{J_T V_T}{J_1 V_1 + J_2 V_2} \tag{1.46}$$

where each cell operates at its maximum power point with $V_T = V_1 + V_2$. $J_T = J_1 = J_2$ for optimal performance of the two terminal tandem solar-cell. The PCEs for all-HOIP tandem cells have reached 26.4% [85], 24.2% for HOIP/CIGSe (copper–indium–gallium-selenide) tandem cells [78, 86, 87], and 29.5% for HOIP-on-silicon tandem cells [88]. The Shockley-Queisser limit for a three terminal multijunction cell approach 49% [1]. For the limit of an infinite number of bandgaps, the smallest bandgap equals to zero and the efficiency limit reaches 69%. This limit approaches the thermodynamic limits of 86% under full concentration [84].

1.3 Time and Frequency Domain Measurements

Spectroscopic measurements are conventionally performed in one of the two domains: frequency or time. Frequency-resolved optical measurements are the most familiar forms of spectroscopy, including UV/Visible absorption, reflectance, transmission, and photo-luminescent emission measurements. Infrared (IR), Raman, and X-ray spectroscopy are also typically done in the frequency domain. The data acquired is typically in the form of light intensity as a function of frequency (or wavelengths/wavenumbers) which can be interpreted as absorbance, emission, or photon scattering depending on the instrument and technique used. In optoelectronic devices, the conventional frequency domain measurements include fluctuation spectroscopy of photocurrents and electroluminescence, intensity-modulated photocurrent spectroscopy (IMPS) and impedance spectroscopy (IS).

In time-domain measurements, the signal is acquired over an interval of time. The signal can be light intensity for optical measurements and photocurrent/electroluminescence intensity for optoelectronic measurements. Time-resolved photoluminescence and Photon Correlation spectroscopy are some examples of time-domain measurements under optical excitation. Transient Photocurrent (TPC), Transient

Photovoltage (TPV), and Transient Electroluminescence (TrEL) are examples of time-domain optoelectronic measurements. Time-resolved spectroscopy is used to study charge carrier and exciton kinetics and timescales in semiconductors.

Some measurements yield data in both time and frequency domains. The most prominent of these techniques is time-gated photoluminescence and time-gated electroluminescence spectroscopy. These measurements include the recording of spectra at discrete time intervals, thus giving information about the spectral evolution with time. This allows excited states to be monitored as they evolve over time and generally result in a three-dimensional spectrum that can be deconstructed to yield both time or frequency-dependent results. Measurement based on time-correlated single photon counting at different wavelengths is one of the most suitable schemes for studying excited state dynamics in semiconductors.

1.3.1 Time-Correlated Single Photon Counting
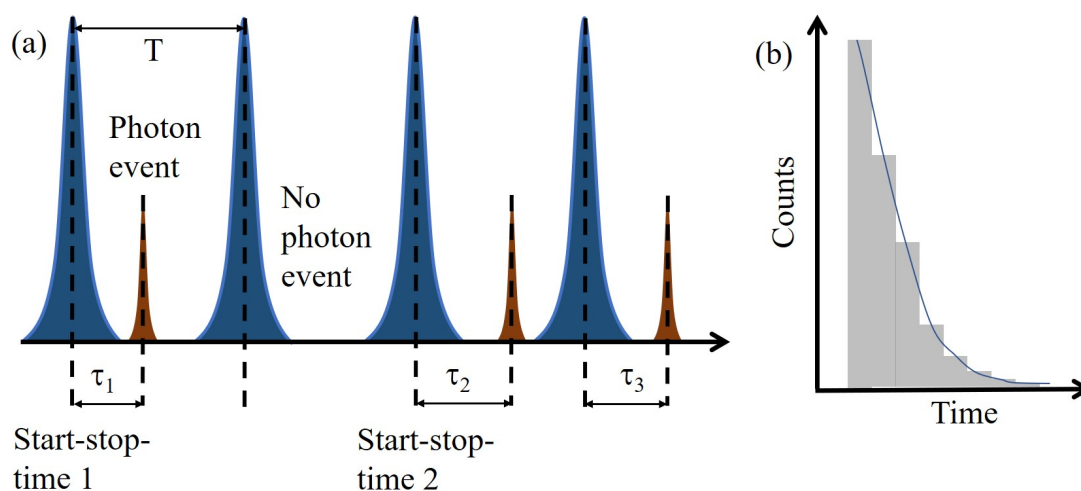
Figure 1.13: (a) Measurement of start-stop times (τ) with TCSPC, (b) Generation of the histogram after binning all the measured τ.

Time-resolved photoluminescence (TRPL) is a powerful analysis tool in the time domain for deriving the radiative lifetime of excited states in a molecule. It captures the time-dependent intensity profile of the photo-luminescent emission upon excitation by short light

pulses. Time-Correlated Single Photon Counting (TCSPC) method is generally implemented to record a molecule's time-dependent emission intensity profile. It is based on precisely registering photons coming from an excited molecule repetitively [5, 89]. The excitation pulse is the reference for timing and is generally termed the "sync" input to the TCSPC card.

Figure 1.13a illustrates the methodology that utilizes histograms generated over multiple cycles. The molecule is excited repetitively by short laser pulses. The difference in time τ between excitation and the first emitted photon is measured like a stopwatch. The stopwatch readings τ are sorted into time bins to generate a histogram. The width of the time bins is typically the resolution of the stopwatch. The result after histogramming is an exponential decay curve corresponding to the lifetime of the excited state (Figure 1.13b).

Detectors and electronics used in TCSPC measurements have a "dead" time after detecting a photon event, during which no other photon events can be processed. Hence, this would lead to typically registering the early photons and missing the following ones causing an over-representation of the initial photons in the histogram. This effect is generally called "pile-up". Typically, the count rate at the detector should be at most 1% to 5% of the laser repetition rate to avoid the pile-up effect.

The TRPL measurements in the laboratory were carried out using a home-built setup, as shown in Figure 1.14(a-b). A Picoquant LDH-P-C-405M laser source with a center wavelength of 405 nm and pulse width of 90 ps was driven by a Picoquant PDL 800-B laser diode driver to excite the sample. A Tektronix AFG1024 Arbitrary Function Generator (AFG) was used to control the repetition rate. The sync output from the laser driver was used as the reference. The emitted photons from the sample under test were recorded using a single photon counter (Picoquant PMA-C-192-M) coupled to Zolix Omni λ300 monochromator. Time tagging of the data was done using Picoquant TimeHarp 260 data acquisition card with a temporal resolution of $\sim$
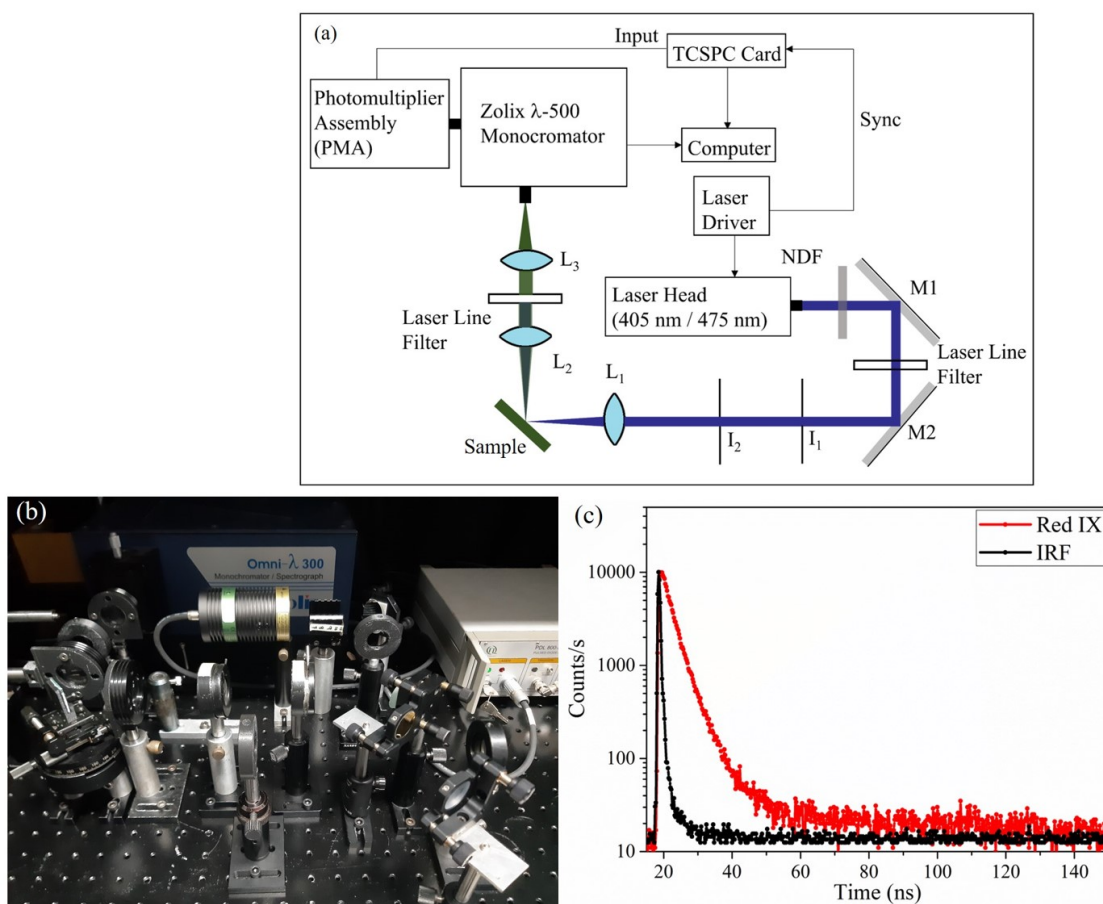
Figure 1.14: (a) Schematic for TRPL setup, (b) Experimental setup for TRPL, (c) TCSPC histograms of Red IX fluorescence dye and instrument response function (IRF).

250 ps. The count rate from the single photon counter is generally adjusted to $< 1\%$ of the laser repetition rate by using neutral density filters (NDF) to prevent pile-up effects. The monochromator was used to select the wavelengths for which the decay dynamics are to be measured. A typical decay profile coming from commercial Red IX dye from Aron dyes is shown in Figure 1.14c. The black curve denotes the instrument response function (IRF), which is typically ~ 1 ns in the custom-built system.

Time-gated emission spectra measurements are useful for studying the spectral evolution over time (especially where long-lived triplets are involved). The time series of the intensity decays are acquired at different wavelengths via Labview interfacing software. The time windows provide glimpses of different stages of the photophysical

process. The data acquired from the measurements can then be reconstructed using MATLAB codes in terms of emission-spectral profiles at different stages of the relaxation process. These measurements are particularly useful for understanding the time constants of the evolution of various states in a semiconductor (e.g., MAPbBr$_3$ single crystals [77]).

The existing literature consisting of solution-processed semiconductors is generally operated in steady-state for light emission and photovoltaics. The use of time and frequency domain measurement techniques decouples the various channels in recombination and charge carrier dynamics which cannot be accessed using the steady-state measurements. The thesis uses these approaches in newer systems such as TADF or tandem cells to disentangle the charge carrier and recombination dynamics. Different phenomena in these systems require different time and frequency domain measurements. For example, TrEL deconvolutes the charge carrier (usually in ns – few μs) and triplet dynamics timescales, giving direct evidence of the bimolecular triplet-triplet annihilation process not usually observed under optical excitation.

1.4 Outline of the Thesis

The thesis focuses on probing the various photophysical and charge transport mechanisms in solution-processed semiconductors using a combination of time and frequency domain measurements. Chapter two deals with the study of charge carrier dynamics using transient photocurrent (TPC) spectroscopy measurements on tandem solar cells under optical excitation. The active layers, composed of direct bandgap HOIP and the indirect band gap Si, have different optoelectronic properties and thicknesses. The TPC measurements directly assess the timescales of photogenerated charge carriers extracted at the electrodes. Spectral dependence of TPC measurements exhibits two distinct lifetime magnitudes: $\tau_1 \sim 500$ ns and $\tau_2 \sim 25$ μs. Further analysis shows that the carriers are extracted via drift and diffusion processes in the perovskite sub-cell, whereas Si sub-cell follows a diffusion-limited carrier extraction process. In the absence of background illumina-

tion, sub-cell processes are uncorrelated, and the current magnitude depends on the shunt resistance of the other sub-cell in the dark. A crossover of the dynamics of the perovskite sub-cell to a coupled regime with the Si sub-cell is observed beyond a threshold dc-light illumination.

The next part of the thesis (Chapter three) focuses on the charge carrier, and triplet dynamics in thermally activated delayed fluorescence (TADF) based organic light-emitting diodes (OLEDs) using temperature-dependent transient electroluminescence (TrEL) measurements. The TADF systems are expected to show increased emissive yield due to efficient back-conversion of non-emissive triplet states to emissive singlet states via reverse intersystem crossing (RISC). A solution-processed TADF molecule, 2,3,4,6-Tetra(9H-carbazol-9-yl)-5-fluorobenzonitrile (4CzFCN) was used in this study. The analysis of the rising edge of the TrEL pulse indicates that the carriers follow multiple trapping, de-trapping, and exciton recombination dynamics. The falling edge of the TrEL pulse provides insights into the monomolecular and bimolecular exciton dynamics, representative of device operational conditions. These studies indicate that triplet harvesting in 4CzFCN molecule occurs via both RISC and triplet-triplet annihilation (TTA). Further, the TADF processes dominate at high temperatures with negligible contribution from TTA.

Chapter four deals with the influence of various coatings on the wall (both phosphorescent and fluorescent) in the non-line of sight visible light communication. The enclosure boundary normally is treated as a classical light diffuser which merely scatters and attenuates the signal [90, 91]. The use of various photo-luminescent coatings on walls acts as active noise sources, which distort the signal and alter the communication characteristics. The possibility of tuning the signal to noise levels by these emitters as a function of the spatial coordinates can be utilized to design smart environments where signal access can be controlled and restricted. Conversely, the signal analysis used in this chapter can also be utilized to provide dynamic information about the environment.

Chapter five deals with the study of photon statistics of TADF dyes at different levels of dilution. These studies are helpful since the dyes might exhibit different photophysical kinetics at dilute concentrations owing to reduced intermolecular interactions. A custom-built confocal microscopy assembly was constructed to study TADF emitters at dilute concentrations. Photon statistics of various concentrations of TADF molecules were measured using a single photon avalanche diode (SPAD) integrated with the microscope. The photon statistics reveal correlations between the emitted photon from a TADF emitter at the initial timescales. An increase in the magnitude of the autocorrelation function was observed with a decrease in the number of TADF molecules.

Finally, chapter six studies the exciton dynamics of TADF molecules and light confinement effects in a fiber fabricated using the electrospinning method. The TADF-dispersed PMMA fibers exhibit high luminescence. The spatially uniform fiber emission suggests a homogenous distribution of dye molecules extended over the fiber. The fibre geometry allows for light confinement and waveguiding effects. Eigenmode analysis suggests the presence of cavity modes where the electric field profiles have nodes at the centre of the fiber.

References

[1] A. Köhler and H. Bässler, *Electronic processes in organic semiconductors: An introduction.* John Wiley & Sons, 2015.

[2] P. W. Atkins and R. S. Friedman, *Molecular quantum mechanics.* Oxford university press, 2011.

[3] M. Schwoerer and H. C. Wolf, *Organic molecular solids.* John Wiley & Sons, 2007.

[4] M. A. Baldo, D. O'brien, M. Thompson, and S. Forrest, "Excitonic singlet-triplet ratio in a semiconducting organic thin film," *Physical Review B*, vol. 60, no. 20, p. 14422, 1999.

[5] J. R. Lakowicz, *Principles of fluorescence spectroscopy.* Springer, 2006.

[6] C. W. Tang and S. A. VanSlyke, "Organic electroluminescent diodes," *Applied physics letters*, vol. 51, no. 12, pp. 913–915, 1987.

[7] J. H. Burroughes, D. D. Bradley, A. Brown, R. Marks, K. Mackay, R. H. Friend, P. L. Burns, and A. B. Holmes, "Light-emitting diodes

based on conjugated polymers," *nature*, vol. 347, no. 6293, pp. 539–541, 1990.

[8] T. Sekitani, H. Nakajima, H. Maeda, T. Fukushima, T. Aida, K. Hata, and T. Someya, "Stretchable active-matrix organic light-emitting diode display using printable elastic conductors," *Nature materials*, vol. 8, no. 6, pp. 494–499, 2009.

[9] M. S. White, M. Kaltenbrunner, E. D. Głowacki, K. Gutnichenko, G. Kettlgruber, I. Graz, S. Aazou, C. Ulbricht, D. A. Egbe, and M. C. Miron, "Ultrathin, highly flexible and stretchable pleds," *Nature Photonics*, vol. 7, no. 10, pp. 811–816, 2013.

[10] S. V. Novikov, D. H. Dunlap, V. M. Kenkre, P. E. Parris, and A. V. Vannikov, "Essential role of correlations in governing charge transport in disordered organic materials," *Physical Review Letters*, vol. 81, no. 20, p. 4472, 1998.

[11] M. Van der Auweraer, F. C. De Schryver, P. M. Borsenberger, and H. Bässler, "Disorder in charge transport in doped polymers," *Advanced materials*, vol. 6, no. 3, pp. 199–213, 1994.

[12] P. Borsenberger and H. Bässler, "Concerning the role of dipolar disorder on charge transport in molecularly doped polymers," *The Journal of chemical physics*, vol. 95, no. 7, pp. 5327–5331, 1991.

[13] M. Singh, Y. Tarutani, and K. Takagi, "Dynamics of carrier hopping in exponential band tails of quasi-one-dimensional systems in electric field," *physica status solidi (b)*, vol. 189, no. 2, pp. 499–508, 1995.

[14] T. Tiedje and A. Rose, "A physical interpretation of dispersive transport in disordered semiconductors," *Solid State Communications*, vol. 37, no. 1, pp. 49–52, 1981.

[15] R. A. Marcus, "On the theory of oxidation-reduction reactions involving electron transfer. i," *The Journal of chemical physics*, vol. 24, no. 5, pp. 966–978, 1956.

[16] Y. N. Gartstein and E. Conwell, "High-field hopping mobility in molecular systems with spatially correlated energetic disorder," *Chemical Physics Letters*, vol. 245, no. 4-5, pp. 351–358, 1995.

[17] A. Miller and E. Abrahams, "Impurity conduction at low concentrations," *Physical Review*, vol. 120, no. 3, p. 745, 1960.

[18] A. Köhler and H. Bässler, "Triplet states in organic semiconductors," *Materials Science and Engineering: R: Reports*, vol. 66, no. 4-6, pp. 71–109, 2009.

[19] N. J. Thompson, M. W. Wilson, D. N. Congreve, P. R. Brown, J. M. Scherer, T. S. Bischof, M. Wu, N. Geva, M. Welborn, and T. V. Voorhis, "Energy harvesting of non-emissive triplet excitons in

tetracene by emissive pbs nanocrystals," *Nature materials*, vol. 13, no. 11, pp. 1039–1043, 2014.

[20] D. Y. Kondakov, "Triplet-triplet annihilation in highly efficient fluorescent organic light-emitting diodes: current state and future outlook," *Philosophical Transactions of the Royal Society A: Mathematical, Physical and Engineering Sciences*, vol. 373, no. 2044, p. 20140321, 2015.

[21] A. Monkman and R. H. Friend, "Organic semiconductor spintronics: utilizing triplet excitons in organic electronics," 2015.

[22] M. A. Baldo, D. F. O'Brien, Y. You, A. Shoustikov, S. Sibley, M. E. Thompson, and S. R. Forrest, "Highly efficient phosphorescent emission from organic electroluminescent devices," *Nature*, vol. 395, no. 6698, pp. 151–154, 1998.

[23] C. Adachi, M. A. Baldo, M. E. Thompson, and S. R. Forrest, "Nearly 100internal phosphorescence efficiency in an organic light-emitting device," *Journal of Applied Physics*, vol. 90, no. 10, pp. 5048–5051, 2001.

[24] S. McGlynn, M. Reynolds, G. Daigre, and N. Christodoyleas, "The external heavy-atom spin-orbital coupling effect. iii. phosphorescence spectra and lifetimes of externally perturbed naphthalenes1, 2," *The Journal of Physical Chemistry*, vol. 66, no. 12, pp. 2499–2505, 1962.

[25] S. McGlynn, T. Azumi, and M. Kasha, "External heavy-atom spin-orbital coupling effect. v. absorption studies of triplet states," *The Journal of Chemical Physics*, vol. 40, no. 2, pp. 507–515, 1964.

[26] D. S. McClure, "Triplet-singlet transitions in organic molecules. lifetime measurements of the triplet state," *The Journal of Chemical Physics*, vol. 17, no. 10, pp. 905–913, 1949.

[27] N. J. Turro, *Modern molecular photochemistry.* University science books, 1991.

[28] S. P. McGlynn, T. Azumi, and M. Kinoshita, "Molecular spectroscopy of the triplet state," 1969.

[29] D. Beljonne, Z. Shuai, G. Pourtois, and J. Bredas, "Spin-orbit coupling and intersystem crossing in conjugated polymers: a configuration interaction description," *The Journal of Physical Chemistry A*, vol. 105, no. 15, pp. 3899–3907, 2001.

[30] M. El-Sayed, "Spin—orbit coupling and the radiationless processes in nitrogen heterocyclics," *The Journal of Chemical Physics*, vol. 38, no. 12, pp. 2834–2838, 1963.

[31] M. El-Sayed, "Comments on contaminating the ground state with triplet character," *The Journal of Chemical Physics*, vol. 38, no. 12, pp. 3032–3033, 1963.

[32] W. Jia, Q. Wang, H. Shi, Z. An, and W. Huang, "Manipulating the ultralong organic phosphorescence of small molecular crystals," *Chemistry–A European Journal*, vol. 26, no. 20, pp. 4437–4448, 2020.

[33] F. Perrin, "La fluorescence des solutions-induction moléculaire.–polarisation et durée d'émission.–photochimie," in *Annales de physique*, vol. 10, pp. 169–275, EDP Sciences.

[34] G. N. Lewis and M. Kasha, "Phosphorescence and the triplet state," *Journal of the American Chemical Society*, vol. 66, no. 12, pp. 2100–2116, 1944.

[35] G. N. Lewis, D. Lipkin, and T. T. Magel, "Reversible photochemical processes in rigid media. a study of the phosphorescent state," *Journal of the American Chemical Society*, vol. 63, no. 11, pp. 3005–3018, 1941.

[36] H. Uoyama, K. Goushi, K. Shizu, H. Nomura, and C. Adachi, "Highly efficient organic light-emitting diodes from delayed fluorescence," *Nature*, vol. 492, no. 7428, pp. 234–238, 2012.

[37] Q. Zhang, B. Li, S. Huang, H. Nomura, H. Tanaka, and C. Adachi, "Efficient blue organic light-emitting diodes employing thermally activated delayed fluorescence," *Nature photonics*, vol. 8, no. 4, pp. 326–332, 2014.

[38] Q. Zhang, J. Li, K. Shizu, S. Huang, S. Hirata, H. Miyazaki, and C. Adachi, "Design of efficient thermally activated delayed fluorescence materials for pure blue organic light emitting diodes," *Journal of the American Chemical Society*, vol. 134, no. 36, pp. 14706–14709, 2012.

[39] S. Y. Lee, T. Yasuda, H. Komiyama, J. Lee, and C. Adachi, "Thermally activated delayed fluorescence polymers for efficient solution-processed organic light-emitting diodes," *Advanced Materials*, vol. 28, no. 21, pp. 4019–4024, 2016.

[40] H. Nakanotani, T. Higuchi, T. Furukawa, K. Masui, K. Morimoto, M. Numata, H. Tanaka, Y. Sagara, T. Yasuda, and C. Adachi, "High-efficiency organic light-emitting diodes with fluorescent emitters," *Nature communications*, vol. 5, no. 1, pp. 1–7, 2014.

[41] H. Noda, X.-K. Chen, H. Nakanotani, T. Hosokai, M. Miyajima, N. Notsuka, Y. Kashima, J.-L. Brédas, and C. Adachi, "Critical role of intermediate electronic states for spin-flip processes in charge-transfer-type organic molecules with multiple donors and acceptors," *Nature materials*, vol. 18, no. 10, pp. 1084–1090, 2019.

[42] Z. Yang, Z. Mao, Z. Xie, Y. Zhang, S. Liu, J. Zhao, J. Xu, Z. Chi, and M. P. Aldred, "Recent advances in organic thermally activated delayed fluorescence materials," *Chemical Society Reviews*, vol. 46, no. 3, pp. 915–1016, 2017.

[43] P. L. dos Santos, M. K. Etherington, and A. P. Monkman, "Chemical and conformational control of the energy gaps involved in the thermally activated delayed fluorescence mechanism," *Journal of Materials Chemistry C*, vol. 6, no. 18, pp. 4842–4853, 2018.

[44] Y. Tao, K. Yuan, T. Chen, P. Xu, H. Li, R. Chen, C. Zheng, L. Zhang, and W. Huang, "Thermally activated delayed fluorescence materials towards the breakthrough of organoelectronics," *Advanced materials*, vol. 26, no. 47, pp. 7931–7958, 2014.

[45] J. Grune, N. Bunzmann, M. Meinecke, V. Dyakonov, and A. Sperlich, "Kinetic modeling of transient electroluminescence reveals tta as an efficiency-limiting process in exciplex-based tadf oleds," *The Journal of Physical Chemistry C*, vol. 124, no. 47, pp. 25667–25674, 2020.

[46] N. Aizawa, Y. Harabuchi, S. Maeda, and Y.-J. Pu, "Kinetic prediction of reverse intersystem crossing in organic donor-acceptor molecules," *Nature communications*, vol. 11, no. 1, pp. 1–6, 2020.

[47] M. Y. Wong and E. Zysman-Colman, "Purely organic thermally activated delayed fluorescence materials for organic light-emitting diodes," *Advanced Materials*, vol. 29, no. 22, p. 1605444, 2017.

[48] Z. He, C. Wang, J. Zhao, X. Du, H. Yang, P. Zhong, C. Zheng, H. Lin, S. Tao, and X. Zhang, "Blue and white solution-processed tadf-oleds with over 20% eqe, low driving voltages and moderate efficiency decrease based on interfacial exciplex hosts," *Journal of Materials Chemistry C*, vol. 7, no. 38, pp. 11806–11812, 2019.

[49] C.-Y. Chan, M. Tanaka, Y.-T. Lee, Y.-W. Wong, H. Nakanotani, T. Hatakeyama, and C. Adachi, "Stable pure-blue hyperfluorescence organic light-emitting diodes with high-efficiency and narrow emission," *Nature Photonics*, vol. 15, no. 3, pp. 203–207, 2021.

[50] Wisechip, "Wisechip launches the world's first hyperfluoresence oled display - a 2.7" yellow."

[51] A. Walsh, "Principles of chemical bonding and band gap engineering in hybrid organic–inorganic halide perovskites," *The Journal of Physical Chemistry C*, vol. 119, no. 11, pp. 5755–5760, 2015.

[52] V. M. Goldschmidt, "Die gesetze der krystallochemie," *Naturwissenschaften*, vol. 14, no. 21, pp. 477–485, 1926.

[53] W. Travis, E. Glover, H. Bronstein, D. Scanlon, and R. Palgrave, "On the application of the tolerance factor to inorganic and hybrid halide perovskites: a revised system," *Chemical science*, vol. 7, no. 7, pp. 4548–4556, 2016.

[54] Y. Zhao and K. Zhu, "Organic-inorganic hybrid lead halide perovskites for optoelectronic and electronic applications," *Chemical Society Reviews*, vol. 45, no. 3, pp. 655–689, 2016.

[55] C. Motta, F. El-Mellouhi, S. Kais, N. Tabet, F. Alharbi, and S. Sanvito, "Revealing the role of organic cations in hybrid halide perovskite ch3nh3pbi3," *Nature communications*, vol. 6, no. 1, pp. 1–7, 2015.

[56] Y. Yang, D. P. Ostrowski, R. M. France, K. Zhu, J. Van De Lagemaat, J. M. Luther, and M. C. Beard, "Observation of a hot-phonon bottleneck in lead-iodide perovskites," *Nature Photonics*, vol. 10, no. 1, pp. 53–59, 2016.

[57] M. R. Filip, G. E. Eperon, H. J. Snaith, and F. Giustino, "Steric engineering of metal-halide perovskites with tunable optical band gaps," *Nature communications*, vol. 5, no. 1, pp. 1–9, 2014.

[58] T. J. Jacobsson, J.-P. Correa-Baena, M. Pazoki, M. Saliba, K. Schenk, M. Grätzel, and A. Hagfeldt, "Exploration of the compositional space for mixed lead halogen perovskites for high efficiency solar cells," *Energy & Environmental Science*, vol. 9, no. 5, pp. 1706–1724, 2016.

[59] W. Zhu, C. Bao, F. Li, T. Yu, H. Gao, Y. Yi, J. Yang, G. Fu, X. Zhou, and Z. Zou, "A halide exchange engineering for ch3nh3pbi3- xbrx perovskite solar cells with high performance and stability," *Nano Energy*, vol. 19, pp. 17–26, 2016.

[60] B. Wenger, P. K. Nayak, X. Wen, S. V. Kesava, N. K. Noel, and H. J. Snaith, "Consolidation of the optoelectronic properties of ch3nh3pbbr3 perovskite single crystals," *Nature communications*, vol. 8, no. 1, pp. 1–10, 2017.

[61] M.-C. Tang, H. X. Dang, S. Lee, D. Barrit, R. Munir, K. Wang, R. Li, D.-M. Smilgies, S. De Wolf, and D.-Y. Kim, "Wide and tunable bandgap mapbbr3- xclx hybrid perovskites with enhanced phase stability: In situ investigation and photovoltaic devices," *Solar RRL*, vol. 5, no. 4, p. 2000718, 2021.

[62] M. Caputo, N. Cefarin, A. Radivo, N. Demitri, L. Gigli, J. R. Plaisier, M. Panighel, G. Di Santo, S. Moretti, and A. Giglia, "Electronic structure of mapbi3 and mapbcl3: importance of band alignment," *Scientific reports*, vol. 9, no. 1, pp. 1–11, 2019.

[63] G. Kim, H. Min, K. S. Lee, D. Y. Lee, S. M. Yoon, and S. I. Seok, "Impact of strain relaxation on performance of α-formamidinium lead iodide perovskite solar cells," *Science*, vol. 370, no. 6512, pp. 108–112, 2020.

[64] J. M. Richter, K. Chen, A. Sadhanala, J. Butkus, J. P. Rivett, R. H. Friend, B. Monserrat, J. M. Hodgkiss, and F. Deschler, "Direct bandgap behavior in rashba-type metal halide perovskites," *Advanced Materials*, vol. 30, no. 52, p. 1803379, 2018.

[65] K. Galkowski, A. Mitioglu, A. Miyata, P. Plochocka, O. Portugall, G. E. Eperon, J. T.-W. Wang, T. Stergiopoulos, S. D. Stranks,

and H. J. Snaith, "Determination of the exciton binding energy and effective masses for methylammonium and formamidinium lead trihalide perovskite semiconductors," *Energy & Environmental Science*, vol. 9, no. 3, pp. 962–970, 2016.

[66] A. Miyata, A. Mitioglu, P. Plochocka, O. Portugall, J. T.-W. Wang, S. D. Stranks, H. J. Snaith, and R. J. Nicholas, "Direct measurement of the exciton binding energy and effective masses for charge carriers in organic-inorganic tri-halide perovskites," *Nature Physics*, vol. 11, no. 7, pp. 582–587, 2015.

[67] J. Even, L. Pedesseau, and C. Katan, "Analysis of multivalley and multibandgap absorption and enhancement of free carriers related to exciton screening in hybrid perovskites," *The Journal of Physical Chemistry C*, vol. 118, no. 22, pp. 11566–11572, 2014.

[68] J. Tilchin, D. N. Dirin, G. I. Maikov, A. Sashchiuk, M. V. Kovalenko, and E. Lifshitz, "Hydrogen-like wannier-mott excitons in single crystal of methylammonium lead bromide perovskite," *ACS nano*, vol. 10, no. 6, pp. 6363–6371, 2016.

[69] M. Hu, C. Bi, Y. Yuan, Z. Xiao, Q. Dong, Y. Shao, and J. Huang, "Distinct exciton dissociation behavior of organolead trihalide perovskite and excitonic semiconductors studied in the same system," *small*, vol. 11, no. 18, pp. 2164–2169, 2015.

[70] H. Kunugita, T. Hashimoto, Y. Kiyota, Y. Udagawa, Y. Takeoka, Y. Nakamura, J. Sano, T. Matsushita, T. Kondo, and T. Miyasaka, "Excitonic feature in hybrid perovskite ch3nh3pbbr3 single crystals," *Chemistry Letters*, vol. 44, no. 6, pp. 852–854, 2015.

[71] K. Lin, J. Xing, L. N. Quan, F. De Arquer, X. Gong, J. Lu, L. Xie, W. Zhao, D. Zhang, and C. Yan, "Perovskite light-emitting diodes with external quantum efficiency exceeding 20 per cent," *Nature*, vol. 562, no. 7726, pp. 245–248, 2018.

[72] N. Zhang, Y. Fan, K. Wang, Z. Gu, Y. Wang, L. Ge, S. Xiao, and Q. Song, "All-optical control of lead halide perovskite microlasers," *Nature communications*, vol. 10, no. 1, pp. 1–7, 2019.

[73] D. A. Neamen, *Semiconductor physics and devices: basic principles*. McGraw-hill, 2003.

[74] W. Shockley and H. J. Queisser, "Detailed balance limit of efficiency of p-n junction solar cells," *Journal of applied physics*, vol. 32, no. 3, pp. 510–519, 1961.

[75] R. N. Hall, "Electron-hole recombination in germanium," *Physical review*, vol. 87, no. 2, p. 387, 1952.

[76] W. Shockley and W. Read Jr, "Statistics of the recombinations of holes and electrons," *Physical review*, vol. 87, no. 5, p. 835, 1952.

[77] N. Ganesh, A. Ghorai, S. Krishnamurthy, S. Banerjee, K. Narasimhan, S. B. Ogale, and K. Narayan, "Impact of trap filling on carrier diffusion in mapb br 3 single crystals," *Physical Review Materials*, vol. 4, no. 8, p. 084602, 2020.

[78] See https://www.nrel.gov/pv/cell-efficiency.html for , "NREL Best Research-Cell Efficiency Chart," 2022.

[79] N. Jensen, R. Hausner, R. Bergmann, J. Werner, and U. Rau, "Optimization and characterization of amorphous/crystalline silicon heterojunction solar cells," *Progress in Photovoltaics: Research and Applications*, vol. 10, no. 1, pp. 1–13, 2002.

[80] Q. Jiang, Y. Zhao, X. Zhang, X. Yang, Y. Chen, Z. Chu, Q. Ye, X. Li, Z. Yin, and J. You, "Surface passivation of perovskite film for efficient solar cells," *Nature Photonics*, vol. 13, no. 7, pp. 460–466, 2019.

[81] W. S. Yang, B.-W. Park, E. H. Jung, N. J. Jeon, Y. C. Kim, D. U. Lee, S. S. Shin, J. Seo, E. K. Kim, and J. H. Noh, "Iodide management in formamidinium-lead-halide-based perovskite layers for efficient solar cells," *Science*, vol. 356, no. 6345, pp. 1376–1379, 2017.

[82] J. Huang, Y. Yuan, Y. Shao, and Y. Yan, "Understanding the physical properties of hybrid perovskites for photovoltaic applications," *Nature Reviews Materials*, vol. 2, no. 7, pp. 1–19, 2017.

[83] U. Rau, "Reciprocity relation between photovoltaic quantum efficiency and electroluminescent emission of solar cells," *Physical Review B*, vol. 76, no. 8, p. 085303, 2007.

[84] J. A. Nelson, *The physics of solar cells.* World Scientific Publishing Company, 2003.

[85] R. Lin, J. Xu, M. Wei, Y. Wang, Z. Qin, Z. Liu, J. Wu, K. Xiao, B. Chen, and S. M. Park, "All-perovskite tandem solar cells with improved grain surface passivation," *Nature*, pp. 1–9, 2022.

[86] A. Al-Ashouri, A. Magomedov, M. Rob, M. Jost, M. Talaikis, G. Chistiakova, T. Bertram, J. A. Márquez, E. Köhnen, and E. Kasparavičius, "Conformal monolayer contacts with lossless interfaces for perovskite single junction and monolithic tandem solar cells," *Energy & Environmental Science*, vol. 12, no. 11, pp. 3356–3369, 2019.

[87] T. Todorov, T. Gershon, O. Gunawan, Y. S. Lee, C. Sturdevant, L. Chang, and S. Guha, "Monolithic perovskite-cigs tandem solar cells via in situ band gap engineering," *Advanced Energy Materials*, vol. 5, no. 23, p. 1500799, 2015.

[88] A. Al-Ashouri, E. Köhnen, B. Li, A. Magomedov, H. Hempel, P. Caprioglio, J. A. Márquez, A. B. M. Vilches, E. Kasparavicius,

and J. A. Smith, "Monolithic perovskite/silicon tandem solar cell with > 29hole extraction," *Science*, vol. 370, no. 6522, pp. 1300–1309, 2020.

[89] D. O'Connor, *Time-correlated single photon counting.* Academic press, 2012.

[90] Y. H. Chung and S.-b. Oh, "Efficient optical filtering for outdoor visible light communications in the presence of sunlight or articifical light," in *2013 International Symposium on Intelligent Signal Processing and Communication Systems*, pp. 749–752, IEEE, 2013.

[91] Y. Zhao and J. Vongkulbhisal, "Design of visible light communication receiver for on-off keying modulation by adaptive minimum-voltage cancelation," *Engineering Journal*, vol. 17, no. 4, pp. 125–130, 2013.

2

Insights into the charge carrier dynamics in perovskite/Si tandem solar cells using transient photocurrent spectroscopy

2.1 Introduction

The facile methods to tune the bandgaps of perovskite, coupled with their high efficiencies, makes them a valuable choice for 'two-terminal' tandem solar cells. It consists of two solar cells (one wide bandgap and one narrow bandgap) connected in series using a recombination layer. The easy processability of perovskite solar cells provides facile deposition on silicon solar cells and can increase the efficiencies of commercial PVs, maintaining the economics of scaling [2]. The efficiency limits of these perovskite-based tandem solar cells are well above 30% and provide much scope for further improvement [3].

The efficiency of a tandem solar cell strongly depends on the absorbance of the active layers in each of the sub-cells, the interfacial and bulk traps or defects present in the active materials, which can reduce the charge-carrier collection, and the inter sub-cell current matching condition [4]. The tandem solar cells are then generally designed and fabricated based on the optical characteristics of each of the active materials in respective sub-cells. The bandgap of the top perovskite sub-cell is tailored in such a way (theoretically in the range of 1.6 eV -1.75 eV) [5–8] so that the optimum efficiency is reached when coupled to a silicon sub-cell. It was observed that a perovskite bandgap of 1.66

eV with an active layer thickness of 500 nm was optimum for arriving at the current matching condition [9, 10]. We explore the possibility of further fine-tuning the sub-cells by controlling their carrier dynamics. The coupling of the two sub-cells in series makes it difficult to deconvolve the dynamics in the sub-cells necessary for optimising the tandem solar cells.

This chapter provides insight into the charge-carrier dynamics in the individual sub-cells using transient photocurrent (TPC) spectroscopy in the tandem configuration, which helps us to understand the generation and recombination dynamics of charge-carriers in complete tandem devices. The TPC measurements help us assess the timescales of photogenerated charge carriers extracted to the electrodes. The pathway for losses in external quantum efficiency (EQE) via recombination (both radiative and non-radiative) can be directly probed by TPC. When a short pulse (< 1 ns) is used as the excitation source, the generation duration can be considered almost instantaneous, as compared to the other processes in the device (namely recombination and carrier dynamics). The current due to photogenerated excess carriers (δn) can be expressed as [11]

$$I = \frac{d(\delta n)}{dt} = D\frac{\partial^2(\delta n)}{\partial x^2} + \mu E\frac{\partial(\delta n)}{\partial x} - R \tag{2.1}$$

where R is the recombination term, D and μ are the diffusion coefficient and mobility of carriers, respectively. In the case of thick silicon cells, $E \approx 0$, which is attributed to the diffusion-limited transport in Si. However, in the case of perovskite, there are contributions from carrier recombination lifetime and carrier-transit time in the TPC profiles. The response profiles of the transient as a function of different parameters under a model framework can explain the performance of tandem solar cells under continuous white-light excitation.

2.2 Fabrication of perovskite/Si tandem solar cell

The tandem solar cells were fabricated in Oxford, UK. N-doped FZ c-Si wafers (4 in., $< 100 >$ orientation, 270 μm, 3 Ω-cm) with both sides polished were used. The front side of the wafers was covered with

a SiO_x protective layer, and the substrates were chemically treated to obtain random pyramids with $< 111 >$ oriented facets and a final wafer thickness of 250 μm. All silicon layer depositions were carried out in an Applied Materials PECVD cluster tool (AKT1600) operating at 13.56 MHz plasma excitation frequency (electrode area of 2000 cm^2) using SiH_4, H_2, PH_3, B_2H_6 and CO_2 as process gases. Before the PECVD process, the wafers were cleaned by the RCA procedure [12], dipped in HF, and diluted to 1% H_2O for 3 min to remove the native oxide. The front side of the c-Si substrates was covered by $\approx$ 5 nm thick (i)α-Si:H and (n)nc-SiO_x:H (variable thickness and oxygen content) layers, while on the rear side, the (i)α-Si/(p)α-Si:H (4 nm/7 nm) stack was grown on the textured surface. More details can be found in Reference [13]. Afterwards, transparent conducting oxides and metal are DC sputtered in a Leybold A600V7 by means of aligned sputtering masks to obtain rectangular cells with an area of 1 cm^2. In particular, 25 nm of In_2O_3:Sn (ITO) was deposited on the polished side from a 3 wt% Sn-doped ITO target at a set temperature of 220 ^oC using an argon/oxygen mixture as process gas. The rear (textured) side is completed with 70 nm aluminium zinc oxide (ZnO:Al, AZO) sputtered from a ZnO target doped with 1 wt% Al_2O_3 in an argon/oxygen mixture, followed by the deposition of a 400 nm Ag electrode. This latter was sputtered at room temperature. The completed Si bottom-cell wafers were diced into 3 cm $\times$ 3 cm individual substrates by laser scribing to allow more feasible subsequent solution-based processing steps.

The perovskite top cells were processed directly onto the front side of the completed Si sub-cells to form the monolithic perovskite/Si tandem cells. The processing parameters were the same as described in Reference [14], with 10 nm C_{60} deposited by evaporation, 20 nm SnO_2 and 80 nm ITO deposited via atomic layer deposition (ALD) and sputtering.

The final device structure of the fabricated tandem solar was ITO (80 nm)/ SnO_2 (20 nm)/C_{60} (10 nm)/$Cs_{0.05}(FA_{0.83}MA_{0.17})_{0.95}Pb(I_{0.77}Br_{0.23})_3$ (500 nm)/Poly-TPD (5 nm)/ITO (25 nm)/(nc)SiO_x:H (110 nm)/(i)$\alpha-$Si:H (5 nm)/(n)c-Si (250 μm)/(i)α-Si:H (5 nm)/(p)α-Si:H (5 nm)/AZO (70 nm)/Ag (400
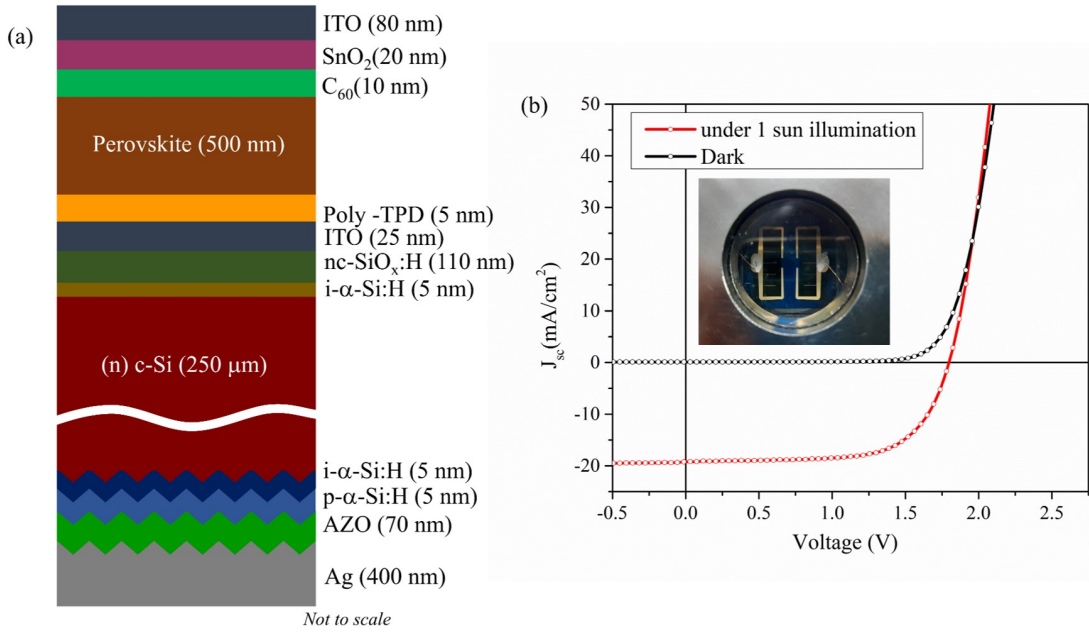
Figure 2.1: (a) Device architecture of two-terminal perovskite/Si tandem solar cell, (b) typical J – V characteristics of the tandem solar cell under simulated AM 1.5G (100 mW/cm^2) illumination (inset shows the picture of tandem device).Reproduced from A. Ghorai, P. Kumar, S. Mahesh, Y.-H. Lin, H. J. Snaith, K. Narayan, Applied Physics Letters 2022, 120, 173504. [1], with the permission of AIP Publishing

nm). Figure 1a shows the device architecture of the tandem solar cell with an active area of 1.1cm^2.

The J–V characteristics (Figure 1b) of the tandem solar cell under simulated AM1.5G (100 mW/cm^2) illumination were performed for the determination of typical solar cell parameters. These parameters are listed in Table 2.1.

Table 2.1: Solar Cell parameters for the fabricated perovskite/Si Tandem Solar Cell

Efficiency	Fill Factor	J_{sc} (mA/cm^2)	V_{oc} (V)
23.0%	66.44%	19.23	1.80

2.3 Light Beam Induced Current Imaging

Light-Beam Induced Current (LBIC) imaging of the solar cell verifies the active area and the degree of homogeneity [15]. LBIC images directly highlight the presence of defective regions [16–18]. The measure-
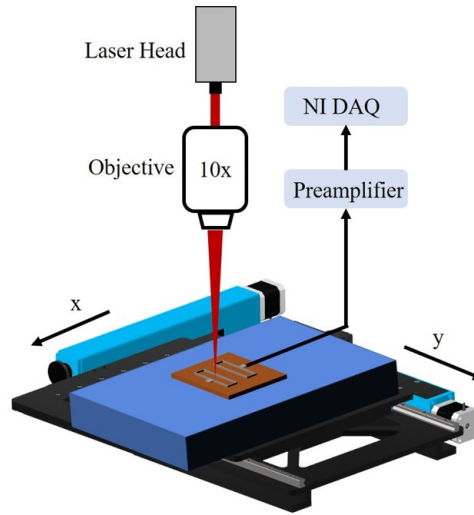
Figure 2.2: Schematic of the LBIC imaging experimental setup.

ment was carried out using a home-built LBIC setup with 650 nm as the excitation wavelength (Figure 2.2). The CW laser light of centre wavelength 650 nm and power 10 mW was focused using a microscope objective ($10\times$, 0.25 NA) on the tandem device. This laser spot is translated throughout the device area using a stepper motor assembly. A pre-amplifier (SRS 570) was used to amplify the short circuit current signal, I_{ph}, from the device to an output voltage. This voltage signal was recorded using an NI cDAQ-9232 module as a function of $x - y$ coordinate to obtain the respective LBIC image.
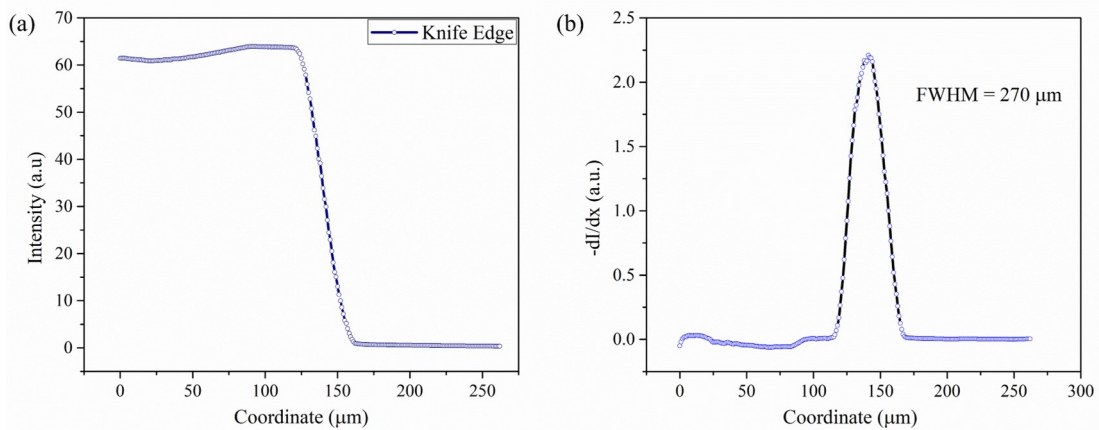
Figure 2.3: (a)The intensity profile as the focussed beam spot is translated across the knife edge (b) First order differential of the intensity profile. The FWHM gives the beam spot. Reproduced from A. Ghorai, P. Kumar, S. Mahesh, Y.-H. Lin, H. J. Snaith, K. Narayan, Applied Physics Letters 2022, 120, 173504. [1], with the permission of AIP Publishing

The laser's spot size was measured using the knife-edge technique [19]. The technique involves a knife edge being translated across the focussed

beam in the line of light incident on the detector. With the knife edge translation, the light intensity on the detector varies, as shown in Figure 2.3a. The first differential plot of the intensity indicates the beam profile used to give the spot size, shown in Figure 2.3b. The spot used in scanning the tandem cell had an FWHM of ~ 270 μm.
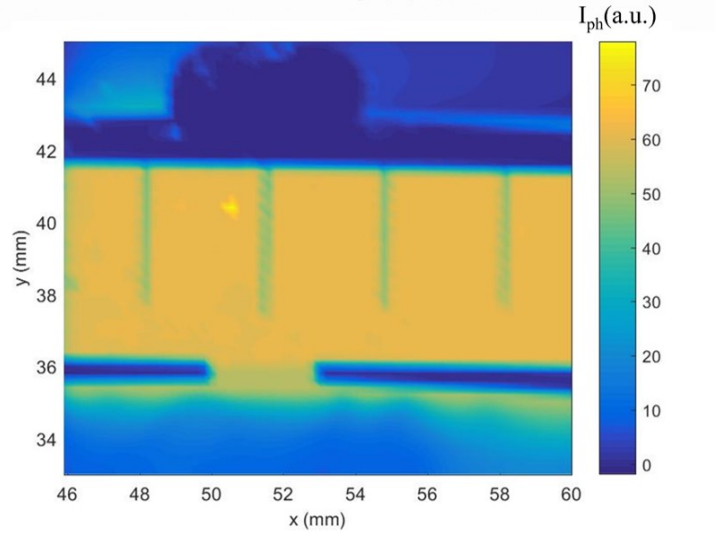
Figure 2.4: A 2D LBIC image of the perovskite/Si tandem solar cell. Reproduced from A. Ghorai, P. Kumar, S. Mahesh, Y.-H. Lin, H. J. Snaith, K. Narayan, Applied Physics Letters 2022, 120, 173504. [1], with the permission of AIP Publishing

The LBIC image of the tandem cell is shown in Figure 2.4. The image shows a uniform charge-carrier generation region throughout the device, measured at a resolution of 270 μm.

2.4 Transient Photocurrent Spectroscopy

Supercontinuum laser pulses for the wavelength range of 400 nm to 2400 nm (YSL Supercontinuum SC-Pro) with a pulse width of 100 ps and a repetition rate of 10 kHz were used to excite the tandem device (Figure 2.5). The transient photocurrent (TPC) profiles were recorded using a Tektronix MDO34 digital signal oscilloscope. A voltage drop generated across the device was measured using an internal 50 Ω termination resistor inside the oscilloscope [20–23]. λ-dependent TPC measurements were achieved by coupling the supercontinuum laser to an Acousto-Optic Tunable Filter (AOTF). The intensity of the monochromatic laser pulses was controlled using the AOTF. For the application of a reverse bias voltage, a Keithley 2231A-30-3 triple-channel DC power supply was used.
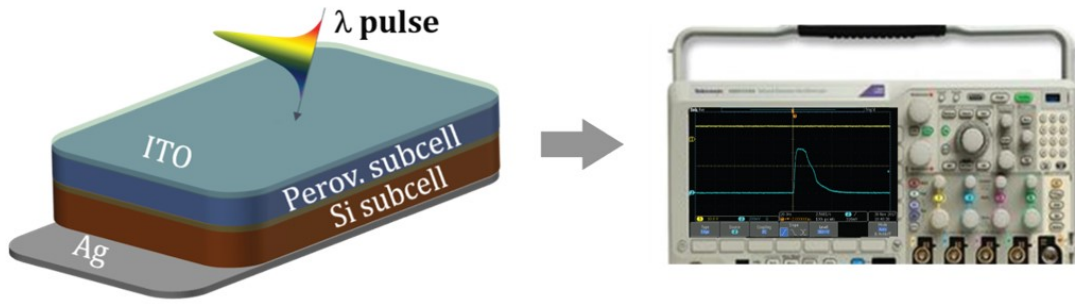
Figure 2.5: Schematic for TPC measurements. Reproduced from A. Ghorai, P. Kumar, S. Mahesh, Y.-H. Lin, H. J. Snaith, K. Narayan, Applied Physics Letters 2022, 120, 173504. [1], with the permission of AIP Publishing

All the experiments were performed in a nitrogen environment to avoid degradation. TPC experiments in the presence of background illumination were performed using: (a) 470 nm laser for selectively exciting the HOIP sub-cell and (b) a Fianium Whitelase Micro supercontinuum laser (wavelength range of 850 nm - 2000 nm ensured using 850 nm LP filter) driven at 30 MHz for exciting the Si sub-cell.
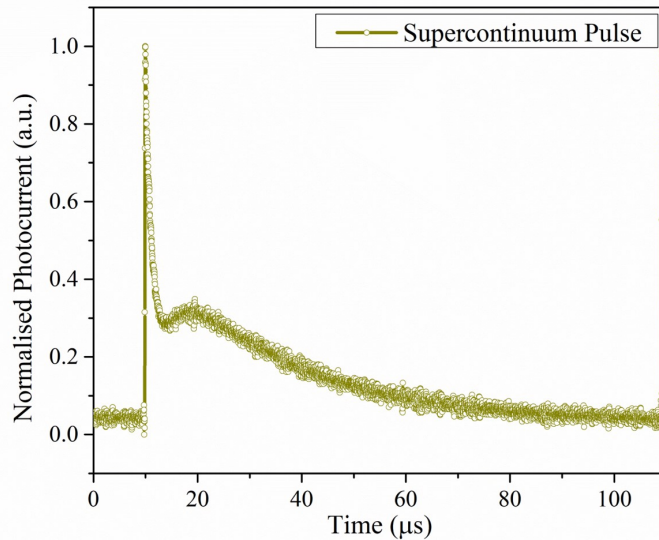
Figure 2.6: Transient Photocurrent profile for the tandem solar cell in response to a supercontinuum pulse (wavelength range 400 nm – 2400 nm). Reproduced from A. Ghorai, P. Kumar, S. Mahesh, Y.-H. Lin, H. J. Snaith, K. Narayan, Applied Physics Letters 2022, 120, 173504. [1], with the permission of AIP Publishing

The response of the tandem cell to a supercontinuum pulse is shown in Figure 2.6. From the response, it is evident that two distinct TPC
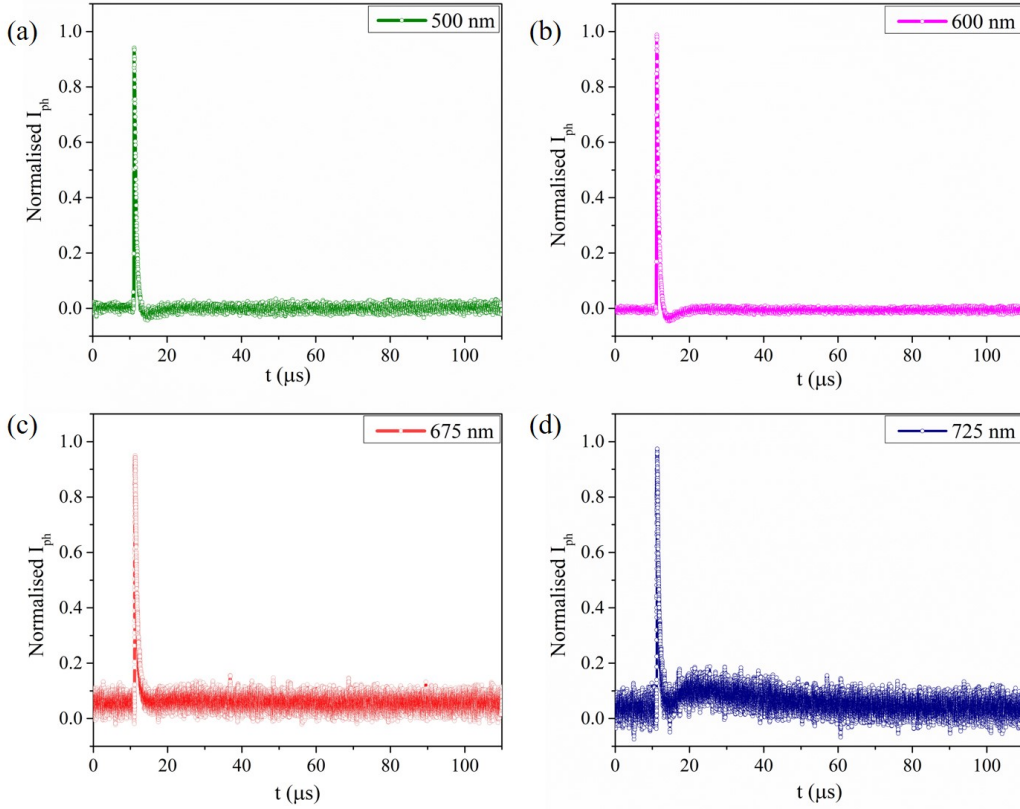
Figure 2.7: Transient photocurrent profiles of the tandem solar cell for excitation λs of (a) 500 nm, (b) 600 nm, (c) 675 nm and (d) 725 nm. Reproduced from A. Ghorai, P. Kumar, S. Mahesh, Y.-H. Lin, H. J. Snaith, K. Narayan, Applied Physics Letters 2022, 120, 173504. [1], with the permission of AIP Publishing

signatures are present. The TPC profiles were recorded as a function of the excitation wavelength to understand the origin of these two distinct signatures. The TPC measurements were also carried out with different background light intensities and electrical bias conditions.

2.5   Single subcell excitation

A series of TPC measurements were carried out at different λ. The TPC profiles corresponding to excitation wavelengths of 500 nm, 600 nm, 675 nm and 725 nm are shown in Figure 2.7. The dynamics of the photogenerated carriers in the perovskite sub-cell dominate the TPC response in the high-energy spectral region (< 700 nm). Even though the $I_{ph}(t)$ for the perovskite sub-cell in the tandem consists of multiple contributions, the decay is dominantly described by a single
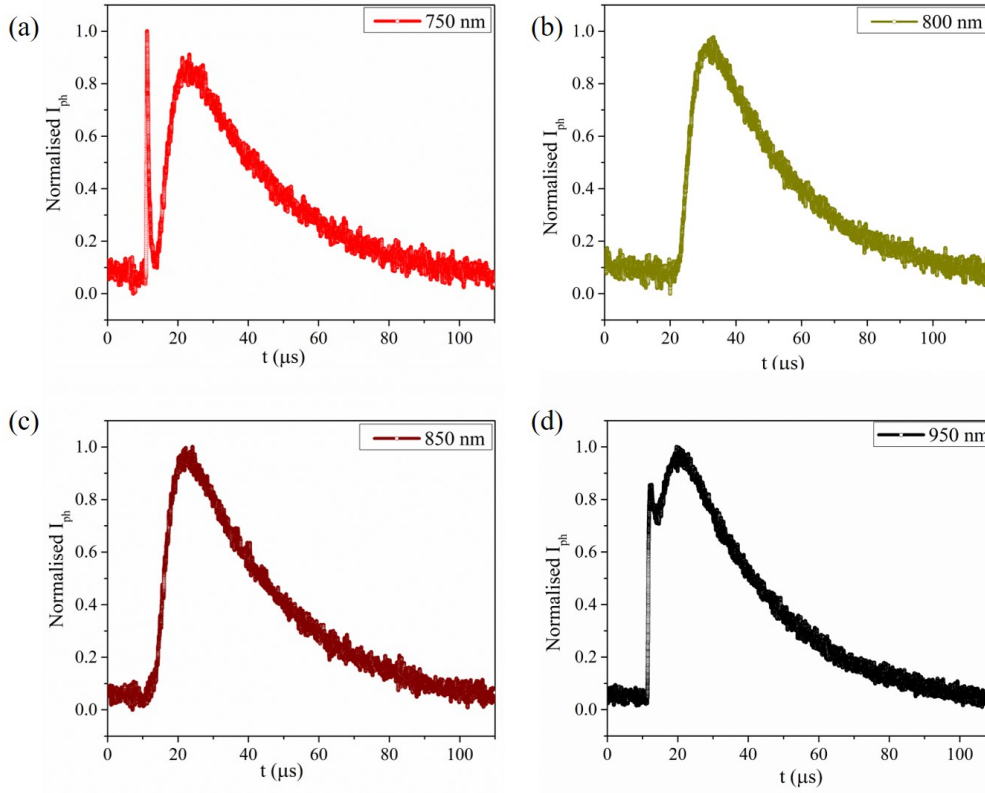
Figure 2.8: Transient photocurrent profiles of the tandem solar cell for excitation λs of (a) 750 nm, (b) 800 nm, (c) 850 nm and (d) 950 nm. Reproduced from A. Ghorai, P. Kumar, S. Mahesh, Y.-H. Lin, H. J. Snaith, K. Narayan, Applied Physics Letters 2022, 120, 173504. [1], with the permission of AIP Publishing

exponential. The corresponding TPC lifetime τ_1 is obtained by fitting the decay profiles to single exponentials in this spectral region with $\tau_1 \approx 500$ ns.

The dynamics of the photogenerated carriers in the silicon sub-cell (Figure 2.8) dominate the TPC in the lower energy spectral region (> 750 nm) with a slower decay lifetime of ≈ 25 μs. The intermediate region (675 nm - 750 nm excitation), as shown in Figure 2.7(c-d) and Figure 2.8a, shows the distinct contributions of TPC profiles that arise from both the perovskite as well as Si sub-cells. The transient photocurrent decay in both the spectral regions can be modelled to a single exponential reasonably and a distinct crossover from the carrier relaxation processes in the perovskite layer to Si sub-cells as a function of incident light λ can be observed. The TPC profile corresponding to the perovskite sub-cell reduced considerably
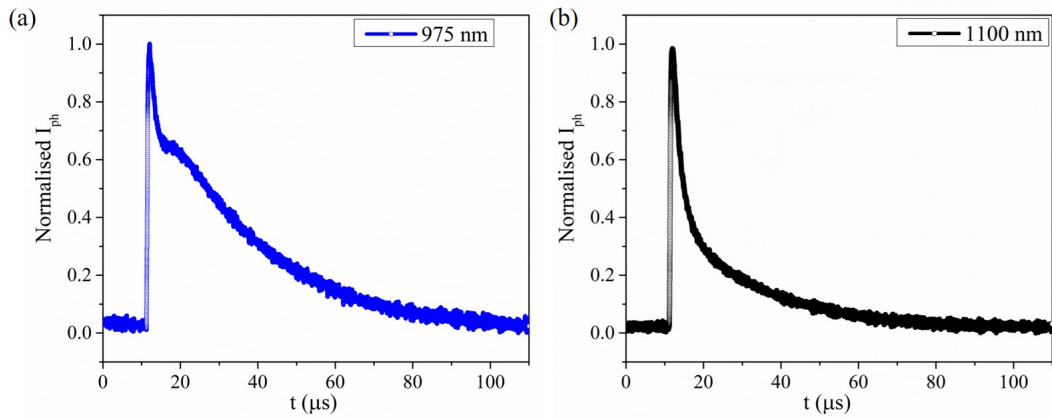
Figure 2.9: Transient photocurrent profiles of the tandem solar cell for excitation λs of (a) 975 nm and (b) 1100 nm. Reproduced from A. Ghorai, P. Kumar, S. Mahesh, Y.-H. Lin, H. J. Snaith, K. Narayan, Applied Physics Letters 2022, 120, 173504. [1], with the permission of AIP Publishing

beyond 700 nm and is negligible beyond 800 nm of excitation. Thus, for $\lambda > 800$ nm, the TPC profiles represents the Si sub-cell response exclusively. In the region $\lambda > 900$ nm, the TPC decay profile evolved from being a single exponential to a bi-exponential decay given by $I_{ph}(t) = Bexp(-t/\tau_2) + Cexp(-t/\tau_3) + d$ with τ_2 continuing to be in the range of ≈ 25 μs and $\tau_3 \approx 2$ μs (Figure 2.9). The variation of TPC lifetimes corresponding to Si (τ_2 and τ_3) with λ are shown in Figure 2.14.
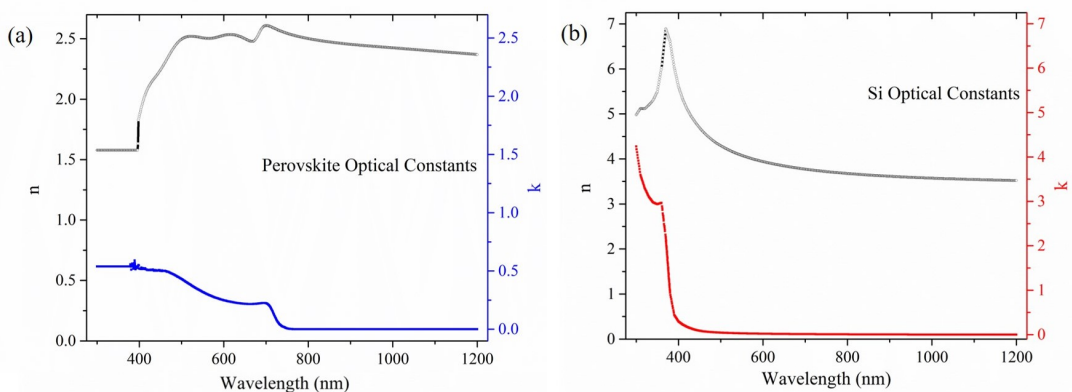
Figure 2.10: Real and Imaginary components of refractive indices for (a) perovskite (b) Si as a function of wavelength measured from ellipsometry. Reproduced from A. Ghorai, P. Kumar, S. Mahesh, Y.-H. Lin, H. J. Snaith, K. Narayan, Applied Physics Letters 2022, 120, 173504. [1], with the permission of AIP Publishing

2.6 Carrier Generation Profiles
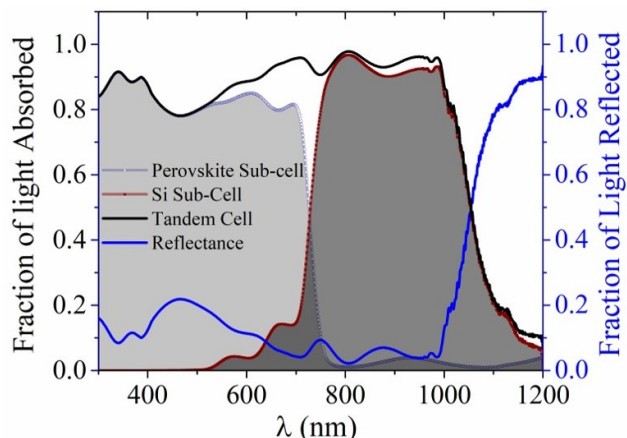
Figure 2.11: Fraction of light absorbed by perovskite sub-cell, Si sub-cell and tandem cell plotted in left y-axis; fraction of light reflected from the tandem cell plotted in the right y-axis (both derived from scattering matrix formalism). Reproduced from A. Ghorai, P. Kumar, S. Mahesh, Y.-H. Lin, H. J. Snaith, K. Narayan, Applied Physics Letters 2022, 120, 173504. [1], with the permission of AIP Publishing

The three timescales τ_1, τ_2 and τ_3, can be interpreted in terms of the multi-layered structure using a scattering-matrix optical model [24] (Appendix A). The scattering matrices for each layer in the tandem
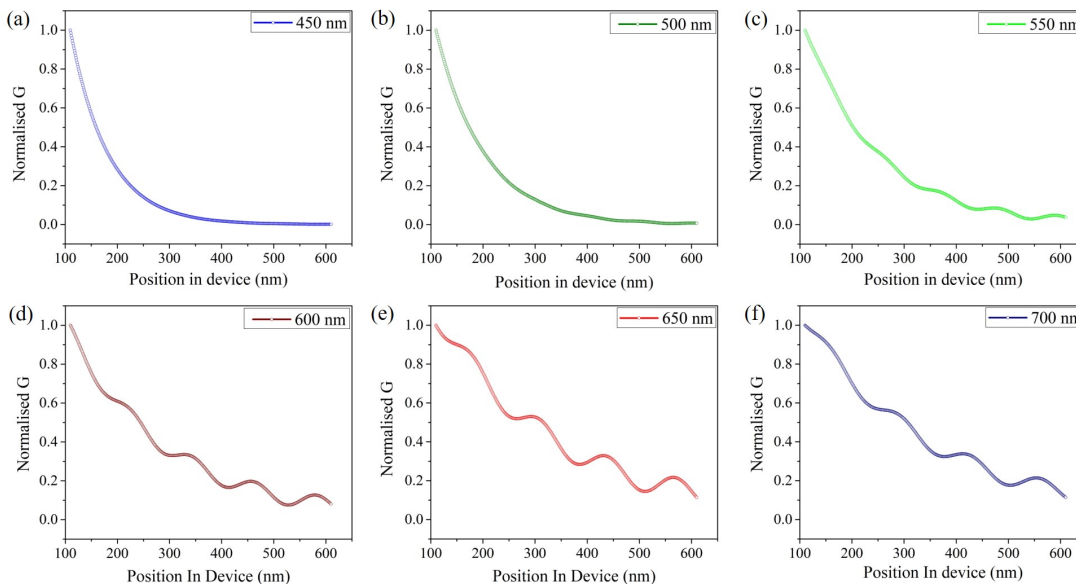
Figure 2.12: Carrier Generation (G) profiles in perovskite active layer for (a) 450 nm (b) 500 nm (c) 550 nm (d) 600 nm (e) 650 nm (f) 700 nm excitation derived from scattering matrix formalism. Reproduced from A. Ghorai, P. Kumar, S. Mahesh, Y.-H. Lin, H. J. Snaith, K. Narayan, Applied Physics Letters 2022, 120, 173504. [1], with the permission of AIP Publishing

solar cell were derived for each wavelength using their corresponding refractive index dispersion curves using MATLAB. The variation of n and k for perovskite and Si as a function of λ is given in Figure 2.10. Figure 2.11 shows the fraction of light absorbed by the individual sub-cell of perovskite and Si. The fraction of light reflected from the whole tandem cell is also indicated in Figure 2.11.
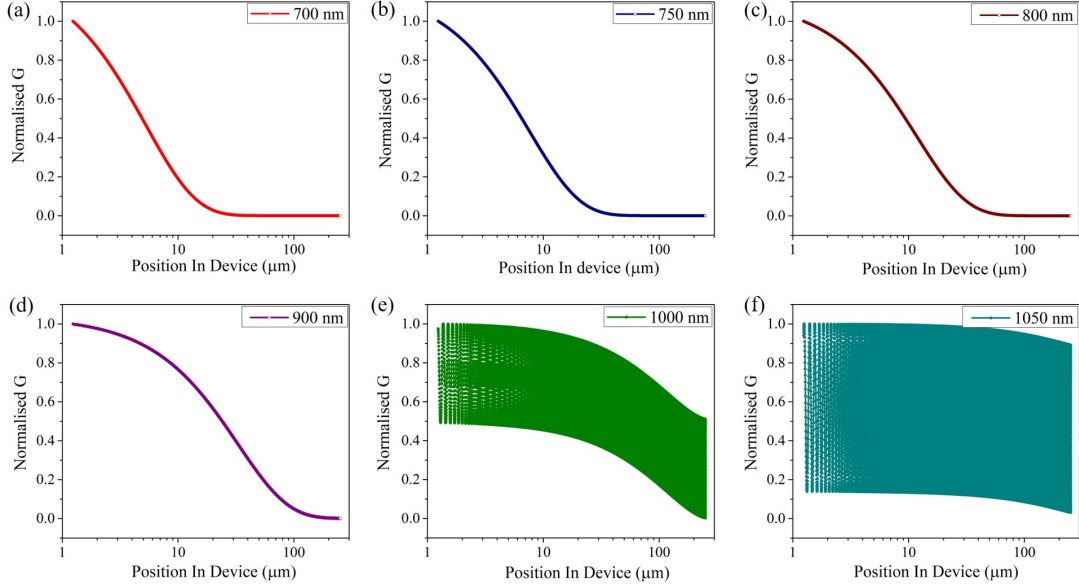
Figure 2.13: Carrier Generation (G) profiles in Si active layer for (a) 700 nm (b) 750 nm (c) 800 nm (d) 900 nm (e) 1000 nm (f) 1050 nm excitation derived from scattering matrix formalism. Reproduced from A. Ghorai, P. Kumar, S. Mahesh, Y.-H. Lin, H. J. Snaith, K. Narayan, Applied Physics Letters 2022, 120, 173504. [1], with the permission of AIP Publishing

The internal electric fields were calculated at each of the layers from the scattering matrices generated for each layer. These internal electric field profiles were generated for the λ range between 500 nm and 1100 nm. The charge-carrier generation at each of the layers is proportional to the square of the modulus of the internal electric field and expressed as [25, 26]

$$
G = \frac{\lambda}{hc}Q
$$
$$
Q = 4\pi c \frac{\epsilon_0 k(\lambda) n(\lambda)}{2\lambda}|E(x)|^2
$$

(2.2)

where $k(\lambda)$ and $n(\lambda)$ are the real and imaginary parts of the refractive

index.

The carrier generation profiles for both the perovskite layer and Si layer are estimated for different λ (Figure 2.12 and Figure 2.13). From the carrier generation profiles for Si, a parameter of excess carrier density decay length, L, is determined by fitting a single exponential. A lower L magnitude is indicative of the larger distance of the charge-carrier generation region from the electrode.

Figure 2.14 shows the non-linear variation of L with λ with a drastic rise beyond 1000 nm. Thus, for $\lambda > 950$ nm, more charge carriers are generated near the electrode in contrast to lower wavelengths, thus creating an initial charging at the electrode. This gives rise to a quite observable displacement current with a lifetime τ_3 for the $\lambda > 950$ nm. The inverse effect considering the perovskite sub-cell can also be observed where a negative displacement current is observed for the wavelength range $\lambda < 650$ nm as more charges are generated near the top electrode.
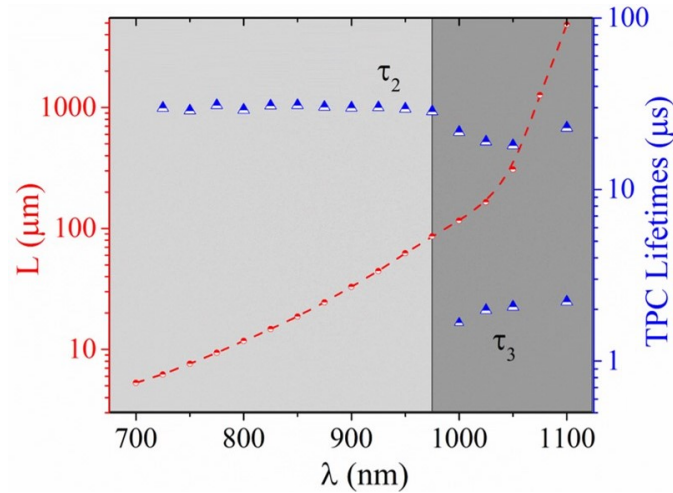
Figure 2.14: L as a function of λ inside the Si sub-cell derived from the scattering matrix formalism (left y-axis); Variation of TPC lifetimes (τ_2 and τ_3) with λ (right y-axis). Reproduced from A. Ghorai, P. Kumar, S. Mahesh, Y.-H. Lin, H. J. Snaith, K. Narayan, Applied Physics Letters 2022, 120, 173504. [1], with the permission of AIP Publishing
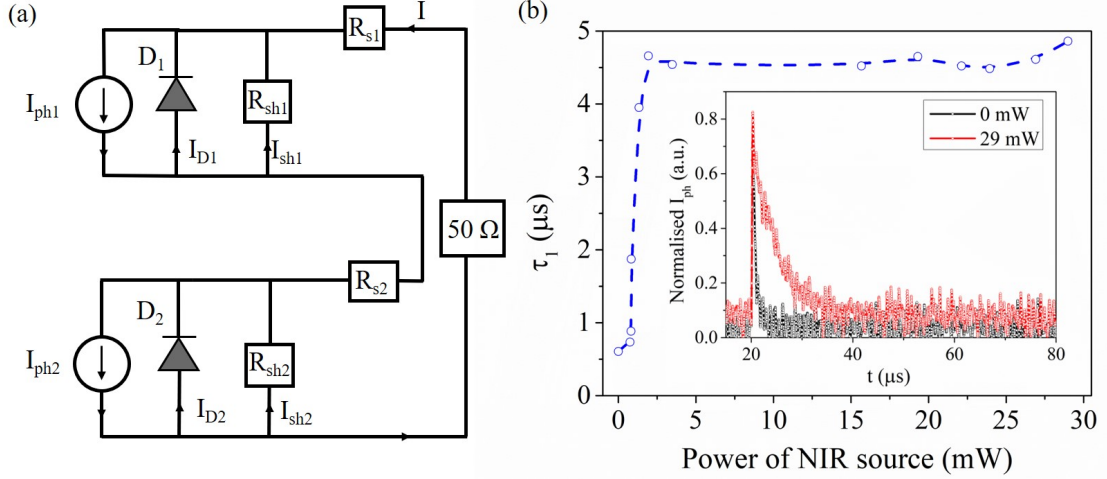
Figure 2.15: (a) Equivalent circuit for a tandem solar cell with series-connected sub-cells. The positive direction of current flow is indicated by an arrow in each branch, RShi represents the shunt resistance in cell i (b) Variation of τ_1 corresponding to 550 nm pulsed excitation with the intensity of background NIR illumination (700 nm – 1100 nm) exciting the Si sub-cell (inset shows the comparison of TPC profile under 29 mW background illumination). Reproduced from A. Ghorai, P. Kumar, S. Mahesh, Y.-H. Lin, H. J. Snaith, K. Narayan, Applied Physics Letters 2022, 120, 173504. [1], with the permission of AIP Publishing

2.7   Simultaneous excitation of both sub-cells

In case of the $I_{ph}(t)$ response to incident monochromatic light exciting the perovskite sub-cell, the finite shunt value of the Si sub-cell in the dark provides the pathway to the current. The ratio of the shunt resistances (R_{sh1}/R_{sh2}) is $\approx$ 1 : 13 as obtained from λ dependent TPC measurements. Thus the shunt resistance corresponding to the Si sub-cell is an order of magnitude higher than the perovskite sub-cell as also seen in previous literature [27]. The introduction of light bias during $I_{ph}(t)$ measurement opens up transport in both cells and increases the magnitude of $I_{ph}(t)$. The TPC lifetime τ_1 shows an abrupt transition from $\sim$ 500 ns to 4.5 μs as the background light bias excitation of the Si sub-cell is increased (Figure 2.15b). This observation can be described using an equivalent circuit model (Figure 2.15a) [4, 28]. The current generated in a sub-cell is given as $I_i = I_{Di} + I_{shi} - I_{phi}$. I_{phi} consists of photocurrent generated by external illumination in the ith sub-cell. I_{Di} is the current across the diode, Di given by $I_{Di} = I_{Di}^0[exp(-\frac{eV_i}{mk_BT}) - 1]$ with $m > 1$. Here V_i is the voltage across the ith sub-cell with k_BT/e being the thermal voltage.
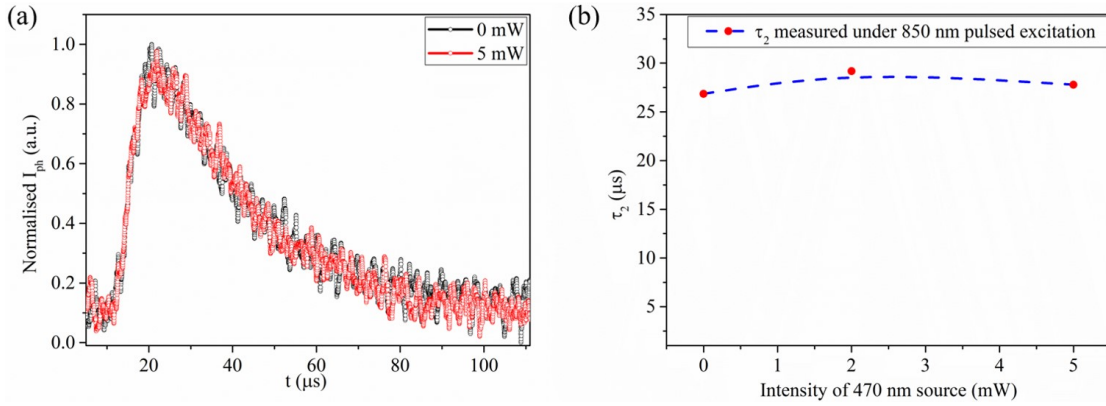
Figure 2.16: (a) TPC profile for Si subcell under 850 nm pulsed excitation under 470 nm excitation (b) TPC lifetimes for Si sub-cell for 850 nm pulsed excitation with different intensities of 470 nm background illumination. Reproduced from A. Ghorai, P. Kumar, S. Mahesh, Y.-H. Lin, H. J. Snaith, K. Narayan, Applied Physics Letters 2022, 120, 173504. [1], with the permission of AIP Publishing

I_{shi} is the current flowing through the shunt resistance of the ith sub-cell.

In the absence of background light bias, τ_1 is primarily decided by the carrier dynamics in the charge-generating regions, which is the perovskite in this case. The magnitude of the TPC is, however, dominantly governed by the shunt resistance of the other sub-cell (R_{sh2}). This is because D_2 is in reverse bias condition and I_{D2} is composed of current from only the minority carriers in the Si. Thus, the net transient photocurrent, in this case, is $I(t) \approx I_{sh2}(t)$. As the NIR background illumination (> 850 nm) is increased, I_{ph2} starts increasing, thus forward biasing D_2. At sufficiently high background illumination, V_2 is large enough to drive $D_2$ as the conducting channel for the photogenerated carriers from the perovskite sub-cell. The total transient photocurrent then is $I(t) \approx I_{D2}(t) + I_{sh2}(t)$ with I_{D2} having contributions from both $I_{ph1}(t)$ and I_{ph2}. Thus $I(t)$ profile embeds the carrier dynamics of the Si sub-cell in the $I_{D2}(t)$ response, along with the already existing $I_{sh2}(t)$. The recombination carrier lifetime in the Si is large and is dominantly mediated by the defect centres with $\frac{1}{\tau_{rec}} \approx \frac{1}{\tau_{rad}} + \frac{1}{\tau_{SRH}}$. This creates a much higher time constant for $I(t)$ which is basically the effective time constant derived from $I_{sh2}(t)$ and $I_{D2}(t)$ which explains the abrupt increase of τ_1 by order of magnitude as the background illumination is increased. In contrast, however, it is observed that τ_2 do not show any change when the Si sub-cell is

excited with a picosecond pulse ($\lambda > 800$ nm) while simultaneously light-biasing the perovskite sub-cell with 470 nm excitation (Figure 2.16). This is because the time constants associated with the perovskite sub-cell (a direct bandgap semiconductor and of much lower thickness) are orders of magnitude lower than the Si sub-cell. These results assert that the carrier dynamics of one sub-cell are decoupled with the other under single sub-cell excitation. However, the carrier dynamics of the sub-cells become coupled when both are simultaneously excited and are dominated by the sub-cell having slower charge-carrier dynamics.

2.8 Bias Dependence
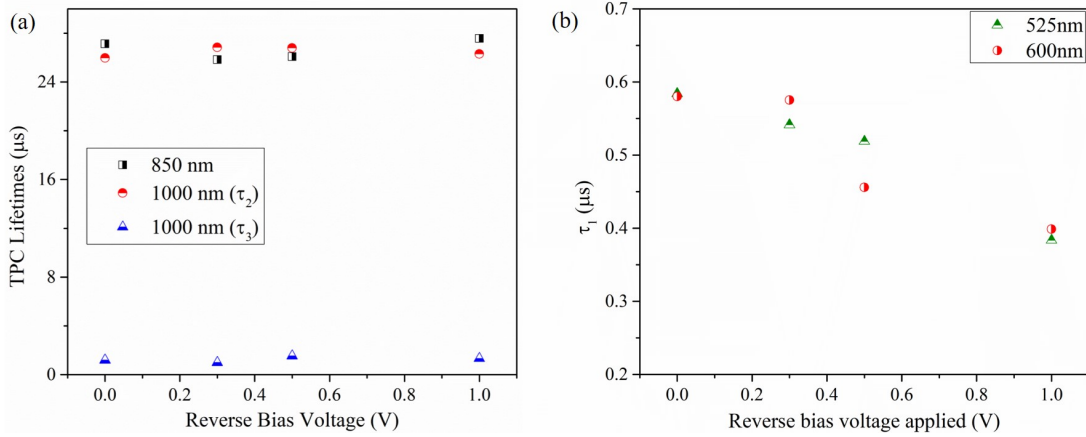
Figure 2.17: Variation of τ_2 and τ_3 with reverse bias voltage for 850 nm, 1000 nm and 1100 nm excitations (d) Variation of τ_1 with reverse bias voltage for 525 nm and 600 nm. Reproduced from A. Ghorai, P. Kumar, S. Mahesh, Y.-H. Lin, H. J. Snaith, K. Narayan, Applied Physics Letters 2022, 120, 173504. [1], with the permission of AIP Publishing

The subtle differences in the operation of sub-cells is also evident in studies carried out with an applied reverse bias voltage. For $\lambda > 700$ nm i.e., region falling under the Si sub-cell absorption spectrum (Figure 3(a)), there is no dependence of the TPC lifetime on the applied reverse bias voltage (Fig. 2.17(a)). This feature is indicative of the diffusive mode of transport in the Si sub-cell. The excess carrier density from TPC experiments is $\sim 10^{15}$ which suggests that the average recombination lifetime of minority carriers forms a component in the decay times along with diffusion limited transport transit time as explained by Eq. 2.1. However, for the region of $\lambda < 700$ nm i.e., the

region falling under the perovskite absorption spectrum (Figure 3(a)) there is a clear reduction in the TPC lifetime as the reverse bias voltage is increased (Fig. 2.17(b)). This observation is attributed to a considerable drift component in the perovskite sub-cell response enabling a faster extraction. Thus, unlike Si sub-cell internal electric fields in perovskite sub-cell plays an important role in charge-carrier transport. For the perovskite sub-cell, TPC lifetime has contributions from the carrier-transit time (having both drift and diffusion components) as well as from the average carrier-recombination lifetime. The difference in nature of charge-carrier transport in the two sub-cells results in the two orders of magnitude difference in the values of τ_1 and τ_2. This contrast in τ can possibly play a role of limiting the fill-factor of the tandem solar cell.

2.9 Conclusions
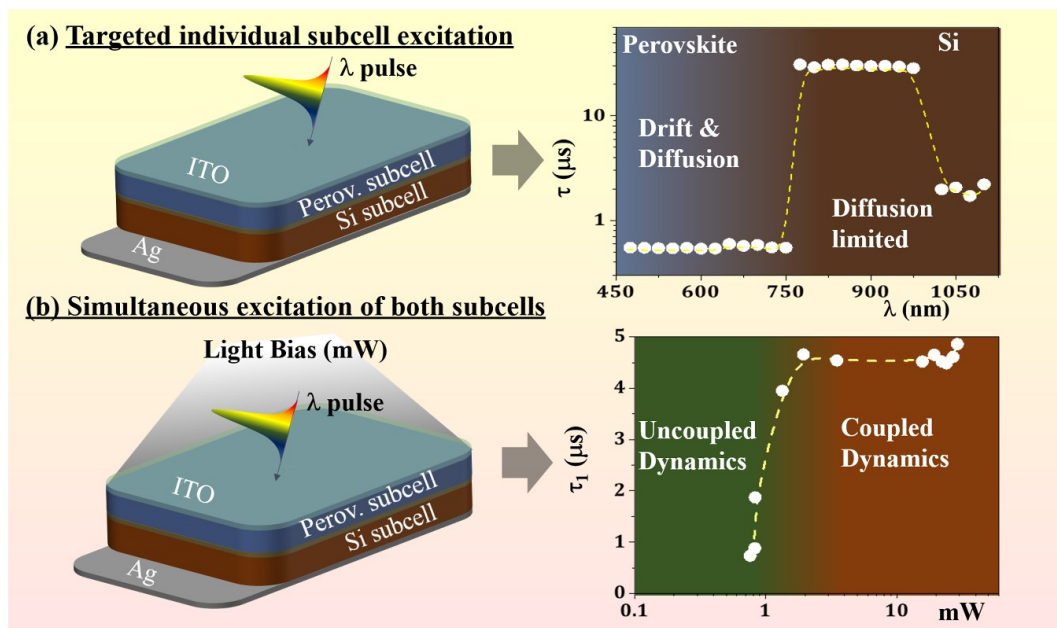
Figure 2.18: Schematic showing the carrier transport mechanisms in the perovskite/Si tandem solar cell under (a) targeted individual sub-cell excitation (b) when both the sub-cells are simultaneously excited. Reproduced from A. Ghorai, P. Kumar, S. Mahesh, Y.-H. Lin, H. J. Snaith, K. Narayan, Applied Physics Letters 2022, 120, 173504. [1], with the permission of AIP Publishing.

The TPC measurements directly help us assess the timescales of photogenerated charge carriers extracted to the electrodes. Figure 2.18 summarizes the governing charge carrier extraction dynamics when a

targeted sub-cell is excited and when both the sub-cells are operational. The time constants associated with the perovskite sub-cell (a direct bandgap semiconductor and of much lower thickness) are orders of magnitude faster than the Si sub-cell. The thickness of the active layers in multijunction solar cells should be optimized to minimize the recombination losses and achieve the highest EQE, fill factor and Voc. Optimization of series resistances, shunt resistances and surface recombination velocities need to be achieved using TPC spectroscopy for sub-cells for better multi-junction devices with enhanced performance parameters.

In conclusion, we observe a spectral dependence of transient photocurrent lifetime which can be classified into two distinct timescales. The first timescale, $\tau_1 \sim 500$ ns represents the absorption in the top perovskite sub-cell (λ - 300 nm to 750 nm). The other timescale regime of $\tau_2 \sim 25$ μs and $\tau_3 \sim 2$ μs corresponds to absorption in the rear Si sub-cell ($\lambda > 700$ nm). We infer that the transport processes in perovskite sub-cell are influenced by high field strength. Hence, the carriers are extracted via both drift and diffusion process in the perovskite sub-cell whereas Si sub-cell follows a diffusion limited carrier extraction process. However, this can lead to ion transport in the perovskite sub-cell which will have an effect on the degradation process which needs to be examined further. In the absence of background illumination, sub-cell processes are uncorrelated, and the current magnitude is dependent on the shunt resistance of the other sub-cell in the dark. A crossover of the dynamics of the perovskite sub-cell to a coupled-regime with the Si sub-cell beyond a threshold dc-light illumination is observed. Fine-tuning of the two active layer thicknesses can further optimize absorption, carrier transit times and lifetimes and lead to higher efficiencies.

References

[1] A. Ghorai, P. Kumar, S. Mahesh, Y.-H. Lin, H. J. Snaith, and K. Narayan, "Insights into the charge carrier dynamics in perovskite/si tandem solar cells using transient photocurrent spectroscopy," *Applied Physics Letters*, vol. 120, no. 17, p. 173504, 2022.

[2] F. Fu, J. Li, T. C.-J. Yang, H. Liang, A. Faes, Q. Jeangros, C. Ballif, and Y. Hou, "Monolithic perovskite-silicon tandem solar cells: from the lab to fab?," *Advanced Materials*, p. 2106540, 2022.

[3] M. T. Horantner, T. Leijtens, M. E. Ziffer, G. E. Eperon, M. G. Christoforo, M. D. McGehee, and H. J. Snaith, "The potential of multijunction perovskite solar cells," *ACS Energy Letters*, vol. 2, no. 10, pp. 2506–2513, 2017.

[4] M. Boccard and C. Ballif, "Influence of the subcell properties on the fill factor of two-terminal perovskite–silicon tandem solar cells," *ACS Energy Letters*, vol. 5, no. 4, pp. 1077–1082, 2020.

[5] H. Shen, D. Walter, Y. Wu, K. C. Fong, D. A. Jacobs, T. Duong, J. Peng, K. Weber, T. P. White, and K. R. Catchpole, "Monolithic perovskite/si tandem solar cells: pathways to over 30% efficiency," *Advanced Energy Materials*, vol. 10, no. 13, p. 1902840, 2020.

[6] T. Leijtens, K. A. Bush, R. Prasanna, and M. D. McGehee, "Opportunities and challenges for tandem solar cells using metal halide perovskite semiconductors," *Nature Energy*, vol. 3, no. 10, pp. 828–838, 2018.

[7] J. Werner, B. Niesen, and C. Ballif, "Perovskite/silicon tandem solar cells: Marriage of convenience or true love story?–an overview," *Advanced Materials Interfaces*, vol. 5, no. 1, p. 1700731, 2018.

[8] B. Chen, N. Ren, Y. Li, L. Yan, S. Mazumdar, Y. Zhao, and X. Zhang, "Insights into the development of monolithic perovskite/silicon tandem solar cells," *Advanced Energy Materials*, vol. 12, no. 4, p. 2003628, 2022.

[9] Y.-H. Lin, N. Sakai, P. Da, J. Wu, H. C. Sansom, A. J. Ramadan, S. Mahesh, J. Liu, R. D. Oliver, J. Lim, *et al.*, "A piperidinium salt stabilizes efficient metal-halide perovskite solar cells," *Science*, vol. 369, no. 6499, pp. 96–102, 2020.

[10] S.-H. Turren-Cruz, A. Hagfeldt, and M. Saliba, "Methylammonium-free, high-performance, and stable perovskite solar cells on a planar architecture," *Science*, vol. 362, no. 6413, pp. 449–453, 2018.

[11] D. A. Neamen, *Semiconductor physics and devices: basic principles.* McGraw-hill, 2003.

[12] W. Kern, "The evolution of silicon wafer cleaning technology," *Journal of the Electrochemical Society*, vol. 137, no. 6, p. 1887, 1990.

[13] L. Mazzarella, A. B. Morales-Vilches, M. Hendrichs, S. Kirner, L. Korte, R. Schlatmann, and B. Stannowski, "Nanocrystalline n-type silicon oxide front contacts for silicon heterojunction solar cells: photocurrent enhancement on planar and textured substrates," *IEEE Journal of Photovoltaics*, vol. 8, no. 1, pp. 70–78, 2017.

[14] L. Mazzarella, Y.-H. Lin, S. Kirner, A. B. Morales-Vilches, L. Korte, S. Albrecht, E. Crossland, B. Stannowski, C. Case, H. J. Snaith, *et al.*, "Infrared light management using a nanocrystalline silicon oxide interlayer in monolithic perovskite/silicon heterojunction tandem solar cells with efficiency above 25%," *Advanced Energy Materials*, vol. 9, no. 14, p. 1803241, 2019.

[15] S.-W. Lee, S. Bae, J.-K. Hwang, W. Lee, S. Lee, J. Y. Hyun, K. Cho, S. Kim, F. D. Heinz, S. Bin Choi, *et al.*, "Perovskites fabricated on textured silicon surfaces for tandem solar cells," *Communications Chemistry*, vol. 3, no. 1, pp. 1–11, 2020.

[16] Z. Song, S. C. Watthage, A. B. Phillips, B. L. Tompkins, R. J. Ellingson, and M. J. Heben, "Impact of processing temperature and composition on the formation of methylammonium lead iodide perovskites," *Chemistry of Materials*, vol. 27, no. 13, pp. 4612–4619, 2015.

[17] M. C. Schubert, L. E. Mundt, D. Walter, A. Fell, and S. W. Glunz, "Spatially resolved performance analysis for perovskite solar cells," *Advanced Energy Materials*, vol. 10, no. 26, p. 1904001, 2020.

[18] A. Singh, P. K. Nayak, S. Banerjee, Z. Wang, J. T.-W. Wang, H. J. Snaith, and K. Narayan, "Insights into the microscopic and degradation processes in hybrid perovskite solar cells using noise spectroscopy," *Solar RRL*, vol. 2, no. 1, p. 1700173, 2018.

[19] M. A. de Araújo, R. Silva, E. de Lima, D. P. Pereira, and P. C. de Oliveira, "Measurement of gaussian laser beam radius using the knife-edge technique: improvement on data analysis," *Applied optics*, vol. 48, no. 2, pp. 393–396, 2009.

[20] S. Valouch, M. Nintz, S. W. Kettlitz, N. S. Christ, and U. Lemmer, "Thickness-dependent transient photocurrent response of organic photodiodes," *IEEE Photonics Technology Letters*, vol. 24, no. 7, pp. 596–598, 2012.

[21] N. Christ, S. W. Kettlitz, J. Mescher, and U. Lemmer, "Extracting the charge carrier mobility from the nanosecond photocurrent response of organic solar cells and photodiodes," *Applied Physics Letters*, vol. 104, no. 5, p. 25_1, 2014.

[22] M. Pazoki, A. Hagfeldt, and T. Edvinsson, *Characterization Techniques for Perovskite Solar Cell Materials.* Elsevier, 2019.

[23] J. Shi, H. Zhang, X. Xu, D. Li, Y. Luo, and Q. Meng, "Interplays between charge and electric field in perovskite solar cells: charge transport, recombination and hysteresis," *arXiv preprint arXiv:1604.02819*, 2016.

[24] R. C. Rumpf, "Improved formulation of scattering matrices for semi-analytical methods that is consistent with convention," *Progress In Electromagnetics Research B*, vol. 35, pp. 241–261, 2011.

[25] L. A. Pettersson, L. S. Roman, and O. Inganäs, "Modeling photocurrent action spectra of photovoltaic devices based on organic thin films," *Journal of Applied Physics*, vol. 86, no. 1, pp. 487–496, 1999.

[26] P. Peumans, A. Yakimov, and S. R. Forrest, "Small molecular weight organic thin-film photodetectors and solar cells," *Journal of Applied Physics*, vol. 93, no. 7, pp. 3693–3723, 2003.

[27] M. Jošt, G. Matič, E. Köhnen, B. Li, B. Glažar, M. Jankovec, S. Albrecht, and M. Topič, "Subcell operation and long-term stability analysis of perovskite-based tandem solar cells using a bichromatic light emitting diode light source," *Solar RRL*, vol. 5, no. 8, p. 2100311, 2021.

[28] D. Lan and M. A. Green, "Equivalent circuit analysis of radiative coupling in monolithic tandem solar cells," *Applied Physics Letters*, vol. 106, no. 26, p. 263902, 2015.

<div style="text-align: right;">*3*</div>

Probing charge carrier and exciton dynamics in TADF-OLEDs using transient electroluminescence measurements

3.1 Introduction

The performance of the OLED can be improved with suitable techniques to minimize non-radiative energy losses and enhance the emissive layer's radiative efficiency. Traditionally, the triplet excitons are an undesirable energy loss channel in fluorescent OLEDs because they are spin forbidden for light emission [1–5]. Phosphorescent emitters overcame this limit through intersystem crossing (ISC) by incorporating transition metals such as Iridium and Platinum. The heavy metal facilitates spin-orbit coupling by enhancing the ISC to harvest triplet and singlet excitons [6, 7]. However, these phosphors suffered from stability, especially for blue and white emissions. The scarcity and expense of these heavy transition metals also restricted them from commercialization.

The triplet loss pathways were further minimized by harvesting the 'dark' triplet excitons via alternative processes to convert them into emissive singlet states. Triplet-triplet annihilation (TTA) is one of the bimolecular processes by which two triplets fuse to give rise to an emissive singlet state, resulting in delayed fluorescence. The theoretical limit of IQE of LEDs via this process of triplet harvesting is 62.5%, leading to enhanced OLED efficiencies [8]. Other than TTA-enhanced OLEDs, Adachi and co-workers exploited thermally activated delayed fluorescence (TADF) to convert triplets to singlets using all organic

materials [9]. These systems can achieve 100% IQE by upconverting the triplet states into emissive singlet states via reverse intersystem crossing (RISC). The up-conversion process is achieved via thermal energy when a small energy gap ΔE_{ST} between the first excited singlet and triplet states is present. The small energy gap is achieved by minimizing the overlap between the lowest unoccupied molecular orbital (LUMO) and the highest occupied molecular orbital (HOMO) [10].

The excited state dynamics of TADF mainly had been studied under optical excitation, generating 100% singlets. The emission in TADF systems has three components: prompt fluorescence, delayed fluorescence and phosphorescence. In some molecules, all three components are known to be present [11]. However, some fraction of the delayed radiative singlet emission is due to triplet-triplet annihilation (TTA) in the background of RISC arising from the 75% triplet fraction under electrical excitation. Triplet depopulation via TTA may limit the external quantum efficiency (EQE) of LEDs owing to it being a bimolecular process. The bimolecular annihilation processes will play a much dominant role under electrical excitation due to the higher proportion of triplets in the molecules. In this context, investigating the triplet dynamics in OLEDs using pulsed electrical excitation is quite informative.

The charge-carrier dynamics along with exciton dynamics in a donor-acceptor-based intramolecular TADF system 2,3,4,6-Tetra(9H-carbazol-9-yl)-5-fluorobenzonitrile (4CzFCN, depicted in Figure 3.1a) is probed using transient electroluminescence (TrEL) spectroscopy measurements. The TrEL measurements explore the carrier dynamics and recombination timescales in these 4CzFCN-based OLEDs. The pathways for losses in external quantum efficiency (EQE) under electrical excitation via various bimolecular processes can be further understood using TrEL measurements. This experiment uses an electrical pulse with a long FWHM to approximate the steady-state injection conditions. The TrEL profiles from the OLEDs exhibit a steady-state region between a characteristic rising edge and the trailing edge of the pulse. The rising edge has contributions from the charge carrier and
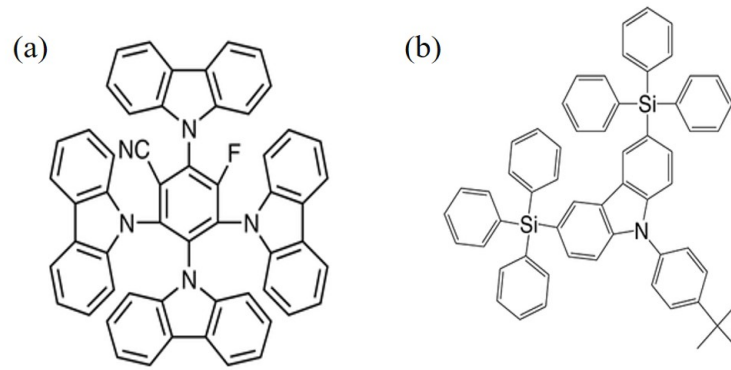
Figure 3.1: (a) Molecular structure of 4CzFCN dopant, (b) Molecular structure of SiCz host.

the exciton dynamics, whereas the trailing edge has contributions from only the exciton dynamics. The joule heating and electric field effects on the excitons are negligible during the trailing edge of the pulse since the fall time of the exciting electric pulse will be orders of magnitude lower than that of the EL pulse. The RC constant of the device is dependent on the transit timescales of the electrons and holes.

3.2 Photo-physics of 4CzFCN molecule in CzSi host

In OLED devices, a host is generally used for dispersing to reduce the aggregation effects of the TADF molecule and obtain smooth films via solution processing. The host matrix is characterized by a triplet level higher than the TADF dopant and facilitates carrier transport upon injection. The host matrix in this work is 9-(4-tert-Butylphenyl)-3,6-bis(triphenylsilyl)-9H-carbazole (SiCz). The molecular structures of both SiCz and 4CzFCN are shown in Figure 3.1.

The steady-state and time-gated PL spectra of the 4CzFCN molecule are shown in Figure 3.2a. The gated PL spectra verify that the extended lifetime component is due to the delayed fluorescence. A decrease in temperature causes a decrease in τ_{DF} owing to a reduction in the reverse intersystem crossing of the triplets [12]. Consequently, the PL intensity decreases with temperature (Figure 3.2b). The decrease in overall emission suggests that the ISC-generated triplets are nonemissive.
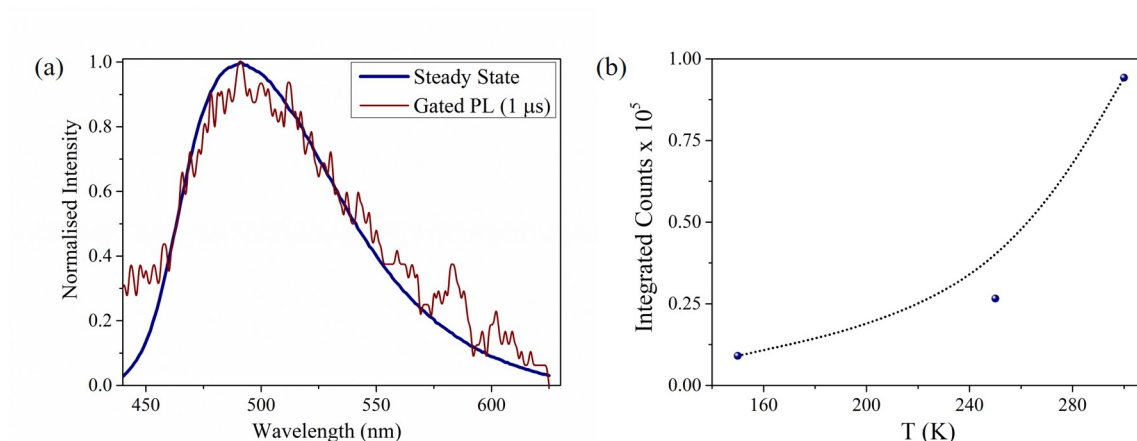
Figure 3.2: (a) Steady state and gated emission spectra of 15wt% 4CzFCN molecule doped in SiCz (b) Temperature dependent PL intensity in 4CzFCN molecule

3.3 Fabrication of TADF LEDs
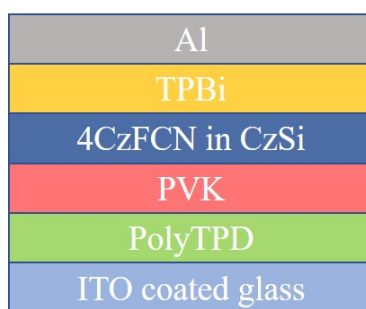
Figure 3.3: Device structure of the fabricated OLED

The OLEDs were fabricated over indium tin oxide (ITO) precoated glass substrates with a size 1.44 cm^2. In the device architecture, Poly(N,N'-bis-4-butylphenyl-N,N'-bisphenyl)benzidine (Poly-TPD) has been used as the hole transporting layer (HTL), Poly(N-vinylcarbazole) (PVK) as the electron blocking layer (EBL) and 2,2',2"-(1,3,5-Benzinetriyl)-tris(1-phenyl-1-H-benzimidazole) (TPBi) as the electron transporting layer (ETL).

Precleaned substrates were spin-coated with 20 mg/mL poly-TPD (Lumtec) solution at 2500 rpm and annealed at 120°C for 60 minutes. The PVK (Lumtec) layer was spin-coated from a 13 mg/mL solution in chlorobenzene at 2000 rpm and annealed at 120°C for 15 minutes. The doping concentration for 4CzFCN (Lumtec) with SiCz (Lumtec)
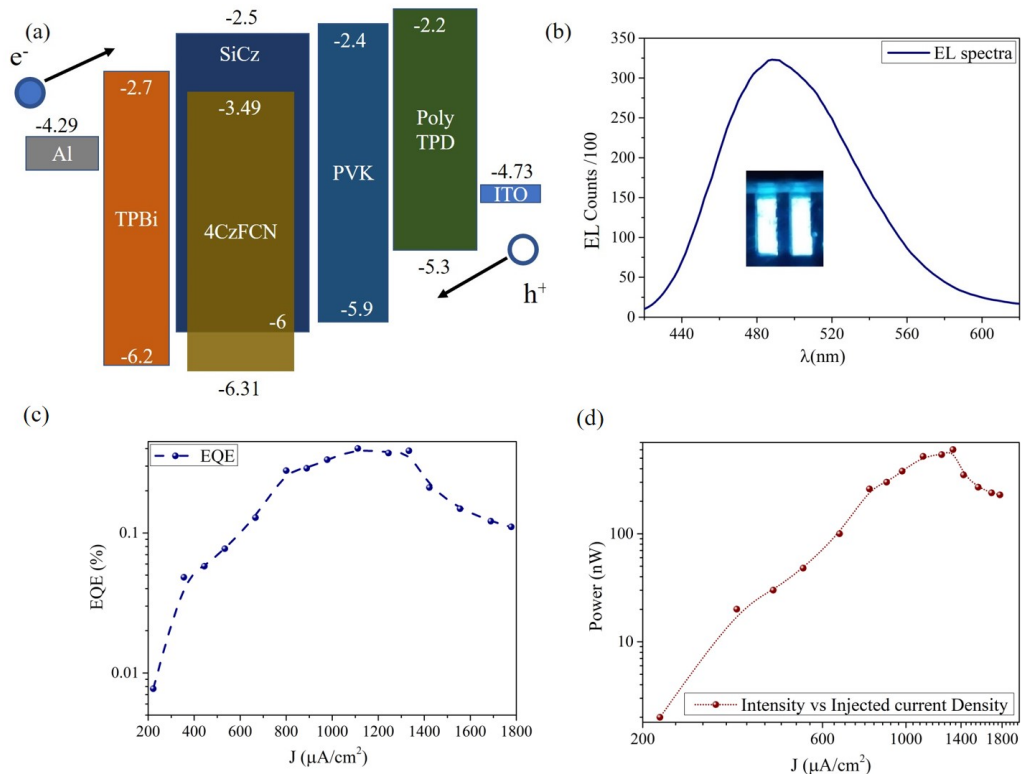
Figure 3.4: (a) Energy level diagram of the layers used in the device, (b) Electroluminescent Spectra of the TADF OLED, (c) EQE curve of OLED as a function of current density, (d) EL power intensity as a function of current density

was 13.67%, and the active layer's final concentration was 25 mg/mL in toluene. The active layer was spin-coated at 2000 rpm and baked at 120°C for 15 minutes. The spin coating of all the layers was performed inside an N$_2$ glove box. TPBi (20nm), and Al (100 nm) were vacuum-deposited at a base pressure of 10^{-6} mbar The final fabricated device structure was ITO/Poly-TPD (30 nm)/PVK (40 nm)/4CzFCN:SiCz (50 nm)/TPbi (20 nm)/Ag(100nm). The energy level diagram of the device is shown in Figure 3.4a. All the thicknesses of the individual layers were measured using JPK Nanowizard Atomic Force Microscope. The device area of the OLED was 4.5 mm^2. The EL spectra were recorded by applying a dc bias across the electrodes, as shown in Figure 3.4b.

3.4 Transient Electroluminescence Measurements

The TrEL profiles are conventionally captured using a photodiode and visualized using an oscilloscope [13, 14]. The temperature-dependent

TrEL profiles in this work were recorded using a time-correlated single photon counting (TCSPC) technique. The details of the experiment are presented below (Figure 3.5). The TrEL profiles were recorded as a function of bias intensities at different temperatures.

Transient EL measurements were performed using a custom-designed Printed circuit board (PCB). A Tektronix AFG Function generator was coupled with a Keithley 2400 source-meter using P90nf03 MOSFET on a PCB. The source-meter was used to control the bias for the LED, and the function generator was used to set the pulsing parameters of the source-meter output. The pulse frequency was set at 100 Hz with a duty cycle of 50%. The light emitted from the TADF OLED was captured using a SensL S/N 00558 SPMMini detector and recorded on a Tektronix MDO34 digital signal oscilloscope. The time-dependent profile of the Electroluminescence (EL) intensity for the TADF OLED during the ON and OFF cycle for an applied voltage pulse of 18 V is shown in Figure 3.6. The temperature-dependent measurements were performed using a Linkam LTS-420 temperature controller stage. The emission was captured from a narrow pinhole on the stage using a Picoquant PMA-C-192-M photomultiplier assembly. Time tagging of the data was done using a Picoquant TimeHarp 260 data acquisition card based on TCSPC to derive the TrEL profile. The time-resolved decay profiles were obtained for the wavelength range of 420 nm to 630 nm using a Zolix Omni λ-300 monochromator. The time-gated EL emission was derived from these decay profiles using MATLAB.
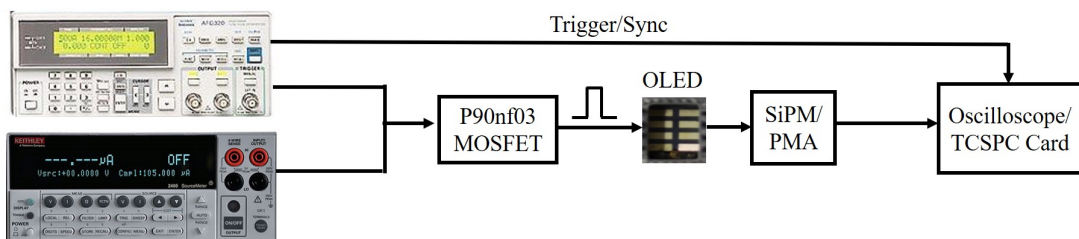
Figure 3.5: Scheme of transient electroluminescence measurements
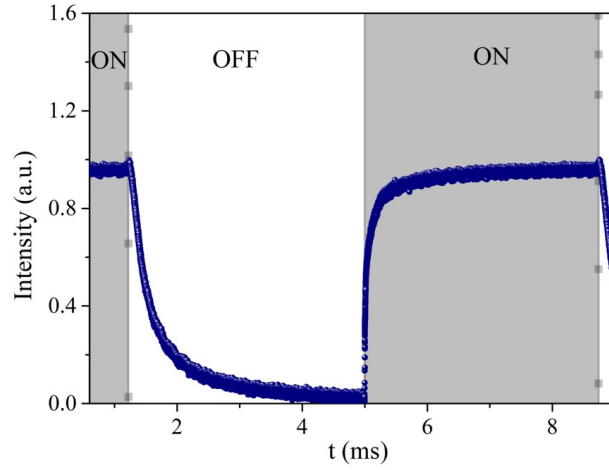
Figure 3.6: Electroluminescence profile from the OLED as recorded by the oscilloscope during the ON and OFF cycle.
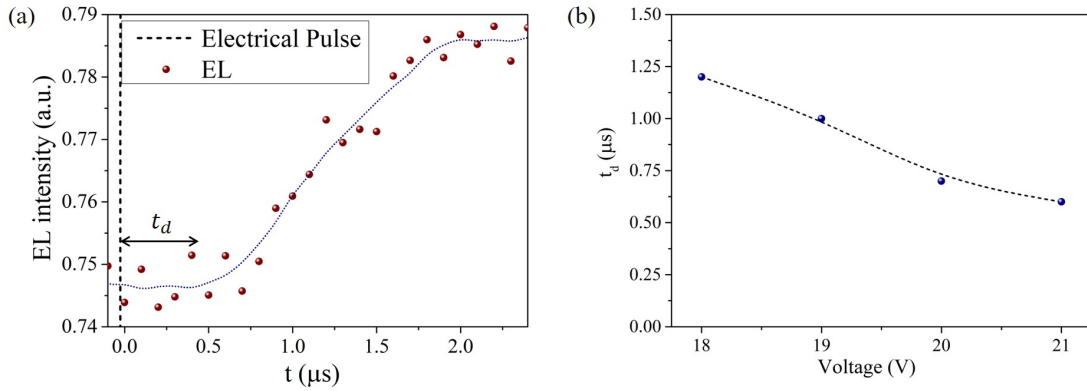
Figure 3.7: (a) Delay time between the exciting pulse and the onset of EL (t_d), (b) Variation with t_d with applied voltage.

3.5 Rising edge of the TrEL pulse

The rising edge of the TrEL profile is initially characterized by an onset time (t_d) for electroluminescence and a rise time (t_r). The rising edge of the TrEL response $I(t)$ is governed by [15]

$$I(t) = \begin{cases} 0 & t < t_d \\ I_\infty(1 - exp(t - t_d)) & t \geq t_d \end{cases} \tag{3.1}$$

The t_d, is associated with the delay period before the radiative recombination of excitons (Figure 3.7a). The magnitude of t_d, is governed

by the transport of carriers and space charge generated in the interfaces around the active layer, as seen from the dependence of t_d on the applied bias (Figure 3.7b). The rise time t_r, then inherently includes contributions from both the carrier and exciton dynamics. The rising edge of the TrEL profile consists of a fast component and a slow component, as seen in Figure 3.8. The fast component is associated with the initial recombination of electrons and holes at the active layer interface. The slow component of the EL emission results from carriers followed by multiple trapping, de-trapping, and recombination [15]. The electrically injected carriers in a TADF molecule form excitons followed by Langevin recombination. The spin statistics favour the creation of singlet and triplet states in the ratio 1:3. After an equilibration period, the singlets, triplets, and charge carriers reach a steady EL emission rate.
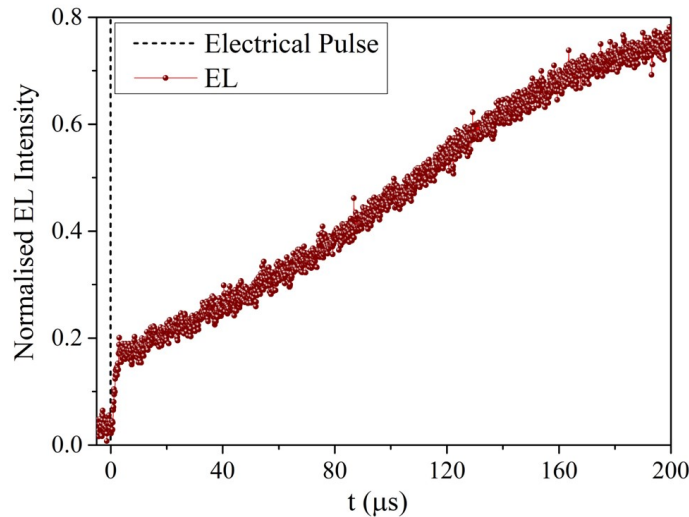
Figure 3.8: Rising edge of the TrEL profile showing the fast and slow components in the rise time. The bias voltage has an amplitude of 20V.

3.6 Falling Edge of the TrEL Pulse

Upon switching the bias off, the EL magnitude momentarily increases in magnitude. This EL overshoot feature is shown in Figure 3.9. When the bias is switched OFF, the injected carriers, under the presence of an internal field, drift back to their respective electrodes. In the process, the back-propagating charges form excitons with the trapped carriers,

carriers, and their lifetimes would be dominated hereon by the various excitonic processes [15]. Both monomolecular and bimolecular exciton dynamics dominate the decay processes beyond the EL overshoot period. The monomolecular processes include the decay of S_1 (k_S), ISC for S_1 to T_1 (k_{ISC}) and RISC from T_1 to S_1 (k_{RISC}). The probability of bimolecular annihilation processes in triplets is much higher compared to singlets owing to the higher lifetime in triplets. The bimolecular processes include TTA, singlet-triplet annihilation (STA), singlet-singlet annihilation (SSA), and triplet-polaron annihilation (TPA), with corresponding rates being k_{TT}, k_{SS}, k_{ST} and k_{TP}, respectively.
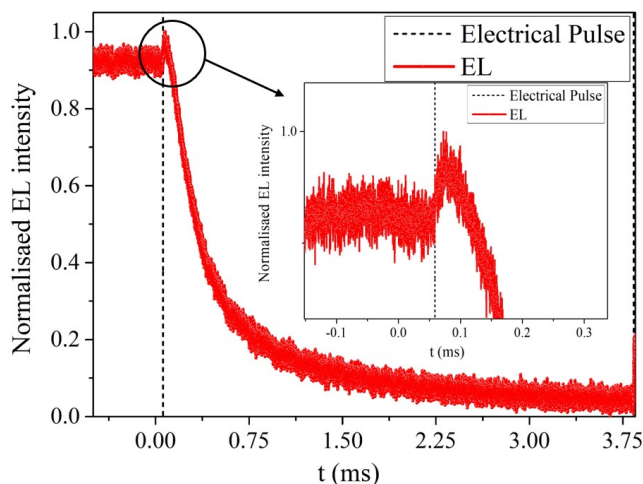
Figure 3.9: Falling edge of the TrEL profile (Inset shows the EL overshoot feature). The bias voltage has an amplitude of 20V.

3.7 Bimolecular Excitonic Processes

Under TTA, the interaction of two triplets leads to the formation of an intermediate state X, which transforms into one singlet, three triplets, or five quintet state according to spin statistics [16]. The contribution of quintet states is generally neglected because they are higher in energy than the two initial triplet states [2]. Thus, the possible pathways for TTA can be written as follows:

$$T_1 + T_1 \xrightarrow{k_{TT}} X \xrightarrow{k_{TT}} \begin{cases} T_1 + S_0 \\ S_1 + S_0 \end{cases} \tag{3.2}$$

81
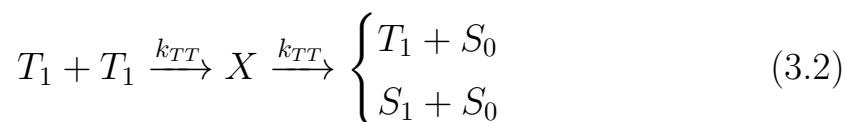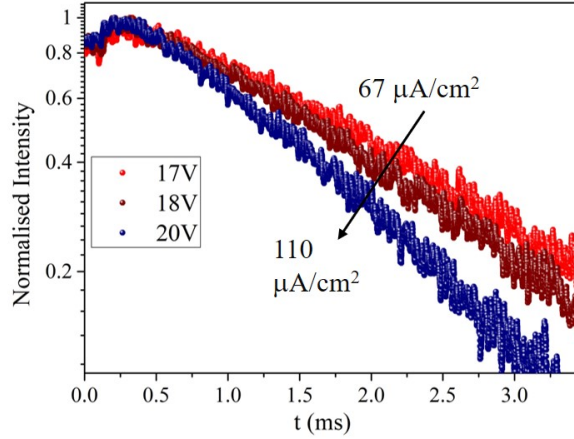
Figure 3.10: TrEL decay profiles for different current densities at 300 K.

Dipole-dipole interactions primarily govern SSA, and the spin remains conserved while no triplets are formed [17]. Usually, SSA is more dominant in crystalline systems than in amorphous materials [16] due to higher diffusion constants in crystalline materials. SSA will also be a dominant component when a material is excited optically (as opposed to electrical injection) due to spin statistics [14]. Further, since the lifetime of singlet states is orders of magnitude lesser than triplets, SSA will dominate only initially from a few $\sim$ns to $\sim\mu$s, and their contribution to the TrEL trailing edge can be neglected for TADF molecules. During STA, the triplet exciton undergoes a spin-allowed transition from T_1 to T_n with the relaxation of S_1 to S_0. STA is generally dominant when the triplet densities are high. Lastly, the annihilation of triplet states with a polaron spin state (free or trapped charge carriers) referred to as TPA is also probable.

$$S_1 + T_1 \xrightarrow{k_{ST}} S_0 + T_n \xrightarrow{k_{ST}} S_0 + T_1 \tag{3.3}$$

$$T_1 + n \xrightarrow{k_{TP}} S_0 + n^* \tag{3.4}$$
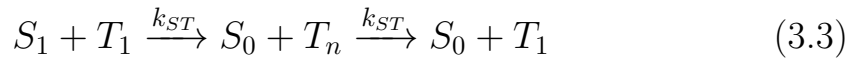
3.8 Exciton Density dependent Dynamics

The TrEL decay profiles from the OLEDs were excited with pulses of different current magnitudes and are shown in Figure 3.10. The pulse decay profiles are mono-exponential, with the dynamics becoming faster with an increase in injected current density. The dependence
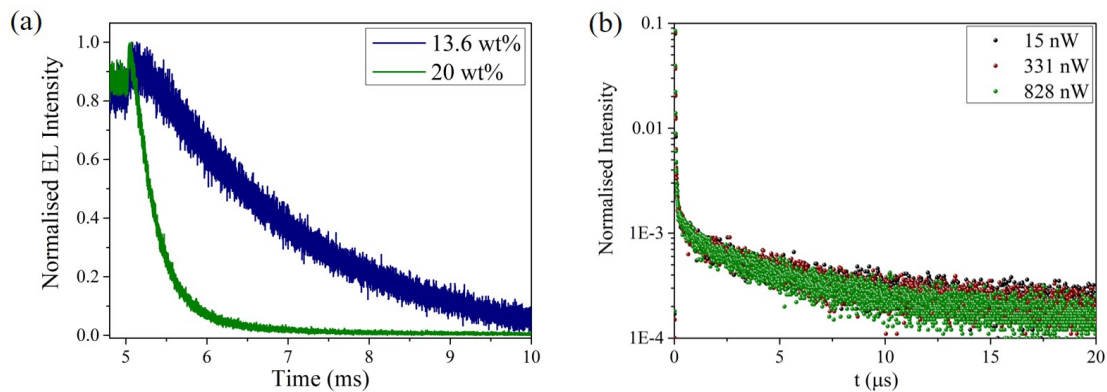
Figure 3.11: (a) TrEL profiles as a function of concentration of TADF dopant, (b) TrPL profiles as a function of excitation intensity.

of the TrEL profiles on the bias magnitudes highlights the presence of a competing process for harvesting the triplets back to singlets via RISC. Unlike RISC, TTA depends on population density. Hence its occurrence scales with triplet density.

Concentration-dependent TrEL measurements also highlight the presence of TTA, resulting in faster decay with the increase in the concentration of the TADF dopant (Figure 3.11a). These results reveal the contribution of the bimolecular TTA process to the magnitude of delayed fluorescence. Similar measurements have also been performed where the photoluminescence emission decay profiles have been recorded as a function of optical excitation intensity (Figure 3.11b). However, the time constants corresponding to the PL decays remained almost similar, ascertaining a negligible contribution of TTA under optical excitation. This highlights the difference in triplet dynamics under electrical excitation compared to optical excitation.

3.9 Time Gated Electroluminescence Spectra

The time evolution of the EL has been performed to verify whether the delayed emission originates from the singlet states. Figure 3.12 highlights the time evolution of EL spectra at room temperature. The maxima of the time-gated spectra were found to be overlapping with the spectra derived from the time when the pulse was ON. This sub-
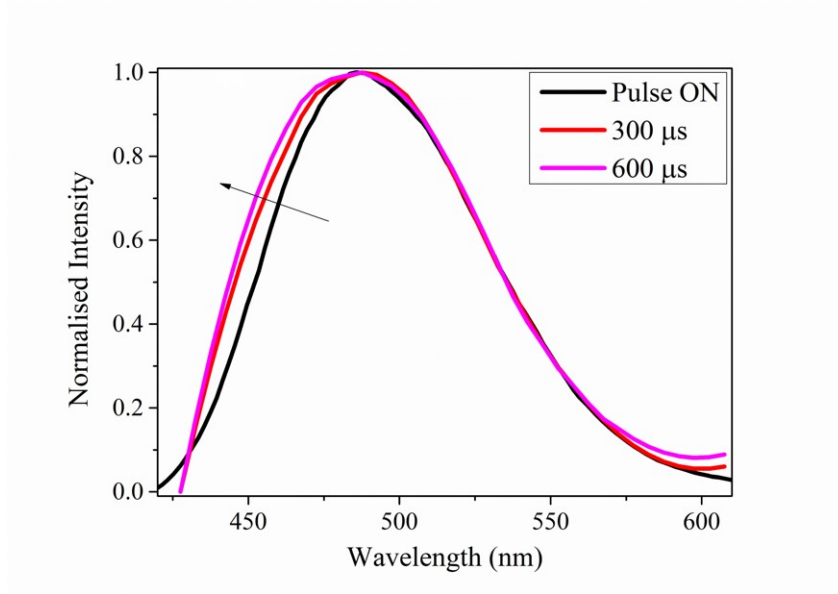
Figure 3.12: Time evolution of the EL spectra after the pulse is switched OFF

stantiates the delayed emission originating from the S_1 state. Further, the inhomogeneous broadening of the delayed emission spectrum indicates a higher lifetime for the higher vibrational states in the S_1 state. Temperature-dependent TrEL at different biases are useful to verify the contribution of RISC and bimolecular emissions in the EL spectrum.

3.10 Simulation of TrEL profiles
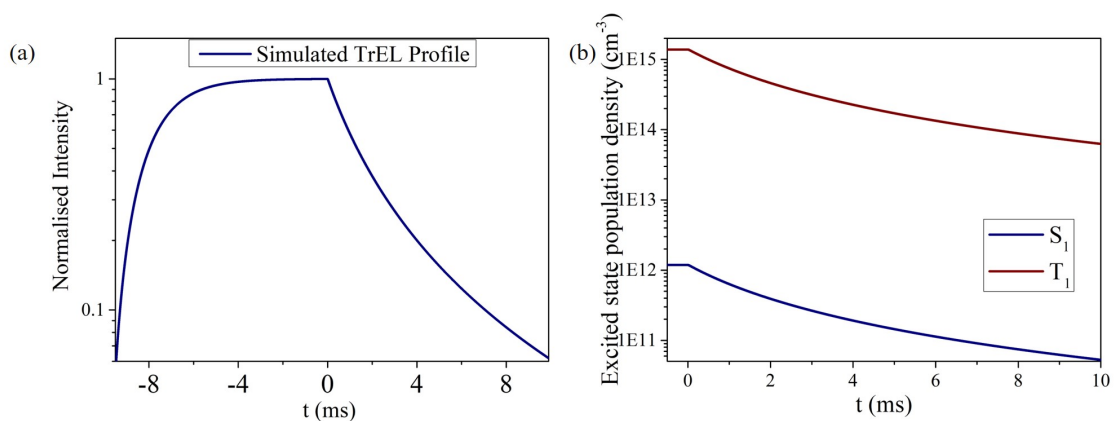
Figure 3.13: (a) A simulated TrEL profile, (b) Evolution of excited state population densities of singlets and triplets after the pulse is switched OFF.

The singlet exciton decay with lifetimes ($\sim$ ns) dominates the initial radiative processes upon switching OFF of the excitation pulse. It is to

be noted that the TrEL time constants are in the range of milliseconds, suggesting the processes involving triplets would dominate the longer regimes of the TrEL profiles. Thus, the effects of SPA and SSA can be disregarded in their contributions to the TrEL profiles. The product of triplet and singlet population densities determines the magnitude of STA. However, the TrEL decay profiles depend on the injected current densities, thus proving that the effect of STA is not dominant [16, 18]. Due to the large population and lifetime of triplets, TPA and TTA will have more contributions at the trailing edge of the TrEL profiles. The charge imbalances in the active layer along with the transit time of polarons in the device, contribute to the process of TPA [19]. The extent of TPA and TTA will depend on the population of the contributing species. The kinetics of the polarons, singlets, and triplets in the OLED is given by the following rate equations [18]

$$\frac{dn}{dt} = \frac{J}{ed} - \gamma n^2 \tag{3.5}$$

$$\frac{dS_1}{dt} = -k_S S_1 - k_{isc} S_1 + k_{risc} T_1 + \frac{1}{4} k_{TT} T_1^2 - k_{ST} T_1 S_1 + \frac{1}{4} \gamma n^2 \tag{3.6}$$

$$\frac{dT_1}{dt} = -k_T T_1 + k_{ISC} S_1 - k_{RISC} T_1 + \frac{5}{4} k_{TT} T_1^2 - 2k_{TP} T_1 n + \frac{3}{4} \gamma n^2 \tag{3.7}$$

where γ is the Langevin recombination constant, n is the polaron density, S_1 is the singlet density and T_1 the triplet density.

Figure 3.13a shows a simulated TrEL profile for a current density of 85 μA/cm^2 using equations 3.5, 3.6, and 3.7. The various rate constants used in the simulations used were $\gamma = 1.45 \times 10^{-15}$ s^{-1}; $k_S = 8.14x10^{-7}$ s^{-1}; $k_T = 113.53$ s^{-1}; $k_{RISC} = 6.14x10^7$ s^{-1}; $k_{ISC} = 1.03 \times 10^5$ s^{-1}; $k_{TP} = 10^{-14}$ cm^3 s^{-1}; $k_{TT} = 10^{-12}$ cm^3 s^{-1}; $k_{ST} = 10^{-13}$ cm^3 s^{-1}; $k_{SP} = 10^{-14}$ cm^3 s^{-1}. The values of k_S, k_T, k_{ISC} and k_{RISC} were obtained from the values of the prompt (ϕ_{prompt}) and delayed fluorescence component ($\phi_{delayed}$) and k_D in Reference [12]
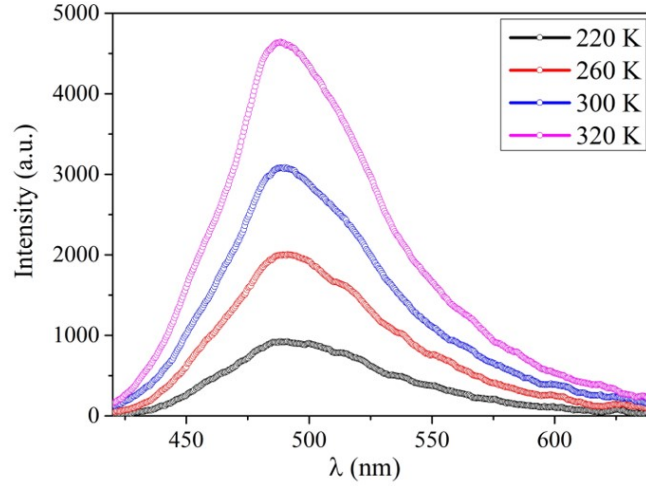
Figure 3.14: Temperature dependence of steady-state EL.

using the following expressions:

$$k_S = k_P \phi_{prompt}$$
$$k_{ISC} = k_P(1 - \phi_{prompt})$$
$$k_{RISC} = \frac{k_D k_P}{k_{ISC}} \frac{\phi_{delayed}}{\phi_{prompt}} \quad (3.8)$$
$$k_T = k_D - \phi_{prompt} k_{RISC}$$

The singlet and triplet population densities are also shown in Figure 3.13b after the pulse has been switched OFF. The triplet population densities are three orders of magnitude higher than that of singlets. The polaron population reduces faster than the excitons after switching the pulse OFF. This asserts the dominance of TTA among other bimolecular annihilation processes on the kinetics of EL after the pulse has been switched OFF.

3.11   Temperature Dependent exciton dynamics

RISC is a temperature-dependent process, and with the reduction of temperature, the delayed fluorescence component reduces under optical excitation. This causes a reduction in the overall PL intensity (Figure 3.2b) and the delayed lifetime in 4CzFCN [12]. Temperature-dependent EL measurements is performed to investigate the presence of TTA in

delayed fluorescence. The steady-state EL magnitude is observed to reduce with temperature for a fixed bias, similar to that observed for optical excitation (Figure 3.14). However, it is observed that at 200 K, the delayed emission component of the normalized TrEL decays is enhanced (Figure 3.15) compared to 340 K. This trend is contrary to the case of photoexcited processes [12]. It is expected then that the delayed fluorescence component consists of contributions both from TTA and RISC.
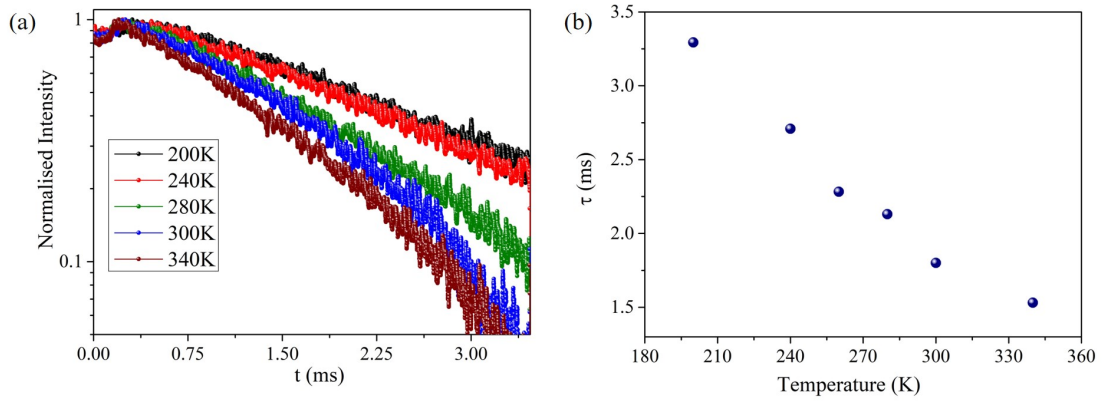
Figure 3.15: (a) Temperature-dependent TrEL decay profiles, (b) Variation of TrEL time constants as a function of temperature.

Figure 3.16(a-b) highlight the bias dependence of TrEL profiles at 200 K and 340 K. The TrEL profiles decay faster with an increase in the injected current densities at 200 K. This highlights the presence of TTA at 200 K, which is a population density-dependent process.
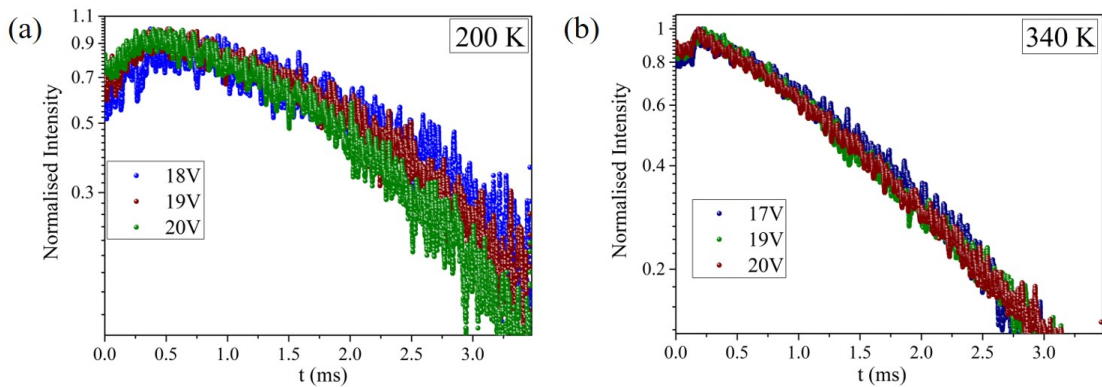
Figure 3.16: (a) Bias-dependent TrEL decay profiles at (a) 200K and (b) 340K.

However, at 340 K, the TrEL profiles are observed to be independent of the applied bias. This highlights the dominance of the RISC process at 340 K, which is a temperature-dependent monomolecular process. Further, the ΔE_{ST} in the case of 4CzFCN has been observed to be $\approx$ 60 meV and that can substantially reduce the RISC processes at low temperatures [12]. These trends confirm the dominant influence of TTA in long-lived delayed emission at low temperatures and RISC kinetics at high temperatures (300 K - 340 K).

TTA is a process of harvesting 'dark' triplets, and only 25% of them generate singlet excitons [2]. Thus, triplet harvesting via RISC is almost four times more efficient than the TTA events, ascertaining that molecules should be designed to significantly reduce bimolecular annihilation (observed at 340 K). These observations highlight the utility of the sensitive TrEL measurements for studying triplet dynamics in molecules upon electrical injection.

3.12   Conclusions

In conclusion, TrEL measurements in TADF OLEDs provide valuable insights into the charge carrier and recombination dynamics. A delay between the excitation pulse and the EL onset is observed. The delay
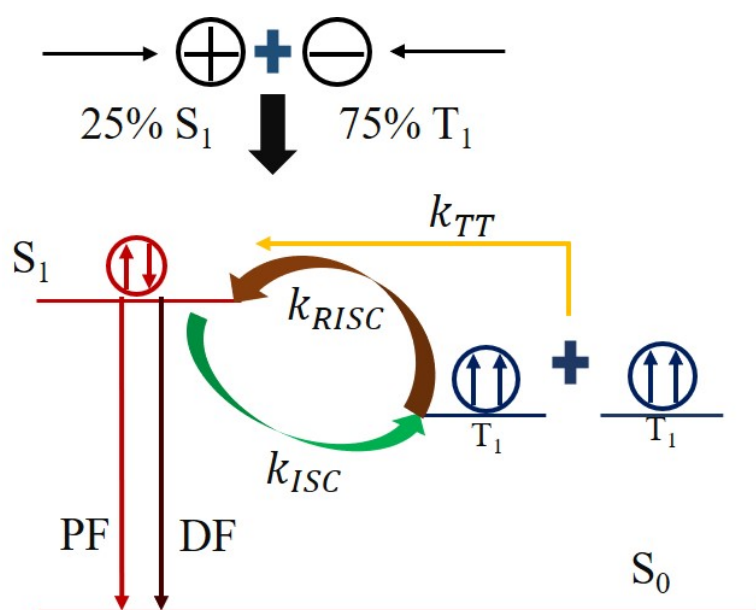
Figure 3.17: Processes contributing to the delayed fluorescence in TADF OLEDs.

time arises from the transit time of carrier and space charge creation in the interfaces around the active layer. The rising edge of the EL emission response can be described in terms of two-time constants, one associated with the initial recombination of electrons and holes at the active layer interface and the other resulting from multiple trapping of carriers, de-trapping, and recombination. On turning OFF the electrical pulse, the EL intensity shoots up due to injected charges stalling and reversing with an increased radiative trap-mediated exciton decay. The emission decay occurs over a long time ($\sim$ ms) and can be interpreted based on monomolecular and bimolecular exciton dynamics. Bias-dependent TrEL measurements at different temperatures suggest the presence of both RISC and TTA to be responsible for harvesting the triplets back to singlets (Figure 3.17). At high temperatures (340 K), RISC processes extensively dominate the delayed fluorescence magnitude. It is emphasized that TrEL measurements serve as a standard tool to study the carrier transport and triplet dynamics to probe efficiency-limiting processes in electrically driven TADF OLEDs.

References

[1] A. Köhler and H. Bässler, *Electronic processes in organic semiconductors: An introduction.* John Wiley & Sons, 2015.

[2] A. Köhler and H. Bässler, "Triplet states in organic semiconductors," *Materials Science and Engineering: R: Reports*, vol. 66, no. 4-6, pp. 71–109, 2009.

[3] N. J. Thompson, M. W. Wilson, D. N. Congreve, P. R. Brown, J. M. Scherer, T. S. Bischof, M. Wu, N. Geva, M. Welborn, and T. V. Voorhis, "Energy harvesting of non-emissive triplet excitons in tetracene by emissive pbs nanocrystals," *Nature materials*, vol. 13, no. 11, pp. 1039–1043, 2014.

[4] D. Y. Kondakov, "Triplet–triplet annihilation in highly efficient fluorescent organic light-emitting diodes: current state and future outlook," *Philosophical Transactions of the Royal Society A: Mathematical, Physical and Engineering Sciences*, vol. 373, no. 2044, p. 20140321, 2015.

[5] A. Monkman and R. H. Friend, "Organic semiconductor spintronics: utilizing triplet excitons in organic electronics," 2015.

[6] M. A. Baldo, D. F. O'Brien, Y. You, A. Shoustikov, S. Sibley, M. E. Thompson, and S. R. Forrest, "Highly efficient phosphorescent

emission from organic electroluminescent devices," *Nature*, vol. 395, no. 6698, pp. 151–154, 1998.

[7] C. Adachi, M. A. Baldo, M. E. Thompson, and S. R. Forrest, "Nearly 100internal phosphorescence efficiency in an organic light-emitting device," *Journal of Applied Physics*, vol. 90, no. 10, pp. 5048–5051, 2001.

[8] D. Kondakov, T. Pawlik, T. Hatwar, and J. Spindler, "Triplet annihilation exceeding spin statistical limit in highly efficient fluorescent organic light-emitting diodes," *Journal of Applied Physics*, vol. 106, no. 12, p. 124510, 2009.

[9] H. Uoyama, K. Goushi, K. Shizu, H. Nomura, and C. Adachi, "Highly efficient organic light-emitting diodes from delayed fluorescence," *Nature*, vol. 492, no. 7428, pp. 234–238, 2012.

[10] S. Y. Lee, T. Yasuda, I. S. Park, and C. Adachi, "X-shaped benzoylbenzophenone derivatives with crossed donors and acceptors for highly efficient thermally activated delayed fluorescence," *Dalton Transactions*, vol. 44, no. 18, pp. 8356–8359, 2015.

[11] S. Kuila, A. Ghorai, P. K. Samanta, R. B. Siram, S. K. Pati, K. Narayan, and S. J. George, "Red emitting delayed fluorescence and room temperature phosphorescence from core substituted naphthalene diimides," *Chemistry–A European Journal*, vol. 25, no. 70, pp. 16007–16011, 2019.

[12] Y. J. Cho, B. D. Chin, S. K. Jeon, and J. Y. Lee, "20% external quantum efficiency in solution processed blue thermally activated delayed fluorescent devices," *Advanced Functional Materials*, vol. 25, no. 43, pp. 6786–6792, 2015.

[13] A. Dey and D. Kabra, "Role of bimolecular exciton kinetics in controlling the efficiency of organic light-emitting diodes," *ACS applied materials & interfaces*, vol. 10, no. 44, pp. 38287–38293, 2018.

[14] M. Hasan, A. Shukla, V. Ahmad, J. Sobus, F. Bencheikh, S. K. McGregor, M. Mamada, C. Adachi, S. Lo, and E. B. Namdas, "Exciton–exciton annihilation in thermally activated delayed fluorescence emitter," *Advanced Functional Materials*, vol. 30, no. 30, p. 2000580, 2020.

[15] V. R. Kishore, M. P. Patankar, N. Periasamy, and K. Narasimhan, "Transient electroluminesence in alloy-based organic light-emitting diodes," *Synthetic metals*, vol. 143, no. 3, pp. 295–303, 2004.

[16] C. Murawski, K. Leo, and M. C. Gather, "Efficiency roll-off in organic light-emitting diodes," *Advanced Materials*, vol. 25, no. 47, pp. 6801–6827, 2013.

[17] S. Babenko, V. Benderskii, V. Gol'Danskii, A. Lavrushko, and V. Tychinskii, "Annihilation of singlet excited states in anthracene

solutions," *Chemical Physics Letters*, vol. 8, no. 6, pp. 598–600, 1971.

[18] J. Grune, N. Bunzmann, M. Meinecke, V. Dyakonov, and A. Sperlich, "Kinetic modeling of transient electroluminescence reveals tta as an efficiency-limiting process in exciplex-based tadf oleds," *The Journal of Physical Chemistry C*, vol. 124, no. 47, pp. 25667–25674, 2020.

[19] M. Hasan, S. Saggar, A. Shukla, F. Bencheikh, J. Sobus, S. K. McGregor, C. Adachi, S.-C. Lo, and E. B. Namdas, "Probing polaron-induced exciton quenching in tadf based organic light-emitting diodes," *Nature communications*, vol. 13, no. 1, pp. 1–7, 2022.

Effect Of Non-Line Of Sight Luminescent Emitters in Visible Light Communication Systems

4.1   Introduction

Light-fidelity (Li-Fi) technology, an offshoot of visible light communication (VLC) based on signalling protocols using standard LEDs and detectors, has been making rapid strides [2]. Free space communication via Li-Fi further utilizes off-the-shelf light-emitting diodes and detectors to realize fully networked wireless systems [3]. Harald Hass and co-workers highlighted that light-emitting diodes (LEDs) are natural beam-formers that enable local containment of Li-Fi signals [4–8]. The availability of flexible and building integrable LEDs and detectors based on the organic, quantum dot and hybrid materials provide a wide range of options with smart features [9–13]. Since this communication technology prevails in a background lighting condition, strategies to mitigate ambient light effects in VLC systems have been implemented both at the communication hardware and signal processing stages [14–16]. Blue LEDs, which employ phosphor converters to generate white light, now employ colour converters with a short radiative lifetime [17], thus pushing the bandwidth limits. In the scheme of the internet-of-things, the wall features such as texture, colour, reflectance, glow etc., can assume significant importance. The enclosure boundary normally is treated as a classical light diffuser which merely scatters and attenuates the signal [15, 18]. Reports have also emphasized the

colour conversion capabilities of the boundary layers, which can, in effect, replace the phosphors around the GaN LED [17, 19–22]. The use of these external emitters as active sources can alter communication characteristics [23, 24]. The introduction of active contributions, which can alter the source-generated signal features, or more specifically, the noise characteristics, forms the central theme of the chapter.

Significant improvements in the light emitter and detector technology have enabled the performance of these devices to reach nearly ideal levels. Efficient LEDs have been shown to exhibit a 3-dB bandwidth of 4 GHz [25]. LEDs with high quantum efficiency are Poissonian photon sources as the noise distribution and reflect the fluctuations in the driving current [26]. With the advent of efficient injecting characteristics in diode lasers and LEDs, the photon fluctuations have improved the noise characteristics and bandwidth by exhibiting sub-Poissonian characteristics [27, 28].

The presence of phosphorescent emitters as paint coated on the walls and boundaries can play a significant role and can be expected to affect the noise distribution of photons coming from the LED source. These coatings, in essence, can control the signal's bandwidth and quality. The absorbed light from a pump source (in this case, the LED) takes the molecule to the excited singlet state from the ground state. The electrons then undergo inter-system crossing and reach the triplet state via a vibrational coupling. This spatially selective signal distortion scheme strategy involves phosphor-based coatings and paints, which provide a unique handle to create different levels of a smart environment.

4.2 Demonstration of non-line-of-sight communication

A typical non-line-of-sight (NLOS) communication system is shown in Figure 4.1. A standard VLC link of 20 Mbps with 0 bits of error using non-return to zero on-off keying (NRZ-OOK) modulation technique was implemented in a 1 m × 0.5 m × 0.5 m enclosure with the detector
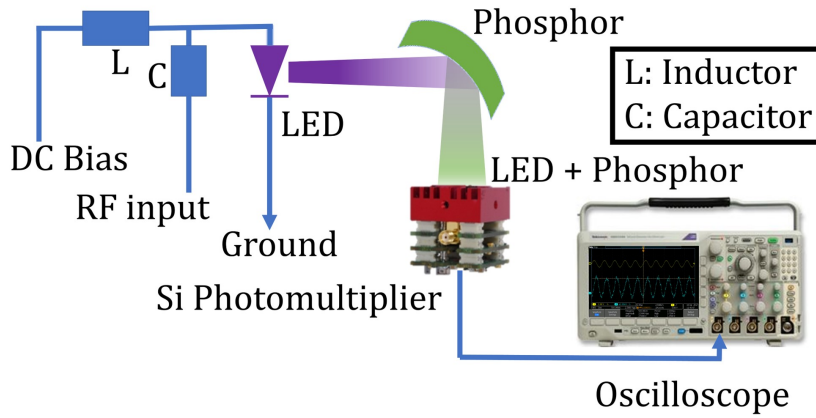
Figure 4.1: Demonstration of NLOS optical communication system. Reproduced from [1]

kept in NLOS configuration. A high-power Lumex 405 nm LED was modulated using Thor Labs LDC500 Laser Diode Controller, which is basically a bias-tee (consists of the addition of signals from an ideal inductor which allows DC bias to pass blocking any RF signal and an ideal capacitor at which the RF pass blocking any DC signal). The modulated light from the LED was detected using SensL S/N 00558 SPMMini silicon photomultiplier module (SPM) of area 1 mm^2 and visualized using Tektronix MDO3024 200 MHz Oscilloscope. The sampling rate of the oscilloscope was kept at 2.5 GSa/s. The SPM has a built-in trans-impedance amplifier which converts and amplifies the photocurrent to photovoltage. The time series data in the oscilloscope was captured using an AC coupling of 1MΩ. Figure 4.2 (a-b) show the modulated light sent and detected respectively in the NLOS configuration.
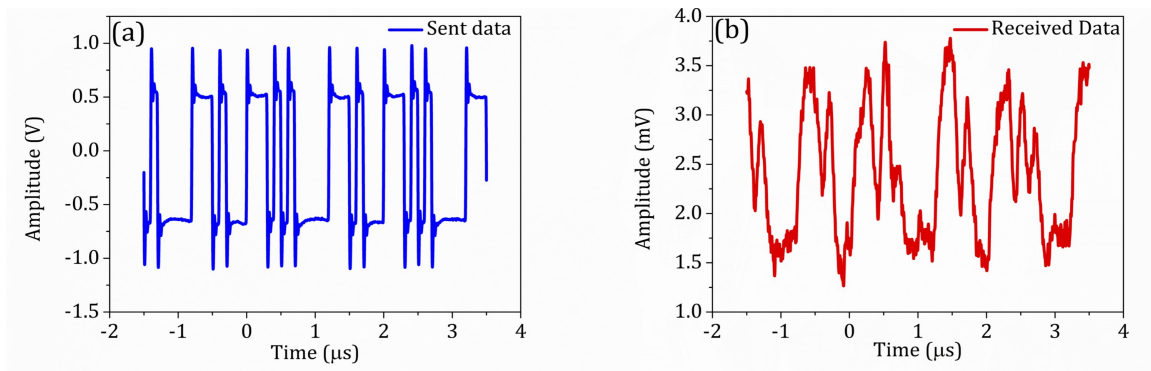
Figure 4.2: (a) Data bits sent in NRZ-OOK type modulation and (b) Received Data. Reproduced from [1]

The magnitude of photon fluctuations in a light source is proportional to the number of photons emitted per unit time. The presence of phosphor enhances the fluctuations in the light signal, increasing the light signal's noise floor. Thus, for an appropriate distance between the light source and the detector, the phosphorescent noise can make up a sizable fraction of the modulation amplitude of the original LED light source.

4.3 Measurement of Photon number fluctuations

4.3.1 Avalanche photodiode array

An array of avalanche photodiodes (APD) in the form of a photomultiplier module that has the ability to measure single photons is commonly used to study photon number fluctuations of light sources. The avalanche photodiodes in the array have their own sources of noise arising from intrinsic processes like fluctuations in the number and the positions at which the dark pairs are generated, apart from the statistical fluctuations of the incident photon flux contributing to the electron-hole generation [29]. In the APD, internal photocurrent multiplication at sufficient reverse bias is used to achieve high sensitivity and is accompanied by excess noise during the multiplication [29]. However, the APD arrays suffer from drawbacks of high thermal noise at high frequencies and optical crosstalk (emission of secondary photons in the array after one APD detects a photon due to hot carrier relaxation). Each of these sources can be modelled, identified and quantified by systematic noise measurement studies as a function of external parameters (light intensity, temperature, bias) and material parameters (mobility, trap density) [30, 31].

The capture of photon number fluctuation by the APD array involves three independent stochastic events [32]. Firstly, the charge carriers responsible for the driving current follow a noise distribution reflected in the intensity fluctuation of the LED. The magnitude by which this fluctuation is transferred to the LED depends on the quantum efficiency of the LED (η_{LED}). Secondly, the emitted light from LED spreads over a large solid angle and even after various focusing

mechanisms, a part of it gets lost before getting detected by the APD array. The efficiency with which the photon gets transferred from the LED to the detector is given by $\eta_{transfer}$. The APD array has very high quantum efficiency (η_{APD}) and converts this stream of photons into a photocurrent which captures the noise distribution of the light source. Thus, the net efficiency with which the whole process of noise can be captured is given as

$$\eta = \eta_{LED}\eta_{APD}\eta_{transfer} \qquad (4.1)$$

However, the individual efficiencies cannot be measured directly. The variance in the currents across the LED and APD array is the measurable quantity and is defined as

$$\Delta^2 i = <i^2> - <i>^2 \qquad (4.2)$$

These fluctuations are then normalized with respect to their mean currents, and their ratio gives the extent by which the fluctuations of photons emitted from a source are captured by the APD.

4.3.2 Sources of noise

- Radiated electric and magnetic fields are the most common means of noise coupling. All circuit elements, whenever charges move through them, radiate electromagnetic waves. In addition, noise from external sources, which include AC power lines, wireless communication waves from radios, TV stations, Wi-fi, and Bluetooth signals, can couple into electric circuits through conducting wires. For example, peaks at 50 Hz and their harmonics are due to the power line and a peak at 2.4 GHz corresponds to Wi-fi and Bluetooth operation.

- Multiple paths to ground currents in a system give rise to ground loops. Several paths of conduction in instruments are arranged to regulate current flows, and all paths are connected to a common ground through a low impedance. This prevents the internal system from being at a floating potential between the AC supply potential and the ground. These multiple paths form a loop and can pick up stray signals by electromagnetic induction. The ground loop also

results in an unwanted current through a conductor connecting two points which are generally supposed to be at the same potential but are actually at different potentials.

- If the dielectric material inside the cable is not in contact with the cable conductors, a charge can be produced on the dielectric, which acts as noise voltage. This is termed as triboelectric effect and is usually caused by the mechanical bending of the cable or if the cable is left hanging without any support.

- There are always stray magnetic fields in the laboratory due to power wiring and other circuits with high currents. If a wire is allowed to move through this field, a noise voltage gets induced. So, the motion of conductors has to be limited as much as possible. This problem is especially troublesome in a vibrational environment.

The interference of environmental electromagnetic noise sources can be diminished enormously by using a shielded metal enclosure. This enclosure is known as the Faraday cage. The setup is made of 2 mm thick aluminium and is cubical in shape. The inside of the Faraday cage was painted black to reduce the noise originating from the reflections from the walls of the enclosure. The ground loop problem was avoided by shorting the Faraday cage with the ground of the digital storage oscilloscope (DSO).

4.3.3   Experimental Setup

The protocol for the noise measurements involved a high-efficiency Lumex 405 nm LED powered using a Thor Labs LDC 500 Laser Diode driver and collimation using the plano-convex lens and coupled to a beam-splitter. The fluctuations representing the light intensity from the LED source was detected using SensL S/N 00558 SPMMini Silicon photomultiplier module (SPM), and the light scattered off the phosphorescent (ZnS) or fluorescent (Green IXT) layers were monitored using another SensL S/N 00638 SPMMini Silicon Photomultiplier Module (SPM). The time series data from both the Silicon Photomultiplier Modules was captured simultaneously using a four-channel Tektronix
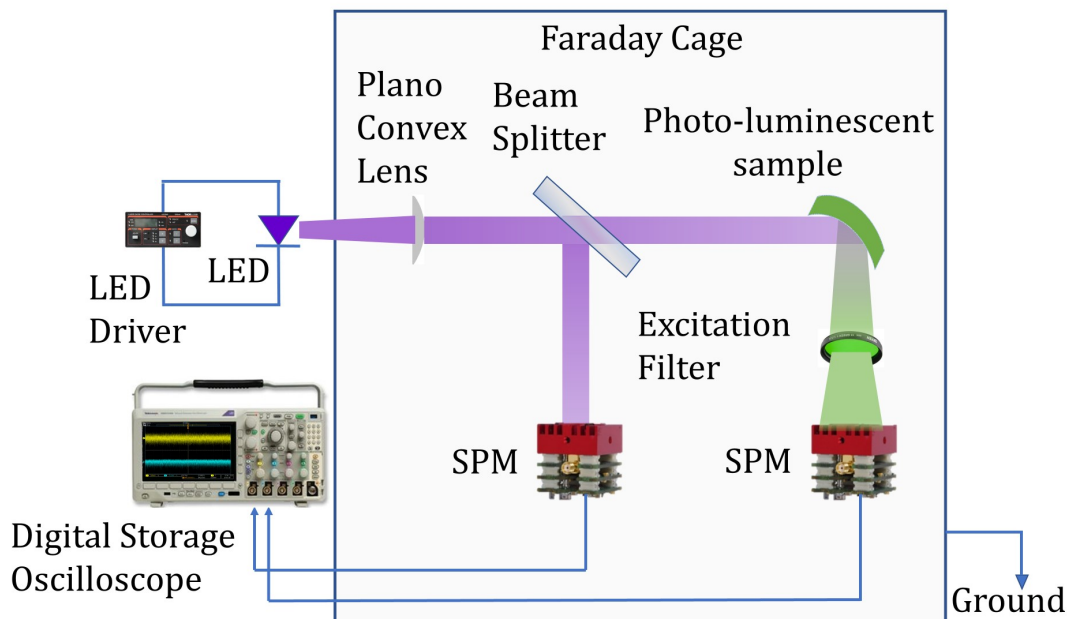
Figure 4.3: Schematic for measuring the photon number fluctuation from the phosphorescent or fluorescent sample. Reproduced from [1]

MDO3024 200 MHz oscilloscope at a sampling rate of 100 kSa/s for 10 s and analyzed using MATLAB. Measurements were repeated a sufficient number of times to ensure reproducibility. In our studies, the luminescent coatings were optically planar surfaces and located at a distance ($>$ 100 cm) from the source and close to the detector assembly ($<$ 10 cm) to ensure that there is sufficient luminescent light component fraction superimposed on the direct source. The schematic for measuring photon number fluctuations is shown in Figure 4.3.

4.4 Power Spectral Density

Figure 4.4 (a-c) show the time series data for the phosphorescent sample, the fluorescent sample and the LED respectively. The results are represented by the intensity-normalized signals $V(t)$ (scaled by the mean V_{dc} factor). The results clearly reveal a larger fraction of noise emanating from the luminescent media in the detector signal. The noise from these sources are observed to be an order of magnitude more than the direct LED source. The power spectral density (PSD), S_V estimated from

$$S_V = \frac{1}{2T}|\int_{-T}^{T} V(t)exp^{-2\pi ift}dt|^2 \tag{4.3}$$
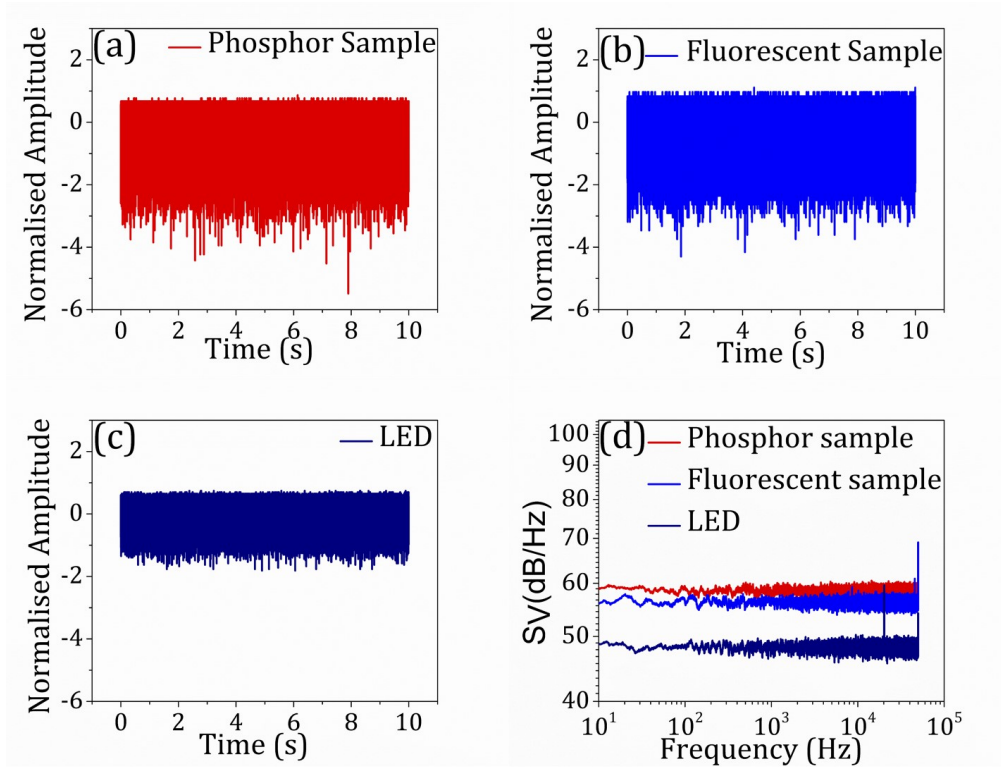
Figure 4.4: Noise measurements in an optical communication system in the presence of active luminescent coatings. The fluctuations from luminescence and LED emission (405 nm, ≈10 μW) were detected with low noise SPM and oscilloscope. Photon number fluctuation from light scattered off the (a) phosphorescent layer, (b) fluorescent sample and (c) directly of the LED; (d) Power spectral density, S_V response. Reproduced from [1]

also reveals the trend in (Figure 4.4d) with appreciable noise power for the phosphorescent emission as compared to the LED. The frequency-independent PSD also points to the dominant noise contribution from the photon sources rather than detector-type noise processes, which take up $1/f$ noise form or variations of it. Here T is the duration of the capture of the time series data. It is seen from Figure 4.5 that the magnitude of photon noise decreases as the photon number is reduced.

4.5 Cross-Correlation Analysis

The noise response can be further examined by measuring and analyzing the cross-correlation function [33], expressed as

$$G_{12} = \frac{c_{12}(\tau)}{\sqrt{c_{11}(0)c_{22}(0)}} \tag{4.4}$$
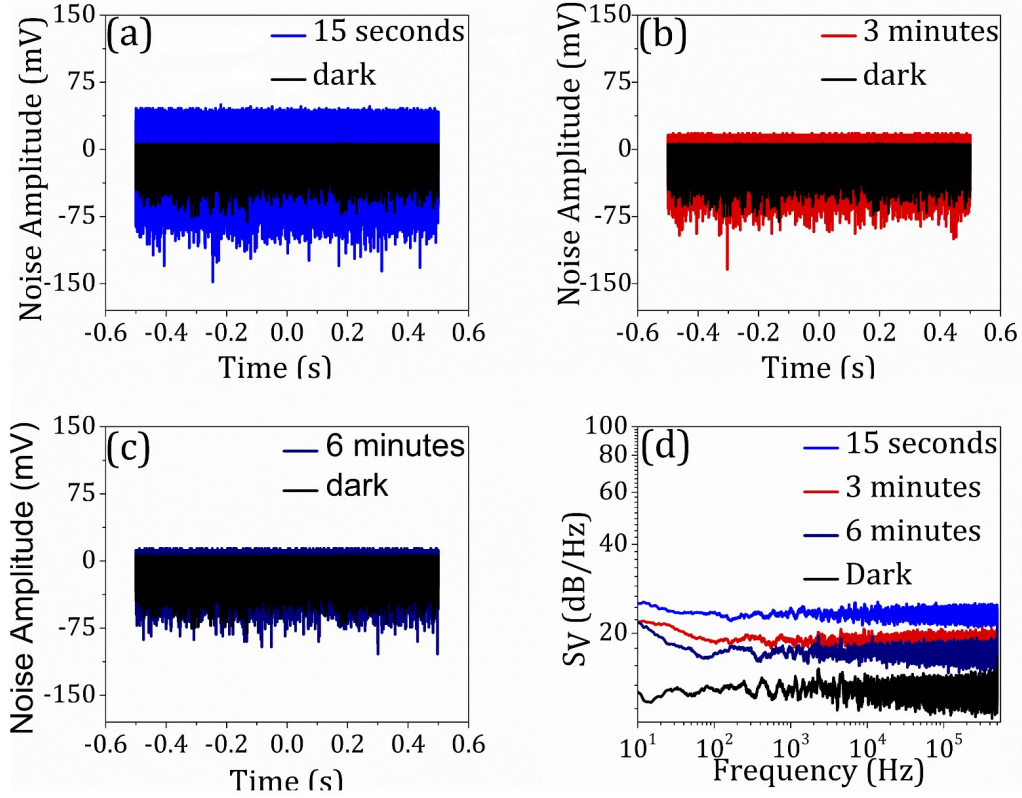
Figure 4.5: Decay of phosphor noise amplitude with time (a) at 15 seconds after excitation is switched off (b) 3 minutes after excitation is switched off (c) 6 minutes after excitation is switched off (d) Power Spectral Density (S_V) plots for the time series data. Reproduced from [1]

where $c_{mn}(\tau)$ is the covariance between the two signals which is defined as

$$c_{mn}(\tau) = < \nu_m(t+\tau)\nu_n(t) \tag{4.5}$$

Here τ is the time lag between the time series data generated by the two SiPM – one recording the LED fluctuations and the other recording the fluctuations coming from the phosphorescent or the fluorescent sample.

Here τ is the time lag between the time series data generated by the two SPMs – recording the (i) LED fluctuations and (ii) fluctuations emanating from the phosphorescent or fluorescent sources. Figure 4.6 shows the time dependence of the cross-correlation function between the two detectors. Under dark conditions, the fluctuations in the stray detector signals are not correlated (Figure 4.6a). The expected correlation of the signal when both the detectors receive the LED signal is shown in Figure 4.6b. In the case of signals arising from the LED and the fluorescent source, a sharp feature in the cross-correlation
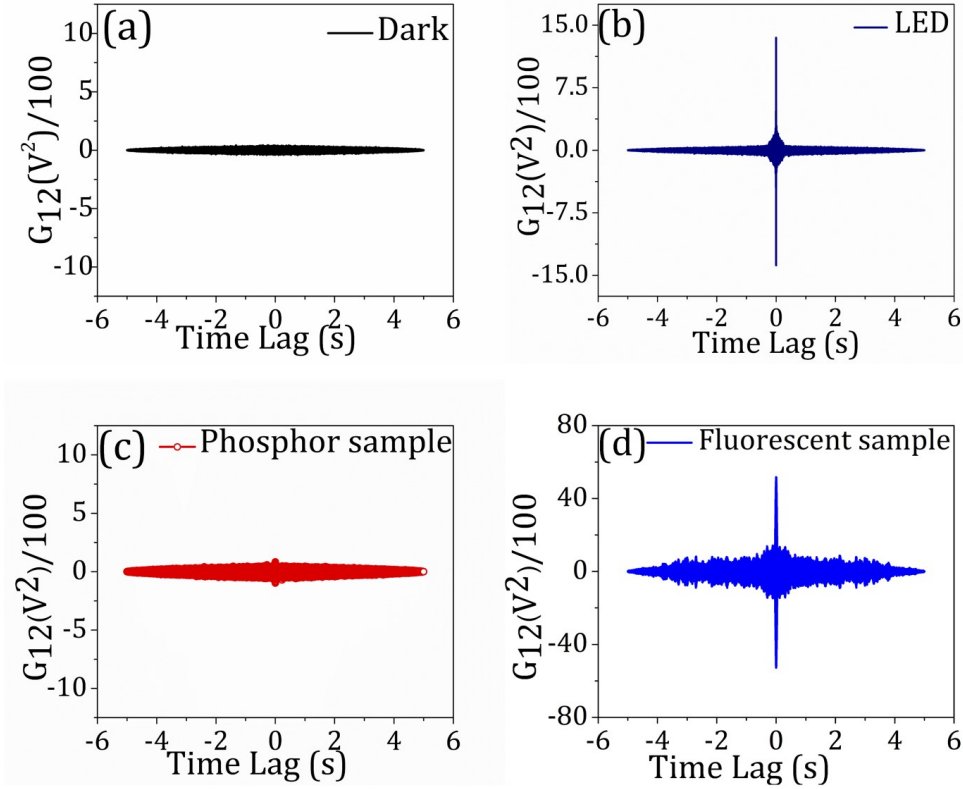
Figure 4.6: Cross-correlation analysis of fluctuations: LED emission along with the luminescent light was captured using a pair of SPM modules simultaneously. Cross-correlation of: (a) the dark background; (b) LED signals captured by the two detectors; (c) LED and phosphorescent sources; (d) LED and fluorescent sources. Reproduced from [1]

function is revealed in the vicinity of $\tau = 0$ and is an estimate for the fluctuations between the LED (Figure 4.6d) and the fluorescence. In the case of the signal arising from the phosphor layer, however, the correlation is significantly reduced (Figure 4.6c). The absence of cross-correlation between the phosphor and the LED signal is closer to the results observed in the $V(t)$ in dark conditions or from two independent LEDs.

The sharp correlation between the LED and fluorescent sample can be understood as follows: It is known that efficient LEDs have a form of fluctuations that follow a Poissonian distribution. Since the intensity of light used in the experiment is high ($> 10\ \mu\text{W/cm}^2$), the number of photons emitted is large, making the noise distribution take up a Gaussian nature. The preserved Gaussian distribution of the LED photons in the reflected and transmitted beams is incident on the luminescent layer. The lifetime of a fluorescent material is of

the order of nanoseconds and retains the source noise in the observed range, i.e., the excitation and de-excitation time interval is less than the time interval between the arrival of two photons successively. This is not the case for the phosphorescent sample, where the presence of a metastable triplet state leads to a large decay lifetime inhibiting the above process. Thus, the nature of the Gaussian distribution changes and the correlation in the phosphorescent emission is absent as compared to the high correlation for the fluorescent emission. This feature demonstrates that the phosphorescent medium has the ability to change the photon number distribution and, in principle, can be programmed to intervene and distort the modulated signal.

4.6 Modulation of phosphor source
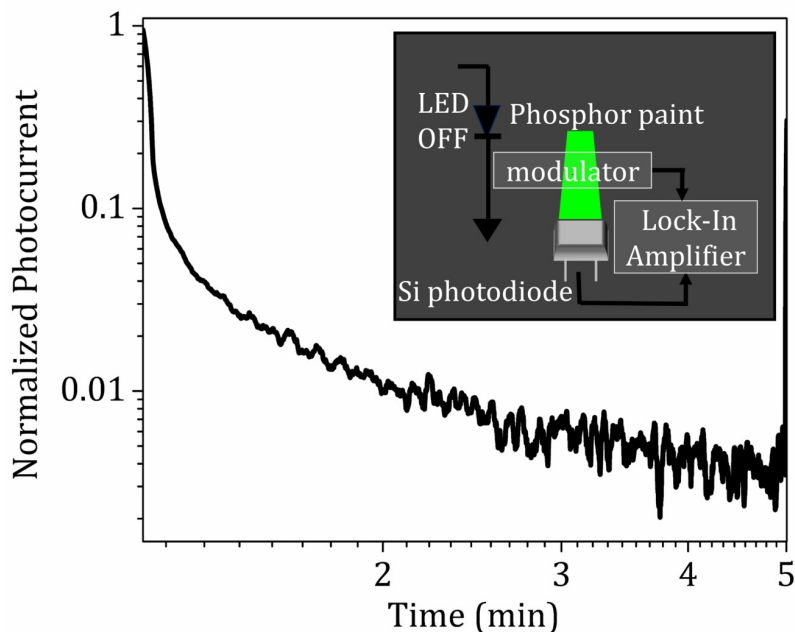
Figure 4.7: Intensity modulated photocurrent at different stages of the Strontium aluminate phosphor glow (after the pump LED is turned off). Inset is the schematic of experiment. Reproduced from [1]

An interesting feature was noted during the course of our studies on the emission from the strontium aluminate phosphor (glow-in-the-dark paint) coating, which has exceptionally high lifetimes. These alkaline earth aluminates have higher efficiencies than zinc compounds, leading to brighter and longer glow duration. This glow from the phosphor

source induced by exposure to the pump-LED source gradually decreases in intensity over a few hours and is utilized as a photon source. The periodic signal is encoded in this remnant light using an acousto-optic modulation technique or standard electromechanical chopper/shutter to demonstrate the possibility of data transmission after the primary pump-LED is turned off. It is noted that the duration of this detection feature in the dark depends on the initial intensity of the LED pump. In the present case, the moderate power of LED ($< 100 \ \mu\mathrm{W} \ cm^{-2}$) resulted in phosphor detection over 5 min, which can be easily extended over a few hours. The acousto- optical modulation rate typically accesses bandwidth to the 40 MHz range and is well suited to signal transmission in this situation. Figure 4.7 depicts the features of the modulated photocurrent using a mechanical chopper from this persisting light source. Since the emission flux varies linearly with the pump excitation, the 5 min decay range can be extended to a few hours by an initial excitation flux ($> 10 \ \mathrm{mW} cm^{-2}$).

4.7 Modulation with acousto-optic modulator
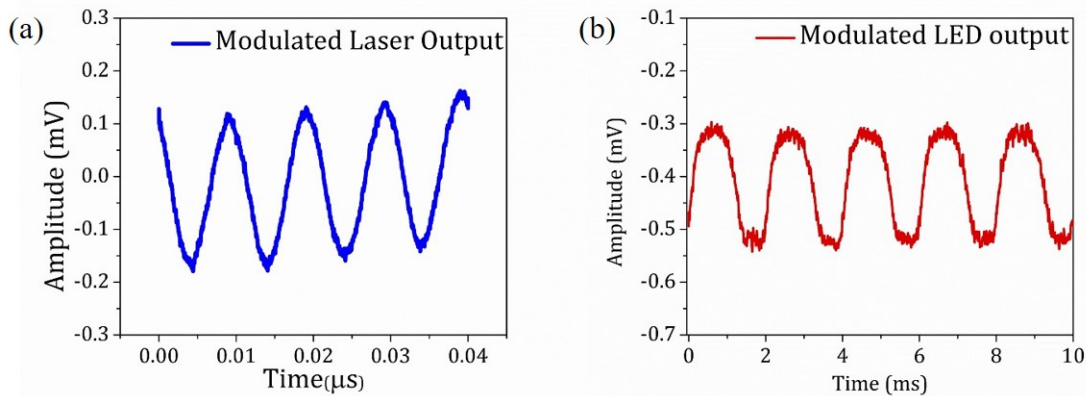
Figure 4.8: Sinusoidal Intensity Modulation of (a) CW Laser and (b) LED using AOM. Reproduced from [1]

A Panasonic EFLM200 acousto-optic modulator (AOM) can be used for modulating light intensities to transmit data in visible light communication systems. The AOM has a centre frequency of 200 MHz and can be used to modulate light intensities up to 40 MHz. The most characteristic feature of using this AOM is that it can be used to modulate both coherent and incoherent sources of light. It was possible to modulate

a coherent 470 nm continuous wave (CW) laser, an incoherent 405 nm LED, and a phosphor white LED by keeping it at a distance of 0.1 m. A sinusoidal amplitude modulated 200 MHz wave from Keysight E4432B ESG-D digital RF signal generator was fed to the AOM to modulate the light intensity. The signal was captured by an ET2000 Si detector. Thus, this concept can be used to modulate the phosphor emission coming from the walls after the excitation light source is switched on, as described in Section 4.6. Figure 4.8 shows the modulated output of both the CW laser and the LED.

4.8 Conclusions

In conclusion, our results indicate the utility of fluorescent and phosphorescent coatings to tailor and modify signal detection attributes in a VLC protocol. The spatial dependence of the light scattering sites offers tunability of the S/N ratio levels. This feature can be utilized to design smart environments where signal access can be controlled and restricted. Phosphorescent coating in the vicinity of the detector can alter the signal characteristics substantially. This option of signal alteration locally will be useful in controlling and accessing VLC usage. Conversely, signal analysis can also be utilized to provide dynamic information about the environment. The feasibility of VLC after the primary LEDs are switched off is also demonstrated, which relies on the persisting emission from the phosphor coatings over a long period.

References

[1] A. Ghorai, P. Walvekar, S. Nayak, and K. Narayan, "Influence of non-line of sight luminescent emitters in visible light communication systems," *Journal of Optics*, vol. 20, no. 1, p. 015703, 2017.

[2] H. Chen, C. Wu, H. Li, X. Chen, Z. Gao, S. Cui, and Q. Wang, "Advances and prospects in visible light communications," *Journal of semiconductors*, vol. 37, no. 1, p. 011001, 2016.

[3] C.-H. Yeh, C.-W. Chow, H.-Y. Chen, Y.-L. Liu, and D.-Z. Hsu, "Investigation of phosphor-led lamp for real-time half-duplex wireless vlc system," *Journal of optics*, vol. 18, no. 6, p. 065701, 2016.

[4] L. Yin, X. Wu, and H. Haas, "On the performance of non-orthogonal multiple access in visible light communication," in *2015 IEEE 26th*

annual international symposium on personal, indoor, and mobile radio communications (PIMRC), pp. 1354–1359, IEEE, 2015.

[5] H. Haas, L. Yin, Y. Wang, and C. Chen, "What is lifi?," *Journal of lightwave technology*, vol. 34, no. 6, pp. 1533–1544, 2015.

[6] S. Rajbhandari, H. Chun, G. Faulkner, K. Cameron, A. V. Jalajakumari, R. Henderson, D. Tsonev, M. Ijaz, Z. Chen, H. Haas, *et al.*, "High-speed integrated visible light communication system: Device constraints and design considerations," *IEEE Journal on Selected Areas in Communications*, vol. 33, no. 9, pp. 1750–1757, 2015.

[7] H. Chun, S. Rajbhandari, G. Faulkner, D. Tsonev, E. Xie, J. J. D. McKendry, E. Gu, M. D. Dawson, D. C. O'Brien, and H. Haas, "Led based wavelength division multiplexed 10 gb/s visible light communications," *Journal of lightwave technology*, vol. 34, no. 13, pp. 3047–3052, 2016.

[8] D. Tsonev, S. Videv, and H. Haas, "Towards a 100 gb/s visible light wireless access network," *Optics express*, vol. 23, no. 2, pp. 1627–1637, 2015.

[9] P. A. Haigh, Z. Ghassemlooy, S. Rajbhandari, and I. Papakonstantinou, "Visible light communications using organic light emitting diodes," *IEEE Communications Magazine*, vol. 51, no. 8, pp. 148–154, 2013.

[10] S. Zhang, D. Tsonev, S. Videv, S. Ghosh, G. A. Turnbull, I. D. Samuel, and H. Haas, "Organic solar cells as high-speed data detectors for visible light communication," *Optica*, vol. 2, no. 7, pp. 607–610, 2015.

[11] P. A. Haigh, Z. Ghassemlooy, I. Papakonstantinou, F. Arca, S. F. Tedde, O. Hayden, and E. Leitgeb, "A 1-mb/s visible light communications link with low bandwidth organic components," *IEEE photonics technology letters*, vol. 26, no. 13, pp. 1295–1298, 2014.

[12] A. M. Vegni and M. Biagi, "An indoor localization algorithm in a small-cell led-based lighting system," in *2012 International Conference on Indoor Positioning and Indoor Navigation (IPIN)*, pp. 1–7, IEEE, 2012.

[13] M. Biagi, S. Pergoloni, and A. M. Vegni, "Last: A framework to localize, access, schedule, and transmit in indoor vlc systems," *Journal of Lightwave Technology*, vol. 33, no. 9, pp. 1872–1887, 2015.

[14] S. Yin and O. Gnawali, "Towards embedded visible light communication robust to dynamic ambient light," in *2016 IEEE Global Communications Conference (GLOBECOM)*, pp. 1–6, IEEE, 2016.

[15] Y. H. Chung and S.-b. Oh, "Efficient optical filtering for outdoor visible light communications in the presence of sunlight or articifical light," in *2013 International Symposium on Intelligent Signal Processing and Communication Systems*, pp. 749–752, IEEE, 2013.

[16] Z. Wang, C. Yu, W.-D. Zhong, J. Chen, and W. Chen, "Performance of a novel led lamp arrangement to reduce snr fluctuation for multi-user visible light communication systems," *Optics express*, vol. 20, no. 4, pp. 4564–4573, 2012.

[17] M. T. Sajjad, P. P. Manousiadis, C. Orofino, D. Cortizo-Lacalle, A. L. Kanibolotsky, S. Rajbhandari, D. Amarasinghe, H. Chun, G. Faulkner, D. C. O'Brien, *et al.*, "Fluorescent red-emitting bodipy oligofluorene star-shaped molecules as a color converter material for visible light communications," *Advanced optical materials*, vol. 3, no. 4, pp. 536–540, 2015.

[18] Y. Zhao and J. Vongkulbhisal, "Design of visible light communication receiver for on-off keying modulation by adaptive minimum-voltage cancelation," *Engineering Journal*, vol. 17, no. 4, pp. 125–130, 2013.

[19] H. Chun, P. Manousiadis, S. Rajbhandari, D. A. Vithanage, G. Faulkner, D. Tsonev, J. J. D. McKendry, S. Videv, E. Xie, E. Gu, *et al.*, "Visible Light Communication Using a Blue GaN μLED and Fluorescent Polymer Color Converter," *IEEE Photonics Technology Letters*, vol. 26, no. 20, pp. 2035–2038, 2014.

[20] M. T. Sajjad, P. P. Manousiadis, H. Chun, D. A. Vithanage, S. Rajbhandari, A. L. Kanibolotsky, G. Faulkner, D. O'Brien, P. J. Skabara, I. D. Samuel, *et al.*, "Novel fast color-converter for visible light communication using a blend of conjugated polymers," *ACS Photonics*, vol. 2, no. 2, pp. 194–199, 2015.

[21] J. Santos, M. Leitao, C. Foucher, B. Guilhabert, S. Watson, A. Kelly, S. Rajbhandari, H. Chun, H. Haas, G. Faulkner, *et al.*, "Colloidal quantum dot color converters for visible light communications," in *2016 IEEE Photonics Conference (IPC)*, pp. 396–397, IEEE, 2016.

[22] I. Dursun, C. Shen, M. R. Parida, J. Pan, S. P. Sarmah, D. Priante, N. Alyami, J. Liu, M. I. Saidaminov, M. S. Alias, *et al.*, "Perovskite nanocrystals as a color converter for visible light communication," *Acs Photonics*, vol. 3, no. 7, pp. 1150–1156, 2016.

[23] C. W. Chow, C. Yeh, Y. Liu, and P. Huang, "Mitigation of optical background noise in light-emitting diode (led) optical wireless communication systems," *IEEE photonics Journal*, vol. 5, no. 1, pp. 7900307–7900307, 2013.

[24] Y. Liu, C. Yeh, Y. Wang, and C.-W. Chow, "Employing nrzi code for reducing background noise in led visible light communication,"

in *OptoElectronics and Communications Conference and Photonics in Switching*, p. TuPR_10, Optical Society of America, 2013.

[25] C.-H. Wu, G. Walter, H. W. Then, M. Feng, and N. Holonyak, "4-GHz Modulation Bandwidth of Integrated 2×2 LED Array," *IEEE Photonics Technology Letters*, vol. 21, no. 24, pp. 1834–1836, 2009.

[26] T. Endo, E. Morimoto, Y. Hirayoshi, and K. Toyoshima, "Dependence of an led noise on current source impedance," *Journal of the Physical Society of Japan*, vol. 66, no. 7, pp. 1986–1988, 1997.

[27] P. Tapster, J. Rarity, and J. Satchell, "Generation of sub-poissonian light by high-efficiency light-emitting diodes," *EPL (Europhysics Letters)*, vol. 4, no. 3, p. 293, 1987.

[28] T. Lunghi, G. De Simoni, V. Piazza, C. A. Nicoll, H. E. Beere, D. A. Ritchie, and F. Beltram, "Anti-bunched photons from a lateral light-emitting diode," *Applied Physics Letters*, vol. 99, no. 13, p. 131103, 2011.

[29] N. Hakim, B. Saleh, and M. Teich, "Generalized excess noise factor for avalanche photodiodes of arbitrary structure," *IEEE transactions on electron devices*, vol. 37, no. 3, pp. 599–610, 1990.

[30] P. Eckert, H.-C. Schultz-Coulon, W. Shen, R. Stamen, and A. Tadday, "Characterisation studies of silicon photomultipliers," *Nuclear Instruments and Methods in Physics Research Section A: Accelerators, Spectrometers, Detectors and Associated Equipment*, vol. 620, no. 2-3, pp. 217–226, 2010.

[31] I. Rech, A. Ingargiola, R. Spinelli, I. Labanca, S. Marangoni, M. Ghioni, and S. Cova, "Optical crosstalk in single photon avalanche diode arrays: a new complete model," *Optics express*, vol. 16, no. 12, pp. 8381–8394, 2008.

[32] H.-A. Bachor, P. Rottengatter, and C. Savage, "Correlation effects in light sources with high quantum efficiency," *Applied physics B*, vol. 55, no. 3, pp. 258–264, 1992.

[33] T. Endo, E. Morimoto, Y. Hirayoshi, and K. Toyoshima, "Anticorrelated noise from parallely connected light emitting diodes," *Journal of the Physical Society of Japan*, vol. 67, no. 9, pp. 3082–3085, 1998.

5

Photon Statistics of TADF Molecular Emission

5.1 Introduction

The investigations on molecules are generally restricted to the ensemble level owing to detection sensitivity or other experimental concerns. This has a direct consequence on the heterogeneity within the sample getting ignored. The recombination kinetics under optical excitation manifested in the photon statistics at dilute concentrations need to be studied where the intermolecular interaction between the dye molecules is significantly reduced. Studying isolated dye molecules enables us to detect rare events with high sensitivity. The advantage of studying molecules at the individual level is that it simplifies the theoretical treatment due to the reduction of environmental factors.

Measurements of the photophysics of dyes at high levels of dilution require elaborate instrumentation. Generally, these measurements are performed in dedicated confocal microscopes integrated with photon correlation spectroscopy (PCS) modules [1]. This chapter presents a custom-built confocal microscope that can image dye molecules and study their photo-physics at nanomolar to picomolar concentrations.

The requirement for performing photophysical studies at dilute concentration can be broadly grouped into three conditions. Firstly, the molecule should be photochemically stable. Secondly, the excitation rate for the dye molecule should be high so that the emission from the molecule is efficiently detected. Lastly, the emission rate of the dye molecule should be reasonably good, i.e., the quantum yield and

the radiative lifetime need to be high. The photo-physics of dilute concentrations of dye molecules are usually studied on molecules that have their lifetimes in the range of hundreds of picoseconds to tens of nanoseconds. This effectively increases the number of switching cycles of the molecules per second, increasing the emission intensity and enhancing the signal-to-noise ratio (SNR). Hence, molecules having lifetimes in the range of microseconds have their SNR orders of magnitude lesser, causing their study at dilute concentrations difficult. In this chapter, we have demonstrated a cost-effective custom-built confocal microscopy setup for studying photon statistics of thermally activated delayed fluorescence (TADF) molecules having lifetimes in the range of microseconds.

Moerner and Kador, in 1989, reported absorption spectroscopy of single molecules at liquid He temperatures for the first time [2]. Orrit and Bernard, in the following year, detected fluorescence from individual pentacene molecules [3]. These measurements led to new insights in the field of single-molecule dynamics, which were previously unobservable [3]. Single-molecule spectroscopies have evolved to include varieties of novel fluorescence methods [4–10] and force spectroscopies [11]. The ability to monitor only one molecule at a time has revealed the presence of sub-populations in a bimolecular system that was previously masked in the ensemble [12, 13].

5.2 Confocal Microscopy

Traditional fluorescence microscopy consists of the excitation of a small region of a sample. This small excitation region is usually defined by the numerical aperture (N.A.) of the objective lens. The light emitted from the molecules within the sample is generally collected using the same objective lens and then projected on a camera to acquire an image of the photoluminescent sample. The intensity of the fluorescence signal is generally weaker than that of the excitation; hence, optical filters are generally used to separate the excitation and emission. The contrast in the image is reduced significantly due to the unfocussed signal captured on the camera. Removing this unfocussed fluorescence

is crucial for identifying single emitters in a sample buried in this background intensity.
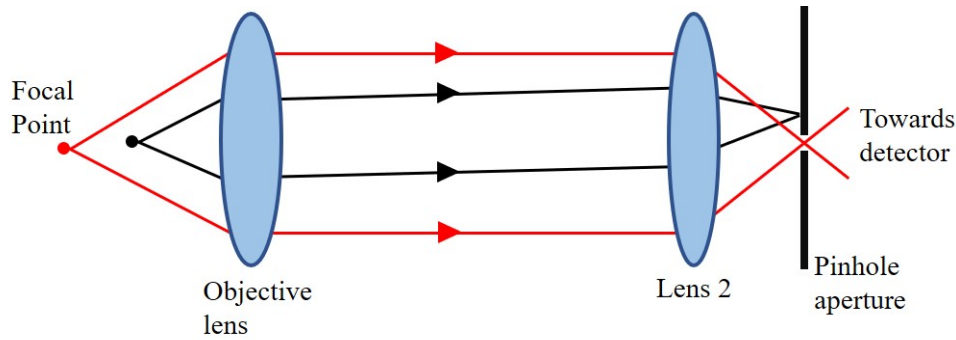
Figure 5.1: Conjugate focal points in a confocal assembly.

A confocal microscope can overcome this problem by minimizing the unwanted unfocussed fluorescent light intensity using a pinhole aperture. This light from a pinhole aperture is then made to incident on a detector. Figure 5.1 shows a simplified pinhole assembly to remove the out-of-focus light from a sample. The red rays represent light coming from the focal point of an objective lens, whereas the black rays represent the unfocussed light that gets captured by the objective. Placing the pinhole at the focal point allows the passage of only the red rays. The pinhole aperture will always block the black rays if they do not originate from the objective focal point. The term "confocal" hence originates from this optical design which involves taking light from the focal point of the objective lens and focussing it to the focal point of a second lens, creating a "conjugate foci" arrangement. The confocal arrangement in a fluorescence microscope gives them excellent optical sectioning arrangements. The optical sectioning capabilities of a confocal microscope allow for high-contrast imaging on the inside of a scattering media, which is an extremely useful tool used in biomedical imaging [14].

The size of the pinhole defines the strength of the optical sectioning capability of the microscope. However, the signal from the sample gets weaker with a decrease in the size of the pinhole. This requires increased excitation power, which will be detrimental to the sample. Further, a limit to contrast enhancement can be achieved by decreasing the size of the pinhole. Thus, a trade-off between the emission (or

scattered) intensity and the strength of the optical sectioning is needed to achieve the best possible contrast in the image.

The presence of a pinhole makes the image to be just a single point on the detector. Therefore, scanning the focussed beam across the region of interest requires a scanning system. The point scanning system is the most commonly used system for a confocal assembly. Generally, the excitation light is scanned in two dimensions over the entire region of interest. The sample's emission from each point is collected and then plotted as a function of that particular coordinate to generate a 2D fluorescence image of the sample. The easiest way to implement a scanning confocal microscopy is to use stage scanning, which allows the whole optical assembly to be stationary. Generally, stepper-motor-based scanners and piezo-stages are used for scanning the sample. However, the major disadvantage of stage scanning is that the scanning speed is too slow for real-time imaging, and it is also limited by mechanical artefacts such as vibrations. These artefacts need to be removed while processing the data obtained from stage scanning setups. The alternative to these scanners is galvo-systems, found in commercial microscopes, which greatly increases the cost of instrumentation.

Lasers are commonly used light sources in a confocal microscope. They are advantageous owing to their high optical power output, stability, and wavelength selectivity over the range, and they can be focused on a small spot on the sample. Generally, the laser sources used in a confocal laser scanning microscope need to have a single mode with Gaussian beam intensity and large Rayleigh lengths [15], i.e., the distance that the laser beam has to travel before it diverges significantly. The presence of higher-order modes in a laser beam would produce unwanted aberrations in the confocal microscope. Therefore, the beam must be shaped into a nearly symmetric Gaussian function before its introduction into the microscope. This is generally achieved via a spatial filter which is usually a pinhole aperture which cuts off the higher-order mode retaining only the Gaussian nature of the beam. For a perfect Gaussian beam, the theoretical lateral resolution (spot size)

of a confocal microscope after the beam gets focussed by the objective lens is given as

$$r_{xy} = \frac{1.22\lambda}{NA} \tag{5.1}$$

where NA is the numerical aperture of the objective and λ the wavelength of the excitation beam. The beam size significantly increases without (or improper) spatial filtering, decreasing the resolution of an image. The NA of an objective defines the resolution of a microscope. It is the solid angle over which the objective lens collects the light, i.e., $NA = nsin(\mu)$, with n being the refractive index and μ the half angle of the solid cone defined by the collected light. The NA also has a substantial effect on the collection efficiency of the objective. For example, NAs of 1.45, 1.3 and 0.95 correspond to collection efficiencies of 40%, 26% and 10%, respectively [16]. Thus, slight improvements in the NA of the objective lenses significantly increases the number of emitted photons that are collected. Single-molecule measurements are generally performed using objectives immersed in fluids such as water and oil, which give NA values greater than 1. Typically, water and oil immersion objectives provide a NA values of up to 1.2 and 1.45 respectively [16].

In a single molecule measurement, the choice of detector is another critical aspect. The detectors should have a high quantum efficiency, low dark noise, lower 'dead time' and good linearity of quantum efficiency over the spectral range of interest. These conditions are mainly fulfilled by photomultiplier tubes (PMT) and single photon avalanche diodes (SPAD). Practically, SPADs have a much higher quantum efficiency than PMTs, and hence they are most widely used in single-molecule measurements. Recent advances in electronics, electro-mechanics, optics, and lasers improved almost every aspect of single molecule detection in the last few decades.

5.2.1 Layout of the custom-built confocal microscope

The custom-built confocal laser scanning microscope is shown in Figure 5.2. The labelled schematic of the microscope is described in Figure 5.3. Light from the laser initially passes through a set of neutral density fil-
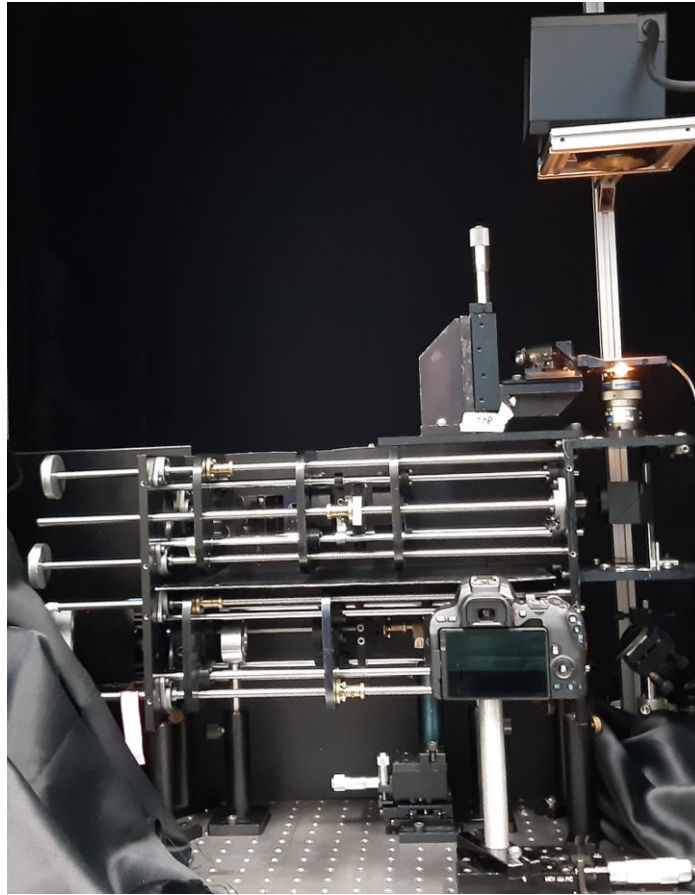
Figure 5.2: The custom-built confocal microscopy setup in the lab.

ters (NDF). The NDFs are used to control the excitation intensity of the laser. The laser is then passed through a short pass filter (SPF) which removes any other higher lasing wavelength to give a spectrally pure excitation wavelength. The laser beam is then guided by two mirrors M_1 and M_2, and coupled to a fiber coupler FC_1 (Thorlabs). A multimode fiber from FC_1 transmits the laser light to the excitation arm of the microscope via FC_2 (Thorlabs). FC_2 is used to collimate the output beam from the multimode fiber (Thorlabs). The use of fiber coupling assembly allows for easy switching of the excitation laser without disturbing the rest of the microscope assembly. Both continuous wave (CW) and pulsed lasers of various wavelengths can be coupled to the microscope depending on the sample to be measured. The excitation arm consists of the spatial filter assembly, and a lens/pinhole/lens system (L_1/P_1/L_2). The lenses L_1 and L_2 have focal lengths of 35 mm. The pinhole P_1 (Thorlabs) is placed precisely at the focus of L_1, which focuses the light to a diffraction-limited spot. The size of the pinhole P_1 was 50 μm and

was mounted on the $x - y$ translation stage for fine adjustments. If the pinhole is matched with the size of the diffraction-limited beam of the lens L_1, then the light propagating from the pinhole will have a near Gaussian intensity profile. The second lens L_2 collimates the diverging beam from the pinhole producing the near Gaussian intensity profile. The spatial filter assembly may also be used as a beam expander when the back aperture of the objective needs to be filled up to achieve a tight focus. Systems having the pinhole size matched with the spot size of lens L_1, the ratio of the focal lengths of the collimating (L_2) and focussing (L_1) lenses give the factor of expansion. However, in the setup described in Figure 5.3, the requirement for beam expansion is not there due to the small size of the objective back aperture. The spatially filtered light is reflected by a dichroic mirror mounted at 45° towards the back aperture of the objective. This creates an episcopic arrangement, and the beam is then focused onto the sample plane using an objective.
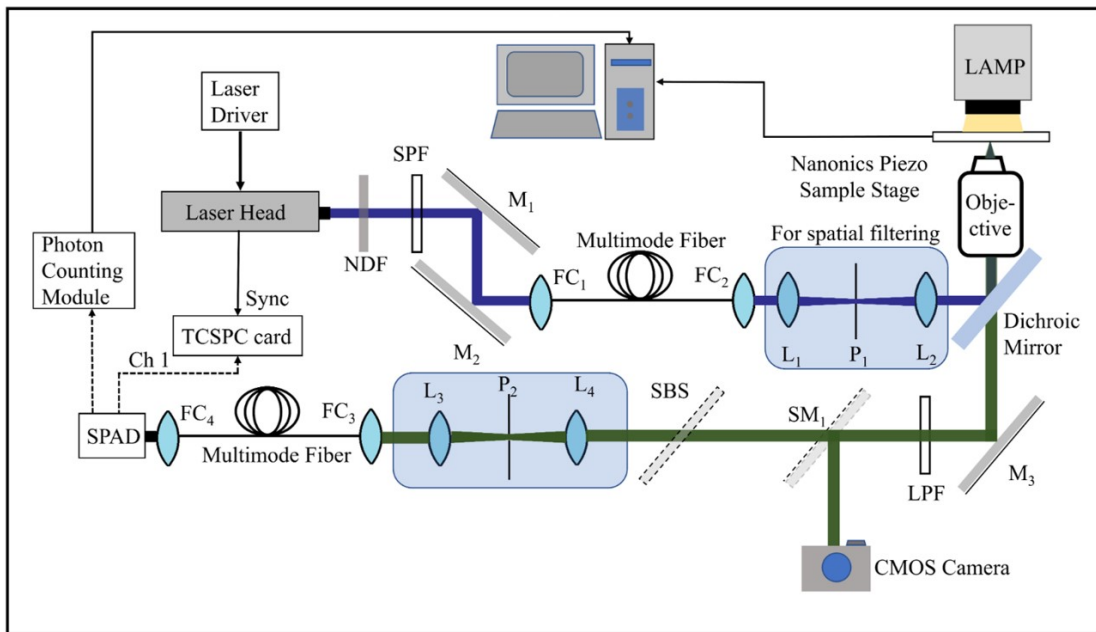
Figure 5.3: Schematic for the custom-made confocal microscope assembly.

The scanning capability in the microscope is provided by the sample stage (Nanonics FlatScan^{TM} Piezo scanning stage). The stage is placed on a kinematic z-axis stage used for routine focusing of the sample. The same objective captures the emitted light from the sample, and it passes through the dichroic mirror towards mirror M_3, which reflects the emitted beam towards the detection arm of the microscope. The dichroic

mirror also filters some part of the scattered unwanted laser excitation captured by the objective. The detection arm initially consists of a long pass filter (LPF from Thorlabs) which filters out the remaining excitation laser intensity from the beam. The filter is followed by a switching mirror (SM) which diverts the beam towards a CMOS camera. This camera is generally used for obtaining brightfield images of samples in the transmission geometry with a tungsten halogen lamp as a source kept on top of the sample stage. In the absence of a switching mirror, the light is directed towards a lens/pinhole/lens (L_3/P_2/L_4) assembly for attaining confocality. A motorized wheel consisting of pinholes of different sizes (25 μm to 2000 μm) was used in this assembly (Thorlabs MPH16-A). The pinhole size is usually chosen to balance the magnitude of emitted light intensities from the sample while achieving the best possible image contrast. The pinhole assembly output (FC_3) is connected to an Excelitas SPCM-AQRH-15-FC fiber coupled (FC_4) single photon avalanche diode (SPAD) via a multimode fibre. The photons from the sample generate TTL pulses as output from the SPAD, which is connected to a Nanonics Photon Counting module (PCM). The PCM converts the frequency of the pulses into a voltage signal which goes to the AUX 2 terminal of the Nanonics SPM Controller, which is also used for controlling the piezo stage. A computer with commercial Nanonics window software (NWS) simultaneously evaluates the scanner position and the amplitude of the PL signal coming from the PCM as voltage. NWS software processes pixel-to-pixel data and give the fluorescence image. The minimum step size of the piezo-scanner is 10 nm, and the maximum area that can be scanned on the sample is 10 μm $\times$ 10 μm.

5.2.2   Laser Beam Profile

Figure 5.4 shows the focussed beam profile (λ =405 nm) of the laser using a Nikon 100$\times$ (NA 0.8) objective. After reflection from a top surface mirror finished glass slide, the laser beam profile was captured using the CMOS camera. The intensity profile of the spot was derived from the image using open-access Image-J software. The distance for a particular pixel was calibrated using a calibration grid. Fitting a Gaussian function to the profile leads to a beam spot size of 760 nm. This spot size can be considered as the actual resolution that can be
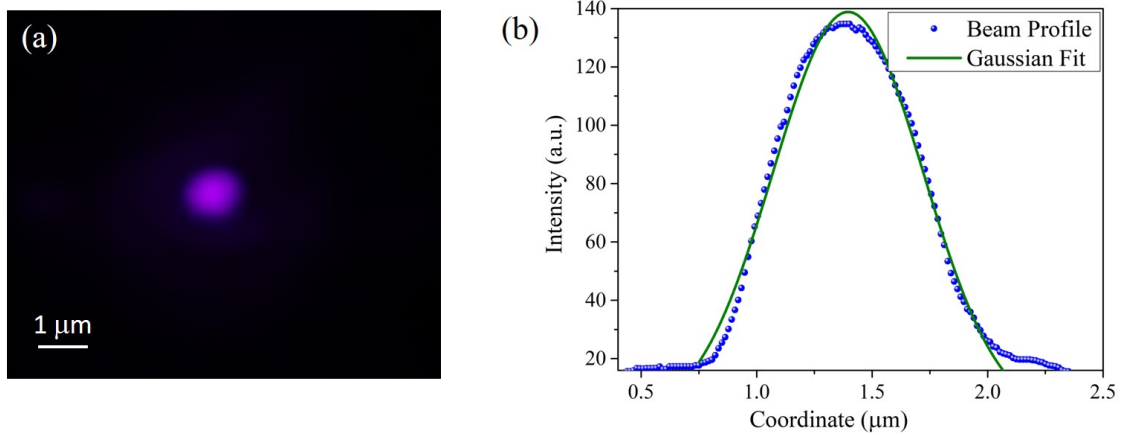
Figure 5.4: The back-scattered beam profile from glass, and b) line profile of the beam.

attained in this custom-built setup for 405 nm laser excitation for an objective lens having NA of 0.85.

5.2.3 Fluorescence Imaging
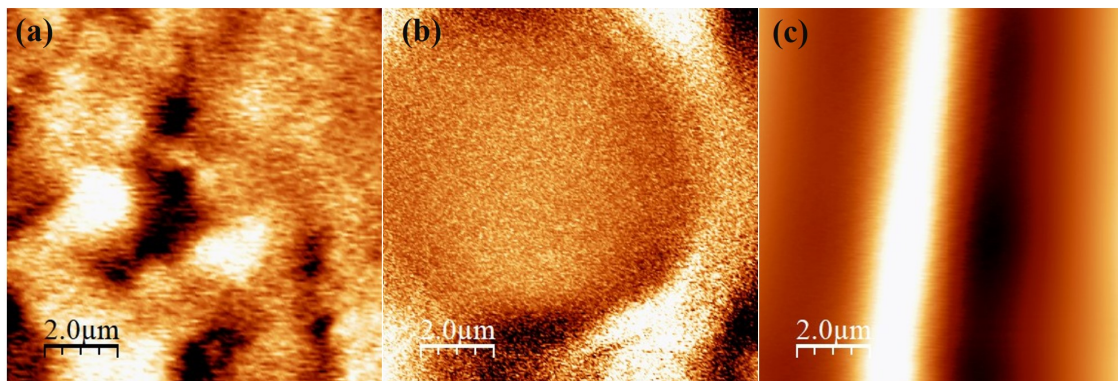
Figure 5.5: Photoluminescence Imaging of (a) NDIPhCz doped PMMA thin film, (b) PMMA ring doped with Red IX dye, (c) 4CzFCN dye-doped PMMA microfiber.

Figure 5.5 (a-c) shows the raw unprocessed images of three different samples. Figure 5.5a showcases the variation in the number of emitters in a film made from spin-coating a solution of Napthelene-Diimide phenyl carbazole (NDIPhCz). The molecule has a quantum yield of 10%, and the image was captured for a pinhole diameter of 300 μm, which gave enough contrast to visualize the non-uniformity in the film. Figure 5.5b shows the image of PMMA rings doped with Red IX dye,

and Figure 5.5c shows the image of dye-doped PMMA fiber. In both these images, the pinhole size was kept at 1000 μm. The confocal microscope showed good contrast in the images, which is at par with the fluorescence images from other microscopes.

Most organic molecules have a problem with stability in air. The degradation in these molecules can be minimized by dispersing them in a Poly (methyl-methacrylate) (PMMA) matrix with low oxygen permeability. Figure 5.6 shows the fluorescence image of Rhodamine-6G (R6G) molecules spin-coated from 2 ng/mL concentrations. The pinhole size was kept at 300 μm, and the wavelength of excitation was 532 nm. The measurements of photon statistics are usually done on the bright regions of the film.
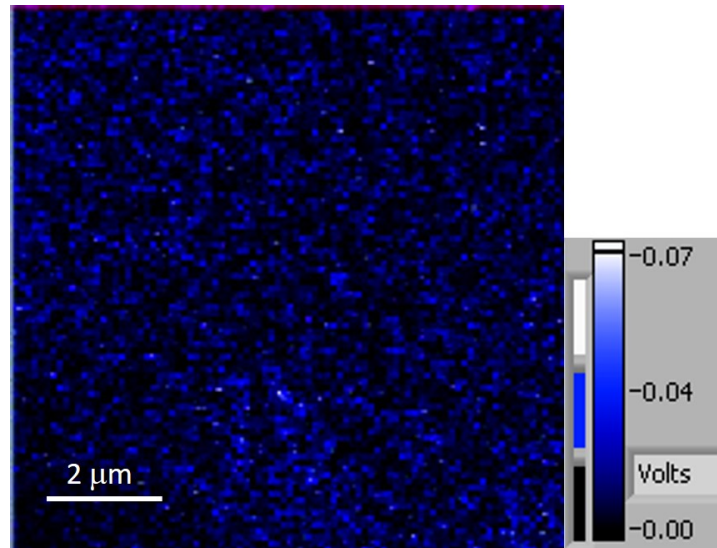
Figure 5.6: Fluorescence image of R6G molecules dispersed in a PMMA film fabricated from a concentration of 2ng/ml R6G.

5.3 Measurement of photon statistics

The overall intensity coming from a light source is defined as the average number of photons passing through a cross-section of the beam area for a unit interval of time. A constant-intensity light source will have fluctuations in the instantaneous number of photons passing through this cross-sectional area. These fluctuations define the photon statistics of the source. Under the classical theory, the light intensity at any

instant of time is [15, 17]

$$I(t) = <I> + \delta I(t) \tag{5.2}$$

where $<I>$ is the average intensity defined as

$$<I> = \int_0^T I(t)dt/I_0 \tag{5.3}$$

and $\delta I(t)$ is the fluctuation in the intensity at an instant of time. The average intensity of a continuous light source will satisfy the relation

$$<I(t)> = <I(t+\tau)> = <I> \tag{5.4}$$

The average value of fluctuation for a continuous light source is zero,
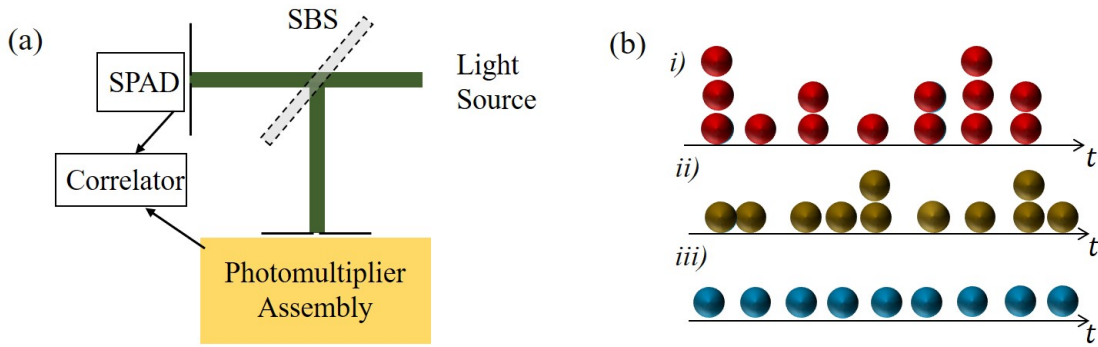
Figure 5.7: (a) Schematic of a Hanbury Brown Twiss interferometer, (b) A simple comparison of (i) Super Poissonian (bunched) source, (ii) Poissonian (coherent) source, and (iii) Sub-Poissonian (anti-bunched) source.

i.e.,

$$<\delta I(t)> = <\delta I(t+\tau)> = 0 \tag{5.5}$$

The photon statistics of the light source is usually characterized using an autocorrelation function $g(\tau)$ defined as

$$g(\tau) = \frac{<I(t)I(t+\tau)>}{<I(t)><I(t+\tau)>} \tag{5.6}$$

where τ is the time lag. In the limit $\tau = 0$, $I(t) = I(t+\tau)$, hence $<I(t)I(t+\tau)>_{\tau=0} = <I^2> = <I>^2 + (\Delta I)^2$ (where variance $(\Delta I)^2 = <I^2> - <I>^2$). However, for the limit $\tau \to \infty$, $I(t)$ is completely uncorrelated with $I(t+\tau)$ and therefore $<I(t)I(t+\tau)>_{\tau\to\infty} = <$

$I(t) >< I(t + \tau) >=< I >^2$. Thus, Eq. 5.6 becomes [17]

$$g(\tau) = \frac{< I(t)I(t + \tau) >}{< I >^2} \begin{cases} 1 + \frac{(\Delta I)^2}{<I>^2}, \tau = 0 \\ 1, \tau \to \infty \end{cases} \qquad (5.7)$$

The photon statistics of various light sources is measured using a Hanbury Brown Twiss (HBT) interferometer integrated with the confocal microscope. The interferometer consists of a beam-splitter (SBS) which splits the incoming beam and diverts them towards single photon counters (SPAD and a photon-multiplier assembly), as shown in Figure 5.7a. The output of the two detectors was sent to a TimeHarp 260 Nano TCSPC card which generates $g(\tau)$ function determining the photon statistics of the source.

The light sources are broadly divided into three types depending on the photon statistics: Super Poissonian light, Poissonian light and sub-Poissonian light [17]. Coherent light sources (lasers) follow Poissonian statistics given as

$$P(n) = \frac{< n >^n}{n!} exp- < n > \qquad (5.8)$$

The most important signature of a Poissonian light is that its correlation
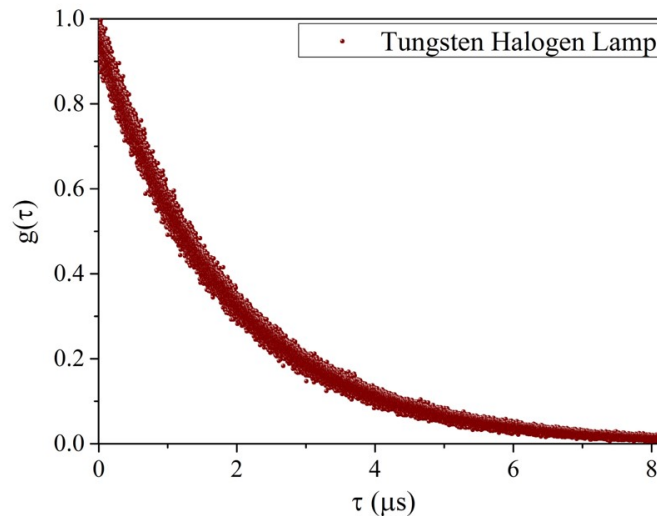
Figure 5.8: Photon bunching feature in a thermal source (tungsten halogen lamp).

function, $g(0) = 1$. Thermal sources typically show Super-Poissonian or bunched photon statistics ($g(0) > 1$). Non-classical light sources such as isolated single molecules follow sub-Poissonian or anti-bunched photon statistics ($g(0) < 1$). This condition is purely a quantum mechanical process and cannot be explained using classical theory. The differences in the three different types of light sources are illustrated in Figure 5.7b when the intensities are highly attenuated. Figure 5.8 shows the bunched photon statistics coming from a tungsten-halogen lamp at low light intensities using the HBT interferometer.

5.4 Photon correlation spectroscopy of TADF molecules
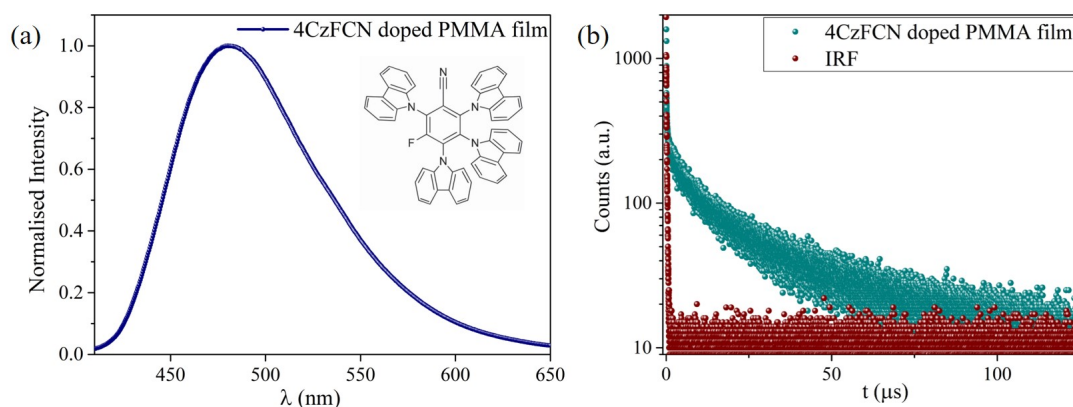
Figure 5.9: (a) Emission spectra and (b) PL Decay profile of 4.5wt% 4CzFCN doped PMMA thin film.

The TADF molecule used in this study is 2,3,4,6-Tetra(9H-carbazol-9-yl)-5-fluorobenzonitrile (4CzFCN). PMMA was used as the host to passivate the triplets generated via an intersystem crossing. A typical steady-state PL spectrum and the decay profile of 4.5 wt% doped 4CzFCN molecule dispersed in the PMMA matrix are shown in Figure 5.9. The steady-state PL spectra were captured under 365 nm excitation with a Hamamatsu C10083CA fibre-coupled spectrometer. The decay profiles of the film were captured using the custom-made TRPL measurement setup in the lab, and the average lifetime was found to be $\sim$14 μs. The photon correlation spectroscopy (PCS) measurements were
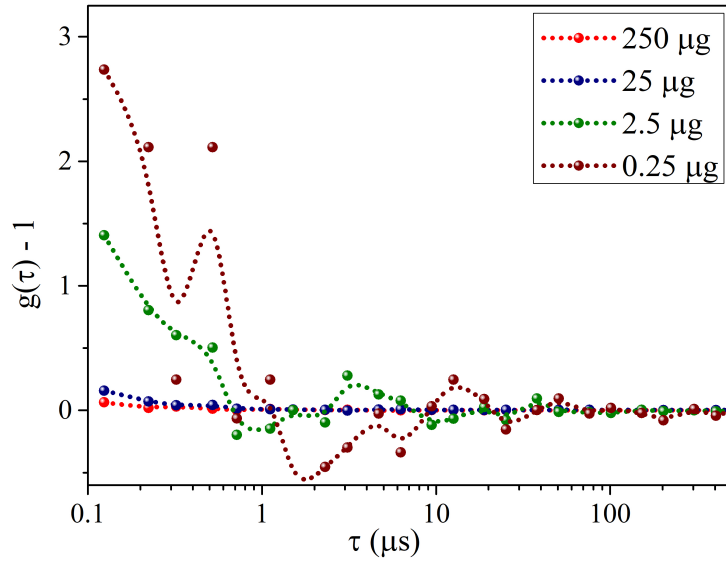
Figure 5.10: Autocorrelation function of the photon statistics for 4CzFCN molecules at different concentrations.

performed at different degrees of dilutions of 4CzFCN molecules. The 4CzFCN molecules were added to 15 mg/ml PMMA concentration in toluene. The final concentrations of the 4CzFCN molecules varied from 250 μg/ml to 0.25 μg/ml. The solutions were spin-coated on pre-cleaned coverslips at 2000 rpm. Films of pure PMMA were also fabricated by spin-coating as a control sample. The samples were excited with a 405 nm CW laser from Thorlabs. A Nikon 63$\times$ water immersion objective (NA 1.2) was used to excite the sample and collect the emission. The pinhole size in all the PCS measurements was maintained at 300 μm. The photomultiplier assembly (PMA) used for the characterization of the photon statistics of the tungsten-halogen lamp had a dark count of 10^3 counts per second (cps) with an external quantum efficiency of $\sim$10%. These limitations make the PMA unsuitable for measuring photon statistics of 4CzFCN molecules at dilute concentrations. These issues necessitated a change in the light detector assembly. The photon statistics were then exclusively measured by the SPAD, which has a much higher quantum efficiency (30% for 470 nm) and a much lower dark count ($\sim$50 cps). Further, the lifetime of the 4CzFCN molecule is in the order of microseconds which is orders of magnitude higher than the dead time of the SPAD. Thus, only one detector is sufficient

for studying the photon statistics of 4CzFCN molecules at dilute concentrations [18, 19].

Figure 5.10 shows the autocorrelation function plots for the spin-coated films at various concentrations. The $g(\tau)$ plots were derived from emission intensity trajectories acquired over 1 s. The autocorrelation function plots reveal photon bunching statistics, i.e., at $\tau = 0$, $g(0) > 0$. The bunching statistics originate from the absence of single resolvable TADF emitters on the films. However, the amplitude of $g(\tau)$ increased with the decrease in the concentration of the 4CzFCN molecules. The magnitude of fluctuations in photon numbers (ΔI) for high concentration sample (250 μg/ml) is much smaller compared to the total signal $< I >$. In contrast, for the film spin-coated from 250 ng/ml concentration of 4CzFCN, the ΔI is comparable to $< I >$. Thus from Eq. 5.7, the magnitude of $g(\tau)$ is higher at low concentrations, in other words, $g(\tau)$ is inversely proportional to the number of emitters present in the sample, i.e.,

$$g(\tau) \propto \frac{1}{N} \qquad (5.9)$$

where N is the number of emitters present in the focal volume.
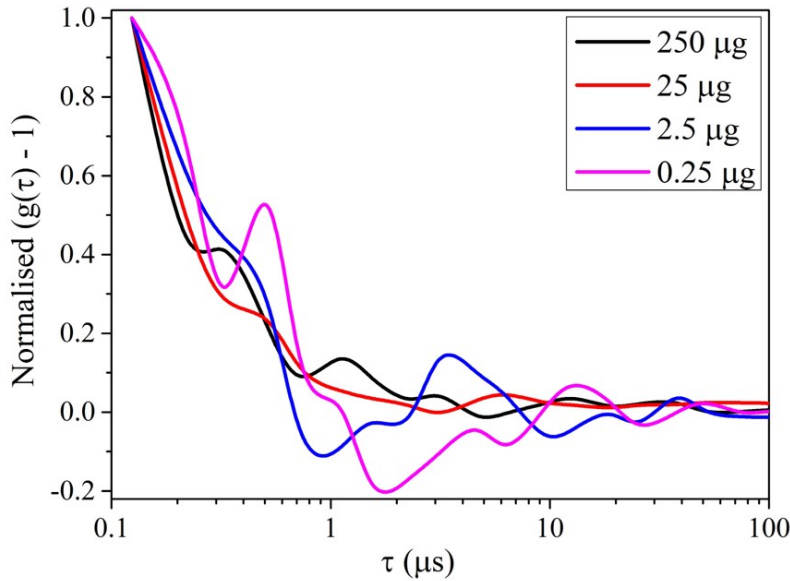
Figure 5.11: Normalized autocorrelation functions at different concentrations.
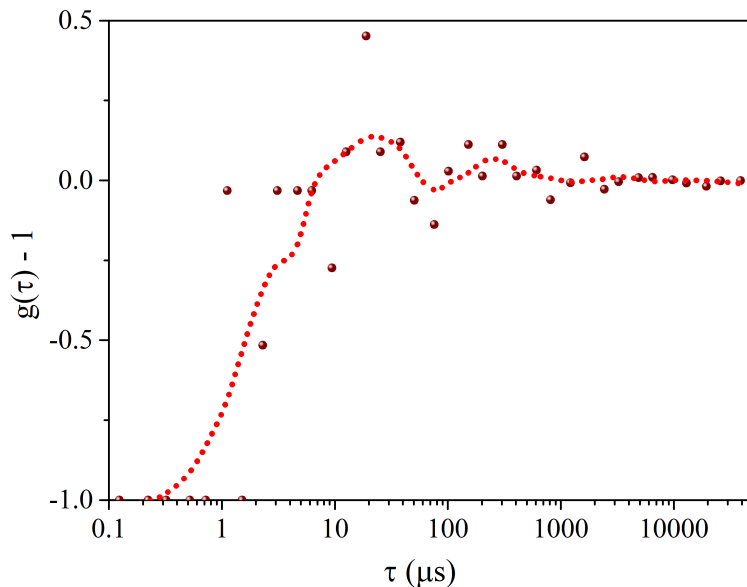
Figure 5.12: Autocorrelation feature resembling photon antibunching like statistics at some spots in the thin film made from 250 ng/ml concentration.

Figure 5.11 shows the normalized plots of the autocorrelation function for films spin-coated from various concentrations. The decay time constant associated with the $g(\tau)$ function do not show any significant change. This suggests that the intramolecular photophysical processes in 4CzFCN do not change appreciably for the concentrations under study. However, the decay associated with $g(\tau)$ is bi-exponential suggesting multi-step proceeses in the molecule [20]. The photo-physics of 4CzFCN molecules is described using a three-level scheme consisting of the ground singlet state (S_0), the first excited singlet state (S_1) and the triplet state (T_1). The T_1 state is populated by ISC and depopulated by RISC. The light emission in TADF systems arises from two types of fluorescence: prompt and delayed. This explains the origin of a bi-exponential decay of the $g(\tau)$ function in 4CzFCN molecules.

A dip in the $g(\tau)$ function for $\tau \rightarrow 0$ has been observed at some regions on the film spin-coated from the 250 ng/ml concentration. This feature is shown in Figure 5.12 and resembles photon antibunching which is associated with sub-Poissonian photon statistics [18, 19]. The photon-antibunching statistics signify emission intensity trajectories coming from a single 4CzFCN molecule.

5.5 Conclusions

In conclusion, a custom-built confocal microscopy assembly that can study photo-physics of molecules having lifetimes in the range of microseconds at dilute concentrations is demonstrated. The PCS measurements were performed on the 4CzFCN molecule, which is a TADF system with $\tau_D \sim 14\mu$s. The photon statistics reveal that the fluctuations follow photon bunching at various concentrations. An autocorrelation feature resembling photon antibunching is observed at sparse regions of the sample fabricated from 250 ng/ml. These measurements reveal that TADF molecules have a great potential to be used for applications requiring quantum emitters.

References

[1] L. Schermelleh, A. Ferrand, T. Huser, C. Eggeling, M. Sauer, O. Biehlmaier, and G. P. Drummen, "Super-resolution microscopy demystified," *Nature cell biology*, vol. 21, no. 1, pp. 72–84, 2019.

[2] W. E. Moerner and L. Kador, "Optical detection and spectroscopy of single molecules in a solid," *Physical review letters*, vol. 62, no. 21, p. 2535, 1989.

[3] M. Orrit and J. Bernard, "Single pentacene molecules detected by fluorescence excitation in a p-terphenyl crystal," *Physical review letters*, vol. 65, no. 21, p. 2716, 1990.

[4] T. Basché, S. Kummer, and C. Bräuchle, "Direct spectroscopic observation of quantum jumps of a single molecule," *Nature*, vol. 373, no. 6510, pp. 132–134, 1995.

[5] W. Moerner and D. P. Fromm, "Methods of single-molecule fluorescence spectroscopy and microscopy," *Review of Scientific instruments*, vol. 74, no. 8, pp. 3597–3619, 2003.

[6] G. Patterson, M. Davidson, S. Manley, and J. Lippincott-Schwartz, "Superresolution imaging using single-molecule localization," *Annual review of physical chemistry*, vol. 61, p. 345, 2010.

[7] R. Roy, S. Hohng, and T. Ha, "A practical guide to single-molecule fret," *Nature methods*, vol. 5, no. 6, pp. 507–516, 2008.

[8] C. Eggeling, J. Fries, L. Brand, R. Günther, and C. Seidel, "Monitoring conformational dynamics of a single molecule by selective fluorescence spectroscopy," *Proceedings of the National Academy of Sciences*, vol. 95, no. 4, pp. 1556–1561, 1998.

[9] T. Ha, T. Enderle, D. Chemla, P. Selvin, and S. Weiss, "Single molecule dynamics studied by polarization modulation," *Physical Review Letters*, vol. 77, no. 19, p. 3979, 1996.

[10] S. Weiss, "Fluorescence spectroscopy of single biomolecules," *Science*, vol. 283, no. 5408, pp. 1676–1683, 1999.

[11] K. C. Neuman and A. Nagy, "Single-molecule force spectroscopy: optical tweezers, magnetic tweezers and atomic force microscopy," *Nature methods*, vol. 5, no. 6, pp. 491–505, 2008.

[12] D. Rueda, G. Bokinsky, M. M. Rhodes, M. J. Rust, X. Zhuang, and N. G. Walter, "Single-molecule enzymology of rna: essential functional groups impact catalysis from a distance," *Proceedings of the National Academy of Sciences*, vol. 101, no. 27, pp. 10066–10071, 2004.

[13] T. E. Tomov, R. Tsukanov, R. Masoud, M. Liber, N. Plavner, and E. Nir, "Disentangling subpopulations in single-molecule fret and alex experiments with photon distribution analysis," *Biophysical journal*, vol. 102, no. 5, pp. 1163–1173, 2012.

[14] W. Amos and J. White, "How the confocal laser scanning microscope entered biological research," *Biology of the Cell*, vol. 95, no. 6, pp. 335–342, 2003.

[15] B. E. Saleh and M. C. Teich, *Fundamentals of photonics*. john Wiley & sons, 2019.

[16] C. Gell, D. Brockwell, and A. Smith, *Handbook of single molecule fluorescence spectroscopy*. Oxford University Press on Demand, 2006.

[17] L. Qi, *Non-classical multi-photon light from clusters of colloidal quantum dots*. Thesis, 2019.

[18] D. Hu and H. P. Lu, "Single-molecule triplet-state photon antibunching at room temperature," *The Journal of Physical Chemistry B*, vol. 109, no. 20, pp. 9861–9864, 2005.

[19] M. Nothaft, S. Höhla, F. Jelezko, N. Frühauf, J. Pflaum, and J. Wrachtrup, "Electrically driven photon antibunching from a single molecule at room temperature," *Nature communications*, vol. 3, no. 1, pp. 1–6, 2012.

[20] J. Yu, R. Lammi, A. J. Gesquiere, and P. F. Barbara, "Singlet-triplet and triplet- triplet interactions in conjugated polymer single molecules," *The Journal of Physical Chemistry B*, vol. 109, no. 20, pp. 10025–10034, 2005.

6

Electrospun Fibers Doped with Emissive TADF Molecules

6.1 Introduction

The field of nanomaterials provides unique structural and chemico-physical properties with applications in various fields [1–4]. The growth of integrated optics has paved the way for the development of various types of materials and devices for microscale and nanoscale photonics [5–8]. Nanostructures composed of organic semiconductors have attracted much interest in recent years due to their potential applications in mesoscale photonics and electronics [9]. Optical micro/nanofibers are low-dimensional structures used to investigate light emission, transmission, detection, and modulation in photonic circuits [10]. The cross-section of these fibers can be tuned from nano-meters to micro-meters (comparable to the visible light wavelengths), with their lengths running to hundreds of millimetres. Mesoscale fibers made of glass have always been used for signal transmission through their mechanical properties are not always compatible with other materials [10–12].

Polymer optical mesoscale fibers are usually fabricated from polymers and doped with other additives to give them various functionalities. They have many useful features compared to glass or inorganic semiconductor-based mesoscale fibers. Firstly, the chemical properties of polymer fibers can be easily modified by simple surface treatments depending on the applications for which it is being used for [13]. Secondly, these fibers can be easily functionalised with dyes (organic,

inorganic, HOIP quantum dots, rare-earth luminescent materials, etc), metal nanostructures, enzymes and even liquid materials and biological samples [14–18]. All these materials can be easily incorporated into the polymer fibers at high doping concentrations. This tunes the characteristics of the fibers making it suitable for various applications involving light emission and other optical functions [14, 19, 20]. Lastly, these fibers are flexible, i.e., the "soft" characteristics greatly simplify the processing technologies. These properties make the production of electrospun fibers at a large scale to be extremely cost-effective [21, 22].

Electrospinning is one of the most commonly used methods for fabricating mesoscale fibers whose diameters range from nm to μm [14, 15, 23]. The fibers are fabricated via extrusion from polymer melts or solutions using high electric fields. This versatile technique allows for fabricating various shapes, sizes and geometry of fibers by tuning the parameters such as solution concentration, electric field, etc. Continuous non-stop production of fibers can be achieved using electrospinning making it one of the most cost-effective processes at the industrial scale [24]. There have been no reports of TADF molecules dispersed in electrospun fiber previously. The confinement and anisotropic distribution of these molecules within this uniaxial matrix can introduce subtle functionalities in the emission. The photoluminescent quantum yield (PLQY) of TADF dyes are quite high making them suitable for lasing and other cavity-based applications.

In this chapter, the fabrication of electrospun fibers doped with a cyan-emitting TADF dye is achieved. The decay kinetics of the emission of these molecules, confined to mirrorless electrospun structures, has been probed at the microscopic level. It is observed that the fibers retain the photoluminescent properties of the dye and exhibit high luminescence. This polymer fiber-based waveguide fabricated is essentially a fluorescence waveguide, i.e., it propagates the dye emission across a relatively large length of the fiber. The modes supported by this dye-doped fiber have also been calculated using the finite difference frequency-domain method. The results demonstrate the potential application of these fiber structures as efficient downconverters in
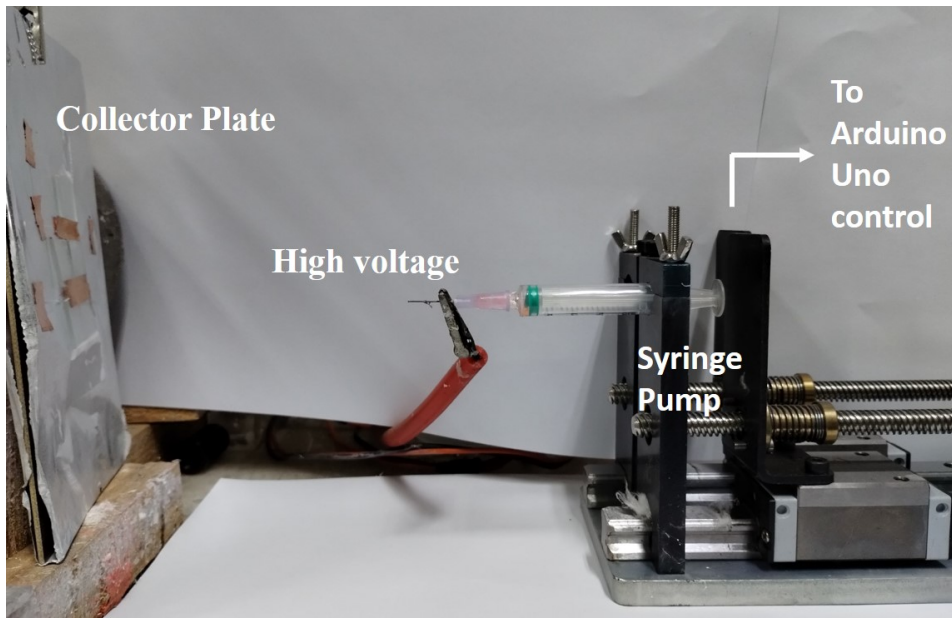
Figure 6.1: Schematic of the custom-built electrospinning setup.

lighting and display devices.

6.2 Electrospinning of TADF doped electrospun fibers

A typical electrospinning setup usually consists of a syringe pump, a high-voltage supply and a metal collection plate [23]. The syringe pump contains the polymer solution. Initially, the syringe pump is slowly dispensed leading to the formation of a polymer solution droplet on the needle (spinneret). The needle is generally kept at a high positive potential with respect to the collector. This application of an electric field creates charges on the droplet surface. The attractive force between the spinneret and the collection plate makes the droplet to be drawn into a cone-like structure referred to as the Taylor cone [25]. Beyond a critical applied field, the repulsive electric force on the droplet overcomes the surface tension force. Thus, a charged jet of the polymer solution gets pulled towards the collector plate. The solvent evaporates along the jet pathway allowing solid fibers to be formed and collected. Increasing the conductance of the electrospun solution (or increasing the field strength), stretching strength increases thereby decreasing the fiber diameter [26–28] and simultaneously the surface roughness [29].
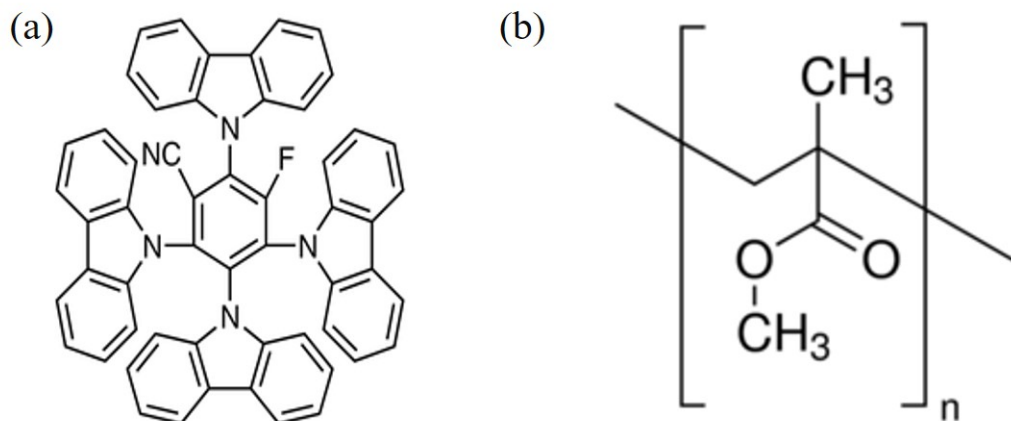
Figure 6.2: (a) Molecular structure of 4CzFCN dopant, (b) Molecular structure of PMMA.

The fiber diameter, as a result, is shaped by factors from viscoelasticity, dynamics of the solvent, and electrostatic force to air drag [15].

The TADF-doped polymer fibers were electrospun using a custom-built setup (Figure 6.1). The pump dispensing the solution out of the syringe was mounted on a linear guideway. The speed of the guide, which effectively controls the flow rate, was controlled via a stepper motor driven using a combination of stepper motor driver and Arduino Uno. The high voltage supply in the setup consisted of a push-pull amplifier coupled with a Cockroft-Walton generator supplied by Zeonics Systech, Bengaluru. A metal plate was used as the collector plate. The TADF molecule used in this study is 2,3,4,6-Tetra(9H-carbazol-9-yl)-5-fluorobenzonitrile (4CzFCN), which has emission in the range of 430nm to 600 nm. The polymer used was PMMA which acts as an excellent encapsulant for 4CzFCN. PMMA also has a refractive index of 1.49, which is very close to that of glass, making it an excellent substitute for glass-based waveguides. The molecular structures for 4CzFCN and PMMA are shown in Figure 6.2.

The fibers were electrospun from a single uniformly mixed solution of PMMA and 4CzFCN dissolved in dimethylformamide (DMF). The concentration of PMMA was 300 mg/ml. 4CzFCN dye dissolved in DMF was added to the PMMA solution in concentrations ranging from 0.2wt% to 10 wt %. The voltage between the needle and the collector
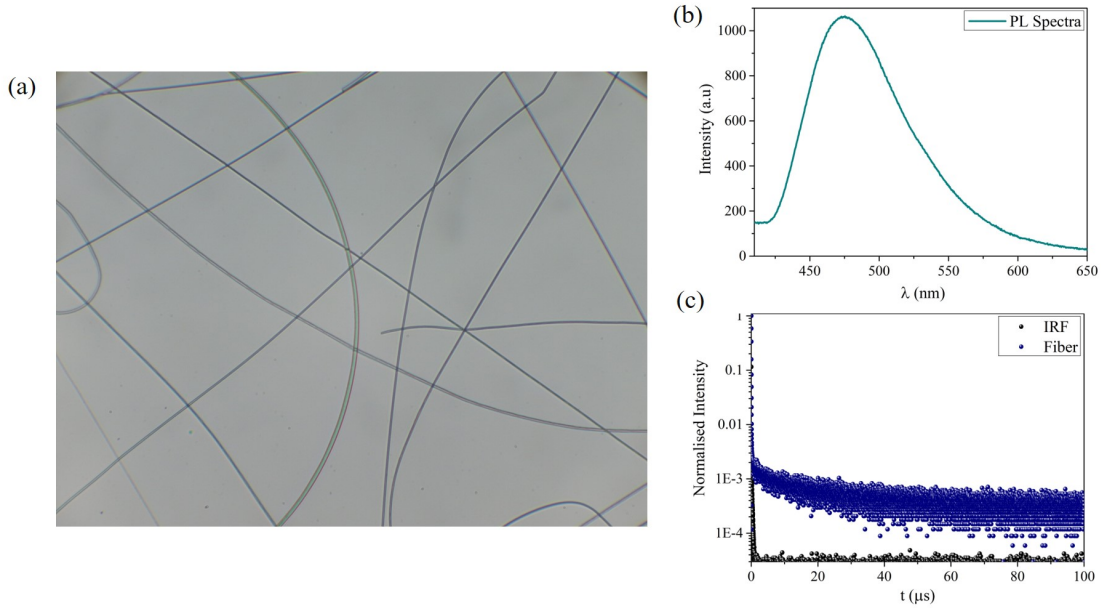
Figure 6.3: (a) Optical image of the electrospun 4CzFCN doped nanofibers, (b) PL spectra of the fiber mesh under 365 nm LED excitation and (c) PL decay profile of the fiber mesh under 405 nm pulsed excitation.

plate was kept at 10 kV and the distance between them was kept at 10 cm.

6.3 4CzFCN doped PMMA fibers

An optical brightfield image of a section of the mesh of the electrospun fibers is shown in Figure 6.3a. The electrospun fiber mesh was white in appearance owing to the absorption of the 4CzFCN and the PMMA dye both lying in the ultraviolet range. A bright cyan luminance from the fiber mesh was seen on excitation with a 365 nm UV lamp (Hamamatsu). The PL spectra of the mesh had been captured using a Hamamatsu C10083CA fiber-coupled CCD spectrometer, shown in Figure 6.3b. The photoluminescent emission of the fiber was higher than that of a film of the same concentration ($PLQY_{film} \sim 55\%$). However, the $PLQY_{fiber}$ could not be measured accurately due to non-uniformity in the fiber distribution. The decay profiles of the fiber mesh (Figure 6.3c) were captured using the custom-made TRPL measurement setup in the lab. The average lifetime of the fibers has been derived to be $\sim$11 μs by fitting a bi-exponential function to the
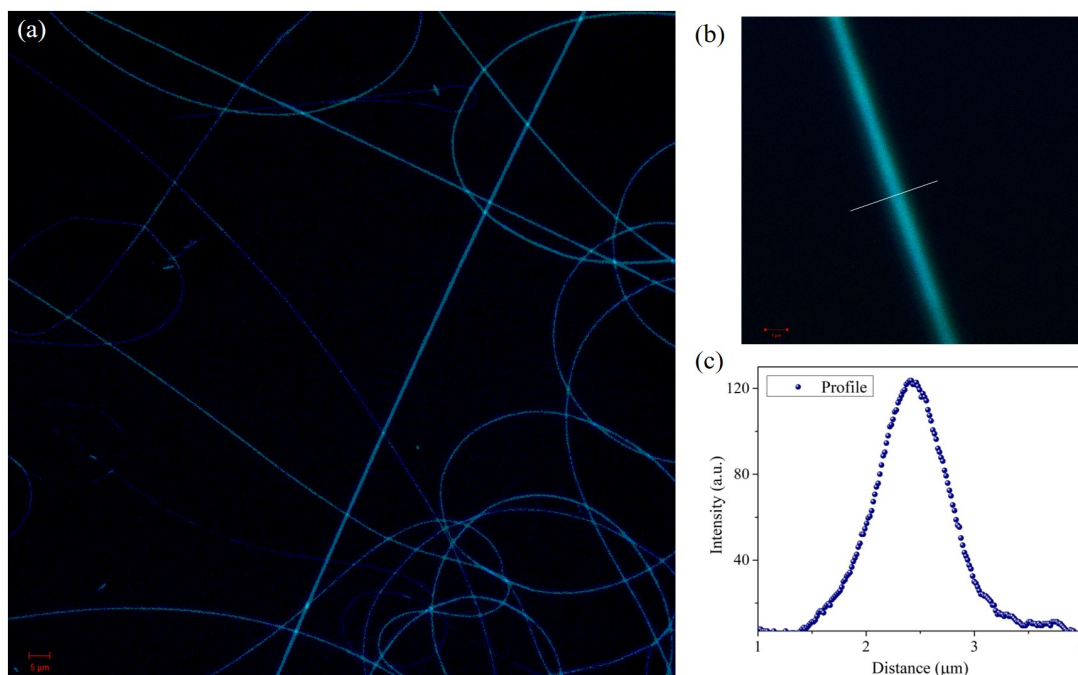
Figure 6.4: (a) Fluorescence laser scanning image of a section of the electrospun 4CzFCN doped PMMA fiber mat, (b) Magnified image of a single 4CzFCN dye-doped PMMA fiber, (c) Line scan profile of fiber

decay profile. A fluorescence microscopy image of the 4CzFCN doped PMMA fiber mesh was obtained using a Zeiss LSM 700 confocal laser scanning microscope (Figure 6.4a). The excitation wavelength used was 405 nm coupled to a Zeiss 40× objective (NA 0.4) for exciting the fiber and collecting the emission. A region was identified where the density of fibers was less and the area was imaged (Figure 6.4b) for determining the diameter of the fiber. A line profile across the width of the fiber was derived from the image (Figure 6.4c). The diameters were obtained by fitting a Gaussian function to the profile. The diameter for a fiber fabricated from 300 mg/mL PMMA concentration was found to be $\sim 1.2\ \mu$m.

The diameters of the fibers were controlled by the concentration of PMMA. A variation in the 4CzFCN doping concentration had a negligible effect on the diameter of the fiber. Fibers were electrospun from solutions of DMF with increasing concentrations of PMMA. All other control parameters of electrospinning, namely the applied potential difference, the piston motion rate and the distance between the needle and the collector plate, were kept constant. Figure 6.5(a-d) shows the fluorescence images of the fibers obtained from different
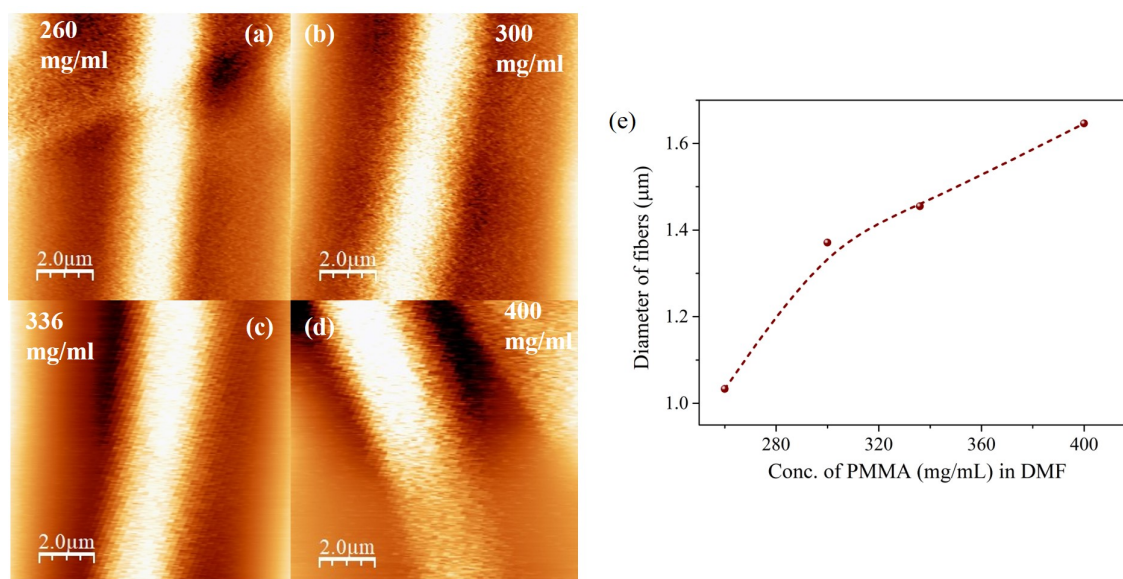
Figure 6.5: Fluorescence image of the 4CzFCN doped PMMA fiber for (a) 260 mg/ml, (b) 300 mg/ml, (c) 336 mg/ml, (d) 400 mg/ml and (e) Variation of diameter of the fibers with concentration of PMMA

concentrations, namely 260 mg/ml, 300 mg/ml, 340 mg/ml and 400 mg/ml. It was observed that the diameter of fibers increased with an increase in the concentration of the PMMA solution. Figure 6.5e showcases this increasing trend in the diameter of the fibers with the concentration of PMMA as obtained from the fluorescence images.
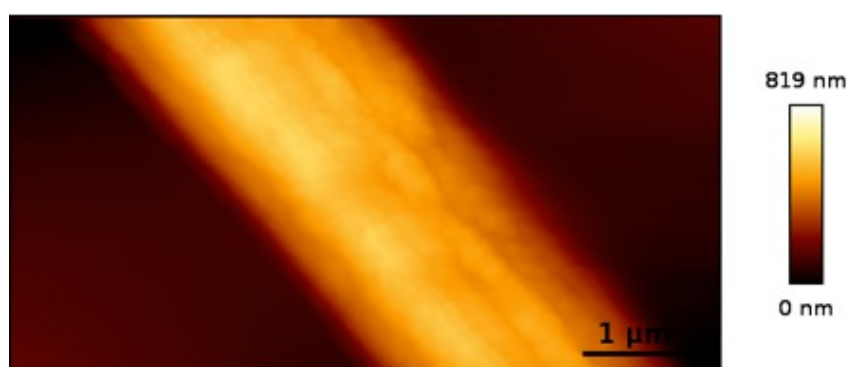
Figure 6.6: Surface morphology image of a single fiber in the atomic force microscope

Further, the fiber surface morphology was investigated using JPK Nanowizard Atomic Force Microscope (AFM). Figure 6.6 shows the surface morphology of a fiber. The image showcases a smooth morphology along the surface of the fiber. When subjected to ageing, the fibers showed no changes in surface morphology or diameter.

6.4 Micro-PL measurements on a single fiber
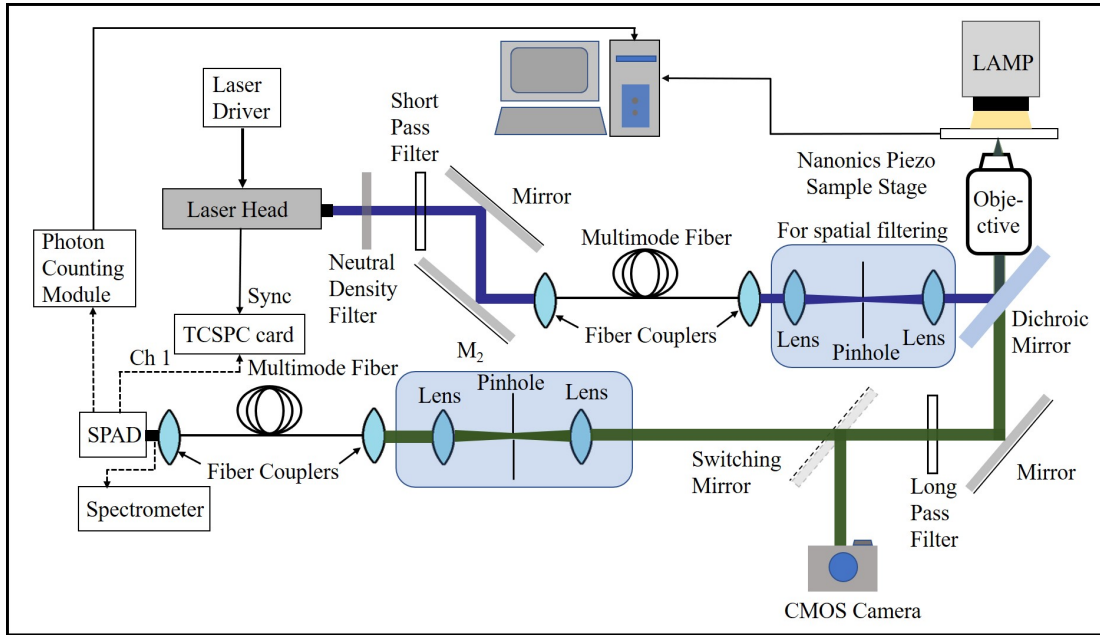
Figure 6.7: Schematic of the custom-built confocal microscopy setup for measuring μ-PL. The dashed lines signify switching connections.

The micro-photoluminescence (μ-PL) measurements were performed in a single isolated fiber to study the spatial uniformity of the photophysical properties. The measurements were done in the custom-built confocal microscope described in the previous chapter. The excitation laser used was Picoquant P-C-405M ($\lambda = 405$ nm). A Nikon 100x objective (0.8 NA) was used to excite the fiber and collect the emission. The pinhole size was kept at 300 μm. For recording the spectra at the microscopic level, the output of the pinhole assembly was connected to a Hamamatsu C10083CA CCD spectrometer. The PL decay profiles were recorded using the Excelitas SPCM-AQRH-15-FC SPAD coupled to TimeHarp 260 TCSPC board. The schematic of the measurement setup is shown in Figure 6.7.

An isolated fibers from the mesh were identified. The PL spectra and decay profiles were recorded at different points along the length of each of the isolated fiber. Figure 6.8a shows the fluorescence image of a fiber under measurement, along with the three regions where the spectra and decay profiles were recorded on the fiber. The normalised PL spectra and decay profiles are shown in Figure 6.8b and Figure
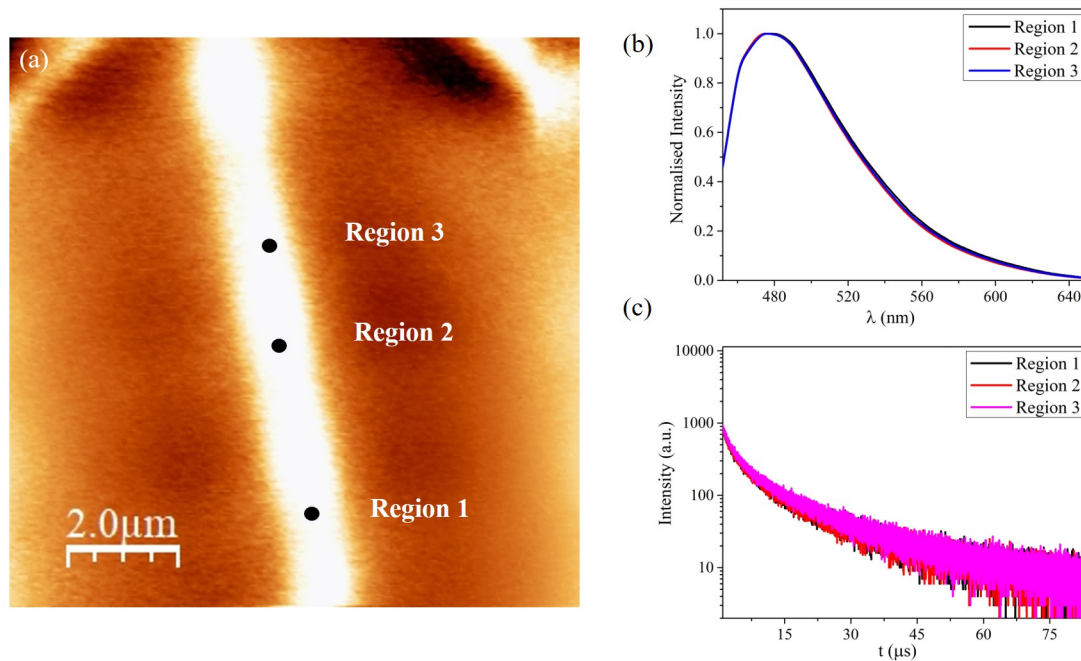
Figure 6.8: (a) Localised emission map of a single fiber, (b) Spectral profile at three regions, (c) PL decay profiles at these three regions.

6.8c. The spectra and decay profiles are identical at these three points. This concludes that the 4CzFCN molecules are equally distributed throughout the length of the fiber. The uniform emission along the fiber length points to the prospect of these fibers being used as emitters in display applications.

6.4.1 Concentration dependence of 4CzFCN

The effects of the aggregation of 4CzFCN molecules in the fiber were studied by changing the doping concentration. The doping concentration was varied from 2 wt% to 12 wt% of PMMA. The fibers were electrospun from a 300 mg/ml PMMA concentration. The fiber's diameter remained unchanged with the concentration of the 4CzFCN molecules increased. The PL spectra and the decay profiles of all these fibers were recorded at the microscopic level. The emission intensity from the fibers increased with the increase in doping concentration of the 4CzFCN dye. The peak position of the PL spectra redshifted, and the FWHM of the spectrum increased with increasing doping concentration (Figure 6.9a). The delayed fluorescence lifetime (τ_{DF}) was observed to decrease
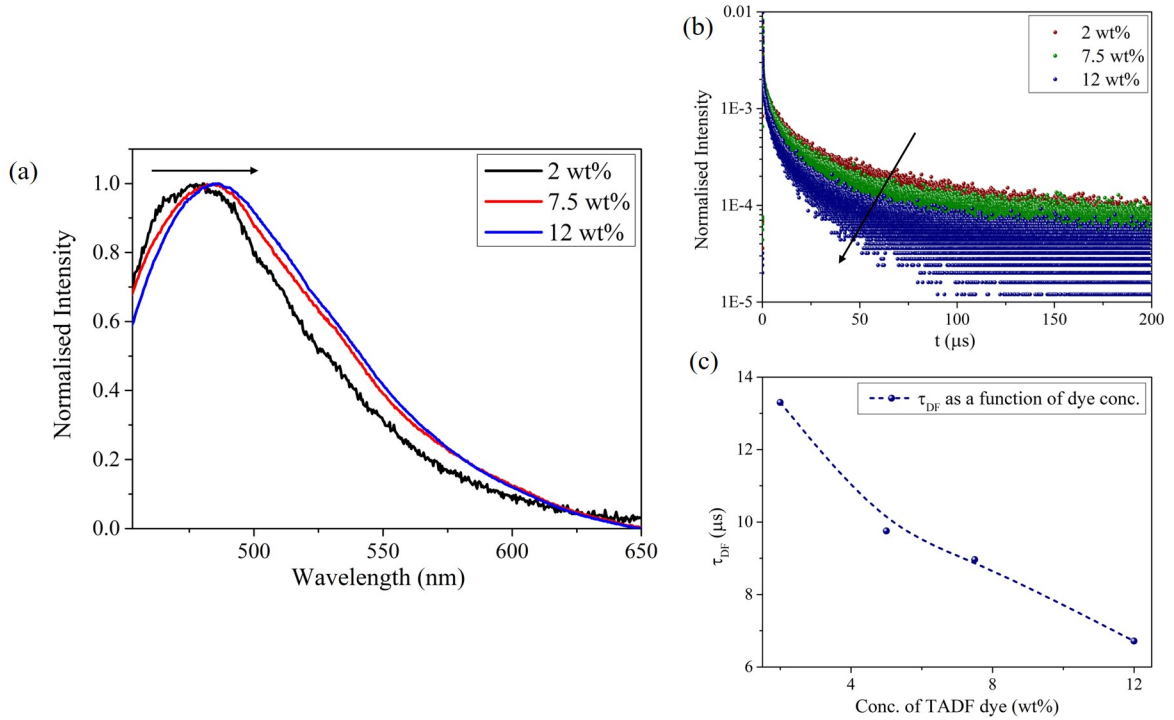
Figure 6.9: (a) Normalised μ-PL emission spectra, (b) Decay profiles at different doping concentrations and (c) Variation of τ_{DF} with concentration.

with the increase in concentration (Figure 6.9b and Figure 6.9c). All these results suggest increasing aggregation effects between the 4CzFCN molecules in the fiber geometry with increasing doping concentration.

6.4.2 Temperature Dependent μ-PL

The TADF character of the electrospun fibers was verified by temperature-dependent μ-PL measurements. The temperature-dependent measurements were performed using a Linkam LTS-420 temperature-controlled stage. The presence of the temperature-controlled stage requires the use of a long working distance objective. Hence, an Olympus $50\times$ objective (NA 0.55) was used to excite the fibers inside the Linkam assembly and collect the emission. Figure 1.10 shows the variation of emission intensity and PL decay profiles with temperature for a single fiber. A decrease in temperature causes a decrease in τ_{DF} owing to a reduction in the reverse intersystem crossing (RISC) of the triplet excitons. As a result, the PL intensity decreases as the temperature is reduced. The decrease in the overall emission of the fibers suggests that the ISC-generated triplets are non-emissive. A
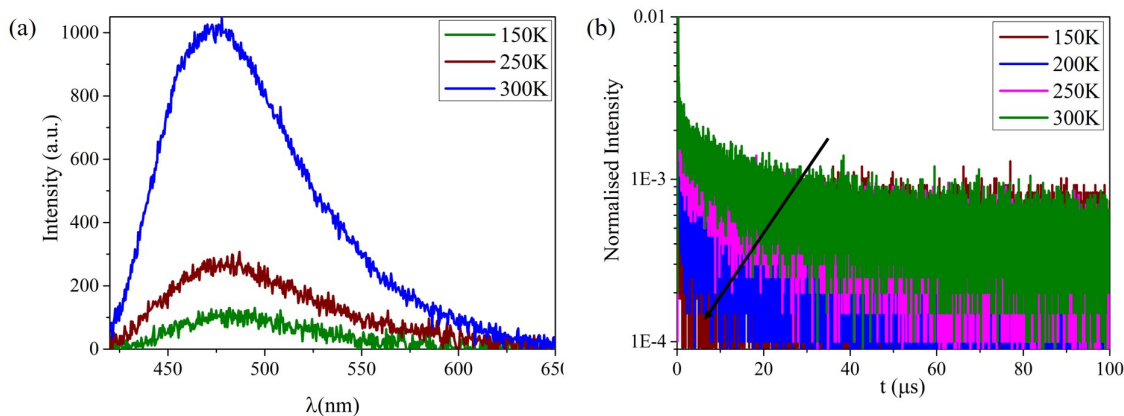
Figure 6.10: (a) μ-PL emission spectra (b) Decay profiles at different temperatures.

slight contraction in the fiber diameter should happen in the fiber due to the positive thermal expansion coefficient of the fiber. However, this will have a negligible effect on the temperature dependent photophysics.

6.4.3 Excitation Intensity dependent μ-PL
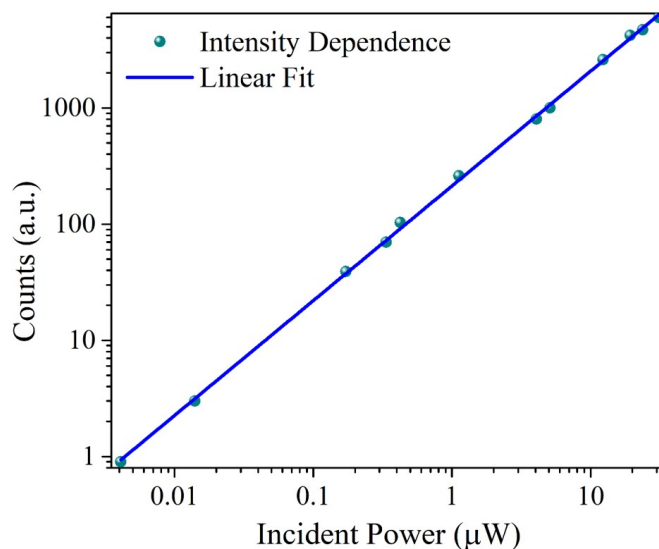
Figure 6.11: Excitation Intensity dependence of the μ-PL.

The 4CzFCN molecules being packed in a small fiber area might enhance the probability of bimolecular processes (such as triplet-triplet annihilation) contributing to the delayed fluorescence magnitude. An ex-

citation intensity-dependent μ-PL measurement was performed to verify whether any bimolecular processes contributed to the delayed fluorescence emission. Figure 6.11 shows the dependence of μ-PL intensity on the excitation intensity. The dependence was linear as expected, with a slope of 0.98, ascertaining the absence of bimolecular processes contributing to the delayed fluorescence emission.

6.5 Emission waveguiding in 4CzFCN-doped PMMA fibers
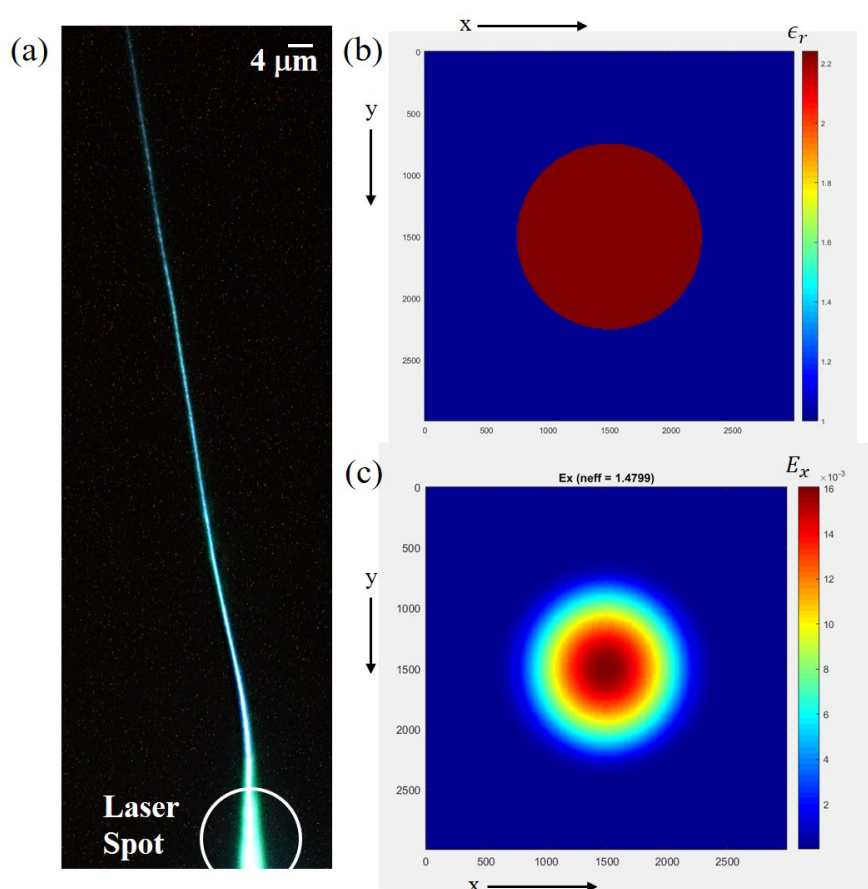
Figure 6.12: (a) Waveguiding of emission inside the 4CzFCN doped PMMA fiber (b) Dielectric constant (ϵ_r) profile of the cross section of the fiber (c) Electric field (E_x) profile of the supported primary mode of the fiber responsible for waveguiding.

The μ-PL measurements demonstrate the absence of any non-emissive regions along the length of the fiber. Thus, these fibers have the capability to show waveguiding with applications in display and localised illumination. The PMMA polymer has a refractive

index ($n = 1.49$) higher than the air. Thus, PMMA fibers act as a suitable waveguiding structure as they have negligible absorbance in the emission region of the 4CzFCN dye. The 4CzFCN dyes act as local emission centres present throughout the fiber. This makes the fiber systems extremely well-suited for studying waveguiding effects.

The waveguiding measurements were performed using the same custom-built microscope. An Olympus 10× objective was used to excite the laser spot at a lower point on a single isolated fiber. The emission from the 4CzFCN dye molecules propagates throughout the fiber and is captured using a CMOS camera. Figure 6.12a shows the captured image of waveguiding of the emitted light through the fiber length. The waveguided emission persists to length scales of $> 50\ \mu$m as illustrated in Figure 6.12a.

The modes supported by the PMMA fiber were simulated using a finite difference-based eigenmode solver. The cross-section of the fiber was used for simulating the modes. The simulation was performed by an in-house developed code in MATLAB using Finite Difference Frequency Domain (FDFD) method. The theory of the modelling procedure is given in Appendix B. The dielectric constant (ϵ_r) profile of the fiber cross-section used for simulation is shown in Figure 6.12b. The wavelength used for the simulation was 473 nm corresponding to the maxima of the emission. However, the mode profiles were seen to remain similar and uniform around the maxima of the emission. The fiber is seen to support multiple guided modes. The primary mode is responsible for waveguiding and the electric field (E_x) profile corresponding to it is shown in Figure 1.12c. The primary guided mode travelled along the length of the fiber with an effective refractive index of ~ 1.48.

6.6 Comparison of fiber photophysics with the bulk

A comparison between the emission of a fiber with a spin-coated film having the same doping concentration (5%), is shown in Figure 6.13. The emission spectra of the fiber are observed to be redshifted and τ_{DF}
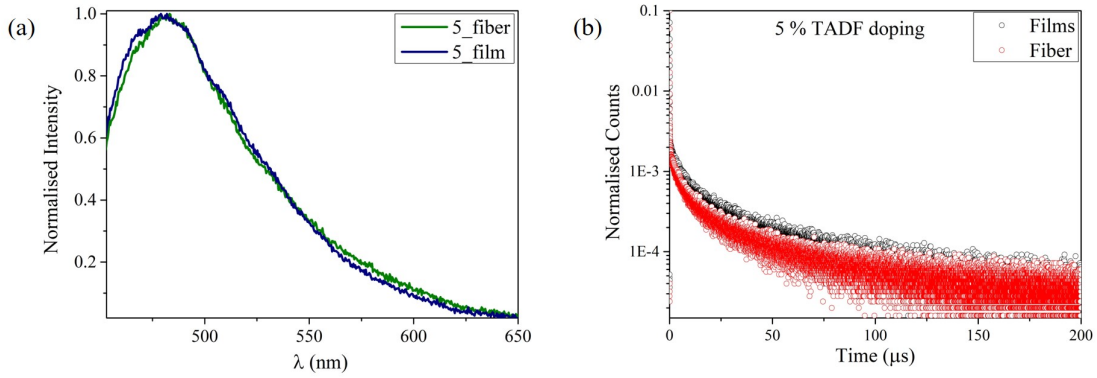
Figure 6.13: Comparison of μ-PL (a) emission spectra and (b) decay profiles for electrospun fibers and spin-coated films with 5% doping concentration.

reduced when compared to the film. These effects can be attributed to the large number of 4CzFCN molecules present at close proximity compared to the film fabricated by spin-coating. However, the FWHM of the fiber emission spectra reduced slightly compared to the film. The lower FWHM is attributed to the interference effects of the emitted light inside the fiber cavity. The higher-order eigenmodes derived from the FDFD simulation explain the modes responsible for narrowing the fiber emission spectra. The E_x profiles of these higher order modes are shown in Figure 6.14. The mode profiles have nodes at the fiber's centre, similar to modes seen in whispering gallery cavities [30, 31].

6.7 Conclusions

In conclusion, the process of electrospinning provides easy and cost-effective fabrication of polymer fibers with added functionalities. The 4CzFCN doped PMMA fibers exhibit high luminescence and stability. The diameter of the fibers is solely dependent on the PMMA concentration, with the fiber diameter increasing with concentration. The μ-PL measurement confirms the uniform distribution of 4CzFCN emitters throughout the length of the fiber. The temperature and intensity-dependent μ-PL measurements confirm the monomolecular TADF process as the sole triplet harvesting mechanism. Additionally, the fiber geometry allows for light confinement and waveguiding effects. FDFD eigenmode analysis of the fiber shows the primary guided mode respon-
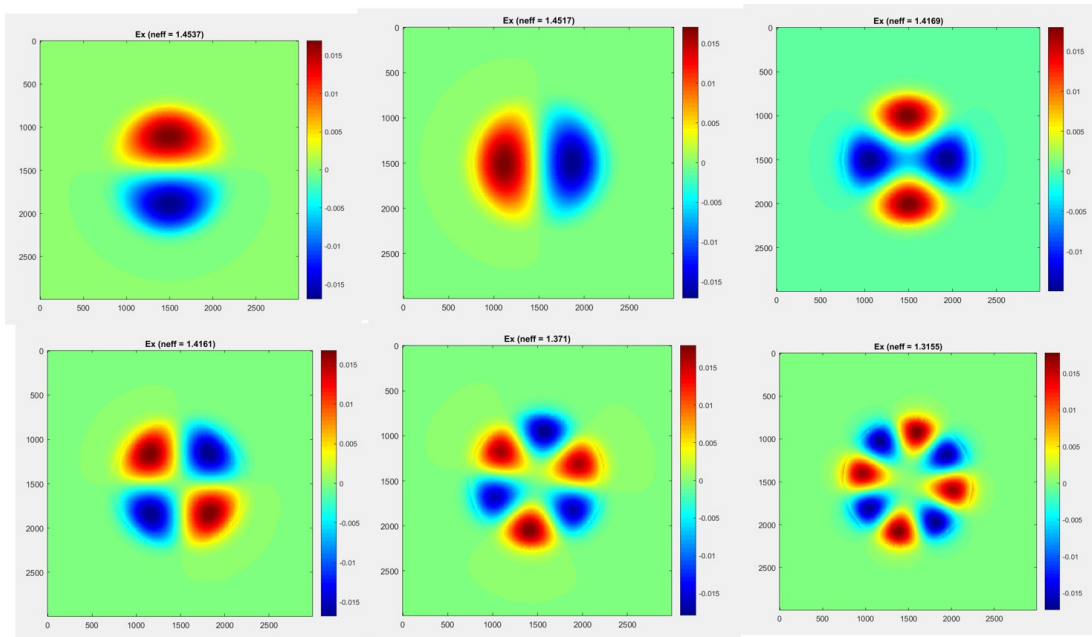
Figure 6.14: Electric field (E_x) profiles of the higher order modes supported by the fiber.

sible for waveguiding of the emitted light across the fiber length has an effective refractive index of ~ 1.49. The fiber shows a slight narrowing in the emission spectra compared to the film whose origin is attributed to the fiber cavity geometry. The eigenmode analysis shows the electric field profiles of these higher-order cavity modes have nodes at the centre of the fiber.

References

[1] G. A. O'Brien, A. J. Quinn, D. A. Tanner, and G. Redmond, "A single polymer nanowire photodetector," *Advanced Materials*, vol. 18, no. 18, pp. 2379–2383, 2006.

[2] E. H. Sargent, "Infrared quantum dots," *Advanced Materials*, vol. 17, no. 5, pp. 515–522, 2005.

[3] D. Wang, R. Kou, D. Choi, Z. Yang, Z. Nie, J. Li, L. V. Saraf, D. Hu, J. Zhang, G. L. Graff, *et al.*, "Ternary self-assembly of ordered metal oxide- graphene nanocomposites for electrochemical energy storage," *ACS nano*, vol. 4, no. 3, pp. 1587–1595, 2010.

[4] G. Zheng, F. Patolsky, Y. Cui, W. U. Wang, and C. M. Lieber, "Multiplexed electrical detection of cancer markers with nanowire sensor arrays," *Nature biotechnology*, vol. 23, no. 10, pp. 1294–1301, 2005.

[5] P. v. Tien, "Light waves in thin films and integrated optics," *Applied optics*, vol. 10, no. 11, pp. 2395–2413, 1971.

[6] C. J. Barrelet, A. B. Greytak, and C. M. Lieber, "Nanowire photonic circuit elements," *Nano Letters*, vol. 4, no. 10, pp. 1981–1985, 2004.

[7] A. W. Sanders, D. A. Routenberg, B. J. Wiley, Y. Xia, E. R. Dufresne, and M. A. Reed, "Observation of plasmon propagation, redirection, and fan-out in silver nanowires," *Nano letters*, vol. 6, no. 8, pp. 1822–1826, 2006.

[8] R. Yan, D. Gargas, and P. Yang, "Nanowire photonics," *Nature photonics*, vol. 3, no. 10, pp. 569–576, 2009.

[9] O. Ostroverkhova, *Handbook of organic materials for electronic and photonic devices*. Woodhead Publishing, 2018.

[10] H. Xia, T. Chen, C. Hu, and K. Xie, "Recent advances of the polymer micro/nanofiber fluorescence waveguide," *Polymers*, vol. 10, no. 10, p. 1086, 2018.

[11] G. Brambilla, F. Koizumi, X. Feng, and D. Richardson, "Compound-glass optical nanowires," *Electron. Lett*, vol. 41, no. 7, pp. 400–402, 2005.

[12] L. Tong, L. Hu, J. Zhang, J. Qiu, Q. Yang, J. Lou, Y. Shen, J. He, and Z. Ye, "Photonic nanowires directly drawn from bulk glasses," *Optics Express*, vol. 14, no. 1, pp. 82–87, 2006.

[13] J. Yoon, Y.-S. Jung, and J.-M. Kim, "A combinatorial approach for colorimetric differentiation of organic solvents based on conjugated polymer-embedded electrospun fibers," *Advanced Functional Materials*, vol. 19, no. 2, pp. 209–214, 2009.

[14] A. J. Das, C. Lafargue, M. Lebental, J. Zyss, and K. Narayan, "Three-dimensional microlasers based on polymer fibers fabricated by electrospinning," *Applied Physics Letters*, vol. 99, no. 26, p. 281, 2011.

[15] P. Kumar, N. Ganesh, and K. Narayan, "Electrospun fibers containing emissive hybrid perovskite quantum dots," *ACS applied materials & interfaces*, vol. 11, no. 27, pp. 24468–24477, 2019.

[16] H. Wang, Q. Liao, H. Fu, Y. Zeng, Z. Jiang, J. Ma, and J. Yao, "Ir (ppy) 3 phosphorescent microrods and nanowires: Promising micro-phosphors," *Journal of Materials Chemistry*, vol. 19, no. 1, pp. 89–96, 2009.

[17] J. M. Moran-Mirabal, J. D. Slinker, J. A. DeFranco, S. S. Verbridge, R. Ilic, S. Flores-Torres, H. Abruña, G. G. Malliaras, and H. G. Craighead, "Electrospun light-emitting nanofibers," *Nano letters*, vol. 7, no. 2, pp. 458–463, 2007.

[18] H. Liu, J. B. Edel, L. M. Bellan, and H. G. Craighead, "Electrospun polymer nanofibers as subwavelength optical waveguides incorporating quantum dots," *Small*, vol. 2, no. 4, pp. 495–499, 2006.

[19] X. Chen, K. Xie, T. Hu, X. Zhang, Y. Yang, J. Ma, J. Zhang, X. Cheng, and Z. Hu, "Whispering gallery mode microlaser based on a single polymer fiber fabricated by electrospinning," *Journal of Physics D: Applied Physics*, vol. 52, no. 47, p. 475104, 2019.

[20] J. E. Cheeney, S. T. Hsieh, N. V. Myung, and E. D. Haberer, "Whispering gallery mode emission from dye-doped polymer fiber cross-sections fabricated by near-field electrospinning," *Nanoscale*, vol. 12, no. 17, pp. 9873–9883, 2020.

[21] H. Ma, A. Jen, and L. R. Dalton, "Polymer-based optical waveguides: materials, processing, and devices," *Advanced materials*, vol. 14, no. 19, pp. 1339–1365, 2002.

[22] D. O'carroll, I. Lieberwirth, and G. Redmond, "Microcavity effects and optically pumped lasing in single conjugated polymer nanowires," *Nature nanotechnology*, vol. 2, no. 3, pp. 180–184, 2007.

[23] H. Karakaş, "Electrospinning of nanofibers and their applications," *Istanbul Technical University, Textile Technologies and Design Faculty*, 2015.

[24] A. Camposeo, L. Persano, and D. Pisignano, "Polymer nanofibers as novel light-emitting sources and lasing material," in *Organic Light Emitting Materials and Devices XVII*, vol. 8829, pp. 94–100, SPIE.

[25] Z.-M. Huang, Y.-Z. Zhang, M. Kotaki, and S. Ramakrishna, "A review on polymer nanofibers by electrospinning and their applications in nanocomposites," *Composites science and technology*, vol. 63, no. 15, pp. 2223–2253, 2003.

[26] N. Savest, T. Plamus, E. Tarasova, M. Viirsalu, I. Krasnou, V. Gudkova, K.-A. Küppar, and A. Krumme, "The effect of ionic liquids on the conductivity of electrospun polyacrylonitrile membranes," *Journal of Electrostatics*, vol. 83, pp. 63–68, 2016.

[27] W. Cheng, Q. Yu, Z. Qiu, and Y. Yan, "Effects of different ionic liquids on the electrospinning of a polyacrylonitrile polymer solution," *Journal of Applied Polymer Science*, vol. 130, no. 4, pp. 2359–2368, 2013.

[28] S.-H. Tan, R. Inai, M. Kotaki, and S. Ramakrishna, "Systematic parameter study for ultra-fine fiber fabrication via electrospinning process," *Polymer*, vol. 46, no. 16, pp. 6128–6134, 2005.

[29] X. Zong, K. Kim, D. Fang, S. Ran, B. S. Hsiao, and B. Chu, "Structure and process relationship of electrospun bioabsorbable nanofiber membranes," *polymer*, vol. 43, no. 16, pp. 4403–4412, 2002.

[30] K. Li, Z. Ma, and H. Choi, "High-q whispering-gallery mode lasing from nanosphere-patterned gan nanoring arrays," *Applied Physics Letters*, vol. 98, no. 7, p. 071106, 2011.

[31] J. Heebner, R. Grover, and T. Ibrahim, *Optical microresonator theory.* Springer, 2008.

7

Summary and Future Directions

The thesis focuses on probing the various photo-physical and charge transport mechanisms in solution-processed semiconductors using a combination of time and frequency domain measurements. Two broad classes of solution-processed semiconductors have been used in this thesis: organic polymers and hybrid organic-inorganic perovskite (HOIP). An introduction to various recombination and charge transport processes both in organic and HOIP semiconductors has been given in the first chapter.

The second chapter deals with the study of charge carrier dynamics using transient photocurrent (TPC) spectroscopy measurements on tandem solar cells. The active layers, composed of direct bandgap HOIP and the indirect band gap Si, have different optoelectronic properties and thicknesses. The TPC measurements directly assess the timescales of photogenerated charge carriers extracted at the electrodes. Spectral dependence of TPC measurements exhibits two distinct lifetime magnitudes: $\tau_1 \sim 500$ ns and $\tau_2 \sim 25$ μs. Further analysis shows that the carriers are extracted via drift and diffusion processes in the perovskite sub-cell, whereas the Si sub-cell follows a diffusion-limited carrier extraction process. In the absence of background illumination, sub-cell processes are uncorrelated, and the current magnitude depends on the shunt resistance of the other sub-cell in the dark. A crossover of the dynamics of the perovskite sub-cell to a coupled regime with the Si sub-cell is observed beyond a certain threshold of dc-light bias.

Chapter three focuses on investigating the charge carrier and triplet

dynamics in thermally activated delayed fluorescence (TADF) based organic light-emitting diodes (OLEDs) using temperature-dependent transient electroluminescence (TrEL) measurements. The TADF systems are expected to show increased emissive yield due to efficient back-conversion of non-emissive triplet states to emissive singlet states via reverse intersystem crossing (RISC). A solution-processed TADF molecule, 2,3,4,6-Tetra(9H-carbazol-9-yl)-5-fluorobenzonitrile (4CzFCN), was used for this study. The analysis of the rising edge of the TrEL pulse indicates that the carriers follow multiple trapping, de-trapping, and exciton recombination dynamics. The falling edge of the TrEL pulse provides insights into the monomolecular and bimolecular exciton dynamics, representative of device operational conditions. These studies indicate that triplet harvesting in 4CzFCN molecule occurs via both RISC and triplet-triplet annihilation (TTA). Further, the TADF processes dominate at high temperatures with negligible contribution from TTA.

Chapter four deals with the influence of various coatings on the wall (both phosphorescent and fluorescent) in the non-line of sight visible light communication. The enclosure boundary is normally treated as a classical light diffuser which merely scatters and attenuates the signal. Using various photo-luminescent coatings on the walls acts as active noise sources, distorting the signal and altering the communication characteristics. The possibility of tuning the signal to noise levels by these emitters as a function of the spatial coordinates can be utilized to design smart environments where signal access can be controlled and restricted. Conversely, the signal analysis used in this chapter can also be utilized to provide dynamic information about the environment.

Chapter five deals with the study of photon statistics of TADF dyes at various concentrations. A confocal microscope was built to study these molecules having lifetimes in the range of microseconds at dilute concentrations. Photon statistics of TADF molecules at various dilution levels were measured using a single photon avalanche diode (SPAD) integrated with the microscope. The high lifetime of 4CzFCN

molecule than the dead time of the SPAD allowed for studying the photon statistics using only a single detector. The measurements reveal that the fluctuations follow photon bunching statistics. An autocorrelation feature resembling photon antibunching is observed at sparse regions of the sample fabricated from 250 ng/ml.

Finally, the photo-physics of 4CzFCN molecules in a mesoscale fiber is studied fabricated using the electrospinning method. The process of electrospinning provides easy and cost-effective fabrication of polymer fibers with added functionalities. The 4CzFCN doped PMMA fibers exhibit high luminescence and stability. The diameter of the fibers is solely dependent on the PMMA concentration, with the fiber diameter increasing with concentration. The μ-PL measurement confirms the uniform distribution of 4CzFCN emitters throughout the length of the fiber. The temperature and intensity-dependent μ-PL measurements confirm the monomolecular TADF process as the sole triplet harvesting mechanism for the triplets. Additionally, the fibre geometry allows for light confinement and waveguiding effects. FDFD eigenmode analysis of the fibre shows the primary guided mode responsible for waveguiding of the emitted light across the fiber length. The fiber also shows a slight narrowing in the emission spectra compared to a film originating from the fiber cavity geometry. The eigenmode analysis shows the electric field profiles of these higher-order cavity modes have nodes at the centre of the fibre.

Future Directions

The difference of the carrier time constants by orders of magnitude in the two sub-cell for tandem structure suggests that there might be an inherent charge-carrier imbalance at the recombination layer even when both the sub-cells generate the same number of carriers. This might lead to improper current matching and requires a detailed study. A thicker perovskite active layer and the presence of shallow traps can slow down the perovskite dynamics significantly to match the timescales of Si dynamics. However, this process of active layer fine-tuning without any detriment to efficiency requires a thorough investigation. Further,

the transport processes in the perovskite sub-cell in the tandem configuration are influenced by high field strength. This can lead to ionic transport in the perovskite sub-cell, leading to degradation processes which needs further examination.

The internal quantum efficiency of TADF molecules has a theoretical limit of 100%, making them excellent candidates for fabricating organic laser diodes. There are almost no reports of organic laser diodes, which require very high exciton densities. Hence, a detailed kinetic study on these molecules is required at high injection densities in a cavity to be used as prospective candidates in organic laser diodes.

Quantum emitters are in demand for their application in quantum information processing, metrology and quantum cryptography. Organic molecular systems with high quantum yields have the added advantage of them being used for LEDs. However, the electrical excitation of a molecular system generates 75% triplets and 25% singlets. This creates a bottleneck for the fluorescent emitters to be used as an electrically driven single photon sources which are otherwise excellent single photon sources under optical excitation. Highly efficient TADF molecules are capable of converting these non-radiative triplets to singlets via RISC making them ideal candidates to be used as quantum emitters. However, the choice of host and transport layers in these systems is extremely crucial as these layers can have background emission making the detection of the single photons difficult. Further, the CT triplet and singlet states in the donor-acceptor-based TADF molecules can act as spin-entangled qubit states. Thus, the nature of these two-spin entangled singlets or triplets in TADF systems needs a detailed investigation.

The photoluminescent quantum yield (PLQY) of TADF dyes are quite high making them suitable for cavity-based applications. The fibers support whispering gallery modes which are known to have very high-quality factors. Whispering gallery cavities reduce the threshold of lasing in dyes, and the primary mode of the fibre can guide this emission across the fibre. These properties of the mirrorless fibre cavities make

them suitable for them to be used in photonic circuits. Therefore, the threshold for amplified spontaneous emission under a high optical pump in these TADF fibres need to be explored further which is one of the essential criteria for observing lasing. However, the triplet absorption ($T_1 \rightarrow T_n$) process significantly raises the threshold for lasing. Thus, the kinetics of all the triplet processes need to be explored under high pump intensities.

Scattering Matrix Modelling

Maxwell Equations

Maxwell equations in the time domain can be written as [1] :

Divergence equations: $\nabla \cdot \vec{D} = \rho_v$ (A.1a)

$$\nabla \cdot \vec{B} = 0 \tag{A.1b}$$

Curl equations: $\nabla \times \vec{E} = -\dfrac{\partial \vec{B}}{\partial t}$ (A.1c)

$$\nabla \times \vec{H} = \vec{J} + \dfrac{\partial \vec{D}}{\partial t} \tag{A.1d}$$

Here $\vec{E}$, $\vec{D}$, $\vec{B}$ and $\vec{H}$ represent the elctric field, electric displacemnt vector, magnetic induction, magnetic field respectively. ρ_v and $\vec{J}$ represent the charge density and current density respectively.

The consitutive relations are written as:

$$\vec{D}(t) = [\varepsilon(t)] * \vec{E}(t) \qquad \vec{B}(t) = [\mu(t)] * \vec{H}(t) \tag{A.2}$$

The quantities $[\varepsilon(t)]$ and $[\mu(t)]$ represents permitivitty tensor and magnetic permeability tensor respectively and $*$ represents convolution.

It can be assumed in the electromagnetic simulations that there are no charge and current sources i.e., $\rho_v = 0$ and $\vec{J} = 0$. Transforming the Maxwell equations to frequency domain [1]:

$$\begin{aligned} \nabla \cdot \vec{D} = 0 \qquad \nabla \times \vec{E} = -j\omega \vec{B} \\ \nabla \cdot \vec{B} = 0 \qquad \nabla \times \vec{H} = j\omega \vec{D} \end{aligned} \tag{A.3}$$

In the frequency domain, the convolutions become simple multiplications.

$$\vec{D} = [\varepsilon]\vec{E} \qquad \vec{B} = [\mu]\vec{H} \qquad (A.4)$$

Substituting the constitutive relations (Eq. A.4) in Maxwell equations (Eq. A.3):

$$\begin{aligned}
\nabla \cdot [\mu]\vec{H} &= 0 & \nabla \times \vec{H} &= j\omega[\varepsilon]\vec{E} \\
\nabla \cdot [\varepsilon]\vec{E} &= 0 & \nabla \times \vec{E} &= -j\omega[\mu]\vec{H}
\end{aligned} \qquad (A.5)$$

Finally, the magnetic field ($\vec{H}$) is normalised such that $\vec{\tilde{H}} = -j\sqrt{\frac{\mu_0}{\varepsilon_0}}\vec{H}$. Hence, Eq. A.5 when expanded in the Cartesian coordinate system become [1]:

$$\begin{aligned}
\frac{\partial E_z}{\partial y} - \frac{\partial E_y}{\partial z} &= k_0\mu_{xx}\tilde{H}_x & \frac{\partial \tilde{H}_z}{\partial y} - \frac{\partial \tilde{H}_y}{\partial z} &= k_0\varepsilon_{xx}E_x \\
\frac{\partial E_x}{\partial z} - \frac{\partial E_z}{\partial x} &= k_0\mu_{yy}\tilde{H}_y & \frac{\partial \tilde{H}_x}{\partial z} - \frac{\partial \tilde{H}_z}{\partial x} &= k_0\varepsilon_{yy}E_y \\
\frac{\partial E_y}{\partial x} - \frac{\partial E_x}{\partial y} &= k_0\mu_{zz}\tilde{H}_z & \frac{\partial \tilde{H}_y}{\partial x} - \frac{\partial \tilde{H}_x}{\partial y} &= k_0\varepsilon_{zz}E_z
\end{aligned} \qquad (A.6)$$

Here $\varepsilon = \varepsilon_0\varepsilon_r$, $\mu = \mu_0\mu_r$ and $k_0 = \omega\sqrt{\mu_0\varepsilon_0}$. The form of Maxwell equations given by Eq. A.6 is the starting point for most of the methods in computational electromagnetics.

Formulation of a 2×2 matrix equation

The transfer matrix method (TMM) assumes that the device consists of a stack of layers with different permitivities and permeabilities. This method have proven to be one of the most computationally efficient for the analysis of layered devices. The layers in the device have their own unique scattering matrix owing to their different permittivities/permeabilities. The scattering matrices for each layer in the device were combined to derive an overall device scattering matrix. The device was then connected to the external transmission and reflection regions to generate a global scattering matrix. The final global scattering matrix estimates the the transmission, reflection and absorption magnitudes from the device.

In the framework of TMM, the layers of the device is assumed to be homogeneous in the transverse direction (x and y direction) but non homogeneous in the longitudinal direction (z direction). Hence, plane wave approximation is used in the x and y direction which implies in Eq. A.6, $\partial/\partial x = jk_x$ and $\partial/\partial x = jk_x$. In the z direction, owing to the non homogeneity of the device, $\partial/\partial z \neq jk_x$. However, z is the only independent variable which implies the partial derivative becomes ordinary i.e. $\partial/\partial z = d/dz$. The z variable is normalised along with the wave vector components ($\vec{k}$) such that $z' = k_0 z$, $\tilde{k}_x = k_x/k_0$, $\tilde{k}_y = k_y/k_0$, $\tilde{k}_z = k_z/k_0$. Putting everything together Eq. A.6 for isotropic systems become [1]:

$$
\begin{aligned}
j\tilde{k}_y E_z - \frac{dE_y}{dz'} = \mu_r \tilde{H}_x \qquad & j\tilde{k}_y \tilde{H}_z - \frac{d\tilde{H}_y}{dz'} = \varepsilon_r E_x \\
\frac{dE_x}{dz'} - j\tilde{k}_x E_z = \mu_r \tilde{H}_y \qquad & \frac{d\tilde{H}_x}{dz'} - j\tilde{k}_x \tilde{H}_x = \varepsilon_r E_y \\
j\tilde{k}_x E_y - j\tilde{k}_y E_x = \mu_r \tilde{H}_z \qquad & j\tilde{k}_x \tilde{H}_y - j\tilde{k}_y \tilde{H}_x = \varepsilon_r E_z
\end{aligned}
\tag{A.7}
$$

The last row in Eq. A.7 was solved for the longitudinal field components, $\tilde{H}_z$ and E_z and then their expressions were substituted in the equations of the first two rows. The final rearranged form of equations are as follows:

$$
\begin{aligned}
\frac{dE_x}{dz'} &= \frac{\tilde{k}_x \tilde{k}_y}{\varepsilon_r} \tilde{H}_x + (\mu_r - \frac{\tilde{k}_x^2}{\varepsilon_r}) \tilde{H}_y \\
\frac{dE_y}{dz'} &= (\frac{\tilde{k}_y^2}{\varepsilon_r} - \mu_r) \tilde{H}_x - \frac{\tilde{k}_x \tilde{k}_y}{\varepsilon_r} \tilde{H}_y \\
\frac{d\tilde{H}_x}{dz'} &= \frac{\tilde{k}_x \tilde{k}_y}{\mu_r} E_x + (\varepsilon_r - \frac{\tilde{k}_x^2}{\mu_r}) E_y \\
\frac{d\tilde{H}_y}{dz'} &= (\frac{\tilde{k}_y^2}{\mu_r} - \varepsilon_r) E_x - \frac{\tilde{k}_x \tilde{k}_y}{\mu_r} E_y
\end{aligned}
\tag{A.8}
$$

The electric field and magnetic field components in Eq. A.8 was written in a compact form as:

$$
\frac{d}{dz'}
\begin{bmatrix} E_x \\ E_y \end{bmatrix}
= P
\begin{bmatrix} \tilde{H}_x \\ \tilde{H}_y \end{bmatrix}
\tag{A.9}
$$

$$\frac{d}{dz'} \begin{bmatrix} \tilde{H}_x \\ \tilde{H}_y \end{bmatrix} = Q \begin{bmatrix} E_x \\ E_y \end{bmatrix} \tag{A.10}$$

where $P = \frac{1}{\varepsilon_r} \begin{bmatrix} \tilde{k}_x \tilde{k}_y & \mu_r \varepsilon_r - \tilde{k}_x^2 \\ \tilde{k}_y^2 - \mu_r \varepsilon_r & -\tilde{k}_x \tilde{k}_y \end{bmatrix}$

and $Q = \frac{1}{\mu_r} \begin{bmatrix} \tilde{k}_x \tilde{k}_y & \mu_r \varepsilon_r - \tilde{k}_x^2 \\ \tilde{k}_y^2 - \mu_r \varepsilon_r & -\tilde{k}_x \tilde{k}_y \end{bmatrix}$

Differentiating Eq. A.9 w.r.t. z' and substituting Eq. A.10 into this result

$$\frac{d^2}{dz'^2} \begin{bmatrix} E_x \\ E_y \end{bmatrix} - \Omega^2 \begin{bmatrix} E_x \\ E_y \end{bmatrix} = \begin{bmatrix} 0 \\ 0 \end{bmatrix} \tag{A.11}$$

with $\Omega^2 = PQ$

Eq. A.11 has the general solution:

$$\begin{bmatrix} E_x \\ E_y \end{bmatrix} = e^{\Omega z'} \mathbf{a}^+ + e^{-\Omega z'} \mathbf{a}^- \tag{A.12}$$

where $\mathbf{a}^+$ and $\mathbf{a}^-$ are the proportionality constants for forward and backward wave propagation. The matrix exponential was written using eigen-values (λ^2) and eigen-vector (W) of the matrix Ω^2 as $We^{\lambda z'}W^{-1}$. Thus,

$$\begin{bmatrix} E_x(z') \\ E_y(z') \end{bmatrix} = We^{\lambda z'} \mathbf{c}^+ + We^{-\lambda z'} \mathbf{c}^- \tag{A.13}$$

W denotes the square eigenvector matrix whose column vectors describe the modes that can exist in each layer. $e^{\pm \lambda z'}$ is a diagonal matrix that describes the propagation mechanism of these modes. It includes the accumulation of the phase as well as decaying or gaining of amplitude. $\mathbf{c}^\pm$ quantifies the amount of power in each mode. The solution for magnetic field will be of the same form, but with its own eigen-vector matrix

V to describe its modes i.e.,

$$\begin{bmatrix} \tilde{H}_x(z') \\ \tilde{H}_y(z') \end{bmatrix} = Ve^{\lambda z'}\mathbf{c}^+ - Ve^{-\lambda z'}\mathbf{c}^- \tag{A.14}$$

However V is directly related to W using Eq. A.10 as follows:

$$V = QW\lambda^{-1} \tag{A.15}$$

Scattering Matrices

Electromagnetic modelling methods employing scattering matrices make them unconditionally stable. The parameters of a scattering matrix have physical meanings and correspond to those measured in the lab. They are very memory efficient and can be used to extract dispersion of various devices. Generally a scattering matrix (Figure A.1) is defined in [1, 2]

$$\begin{bmatrix} \mathbf{c}_1'^- \\ \mathbf{c}_2'^+ \end{bmatrix} = \begin{bmatrix} S_{11} & S_{12} \\ S_{21} & S_{22} \end{bmatrix} \begin{bmatrix} \mathbf{c}_1'^+ \\ \mathbf{c}_2'^- \end{bmatrix} \tag{A.16}$$

The combined electric and magnetic fields in the ith layer, $\psi_i(z_i')$ was written using Eq. A.13 and Eq. A.14 as

$$\psi_i(z_i') = \begin{bmatrix} E_{x,i}(z_i') \\ E_{y,i}(z_i') \\ \tilde{H}_{x,i}(z_i') \\ \tilde{H}_{y,i}(z_i') \end{bmatrix} = \begin{bmatrix} W_i & W_i \\ V_i & -V_i \end{bmatrix} \begin{bmatrix} e^{\lambda_i z_i'} & 0 \\ 0 & e^{-\lambda_i z_i'} \end{bmatrix} \begin{bmatrix} \mathbf{c}_i^+ \\ \mathbf{c}_i^- \end{bmatrix} \tag{A.17}$$

Using boundary conditions at the two interfaces i.e., $\psi_1 = \psi_i(0)$ and
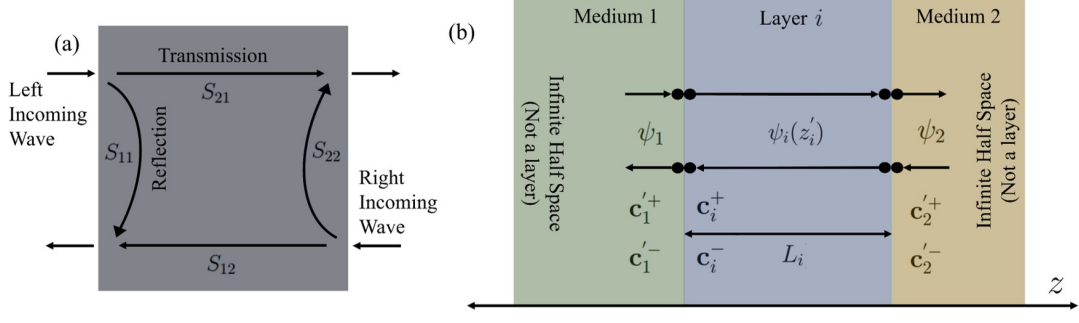
Figure A.1: (a) Definition of a Scattering Matrix, (b) Geometry of a Single Layer.

$\psi(k_0 L_i) = \psi_2$ (Figure A.1b):

$$\begin{bmatrix} W_1 & W_1 \\ V_1 & -V_1 \end{bmatrix} \begin{bmatrix} \mathbf{c}_1^{'+} \\ \mathbf{c}_1^{'-} \end{bmatrix} = \begin{bmatrix} W_i & W_i \\ V_i & -V_i \end{bmatrix} \begin{bmatrix} \mathbf{c}_i^{+} \\ \mathbf{c}_i^{-} \end{bmatrix}$$
$$\begin{bmatrix} W_i & W_i \\ V_i & -V_i \end{bmatrix} \begin{bmatrix} e^{\lambda_i k_0 L_i} & 0 \\ 0 & e^{-\lambda_i k_0 L_i} \end{bmatrix} \begin{bmatrix} \mathbf{c}_i^{+} \\ \mathbf{c}_i^{-} \end{bmatrix} = \begin{bmatrix} W_2 & W_2 \\ V_2 & -V_2 \end{bmatrix} \begin{bmatrix} \mathbf{c}_2^{'+} \\ \mathbf{c}_2^{-} \end{bmatrix} \tag{A.18}$$

Eq. A.18 was solved for the intermediate mode coefficients $\mathbf{c}_i^{+}$ and $\mathbf{c}_i^{-}$ and were eliminated. They were rearranged in the form of Eq. A.16 such that

$$\begin{bmatrix} \mathbf{c}_1^{'-} \\ \mathbf{c}_2^{'+} \end{bmatrix} = S^{(i)} \begin{bmatrix} \mathbf{c}_1^{'+} \\ \mathbf{c}_2^{'-} \end{bmatrix} \tag{A.19}$$

The components of $S^{(i)}$ matrix became:

$$\begin{aligned} S_{11}^{(i)} &= (A_{i1} - X_i B_{i2} A_{i2}^{-1} X_i B_{i1})^{-1} (X_i B_{i2} A_{i2}^{-1} X_i A_{i1} - B_{i1}) \\ S_{12}^{(i)} &= (A_{i1} - X_i B_{i2} A_{i2}^{-1} X_i B_{i1})^{-1} X_i (A_{i2} - B_{i2} A_{i2}^{-1} B_{i2}) \\ S_{21}^{(i)} &= (A_{i2} - X_i B_{i1} A_{i1}^{-1} X_i B_{i2})^{-1} X_i (A_{i1} - B_{i1} A_{i1}^{-1} B_{i1}) \\ S_{22}^{(i)} &= (A_{i2} - X_i B_{i1} A_{i1}^{-1} X_i B_{i2})^{-1} (X_i B_{i1} A_{i1}^{-1} X_i A_{i2} - B_{i2}) \end{aligned} \tag{A.20}$$

where $A_{ij} = W_i^{-1} W_j + V_i^{-1} V_j$, $B_{ij} = W_i^{-1} W_j - V_i^{-1} V_j$ and $X_i = e^{\lambda_i k_0 L_i}$. The scattering matrix of a particular layer are a function of materials outside of the layer.This makes the modelling process very inefficient as the scattering matrix of a particular layer will change depending on its surroundings. The solution to this problem is to separate each of the layers with a gap medium of zero thickness. This makes the medium 1

and 2 around the ith layer symmetric and leads to simplified scttering matrix equation. Thus, the components of $S^{(i)}$ matrix became:

$$
\begin{aligned}
S_{11}^{(i)} &= (A_i - X_i B_i A_i^{-1} X_i B_i)^{-1}(X_i B_i A_i^{-1} X_i A_i - B_i) \\
S_{12}^{(i)} &= (A_i - X_i B_i A_i^{-1} X_i B_i)^{-1} X_i (A_i - B_i A_i^{-1} B_i) \\
S_{21}^{(i)} &= S_{12}^{(i)} \\
S_{22}^{(i)} &= S_{11}^{(i)}
\end{aligned}
\tag{A.21}
$$

where $A_i = W_i^{-1} W_g + V_i^{-1} V_g$, $B_i = W_i^{-1} W_g - V_i^{-1} V_g$ and $X_i = e^{\lambda_i k_0 L_i}$. Subscript g denotes the gap medium of zero thickness [2].

Transfer Matrix Method using scattering matrices

Two scattering matrices may be combined into a single scattering matrix using Redheffer's star product[3].

$$
S^{(AB)} = S^{(A)} \otimes S^{(B)}
$$

$$
\Rightarrow
\begin{bmatrix}
S_{11}^{(AB)} & S_{12}^{(AB)} \\
S_{21}^{(AB)} & S_{22}^{(AB)}
\end{bmatrix}
=
\begin{bmatrix}
S_{11}^{(A)} & S_{12}^{(A)} \\
S_{21}^{(A)} & S_{22}^{(A)}
\end{bmatrix}
\otimes
\begin{bmatrix}
S_{11}^{(B)} & S_{12}^{(B)} \\
S_{21}^{(B)} & S_{22}^{(B)}
\end{bmatrix}
\tag{A.22}
$$

The symbol $\otimes$ denotes Redheffer star product. The components of final scattering matrix $S^{(AB)}$ is given as

$$
\begin{aligned}
S_{11}^{(AB)} &= S_{11}^{(A)} + S_{12}^{(A)}[\mathbf{I} - S_{11}^{(B)} S_{22}^{(A)}]^{-1} S_{11}^{(B)} S_{21}^{(A)} \\
S_{12}^{(AB)} &= S_{12}^{(A)}[\mathbf{I} - S_{11}^{(B)} S_{22}^{(A)}]^{-1} S_{12}^{(B)} \\
S_{21}^{(AB)} &= S_{21}^{(B)}[\mathbf{I} - S_{22}^{(A)} S_{11}^{(B)}]^{-1} S_{21}^{(A)} \\
S_{22}^{(AB)} &= S_{22}^{(B)} + S_{21}^{(B)}[\mathbf{I} - S_{22}^{(A)} S_{11}^{(B)}]^{-1} S_{22}^{(A)} S_{12}^{(B)}
\end{aligned}
\tag{A.23}
$$

For multilayer structures, the scattering matrices for each layer of the device can be calculated for different wavelengths using their corresponding refractive index dispersion curves. The scattering matrices for each layer were combined to derive an overall device scattering matrix, $S^{(device)}$ i.e.,

$$
S^{(device)} = S^{(1)} \otimes S^{(2)} \otimes S^{(3)} \otimes \ldots \otimes S^{(n)}
\tag{A.24}
$$
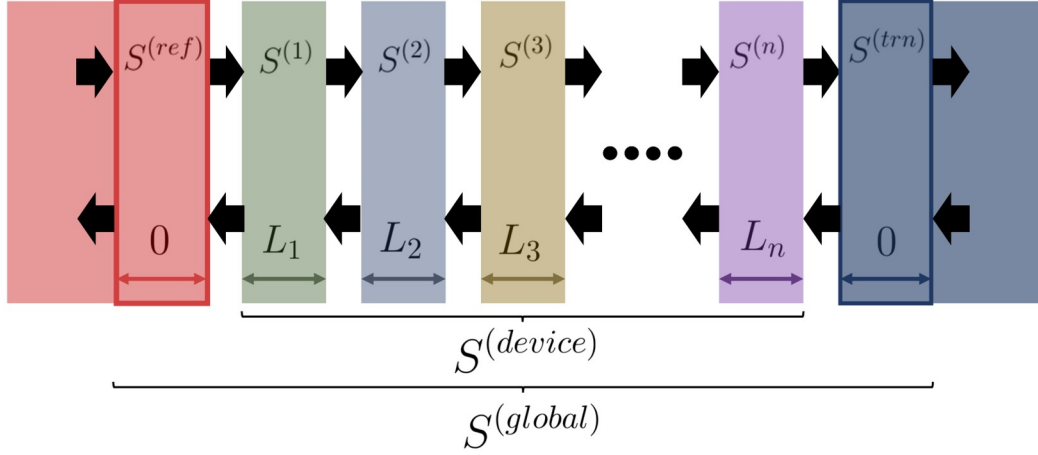
Figure A.2: Derivation of Global Scattering Matrix

The device scattering matrices were then connected to the transmission and reflection regions to generate a global scattering matrix $S_{(global)}$ (Figure A.2).

$$S^{(global)} = S^{(ref)} \otimes [S^{(1)} \otimes S^{(2)} \otimes S^{(3)} \otimes .... \otimes S^{(n)}] \otimes S^{(trn)} \quad (A.25)$$

The reflection-side scattering matrix is

$$
\begin{aligned}
S_{11}^{(ref)} &= -A_{ref}^{-1}B_{ref} \\
S_{12}^{(ref)} &= 2A_{ref}^{-1} \\
S_{21}^{(ref)} &= 0.5(A_{ref} - B_{ref}A_{ref}^{-1}B_{ref}) \\
S_{22}^{(ref)} &= B_{ref}A_{ref}^{-1}
\end{aligned}
\quad (A.26)
$$

where $A_{ref} = W_g^{-1}W_{ref} + V_g^{-1}V_{ref}$ and $B_{ref} = W_g^{-1}W_{ref} - V_g^{-1}V_{ref}$
The transmission-side scattering matrix is

$$
\begin{aligned}
S_{11}^{(ref)} &= B_{trn}A_{trn}^{-1} \\
S_{12}^{(ref)} &= 0.5(A_{trn} - B_{trn}A_{trn}^{-1}B_{trn}) \\
S_{21}^{(ref)} &= 2A_{trnf}^{-1} \\
S_{22}^{(ref)} &= -A_{trn}^{-1}B_{trn}
\end{aligned}
\quad (A.27)
$$

where $A_{trn} = W_g^{-1}W_{trn} + V_g^{-1}V_{trn}$ and $B_{trn} = W_g^{-1}W_{trn} - V_g^{-1}V_{trn}$.
The external fields (i.e. incident wave, reflected wave, transmitted wave)

are related through the global transfer matrix.

$$
\begin{bmatrix} \mathbf{c}_{ref} \\ \mathbf{c}_{trn} \end{bmatrix} = S^{(global)} \begin{bmatrix} \mathbf{c}_{inc} \\ 0 \end{bmatrix} \Rightarrow \quad \begin{array}{l} \mathbf{c}_{ref} = S_{11}^{(global)} \mathbf{c}_{inc} \\ \mathbf{c}_{trn} = S_{21}^{(global)} \mathbf{c}_{inc} \end{array} \tag{A.28}
$$

The transmitted and reflected fields must be calculated from the mode coefficients:

$$
\begin{bmatrix} E_x^{ref} \\ E_y^{ref} \end{bmatrix} = W_{ref} \mathbf{c}_{ref}, \quad \begin{bmatrix} E_x^{trn} \\ E_y^{trn} \end{bmatrix} = W_{trn} \mathbf{c}_{trn} \tag{A.29}
$$

The longitudinal field component E_z are calculated from E_x and E_y using Maxwell's divergence equation to obtain

$$
E_z^{ref} = -\frac{\tilde{k}_x E_x^{ref} + \tilde{k}_y E_y^{ref}}{\tilde{k}_z^{ref}}, \quad E_z^{trn} = -\frac{\tilde{k}_x E_x^{trn} + \tilde{k}_y E_y^{trn}}{\tilde{k}_z^{trn}} \tag{A.30}
$$

Reflectance/transmittance is defined as the fraction of power reflected/transmitted from/through a device.

$$
R = \frac{|\vec{E_{ref}}|^2}{|\vec{E_{inc}}|^2}, \quad T = \frac{|\vec{E_{trn}}|^2}{|\vec{E_{inc}}|^2} \frac{Re[\tilde{k}_z^{trn}/\mu_{r,trn}]}{Re[\tilde{k}_z^{inc}/\mu_{r,inc}]} \tag{A.31}
$$

where $|\vec{E}|^2 = |\vec{E_x}|^2 + |\vec{E_y}|^2 + |\vec{E_z}|^2$ and $\vec{E_{inc}} = P_{TE}\hat{E}_{TE} + P_{TM}\hat{E}_{TM}$ with $|\vec{E}_{inc}| = 1$. The incident wave vector ($\vec{k}_{inc}$), unit vectors ($\hat{E}_{TE}$ and $\hat{E}_{TM}$) and surface normal ($\hat{n}$ or $\hat{E}_z$) is defined as

$$
\hat{E}_{TE} = \begin{cases} \hat{E}_y, & \theta = 0^o \\ \frac{\hat{n} \times \vec{k}_{inc}}{|\hat{n} \times \vec{k}_{inc}|}, & \theta \neq 0^o \end{cases}, \quad \hat{E}_{TM} = \frac{\vec{k}_{inc} \times \hat{E}_{TE}}{|\vec{k}_{inc} \times \hat{E}_{TE}|} \tag{A.32}
$$

with $\vec{k}_{inc} = k_0 n_{inc} \begin{bmatrix} sin\theta cos\phi \\ sin\theta sin\phi \\ cos\theta \end{bmatrix}, \quad \vec{k}_{inc} = k_0 n_{inc} \begin{bmatrix} sin\theta cos\phi \\ sin\theta sin\phi \\ cos\theta \end{bmatrix}.$

For linear, homogeneous and isotropic media [1]:
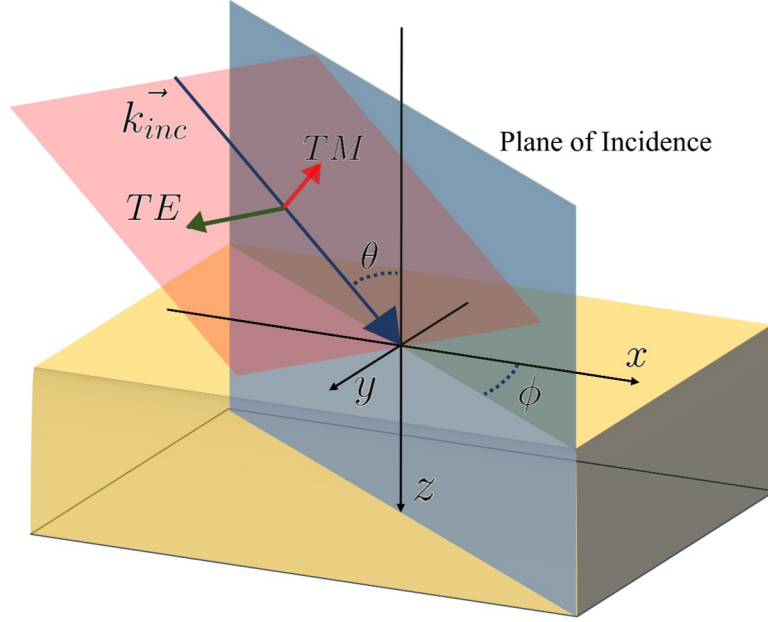
Figure A.3: Visualization of the TE and TM polarization vectors

$$W_i = I = \begin{bmatrix} 1 & 0 \\ 0 & 1 \end{bmatrix}; \quad \Omega_i = j\tilde{k}_{z,i}I; \quad \lambda_i = \Omega_i$$

Thus, the eigenvector of the magnetic field becomes $V_i = Q_i\Omega_i^{-1}$. The intermediate matrices A_i and B_i becomes

$$\begin{aligned} A_i &= I + V_i^{-1}V_g \\ B_i &= I - V_i^{-1}V_g \end{aligned} \tag{A.33}$$

where $V_g = -jQ_g$. This makes the fields and mode coefficients to be same, i.e.,

$$c_{inc} = W_{ref}^{-1} \begin{bmatrix} P_x \\ P_y \end{bmatrix} = \begin{bmatrix} P_x \\ P_y \end{bmatrix}$$

$$\begin{bmatrix} E_x^{ref} \\ E_y^{ref} \end{bmatrix} = W_{ref}S_{11}^{(global)}c_{inc} = S_{11}^{(global)}c_{inc} \tag{A.34}$$

$$\begin{bmatrix} E_x^{trn} \\ E_y^{trn} \end{bmatrix} = W_{trn}S_{21}^{(global)}c_{inc} = S_{211}^{(global)}c_{inc}$$

The reflection side and transmission side scattering matrix simplify to

$$A_{ref} = I + V_g^{-1}V_{ref}$$
$$B_{ref} = I - V_g^{-1}V_{ref}$$
$$A_{trn} = I + V_g^{-1}V_{trn}$$
$$B_{trn} = I - V_g^{-1}V_{trn}$$

(A.35)

Electric Field line profiles

The field inside the ith layer is calculated using Eq. A.38. The global scattering matrix $(S^{(global)})$ is built from left to right as shown in Figure A.2. During the building of the $S^{(global)}$, W_i, V_{N-1}, λ_{N-1})and $S^{(Gi)}$ is recorded for each layer where the internal field needs to be calculated. On reaching the final layer, the external mode coefficients are calculated for each layer from right to left [1]:

$$c_{i1}^- = (S_{12}^{[G(i-1)]})^{-1}(c_{ref} - S_{11}^{[G(i-1)]}c_{inc})$$
$$c_{i1}^+ = S_{21}^{[G(i-1)]}c_{inc} + S_{22}^{[G(i-1)]}c_{i1}^-$$

(A.36)

The internal mode coefficients are calculated as

$$\begin{bmatrix} c_i^+ \\ c_i^- \end{bmatrix} = \begin{bmatrix} W_i & W_i \\ V_i & -V_i \end{bmatrix}^{-1} \begin{bmatrix} W_{i1} & W_{i1} \\ V_{i1} & -V_{i1} \end{bmatrix} \begin{bmatrix} c_{i1}^+ \\ c_{i1}^- \end{bmatrix}$$

(A.37)

Finally, the internal fields are calculated using Eq. A.38 as

$$\psi_i(z_i) = \begin{bmatrix} E_{x,i}(z_i) \\ E_{y,i}(z_i) \\ \tilde{H}_{x,i}(z_i) \\ \tilde{H}_{y,i}(z_i) \end{bmatrix} = \begin{bmatrix} W_i & W_i \\ V_i & -V_i \end{bmatrix} \begin{bmatrix} e^{k_0\lambda_i z_i} & 0 \\ 0 & e^{-k_0\lambda_i z_i} \end{bmatrix} \begin{bmatrix} \mathbf{c}_i^+ \\ \mathbf{c}_i^- \end{bmatrix}$$

(A.38)

References

[1] https://empossible.net/academics/emp5337/, "Computational electromagnetics."

[2] R. C. Rumpf, "Improved formulation of scattering matrices for semi-

analytical methods that is consistent with convention," *Progress In Electromagnetics Research B*, vol. 35, pp. 241–261, 2011.

[3] R. Redheffer, "Difference equations and functional equations in transmission-line theory," *Modern mathematics for the engineer*, vol. 12, pp. 282–337, 1961.

Eigenmode Simulation of waveguides using Finite Difference Frequency Domain method

It is possible to calculate an approximate analytical solution of modes for rectangular waveguides and optical fibers. However, special cases such as integrated optical and photonic crystal waveguides cannot be solved analytically and require numerical simulation. Further, tweaking the parameters of a waveguide with analytical solutions is difficult. The Finite Difference Frequency Domain (FDFD) method helps to calculate the guided modes in any waveguide without difficulty. Waveguides are usually analysed as an eigenvalue problem; hence, sources are not required in the simulation [1].

The starting point of the simulation will be Maxwell equations given by Eq. A.6. On normalising the grid coordinates $x' = k_0 x$, $y' = k_0 y$, $z' = k_0 z$, Eq. A.6 becomes [1, 2]

$$\frac{\partial E_z}{\partial y'} - \frac{\partial E_y}{\partial z'} = \mu_{xx}\tilde{H}_x \qquad \frac{\partial \tilde{H}_z}{\partial y'} - \frac{\partial \tilde{H}_y}{\partial z'} = \varepsilon_{xx}E_x$$

$$\frac{\partial E_x}{\partial z'} - \frac{\partial E_z}{\partial x'} = \mu_{yy}\tilde{H}_y \qquad \frac{\partial \tilde{H}_x}{\partial z'} - \frac{\partial \tilde{H}_z}{\partial x'} = \varepsilon_{yy}E_y \qquad (B.1)$$

$$\frac{\partial E_y}{\partial x'} - \frac{\partial E_x}{\partial y'} = \mu_{zz}\tilde{H}_z \qquad \frac{\partial \tilde{H}_y}{\partial x'} - \frac{\partial \tilde{H}_x}{\partial y'} = \varepsilon_{zz}E_z$$

A mode in the waveguide propagating along the z direction can be mathematically written as [1, 2]

$$\vec{E}(x', y', z') = A(x', y')e^{\gamma z'/k_0} \qquad (B.2)$$

$$\vec{\tilde{H}}(x', y', z') = B(x', y')e^{\gamma z'/k_0} \qquad (B.3)$$

where $A(x', y')$ is the complex amplitude that defines the shape of the mode and $e^{\gamma z'/k_0}$ gives the magnitude of phase accumulated by the mode as it propagates along the waveguide. Thus, the modes supported by a waveguide can be found out by analysing the cross section in $x - y$ plane, which reduces the problem to two dimensions. Here $\gamma = -\alpha + j\beta$ is the complex propagation constant. So, Eq. B.2 can be written as

$$\vec{E}(x, y, z) = A(x, y)e^{-\alpha z}e^{\beta z} \tag{B.4}$$

Here $\alpha = k_0\kappa$ is responsible for attenuation, with κ being the extinction coefficient. $\beta = k_0 n_0$ for wave oscillation with n_0 being the ordinary refractive index. $n_{eff} = n_0 + j\kappa$ is the effective refractive index of the waveguide accounting for gain or loss in the waveguide.

Substituting Eq. B.2 and Eq. B.3 into Eq. B.1

$$
\begin{aligned}
\frac{\partial A_z}{\partial y'} - \tilde{\gamma}A_y = \mu_{xx}B_x \qquad && \frac{\partial B_z}{\partial y'} - \tilde{\gamma}B_y = \varepsilon_{xx}A_x \\
\tilde{\gamma}A_x - \frac{\partial A_z}{\partial x'} = \mu_{yy}B_y \qquad && \tilde{\gamma}B_x - \frac{\partial B_z}{\partial x'} = \varepsilon_{yy}A_y \\
\frac{\partial A_y}{\partial x'} - \frac{\partial A_x}{\partial y'} = \mu_{zz}B_z \qquad && \frac{\partial B_y}{\partial x'} - \frac{\partial B_x}{\partial y'} = \varepsilon_{zz}A_z
\end{aligned}
\tag{B.5}
$$

where $\tilde{\gamma} = jn_{eff}$.

The derivatives can be approximated using finite differences when discretising the field components in the Yee grid scheme [3]. Thus Eq.

B.5 becomes [1]

$$\frac{A_z|_{i,j+1} - A_z|_{i,j}}{\Delta y'} - \tilde{\gamma}A_y|_{i,j} = \mu_{xx}|_{i,j}B_x|_{i,j}$$

$$\tilde{\gamma}A_x|_{i,j} - \frac{A_z|_{i+1,j} - A_z|_{i,j}}{\Delta x'} = \mu_{yy}|_{i,j}B_y|_{i,j}$$

$$\frac{A_y|_{i+1,j} - A_y|_{i,j}}{\Delta x'} - \frac{A_x|_{i,j+1} - A_x|_{i,j}}{\Delta y'} = \mu_{zz}|_{i,j}B_z|_{i,j}$$

$$\frac{B_z|_{i,j} - B_z|_{i,j-1}}{\Delta y'} - \tilde{\gamma}B_y|_{i,j} = \varepsilon_{xx}|_{i,j}A_x|_{i,j}$$

$$\tilde{\gamma}B_x|_{i,j} - \frac{B_z|_{i,j} - B_z|_{i-1,j}}{\Delta x'} = \varepsilon_{yy}|_{i,j}A_y|_{i,j}$$

$$\frac{B_y|_{i,j} - B_y|_{i-1,j}}{\Delta x'} - \frac{B_x|_{i,j} - B_x|_{i,j-1}}{\Delta y'} = \varepsilon_{zz}|_{i,j}A_z|_{i,j}$$

(B.6)

All the sub-equations of Eq. B.6 is written for every discrete cell in the grid containing the waveguide to be simulated. The ε and μ values are stored along the diagonal of a matrix of dimension $m \times n$ where m and n are the number of cells along the x and y direction respectively. The field values of the 2D grid as put as elements in a column vector $(mn \times 1)$. The set of m field values along the x direction is stored as elements of the column matrix. This process is repeated for n rows and are stored one after another in the final $mn \times 1$ column. A derivative matrix $D_{x'}^A$ is constructed for the relation $D_{x'}^A A_z = \frac{\partial A_z}{\partial x'} \cong \frac{A_z|_{i+1,j} - A_y|_{i,j}}{\Delta x'}$

for example for a 3×3 grid as

$$D_{x'} = \frac{1}{\Delta x'} \begin{bmatrix} -1 & 1 & & & & & & & \cdots \\ & -1 & 1 & & & & & & \cdots \\ & & -1 & 1 & & & & & \cdots \\ & & & -1 & 1 & & & & \cdots \\ \cdots & & & & -1 & 1 & & & \\ & \cdots & & & & -1 & 1 & & \\ & & \cdots & & & & -1 & 1 & \\ & & & \cdots & & & & -1 & 1 \\ & & & & \cdots & & & & -1 \end{bmatrix} \qquad (B.7)$$

The matrix $D_{x'}$ is a sparse matrix and is derived from the finite difference expression of Eq. B.6. In deriving the $D_{x'}$ matrix Dirichlet boundary conditions which considers field values to be zero at the boundary of the grid. Since the guided modes will be confined to the centre of the grid, Dirichlet boundary condition is valid for simulating a waveguide. Similar matrix operator expressions can be derived for $D_{y'}$ and other operators for any $m \times n$ grid. Thus Eq. B.6 simplifies to a set of matrix equations as

$$\begin{aligned} D_{y'}^A A_z - \tilde{\gamma} A_y &= \mu_{xx} B_x \quad - (a) \\ \tilde{\gamma} A_x - D_{x'}^A A_z &= \mu_{yy} B_y \quad - (b) \\ D_{x'}^A A_y - D_{y'}^A A_x &= \mu_{zz} B_z \quad - (c) \\ D_{y'}^B B_z - \tilde{\gamma} B_y &= \varepsilon_{xx} A_x \quad - (d) \\ \tilde{\gamma} B_x - D_{x'}^B B_z &= \varepsilon_{yy} A_y \quad - (e) \\ D_{x'}^B B_y - D_{y'}^B B_x &= \varepsilon_{zz} A_z \quad - (f) \end{aligned} \qquad (B.8)$$

Solving for A_z and B_z in Eq. B.8f and Eq. B.8c and then substituting them in B.8a, b, d and e:

$$D^A_{x'}\epsilon^{-1}_{zz}D^B_{y'}B_x - (D^A_{x'}\epsilon^{-1}_{zz}D^B_{x'} + \mu_y y)B_y = -\tilde{\gamma}A_x$$
$$(D^A_{y'}\epsilon^{-1}_{zz}D^B_{y'} + \mu_{xx})B_x - D^A_{y'}\epsilon^{-1}_{zz}D^B_{x'}B_y = -\tilde{\gamma}A_y$$
$$D^B_{x'}\mu^{-1}_{zz}D^A_{y'}A_x - (D^B_{x'}\mu^{-1}_{zz}D^A_{x'} + \epsilon_{yy})A_y = -\tilde{\gamma}B_x$$
$$(D^B_{y'}\mu^{-1}_{zz}D^A_{y'} + \epsilon_{xx})A_x - D^B_{y'}\mu^{-1}_{zz}D^A_{x'}A_y = -\tilde{\gamma}B_y$$

(B.9)

Writing Eq. B.9 in matrix form:

$$P\begin{bmatrix} B_x \\ B_y \end{bmatrix} = -\tilde{\gamma}\begin{bmatrix} A_x \\ A_y \end{bmatrix}$$

$$Q\begin{bmatrix} A_x \\ A_y \end{bmatrix} = -\tilde{\gamma}\begin{bmatrix} B_x \\ B_y \end{bmatrix}$$

(B.10)

where $P = \begin{bmatrix} D^A_{x'}\epsilon^{-1}_{zz}D^B_{y'} & -(D^A_{x'}\epsilon^{-1}_{zz}D^B_{x'} + \mu_y y) \\ (D^A_{y'}\epsilon^{-1}_{zz}D^B_{y'} + \mu_{xx}) & D^A_{y'}\epsilon^{-1}_{zz}D^B_{x'} \end{bmatrix}$

and $Q = \begin{bmatrix} D^B_{x'}\mu^{-1}_{zz}D^A_{y'} & -(D^B_{x'}\mu^{-1}_{zz}D^A_{x'} + \epsilon_{yy}) \\ (D^B_{y'}\mu^{-1}_{zz}D^A_{y'} + \epsilon_{xx}) & D^B_{y'}\mu^{-1}_{zz}D^A_{x'} \end{bmatrix}$

Solving for B in Eq. B.10:

$$\Omega^2\begin{bmatrix} A_x \\ A_y \end{bmatrix} = -\tilde{\gamma}^2\begin{bmatrix} A_x \\ A_y \end{bmatrix}$$

(B.11)

where $\Omega^2 = PQ$ Eq. B.11 is a standard eigen value problem $Fx = \lambda x$ with $F = \Omega^2$ and $\lambda = -\tilde{\gamma}^2$ is the eigen value matrix. x is the eigen vector matrix consisting information of the field distributions.

References

[1] R. C. Rumpf, *Electromagnetic and Photonic Simulation for the Beginner: Finite-Difference Frequency-Domain in MATLAB.* Artech House, 2022.

[2] https://empossible.net/academics/emp5337/, "Computational electromagnetics."

[3] K. Yee, "Numerical solution of initial boundary value problems involving maxwell's equations in isotropic media," *IEEE Transactions on antennas and propagation*, vol. 14, no. 3, pp. 302–307, 1966.